Electronic Many–Body Effects in organic Thin Films and Interfaces

Dissertation zur Erlangung des naturwissenschaftlichen Doktorgrades der Julius–Maximilians Universität Würzburg

vorgelegt von

Marc Häming

aus Bad Friedrichshall

Würzburg, 2010

Eingereicht am 04.11.2010 bei der Fakultät für Physik und Astronomie

Gutachter der Dissertation:

1. Gutachter: Prof. Dr. E. Umbach, Universität Würzburg
2. Gutachter: Prof. Dr. R. Claessen, Universität Würzburg

Prüfungskomitee im Promotionskolloquium:

1. Prüfer: Prof. Dr. E. Umbach, Universität Würzburg
2. Prüfer: Prof. Dr. R. Claessen, Universität Würzburg
3. Prüfer: PD. Dr. R. F. Fink, Universität Würzburg

Tag des Promotionskolloquiums: 11.02.2011

Contents

Zusammenfassung

Die elektronische Struktur spielt eine wichtige Rolle für viele Materialeigenschaften, z. B. bei Katalysatoren und elektronischen Bauteilen. Die Forschung an organischen Materialien hat in den letzten Jahrzehnten stark zugenommen. Dies liegt daran, dass es organische Materialien ermöglichen, effiziente und flexible Bauelemente recht kostengünstig in größeren Massen herzustellen. Besonderes Interesse gilt hierbei den optischen und elektronischen Eigenschaften. Weil elektronische Bauteile in der Regel aus verschiedenen Schichten aus unterschiedlichen Materialien aufgebaut sind, wird ihre Leistungsfähigkeit stark von den elektronischen Eigenschaften an den unterschiedlichen Grenzflächen beeinflusst. Daher ist es für eine gezielte Entwicklung solcher Bauteile wichtig, dass man die fundamentalen elektronischen Eigenschaften im Volumen und an den unterschiedlichen Grenzflächen gut versteht, z. B. an Grenzflächen zwischen Organik und Metall, Organik und Organik sowie zwischen organischen und anorganischen Halbleitern.

Die Ergebnisse dieser Arbeit tragen zu all diesen Aspekten etwas bei. Außerdem wird gezeigt, dass im Allgemeinen Elektronenspektroskopien sehr hilfreich sind, um Oberflächen und Grenzflächen zu untersuchen. Die Daten in dieser Arbeit weisen darauf hin, dass Vielteilchen-Effekte in den untersuchten organischen Dünnschichten eine wichtige Rolle spielen, besonders an Grenzflächen mit starker Wechselwirkung. Diese Effekte können für die Eigenschaften von Materialien durchaus von Bedeutung sein.

Im ersten Teil dieser Dissertation wird eine systematische Serie von Polyacen Molekülen mit NEXAFS Spektroskopie untersucht. Der Vergleich mit Rumpfniveau und IPES Daten zeigt, dass Rumpfanregungen und Rumpfexzitonen als Vielteilchenanregungen verstanden werden müssen. Dieser Befund impliziert zum Beispiel, dass eine große Exzitonenbindungsenergie nicht automatisch bedeutet, dass das angeregte Elektron nahe am Rumpfloch lokalisiert sein muss. Da diese Effekte auch für Valenzexzitonen auftreten, spielen sie auch bei der Separation von Ladungsträgern oder Rekombination von Elektronen und Löchern eine Rolle.

Im nächsten Kapitel werden fundamentale Effekte in organischen Multilagenfilmen und Metall–Organik Grenzflächen mit Rumpfniveau- und NEXAFS Spektroskopie untersucht. Dies wird anhand der systematisch ausgewählten Molekülserie BTCDA, BTCDI, PTCDA, PTCDI durchgeführt. Es wird gezeigt, dass sich im Falle von

starker Wechselwirkung an den Grenzflächen eine Substrat–Adsorbat–Zustandsdichte bildet, die zu starken Ladungstransfersatelliten führen kann, ähnlich wie sie für Übergangsmetallkomplexe bekannt sind. Die experimentellen Daten können mit einem Model verstanden werden, das das *Single Impurity Anderson Modell* mit dem Ansatz von *Sawatzky et al.* zur Beschreibung von Ladungstransfersatelliten in Übergangsmetallkomplexen vereint. Diese Herangehensweise ist equivalent zum Ansatz von Gunnarsson und Schönhammer für Adsorbate. Sie erlaubt jedoch eine relativ einfache semiquantitative Auswertung der experimentellen Daten. Ein Vergleich der Spektren für verschiedene Adsorbatschichten weist darauf hin, dass Vielteilcheneffekte besonders dann stark sind, wenn die vom LUMO abgeleitete Zustandsdichte teilweise gefüllt ist.

Im dritten Teil dieser Arbeit wird exemplarisch jeweils ein organischer Multilagenfilm (SnPc), eine Organik–Metall Grenzfläche mit starker Wechselwirkung (SnPc/Ag) sowie eine Organik–Organik Grenzfläche (SnPc/PTCDA/Ag) mit resonanter Auger Spektroskopie untersucht. Durch den Vergleich der Daten wird der Beitrag der Vielteilcheneffekte zu den Autoionisationsspektren klar. Demnach laufen die Elektron–Vibrations–Kopplung und der Adsorbat–Substrat Ladungstransfer auf der Zeitskala der Rumpflochlebensdauer ab. Außerdem ist die Wechselwirkung an der Organik–Organik Grenzfläche zwischen SnPc und PTCDA sehr schwach, vergleichbar mit der intermolekularen Wechselwirkung in Multilagenschichten trotz einer parallelen Verschiebung aller elektronischen Niveaus in der SnPc Schicht.

Desweiteren wird eine relativ schwache aber dennoch signifikante Elektron–Elektron Korrelation in den oberen Valenzorbitalen gefunden, die eine wichtige Rolle für den Ladungstransfer zwischen Adsorbat und Substrat spielt. Daher werden im letzten Teil dieser Dissertation die stark gekoppelten Adsorbat Filme kurz im Kontext des Hubbard Modells diskutiert. Mit den Daten aus dieser Arbeit können solche Monolagenfilme in den Bereich für mittlere Korrelationsstärke eingeordnet werden. Folglich kann man für solche Adsorbatfilme Eigenschaften erwarten, die dem außergewöhnlichen Verhalten stark korrelierter Systeme ähneln, für die z. B. Mott Metall–Isolator Übergänge, interessante magnetische Eigenschaften und Supraleitung beobachtet wurden.

Zusätzlich werden im Anhang kurz einige Ergebnisse aus den Untersuchungen an einem Schichtsystem diskutiert, das aus einer Monolage Alkylketten auf dem anorganischen Halbleiter Silizium besteht und auch als self–assembled monolayer (SAM) bekannt ist. An den Alkylketten wird exemplarisch gezeigt, dass die elektronische Bandstruktur von kurzen, sich endlich wiederholenden Einheiten sehr gut durch einen relativ einfachen Quantentrog–Ansatz wiedergegeben werden kann. Im Prinzip kann dieser Ansatz auch auf mehrdimensionale Systeme angewendet werden. Daher ist er für die Beschreibung von $E(k)$ Relationen in intermediären Systemen mit endlichen Wiederholeinheiten sehr nützlich. Desweiteren wird in

den Photoelektronen- und NEXAFS Spektren eine starke Wechselwirkung an der alkyl/Si Grenzfläche beobachtet. Es wird gezeigt, dass die Grenzflächenzustände durch moderate Röntgenstrahlung modifiziert werden können, was wiederum die Eigenschaften für Ladungstransport durch die Alkylschicht beeinflusst.

Abstract

The electronic structure plays an important role for many material properties, e.g. for catalysts or electronic devices. Research on organic materials has strongly increased during recent decades. This is predominantly due to the prospect of cheap, efficient and flexible devices. Therefore the optical and electronic properties of organic materials are of particular interest. As electronic devices usually consist of several layers of different materials their performance is very sensitive to the electronic properties at the various interfaces. Therefore a detailed understanding of the fundamental electronic properties in the bulk and at different interfaces, e.g. organic–metal, organic–organic and organic–inorganic semiconductor interfaces, is important for a systematic and specific development of devices.

The results of this thesis contribute to the understanding of all these aspects. Furthermore, it is demonstrated that electron spectroscopies are very useful for studying surfaces and interfaces. Additionally it is shown, that many–body effects are observed for organic thin films, in particular at interfaces with strong interaction. It is discussed that these effects can have implications for the general material properties.

In the first part of this thesis a systematic series of polyacene molecules is investigated with NEXAFS spectroscopy. The comparison of the data with core level and IPES data indicates that core excitations and core excitons need to be understood as many–body excitations. This finding implies for example that a high exciton binding energy is not necessarily associated with strong localization of the excited electron at the hole. As these effects apply also for valence excitons they can be relevant for the separation of charges and for the electron–hole recombination at interfaces.

In the next chapter some fundamental effects in organic multilayer films and at organic–metal interfaces are studied with core level and NEXAFS spectroscopy. In this context a series of selected molecules is investigated, namely BTCDA, BTCDI, PTCDA and PTCDI. It is shown that in case of strong interface interaction a density of adsorbate–substrate states is formed which can lead to significant charge transfer satellites in the PES and NEXAFS spectra, similar to what is known for transition metal compounds. Moreover, it is demonstrated that the data can be

modeled qualitatively by a basic approach which fuses the *single impurity Anderson model* with the description of charge transfer satellites by *Sawatzky et al.* This approach, which is equivalent to that of *Gunnarsson* and *Schönhammer*, allows even a relatively simple semi–quantitative analysis of the experimental data. The comparison of different adsorbate layers indicates that these many–body effects are particularly strong in case of partial occupation of the LUMO derived DOS.

In the third part an organic multilayer film (SnPc), an organic–metal interface with strong coupling (SnPc/Ag) and an organic–organic interface (SnPc/PTCDA/Ag) are studied exemplarily with resonant Auger spectroscopy. The comparison of the data gives evidence for the contribution of many–body effects to the autoionization spectra. Furthermore, it is found that the electron–vibration coupling and the substrate–adsorbate charge transfer occurs on the time scale of the core hole life time. Moreover, the interaction at the organic–organic interface is weak, comparable to the intermolecular interaction in the multilayer films, despite a considerable rigid level shift for the SnPc layer.

Furthermore, weak but significant electron–electron correlation is found for the molecular frontier orbitals, which are important for the substrate–adsorbate charge transfer. Therefore, these strongly coupled adsorbate films are briefly discussed within the context of the Hubbard model in the last part of this thesis. From the data derived in this work it can be estimated that such monolayer films are in the regime of medium correlations. Consequently one can expect for these adsorbate films properties which are related to the extraordinary behavior of strongly correlated materials, for which Mott metal–insulator transitions, sophisticated magnetic properties and superconductivity can be observed.

Additionally some results from the investigation of alkyl/Si self–assembled monolayers are briefly discussed in the appendix. It is demonstrated exemplarily for the alkyl chains that the electronic band structure of short, finitely repeating units can be well modeled by a comparatively simple quantum well approach. In principle this approach can also be applied to higher dimensional systems, which makes it very useful for the description of $E(k)$ relations in the regime of repeating units of intermediate length. Furthermore, the photoelectron and NEXAFS spectra indicate strong interaction at the alkyl/Si interface. It was found that the interface states can be modified by moderate x–ray irradiation, which changes the properties for charge transport through the SAM.

1

Introduction

During the recent decades physics at the nano scale has become more and more important. Chemical reactions and material properties are often related to effects on the molecular scale. The interest in catalytic reactions, downsizing of devices, the use of self-organization effects for tailoring new materials and the prospect of comparatively cheap and simple production of intelligent devices have been driving this field of research. In the meantime a certain level of knowledge and know how has been reached, and nowadays it is already taken advantage of so called nano physics for designing and controlling material properties. However, many aspects are still not understood, and the field is open for exciting discoveries. Therefore, further detailed and fundamental studies on the atomic and molecular scale are essential.

Research on semiconductors made from organic molecules has been growing tremendously during the recent decades. These materials are interesting for a wide range of applications because of their promising, new properties. Organic light emitting diodes (OLEDS) for example are already used in applications where high efficiency, flexible devices and low cost fabrication play a role. However, this is only the beginning of a development which will bring OLEDS, organic solar cells and other organic semiconductor devices in every days life. Moreover, a detailed understanding of the fundamental physics of (well ordered) organic thin films allows to tailor materials and completely new devices, which will improve quality of life significantly while being eco–friendly. [1–3]

In general such semiconductor devices are comparatively complex. Organic solar cells for example usually consist of a blend of different materials or of several thin film layers, so that the device contains many interfaces, e.g. organic–organic interfaces, organic–metal interfaces or organic–inorganic semiconductor interfaces. Hence, the electrical and optical properties of such devices depend not only on the bulk properties of the different layers, but also interfaces play a dominant role. Therefore, they are of particular interest with respect to organics.

This work contributes to all these aspects, to the electronic properties in the bulk of organic thin films (*chapters 3 – 5*) as well as to the properties of different interfaces, in particular organic–metal (*chapters 4* and *5*), organic–organic (*chapter 5*)

and organic–inorganic semiconductor interfaces (*appendix E*). Several methods are established for such investigations which probe the upper valence regime, e.g. scanning tunneling spectroscopy, photoluminescence, UV/VIS and Raman spectroscopy. However, for studying the complete electronic structure, in particular in the case of organics, **p**hoto**e**lectron **s**pectroscopy (PES) is the method of choice. Since *Hertz's*, *Planck's* and *Einstein's* investigations of the photo–effect it is known that the absorption of a photon leads to the emission of one or more electrons, which provides information about the electronic structure. PES is very powerful for studying the electronic structure of thin films and interfaces with high surface sensitivity [4] due to the relatively short electron mean free path and the high photoemission cross section.

This thesis aims primarily at two general aspects: Firstly, it is intended to demonstrate how PES can help to study organic thin films in general and interfaces in particular. Many different samples were investigated with several spectroscopy techniques like core level spectroscopy, **n**ear **e**dge **x**-ray **a**bsorption **f**ine **s**tructure measurements (NEXAFS), resonant Auger spectroscopy and photon–energy dependent **u**ltra–violet **p**hotoelectron **s**pectroscopy (UPS) in order to study various aspects of the electronic structure. Some results appeared already in the literature or are close to publication. [A1–A7] These unpublished results which are considered to be helpful for a detailed understanding of the fundamental electronic properties in organic materials are discussed in detail here. Secondly, some insight should be provided into some effects which have been kind of exotic for organics [5–7] as they are common for inorganic (strongly correlated) materials. In particular many–body effects have been well studied for transition metal compounds, metals and alloys of heavy elements and very recently even for atomic adsorbates. [8–15] They can influence the material properties considerably, which can lead to phenomena like Mott metal–insulator transitions, magnetism, Kondo effect or superconductivity. [13, 16, 17] These many–body effects can be related to characteristic features of the electronic structure which can be well observed in PES experiments, e.g. charge transfer satellites and a very narrow fine structure at the Fermi level. It has not been expected to observe similar material properties for organics. However, it will be shown in the following that one can observe spectral features for organic thin films which seem to be similar to what is known for correlated materials, in particular at organic–metal interfaces. Note that such effects have only been observed for fullerenes and the quasi–one–dimensional organic conductor TTF–TCNQ yet. [5, 18–27]

At first a careful comparison of the C K–NEXAFS spectra with C 1s core level and IPES data of different polyacene multilayer films from benzene to pentacene illustrates the influence of many–body excitations in NEXAFS for weakly interaction adsorbates. Secondly, a core level and NEXAFS investigation of different adsorbate multilayer and monolayer films on a Ag(111) substrate suggests that many–body ex-

citations play a significant role in case of comparatively strong adsorbate–substrate interaction. Moreover, adsorbate–substrate charge transfer is discussed in analogy to the charge transfer satellites for transition metal compounds. Furthermore, it is demonstrated that the core level and NEXAFS spectra can provide qualitative and, to some extent, even quantitative information about the interface interaction when combining the single impurity Anderson model with an approach for charge transfer satellites developed by Sawatzky *et al.* [8, 28]

In the third step a multilayer film, a strongly interacting organic–metal interface and an organic–organic interface are investigated by resonant Auger spectroscopy and compared to each other. Again significant indications to many–body excitations at the organic–metal interface are observed. The interference effects in the resonant Auger spectra show that they occur on the time scale of the core hole life time. Finally, the implications of these many–body effects are briefly discussed taking recent findings from other (former) group members into account.

2

Experimental and technical aspects

The photo–effect was discovered in 1887 by *H. Hertz* and his assistant *W. Hallwachs*. Hertz found out that a sparkover was induced easier when the spark coil was illuminated by ultraviolet light. [29] In more detailed studies Hallwachs observed that irradiation of a zinc plate with UV light induces an electrical current. Later, in 1900 *P. Lenard* discovered that the energy of the emitted electrons does not change but only the number of emitted electrons when tuning the intensity of the incident light. [30] These observations were not in agreement with *J. C. Maxwell's* theory of light. Only in 1905 *A. Einstein* could explain the photo–effect by the wave–particle dualism of light [31] which led to the fundamental relation

$$E_{kin} = h\nu - E_B - \Phi. \tag{2.1}$$

Later *R. A. Millikan* could determine *Planck's* constant in a series of experiments from 1912 to 1915 by tuning the frequency of the UV light and adjusting a retarding voltage to the maximum kinetic energy of the photoemitted electrons. [32]

The principle of photoelectron spectroscopy as it is carried out today is still the same. The light source is either a gas discharge lamp, an x–ray tube or a synchrotron source and the electrons are detected by sophisticated analyzers with high energy resolution and the possibility to map the spatial and angular distribution of the photoelectrons. Depending on the excitation energy these experiments are called *ultra–violet photoelectron spectroscopy* (UPS) for photon energies below 100 eV and *x–ray photoelectron spectroscopy* (XPS) for photon energies above 100 eV. The high brilliance of modern synchrotron radiation sources allows experiments which need high photon flux, high energy resolution, a small spot size of the source and a small divergence of the photon beam. Another advantage of a synchrotron source is that in general the photon energy can be tuned continuously, which allows absorption measurements in the x–ray regime. It is common to refer to those measurements close to the absorption edge as *near edge x–ray absorption fine structure* (NEXAFS) spectroscopy. Furthermore, (core) excited states where a hole was created in a lower lying shell can either decay by emission of a photon (fluorescence decay)

or by emission of an electron (Auger decay), which results in a characteristic energy distribution for the emitted photons or electrons, respectively. These energy distribution curves are measured by *x–ray emission spectroscopy* (XES) and *Auger electron spectroscopy* (AES), respectively. Moreover, *resonant Auger spectroscopy* and *resonant PES* are experiments in which the photon energy is tuned through a NEXAFS regime and for each photon energy the energy distribution of the emitted electrons is recorded which has, to first approximation, contributions from Auger electrons and direct photoelectrons. — See chapter 5 for a more detailed discussion of *autoionization*. — The analog experiment for x–ray emission is known as *resonant inelastic x–ray scattering* (RIXS). As all these spectroscopy techniques are well established they are not discussed here any further but it is referred to [33–36] for more details.

2.1 Experimental conditions

High-resolution core and valence level PES data were recorded at BESSY II at the UE52–PGM undulator beamline ($E/\Delta E > 14000$ at 400 eV photon energy, with cff = 10 and 20 μm exit slit). This beamline is described in detail in [37]. For the PES experiments the setup was adjusted to normal emission geometry with 60° angle of incidence with respect to the surface normal and p–polarized light if not stated differently. A SCIENTA R4000 electron analyzer was operated with a constant pass energy of 50 eV and 300 μm entrance slit, which results in an energy resolution of $\Delta E = 35$ meV. As the energy scale was carefully calibrated to the Ag $3d_{5/2}$ and $3d_{3/2}$ photoemission lines or the Fermi edge after each measurement the absolute accuracy of the energy scale is better than 30 meV. [38]

During the experiments all samples were carefully checked for radiation damage and spurious adsorbates. In order to minimize any effects from irradiation, the light spot was scanned over the sample so that no significant degradation could be observed. Finally, it was averaged over several spectra in order to obtain better statistics.

2.2 Data processing

This work concentrates on PES, NEXAFS spectroscopy and resonant Auger spectroscopy. The respective data needs to be normalized and calibrated carefully in order to obtain detailed and reliable information, in particular the NEXAFS and resonant Auger data. Hence, the normalization of the data is briefly described in the following.

2.2.1 Photoelectron spectra

All core level photoelectron spectra are normalized by the standard procedure. First they are divided by the hight of the secondary electron back ground 3 eV below the peak maximum towards lower binding energy. Then the secondary electron background was approximated by a power law so that the curvature of the background at energies above and below the core level signal was well reproduced. This curve was then subtracted. In case of the monolayer films a Shirley background was subtracted additionally. [33]

2.2.2 NEXAFS spectra

The NEXAFS spectra were carefully normalized as described in [38]. Accordingly the curve for the partial yield signal and the sample current were divided by the ring current and the I_0 flux curve of the beamline. The latter was obtained by recording the respective partial yield signal and the sample current for a clean Ag(111) sample under exactly the same conditions as for the measurements of the organic thin films. Moreover, energy calibration is very important for proper normalization of the NEXAFS spectra. Consequently, the photon energy was calibrated right before or after the NEXAFS scans by recording the Ag 3d lines or the Fermi edge of the Ag(111) substrate, or by recording the Au 4f lines of a gold foil in case of several monolayer thick adsorbate films. The wave length λ of the incident x–ray light was corrected for the respective offset $\Delta\lambda$.

2.2.3 2D autoionization spectra

The 2D autoionization spectra were obtained by tuning the photon energy through the respective NEXAFS regime and recording an angle integrated *energy distribution curve* (EDC) for each photon energy with the photoelectron analyzer. In principle the normalization of these maps is analogous to what has been discussed for the NEXAFS spectra, except that the I_0 curve was not recorded with a partial electron yield detector but also with the electron analyzer. This was done by running the analyzer in fixed mode and *constant initial state* (CIS) mode so that a few eV wide range of the upper valence regime of the clean substrate was directly imaged onto the channel plate of the detector. Then the photon energy was tuned through the NEXAFS regime while always the same range of binding energy was recorded, which resulted in a typical 2D spectrum as it is shown in Fig. 2.1. The I_0 flux curve was then obtained by integrating this spectrum in the kinetic energy direction. Consequently, the 2D autoionization spectra from organic thin films were first carefully calibrated in energy and then divided by the ring current and this I_0 curve.

2.2.4 EDCS in fixed mode

The sensitivity of the detector varies with the position on the channel plate. This inhomogeneity is averaged out when recording a regular angle integrated spectrum in swept mode as it is done for the PES data and the 2D autoionization maps. However, when recording a narrow energy window of the upper valence band in fixed mode this detector response function needs to be taken into account. Therefore a featureless and flat part of the valence regime is recorded in both, fixed mode and swept mode. Consequently, the detector response function can be obtained by dividing the angle integrated fixed mode spectrum by the respective swept mode spectrum as it is illustrated in Fig. 2.2. As a result all fixed mode spectra can be corrected for the inhomogeneous detector response by dividing them by the curve in Fig. 2.2 (b). For the sake of a small signal–to–noise ratio the detector response was approximated by the parabolic curve which is plotted as solid line.

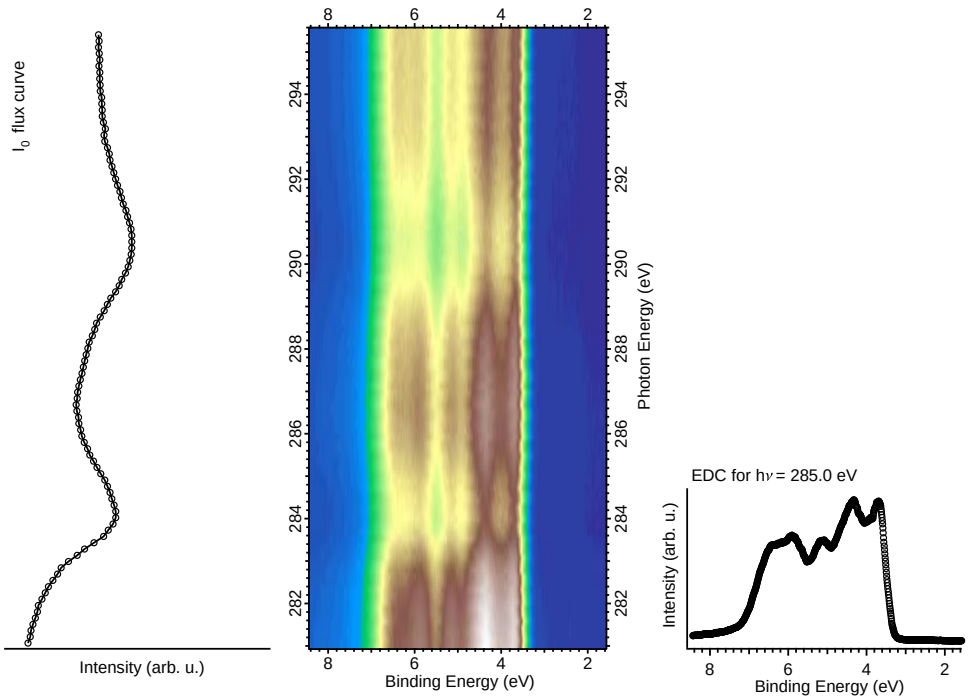

Figure 2.1: Typical I_0 spectra for normalization of 2D autoionization maps. Middle: The 2D spectrum was recorded at 70° angle of incidence and p–polarized light by monitoring the Ag 4d signal of a clean Ag(111) crystal for different photon energies. Left: The 1D spectrum was obtained by integrating the 2D spectrum in the dimension of the kinetic energy or binding energy, respectively. Right: The EDC for $h\nu = 285.0$ eV is plotted.

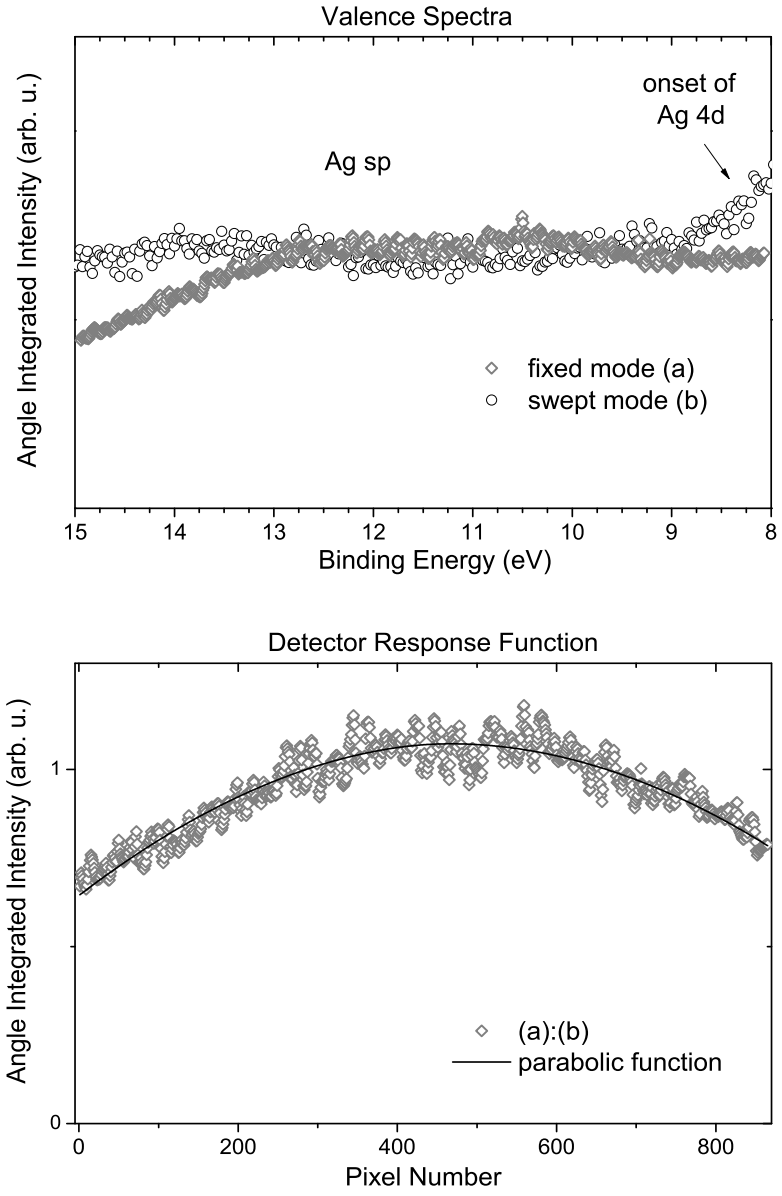

Figure 2.2: R4000 detector response function for fixed mode measurements. Top: Angle integrated spectra of a featureless part of the valence regime measured (a) in fixed mode and (b) in swept mode. Bottom: Experimentally derived detector response function including noise and its approximation by a parabolic curve.

2.3 Sample preparation

As many properties of organic semiconductors are influenced by intermolecular, surface and interface interaction, aspects like growth mode, doping and impurities play an important role. Hence, well defined model systems are very important when studying fundamental physical interrelations. Therefore, all samples were prepared under ultra–high vacuum. For the in–situ film preparation the Ag(111) substrate was cleaned by several sputter and annealing cycles, which resulted in a well ordered, clean substrate as derived from LEED and PES. In general the organic thin films were prepared from sublimated powder (if not stated differently) by organic molecular beam deposition from a Knudsen cell at a pressure better than $1 \cdot 10^{-8}$ mbar. The thickness of the multilayer films was determined by the attenuation of the Ag 3d photoemission lines assuming a homogeneous layer growth.

2.3.1 Polyacenes

Commercially available materials of high purity were purchased from Aldrich and were directly used without further purification. The sample was kept at $-120°$ C during the preparation of the organic multilayer films. Benzene and naphthalene were let into the preparation chamber via a leak valve. Antracene, tetracene and pentacene were deposited from a Knudsen cell with 84° C, 147° C and 260° C evaporation temperature, respectively.

2.3.2 SnPc/Ag(111)

The SnPc/Ag(111) thin films were prepared at $-50°$ C sample temperature so that in case of the multilayer films the roughness of the film was reduced compared to preparations at room temperature. Two times sublimated powder was evaporated from a Knudsen cell at 367° C. For the preparation of a monolayer film the sample was annealed afterwards for 5 min at 290° C. The evaporation rate was calibrated by the attenuation of the Ag 3d substrate signal for film thicknesses of ca. 5 ML, for which the film roughness is still relatively small so that layer–by–layer growth can be assumed. This leads to an accuracy in coverage of better than ± 1 ML for the SnPc multilayer films discussed in *chapter 5*.

2.3.3 SnPc/PTCDA/Ag(111)

The SnPc/PTCDA/Ag(111) heteromolecular thin films were prepared at room temperature from PTCDA and SnPc powder. First, a 1 ML PTCDA/Ag(111) film was prepared by depositing a thick film of PTCDA followed by annealing at 295° C for 5 min. Afterwards, SnPc was evaporated on top of the PTCDA monolayer film. For the monolayer regime the SnPc evaporation rate was calibrated to the intensity of the N 1s signal and double checked by the attenuation of the Ag 3d photoemission lines. Accordingly the accuracy in coverage was better than ±0.15 ML.

2.3.4 Tetracarboxylic acid di-anhydrides and tetracarboxylic acid di-imides

The molecular thin films from 3,3',4,4'–**b**enzophenone **t**etra**c**arboxylic **d**i**a**nhydride (BTCDA), 3,3',4,4'–**b**enzophenone **t**etra**c**arboxylic **d**i**i**mide (BTCDI), 3,4,9,10–**p**erylene **t**etra**c**arboxylic **d**i**a**nhydride (PTCDA) and 3,4,9,10–**p**erylene **t**etra**c**arboxylic **d**i**i**mide (PTCDI) were evaporated from a Knudsen cell onto the clean Ag(111) surface, analogously to what was described for the SnPc/Ag(111) films. In order to get smoother multilayer films the different samples were cooled to temperatures between −100° C and −70° C. The PTCDA and PTCDI monolayer films were obtained by annealing a multilayer film for 5 min at 295° C. The BTCDA monolayer films were prepared by annealing a multilayer sample for 5 min at 60° C. For the BTCDI monolayer films several few minutes long annealing cycles were necessary with temperatures around 110° C as it is described in more detail in *section 4.2.3* and *appendix B*.

2.3.5 Alkyl/Si(111) SAMs

Densely packed **s**elf–**a**ssembled **m**onolayer films (SAM) of alkyl molecules on n-Si(111) substrates (1—15 Ω cm) were prepared by thermally induced hydrosilation of alkanes on H–terminated Si(111) substrates at the Weizmann Institute (Israel) and at the University of New South Wales (Australia). [39–42] Various samples were produced with different alkyl chain lengths between C12 and C18, and were characterized by water contact angle, ellipsometry measurements, and Fourier transform infrared spectroscopy. Only samples with evidence for a dense molecular layer were chosen for further experiments and shipped to BESSY under nitrogen atmosphere. The samples were then checked with PES for contaminations and

possible oxidation of the interface by monitoring the O 1s and Si 2p signals of Si_xO_y.

3

Core excitation and electronic relaxation in molecular multilayer films

Core level photoelectron spectroscopy and NEXAFS can be considered as element and site specific probes of the electronic structure with high sensitivity to the chemical environment. [4,33,35] Each chemical element has a specific electronic structure, which leads to a unique fingerprint in the photoelectron and x–ray absorption spectra. Furthermore, the electronic structure of a certain element is also influenced by its chemical environment, in particular the number and the type of atoms in its environment. Such modifications lead to energy shifts in the photoelectron and in the NEXAFS spectra and to variations of the cross section. [43, 44] Such an energy shift, which is also known as chemical shift, can be of the order of up to several eV. The ionization potential and the binding energy of the C 1s electrons, for example, can differ by up to 10 eV between saturated hydrocarbons and fluorocarbons. [33,35] The modification of the electronic structure is often (methodically) classified by two aspects, namely the change of the electronic ground state and the change of the reaction on the creation of a hole, which is also known as initial and final state effects or electronic relaxation, respectively. Both aspects are of interest when studying the electronic structure. Unfortunately, the relative contribution of each effect to certain spectral modifications can only be estimated by systematic studies and a comprehensive comparison of various spectra, assisted by theoretical considerations.

As the main part of this work deals with π–conjugated molecules, it is useful to demonstrate the implications of these two aspects for this class of materials. Therefore the chemical surrounding of a certain atomic site or molecular fragment is modified systematically and the influence on the electronic structure is monitored. A series of planar molecules of different size with an extended π–system can be a good model system for such an investigation. Hence, the series of polycyclic aromatic hydrocarbons made up of linearly fused benzene rings was chosen for this investigation. Starting from benzene one can monitor the effect of adding more and more benzene–like building blocks. Note that this series of molecules is referred to as polyacenes in this work — benzene included. Furthermore, the electronic properties of these molecules are of general interest because several π–conjugated

molecules, e.g. BTCDA, BTCDI or NTCDA, consist of a polyacene–like aromatic core.

The electronic structure of the polyacene series from benzene to pentacene was studied recently by PES. This investigation is described in detail in [A3], and thus only the general findings will be summarized briefly in the following. The PES data of the valence regime of the various polyacenes indicate — not unexpectedly — that the electronic structure becomes more and more complex with increasing molecular size. Moreover, it was shown that the line shape of the C 1s spectrum of condensed benzene matches that of the gas phase after correcting for inhomogeneous broadening. Consequently, the influence of the intermolecular coupling is comparatively weak and the intramolecular effects are dominant for core level PES of theses molecules. Therefore it is sufficient, to first order, to consider only single molecules for the description of the core level excitations in these multilayer films.

Furthermore, the energy position of the C 1s main line increases from benzene to naphthalene and decreases with further of benzene rings. The lower limit of the C 1s binding energy is reached after four benzene rings and the difference between the highest and the lowest C 1s binding energy of this series is 0.9 eV — naphthalene versus pentacene. A comparison of the intensity and the energy position of the first C 1s satellite, which is attributed to a HOMO–LUMO shake–up [1] with respect to the main line, gives insight into the charge redistribution upon photoexcitation. With increasing molecular size the HOMO–LUMO shake–up decreases in intensity and shifts towards the C 1s main line. The shake–up energy decreases even more than the excitation energy for an optical HOMO–LUMO excitation in the absence of a core hole. Again, the difference between the energy of the optical gap and the shake–up energy stabilizes at 0.9 eV for large molecules consisting of four benzene rings and more. In the discussion of the data it was argued that these effects indicate an improvement of the charge reorganization upon core ionization with increasing molecular size, which leads to a lowering of the respective photoexcitation energy in the order of 1 eV.

The influence of the presence of an additional electron on the molecule is an interesting aspect in this context. In particular the reorganization of the electronic structure upon photoexcitation may be different for an electronic transition of a core electron into a bound unoccupied state than for core ionization. This effect is studied in detail for the polyacene series with NEXAFS spectroscopy with particular focus on the energy position and intensity of the electronic transition with the lowest excitation energy, which can be distinguished from other NEXAFS features.

[1] A shake–up from the *highest occupied molecular orbital* (HOMO) to the *lowest unoccupied molecular orbital* (LUMO).

Furthermore, some information about the electronic reorganization upon photoexciation can be deduced from a comparison of the trends in the NEXAFS to those in the PES study in [A3].

3.1 A brief review of photoexcitation

Before discussing the polyacene NEXAFS data in detail a brief review of some basic concepts for the description of photoexcitation is necessary with respect to similarities and differences between core ionization and electronic transitions into unoccupied bound electronic states.

3.1.1 Basic matrix element for photoabsorption

The Hamiltonian for a molecule with N electrons and P nuclei consists of a kinetic term and three coulomb terms, which describe the electron–electron repulsion, the electron–nuclear attraction and the nuclear–nuclear repulsion. Relativistic and spin-orbit effects are ignored in the following.

$$H = \sum_{j=1}^{N} \frac{\mathbf{p}_j^2}{2m} - \sum_{j=1}^{N}\sum_{n=1}^{P} \frac{Z_n e^2}{|\mathbf{r}_j - \mathbf{R}_n|} + \sum_{j=1}^{N}\sum_{k>1}^{N} \frac{e^2}{|\mathbf{r}_j - \mathbf{r}_k|} + \sum_{l=1}^{P}\sum_{n>1}^{P} \frac{Z_l Z_n e^2}{|\mathbf{R}_l - \mathbf{R}_n|} \tag{3.1}$$

In the Born–Oppenheimer approximation the total wave function of the molecule can be separated into a product of an electronic part Ψ_e and a nuclear part Ψ_n.

$$\Psi_{tot} = \Psi_e \Psi_n \tag{3.2}$$

Consequently, the electronic part can be considered separately in the following. The interaction Hamiltonian between the electrons and a radiation field can be obtained by the transformation $\mathbf{p} \rightarrow \mathbf{p} - e\mathbf{A}/c$, where the vector potential $\mathbf{A} = \mathbf{A}_0 e^{\pm i\mathbf{k}\cdot\mathbf{x}\mp i\omega t}$ represents the radiation field within the framework of the semiclassical theory of radiation. The kinetic term in (3.1) then changes to

$$\sum_j \frac{(\mathbf{p}_j - e\mathbf{A}(\mathbf{x}_j,t)/c)^2}{2m} \tag{3.3}$$

$$= \sum_j [\frac{(\mathbf{p}_j)^2}{2m} + \frac{-e}{2mc}(\mathbf{p}_j \cdot \mathbf{A}(\mathbf{x}_j,t) + \mathbf{A}(\mathbf{x}_j,t)\cdot \mathbf{p}_j) + \frac{e^2}{2mc^2}\mathbf{A}(\mathbf{x}_j,t)^2] \tag{3.4}$$

$$\simeq \sum_j \frac{(\mathbf{p}_j)^2}{2m} + \underbrace{\sum_j \frac{-e}{mc}\mathbf{A}(\mathbf{x}_j,t)\cdot \mathbf{p}_j} \tag{3.5}$$

$$= \sum_j \frac{(\mathbf{p}_j)^2}{2m} \qquad + \qquad H_I. \tag{3.6}$$

The operator $\mathbf{p}_i = i\hbar\nabla$ is a differential operator that acts on everything on its right. Within the transversality condition $\nabla \cdot \mathbf{A} = 0$ it is possible to replace $\mathbf{p}_i \cdot \mathbf{A}(\mathbf{x}_i,t)$ by $\mathbf{A}(\mathbf{x}_i,t)\cdot\mathbf{p}_i$. The quadratic term $\mathbf{A}\cdot\mathbf{A}$ can be neglected when computing the absorption process to lowest order, and the interaction of the electrons with the radiation field is described by H_I.

If H_I is sufficiently small compared to H, the probability for a certain electronic transition can be calculated by the time–dependent perturbation theory developed by Dirac. The electronic wave function Ψ_e can be expanded as

$$\Psi_e = \sum_k c_k(t) u_k(x) e^{-iE_k t/\hbar} \tag{3.7}$$

where $u_k(x)$ is the energy eigenfunction of the molecule with energy E_k satisfying

$$H\ u_k(x) = E_k\ u_k(x) \tag{3.8}$$

in the absence of a time–dependent perturbation. Note that $u_k(x)$ is a multi-electron wave function. The time–dependent Schrödinger equation in the presence of the time–dependent potential H_I is

$$(H + H_I)\Psi_e = i\hbar(\partial\Psi_e/\partial t) \tag{3.9}$$

$$= i\hbar \sum_k (\dot{c}_k u_k e^{-iE_k t/\hbar} - i(E_k/\hbar)c_k u_k e^{-iE_k t/\hbar}) \tag{3.10}$$

using (3.8) the relation for H_I is

$$\sum_k H_I c_k u_k e^{-iE_k t/\hbar} = i\hbar \sum_k \dot{c}_k u_k e^{-iE_k t/\hbar}. \tag{3.11}$$

Multiplying $u_f^* e^{iE_f t/\hbar}$ and integrating over the space coordinate leads to the following differential equation for the transition into the state $\langle f|$

$$\dot{c}_f = \frac{1}{i\hbar} \sum_k \langle f|H_I(t)|k\rangle e^{i(E_f - E_k)t/\hbar} c_k(t). \tag{3.12}$$

Consequently, if only the eigenstate $|i\rangle$ is populated at time $t = 0$, then

$$c_k(0) = \delta_{ki}, \tag{3.13}$$

and with this c_f can be derived by time integration of (3.12)

$$c_f(t) = \frac{1}{i\hbar} \int_0^t dt' \langle f|H_I(t)|i\rangle e^{i(E_f - E_i)t'/\hbar}. \tag{3.14}$$

As the vector potential is $\mathbf{A} = \mathbf{A}_0 e^{i\mathbf{k}\cdot\mathbf{x} - i\omega t}$ for absorption and $\mathbf{A} = \mathbf{A}_0 e^{-i\mathbf{k}\cdot\mathbf{x} + i\omega t}$ for emission, the time–dependent potential H_I can be written as

$$H_I(t) = H_I' e^{\pm i\omega t}, \tag{3.15}$$

with H_I' being the time–independent operator. This leads to

$$c_f(t) = \frac{1}{i\hbar} \langle f|H_I'|i\rangle \int_0^t dt' e^{i(E_f - E_i \pm \hbar\omega)t'/\hbar}. \tag{3.16}$$

After the time integration one obtains

$$|c_f(t)|^2 = \frac{2\pi}{\hbar} |\langle f|H_I'|i\rangle|^2 t \delta(E_f - E_i \pm \hbar\omega). \tag{3.17}$$

Note that the transition probability per unit time is $|c_f(t)|^2/t|$, which is independent of t. In the photoemission and NEXAFS experiments in this work the radiation field is weak enough, so that the $\mathbf{A}\cdot\mathbf{A}$ term in (3.3) is negligible. Therefore the probability for absorption or emission of a photon with the energy $\hbar\omega$ can be simplified using (3.6). Within the dipole approximation ($\mathbf{kx} << 1$), which is satisfied well in the soft x-ray regime, the absorption probability is

$$P_{fi} = \frac{2\pi}{\hbar}|\langle f|\epsilon \cdot \mathbf{p}|i\rangle|^2 \delta(E_f - E_i \pm \hbar\omega), \tag{3.18}$$

with $\mathbf{p} = \sum \mathbf{p}_j$ being the sum of the linear momentum operators of all electrons and ϵ is the unit vector of the vector potential $\mathbf{A}$. Consequently, the photoexcitation cross section in the following PES and NEXAFS spectroscopy experiment can be well described within the dipole approximation.

3.1.2 Transition probability and intensity

Up to this point the electron–vibration coupling has been neglected and the absorption probability has been calculated by considering only the purely electronic part. However, if this is taken into account, equation (3.18) changes to the following

$$P_{fi} = \frac{2\pi}{\hbar}|\langle F|\epsilon \cdot \mathbf{p}|I\rangle|^2 \delta(E_F - E_I \pm \hbar\omega), \tag{3.19}$$

with $|I\rangle$ and $\langle F|$ being the combined electronic–vibronic initial state and final state of the molecule and E_I and E_F the respective energy eigenvalues including the vibronic energy. This can be simplified within the Born–Oppenheimer approximation in (3.2) to

$$P_{fi} = \frac{2\pi}{\hbar}|\langle f_n|i_n\rangle|^2 \langle f_e|\epsilon \cdot \mathbf{p}|i_e\rangle|^2 \delta(E_F - E_I \pm \hbar\omega), \tag{3.20}$$

where $\langle f_n|$ and $|i_n\rangle$ correspond to the vibronic states and $\langle f_e|$ and $|i_e\rangle$ to the electronic states, respectively. The pre–factor $|\langle f_n|i_n\rangle|^2$ is also known as Franck–Condon factor. Particularly in PES and NEXAFS spectroscopy it plays an important role. It was shown that the vibronic fine structure can broaden the NEXAFS transitions by more than 1 eV. If only few vibronic modes are dominant, the vibronic eigenstates of the molecules can be determined from the NEXAFS. [45, 46] Consequently, it is necessary to not only take the dipole matrix element into account when considering the probability for a certain NEXAFS transition, but also the Franck–Condon factors.

In summary, the following aspects need to be considered when evaluating the intensity in the polyacene PES and NEXAFS data:

1. Equation (3.18) indicates that the symmetry of the initial sate $|i\rangle$ and the final state $\langle f|$ wave function is important with respect to the dipole operator $\epsilon\nabla$. The probability for a transition of a 1s electron into a unoccupied p_z or π orbital, for example, is high if the polarization vector is perpendicular to its mirror plain. Therefore one needs to take the different molecular orientations into account.

2. Furthermore, it can be understood with respect to (3.18) that the photoemission cross section is high, when the length of the photoelectron plain wave is of the order of the orbital size from which the photoelectron was excited. The photoemission cross section of the comparatively delocalized sp–bands, for example, is significantly higher for HeI excitation than for HeII excitation and vice versa for the strongly localized d–states. Under certain conditions a similar effect can be expected for a NEXAFS transition of a 1s electron into a π–orbital, for example. If the excited molecular orbital is strongly localized at the core hole site, the matrix element is significantly higher than for a strongly delocalized excited molecular orbital of similar symmetry. This is also known as the core hole localization effect. [35, 47]

3. Particularly in NEXAFS spectroscopy the Franck–Condon factors need to be taken into account when comparing the intensity of certain electronic transitions.

3.1.3 Multi–electron versus one–electron view

In a simple approximation of photoexcitation one can take a one–electron view of the initial and final state wave function in which the electron correlation is ignored. The multi–electron wave functions in equation (3.18) are separated into an "active" one–electron and a "passive" multi–electron part. Accordingly, the transition matrix element becomes

$$M_{fi} = \langle \Psi_f(N)|\epsilon \cdot \sum \mathbf{p}_i|\Psi_i(N)\rangle \tag{3.21}$$

$$= \langle \chi_f|\epsilon \cdot \mathbf{p}_1|\phi_1\rangle\langle \Psi_f(N-1)|\Psi_i(N-1)\rangle + ... \tag{3.22}$$

Here ϕ_1 corresponds to the orbital from which an electron is excited, χ_f to the wave function of the excited electron, and $\Psi_i(N-1)$ and $\Psi_f(N-1)$ are the passive $N-1$ electron remainders. With a further simplification one can assume that the passive orbitals are the same in the initial and in the final state ($\Psi_f(N-1) = \Psi_i(N-1)$), which is known as the *frozen orbital approximation*. Accordingly, the energy which

is necessary for emitting a photoelectron is known as *Koopmans' binding energy*. In this picture the energy, which is necessary for an electronic transition into a bound final state χ_f corresponds to the difference of the Koopmans' energies between states ϕ_1 and χ_f. Of course, this is a strong simplification because one realizes intuitively that the electrons are interrelated and therefore the remaining $N-1$ electrons are also affected by the electronic transition. Consequently, there is finite overlap between $\Psi_i(N-1)$ and various $\Psi_f(N-1)$, which leads to additional satellites at higher energies and to a lower energy for the main line. The centroid of the different, intensity–weighted final state energies corresponds to Koopmans' binding energy. [48,49] Hence, the $\Psi_f(N-1)$ in (3.21) accounts for the electronic relaxation and consequently for the many–body character of the excitation. Note that it is referred to the lowering of the main line with respect to Koopmans' energy as *relaxation energy* in the following.

It is straightforward that for different molecules the electron–electron interrelation and consequently the relaxation can be different, as it was observed for the polyacene core level photoelectron spectra. [A3] Furthermore, it is expected that the electronic reorganization is different for core ionization, the excitation of core electrons into bound unoccupied states (NEXAFS) and for valence ionization (UPS and IPES). However, Koopmans' energy and consequently the relaxation energies cannot be measured directly. Nevertheless, at least an estimate of the different relaxation energies can be obtained for a systematic series of molecules from a comparison of the trend in the measured excitation and binding energies, respectively. It is shown in the following that for the polyacene series, for example, a comparison between core level PES, NEXAFS and IPES data can be helpful.

3.2 C K–NEXAFS of polyacenes

Fig. 3.1 shows the C K–NEXAFS spectra for a series of polyacene molecules, namely benzene, naphthalene, anthracene, tetracene and pentacene. These molecules have distinct features below the absorption edge, which correspond to electronic transitions into π^* orbitals. The larger the molecules are, the more complex the pre–edge structure is. In order to be able to compare the respective spectra between the different molecules, it is necessary to identify and assign the electronic transitions, which is done briefly in the following with respect to Hartree–Fock calculations of the C K–NEXAFS spectra of polyacenes. [50]

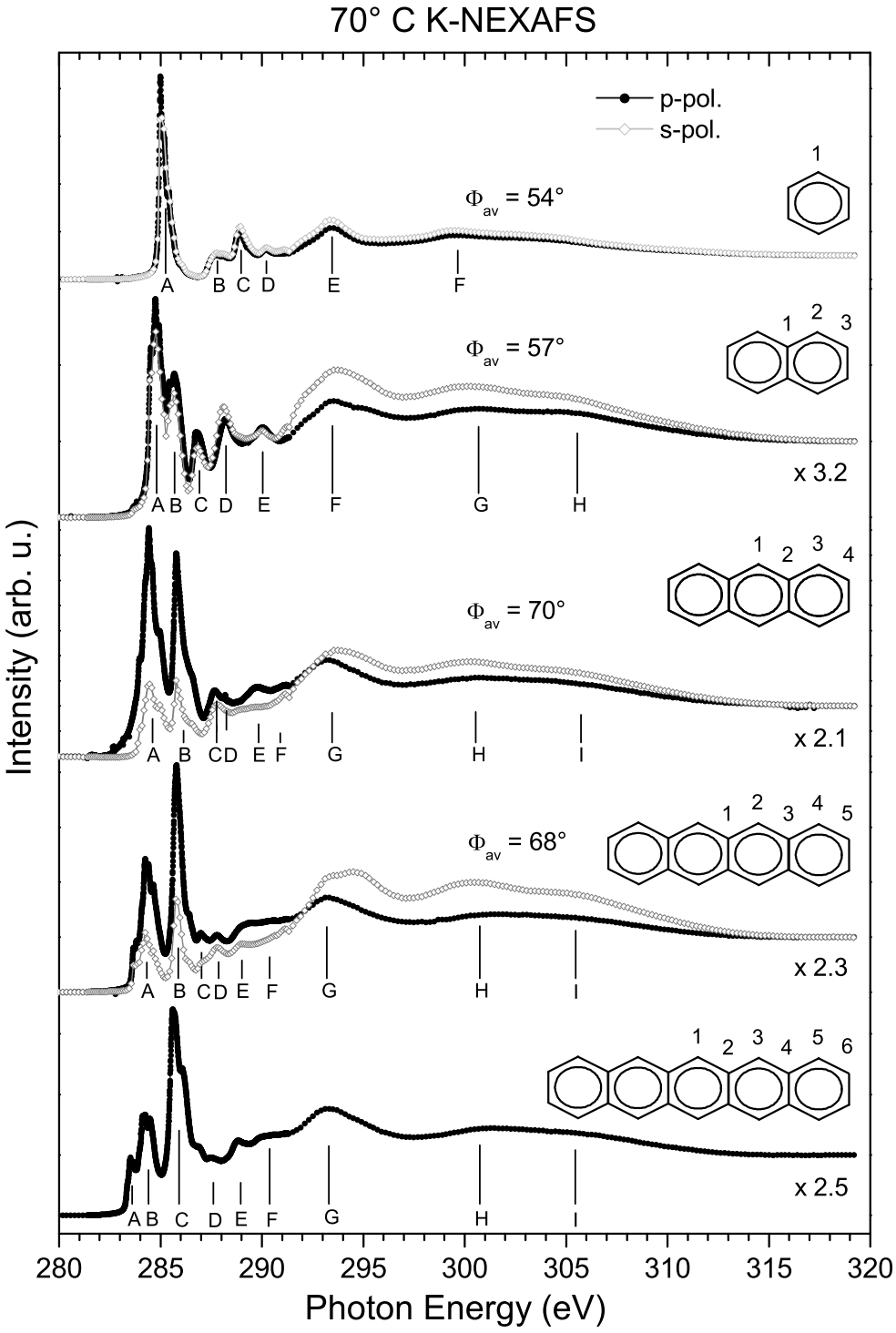

Figure 3.1: C K–NEXAFS of benzene, naphthalene, anthracene, tetracene and pentacene with 70° angle of incidence from the surface normal. For benzene the total electron yield signal is shown and for the other molecules the partial electron yield signal with 150 V retarding field. The average inclination angle Φ_{av} between the molecular plain and the surface normal is obtained from the dichroism in the pre–edge regime.

3.2.1 Benzene

The C K–NEXAFS of benzene in Fig. 3.1 consists of six significant features (A – F) at 285.0 eV, 287.8 eV, 288.9 eV, 290.2 eV, 293.4 eV and 299.6 eV. This contradicts the building block picture, which predicts only one π^* and one σ^* resonance in the NEXAFS because of the equivalence of all carbon atoms. Therefore several experimental and theoretical studies have been carried out which corroborate the calculations in ref. [50]. Accordingly, peak A corresponds to electronic transitions into the *lowest excited molecular orbital* (LEMO), namely C 1s $\rightarrow$ LEMO(π^*e_{2u}). Note that in Fig. 3.2 it can be seen that feature A has a vibronic fine structure. According to the assignment in [51, 52] the 0–0 peak refers to the adiabatic transition, the shoulders α and γ correspond to a C–H bending and stretching mode, respectively, and peak β can be attributed to a C–C stretching mode. Features B, C and D at 287.8 eV, 298.9 eV and 290.2 eV have mixed σ_{CC}, σ^*_{CC}, σ^*_{CH} and Rydberg character. [53–56]. Peak D has additional contributions from a C 1s $\rightarrow$ π^*b_{2g} excitation, which can be considered as a shake transition with respect to the π^*e_{2u} resonance. [50] The features E and F, which are located above the absorption edge have mainly σ^*_{CC} character. [56]

3.2.2 Naphthalene

The C K–NEXAFS spectrum of naphthalene in Fig. 3.1 is similar to that of benzene but more complex. Two peaks, A and B, can be resolved in the π^* region at 284.7 eV and 285.6 eV, respectively, in contrast to [54, 57]. Accordingly more than one resonance contribute to the signal in contrast to benzene. Additionally the trailing edge of feature F at 293.4 eV contains a broad shoulder at 295.0 eV, which indicates additional contributions compared to peak E of the benzene NEXAFS. This can be explained by the presence of three chemically different carbon sites in the naphthalene molecule — *mid–top*, *mid–bottom* and *end–botto*m, which are labeled 1, 2, 3 in the structural formula in Fig. 3.1. With respect to previous theoretical and experimental investigations NEXAFS of naphthalene can be understood to first order as the sum of three benzene–like contributions which are related to the different atomic sites. [50,52,54,57] Accordingly, peak A has contributions from two electronic transitions, namely C_2 1s $\rightarrow$ LEMO(π^*) and C_3 1s $\rightarrow$ LEMO(π^*) at atom 2 and 3, respectively. [50,52,54,57]. Furthermore, GSCF3 calculations indicate that the C_1 1s $\rightarrow$ LEMO(π^*) transition is symmetry forbidden, and that peak B can be assigned to transitions from the C_1 1s and the C_3 1s level into the LEMO+1. [52] Peak C can be attributed to four electronic transitions, namely to excitations from C_2 1s and C_3 1s into the LEMO+2, which is confirmed by the dichroism, and two transitions with σ–symmetry, C_1 1s $\rightarrow$ LEMO+4 and C_2 1s$\rightarrow$ LEMO+5. [52,57,58]

Note that the dichroism of peak D is opposite to that of peak A, B, C and E. Therefore the dominant contribution to D can be associated with σ^*_{CH} excitations. The signature of the C K–NEXAFS above 288 eV is similar to that of benzene. Hence, a predominant σ^*_{CC} character can be assigned to the features F – H above the absorption step. [57]

3.2.3 Anthracene, Tetracene and Pentacene

The general signature of the NEXAFS spectra of larger polyacene molecules is similar to the naphthalene spectrum. They can also be understood as a sum of benzene like contributions from different atomic sites. The distinct feature A at low energy can be attributed to C 1s → LEMO excitations at different carbon sites. Note that for all molecules the excitation with the lowest energy is related to the *mid–top* atom. For anthracene and pentacene this corresponds to a C_1 1s → LEMO transition at carbon atom 1, and for tetracene to a C_2 1s → LEMO transition at atom 2. [50] As for the larger molecules more transitions from chemically different carbon sites contribute to the signal compared to naphthalene, the respective features above 287 eV are less distinct, but it can be assumed that their character is similar to that of the corresponding features in the naphthalene NEXAFS.

3.2.4 General trends from small to large molecules

Apart from the increasing complexity with increasing molecular size, several other trends can be observed in the polyacene C K–NEXAFS. The dichroism in the C K–NEXAFS increases with increasing molecule size, in particular in the π^* region. The intensity of the features A and B in the tetracene spectrum decrease strongly when the polarization of the x-rays is changed from p to s, whereas the benzene NEXAFS does not depend significantly on polarization. Considering the dipole selection rule for an optical transition from a radial symmetric orbital into a π^* orbital, this observation indicates that the tetracene molecules are lying nearly flat on the surface with an average angle of $\Phi_{av} = 68°$ between the molecular plane and the surface normal. The trend in the dichroism in Fig. 3.1 suggests that the benzene molecules are randomly oriented, and that the molecules are preferentially lying flat with increasing size. In particular the average inclination angle is $\Phi_{av} = 54°$, 57°, 70° and 68° for benzene, naphthalene, anthracene and tetracene, respectively.

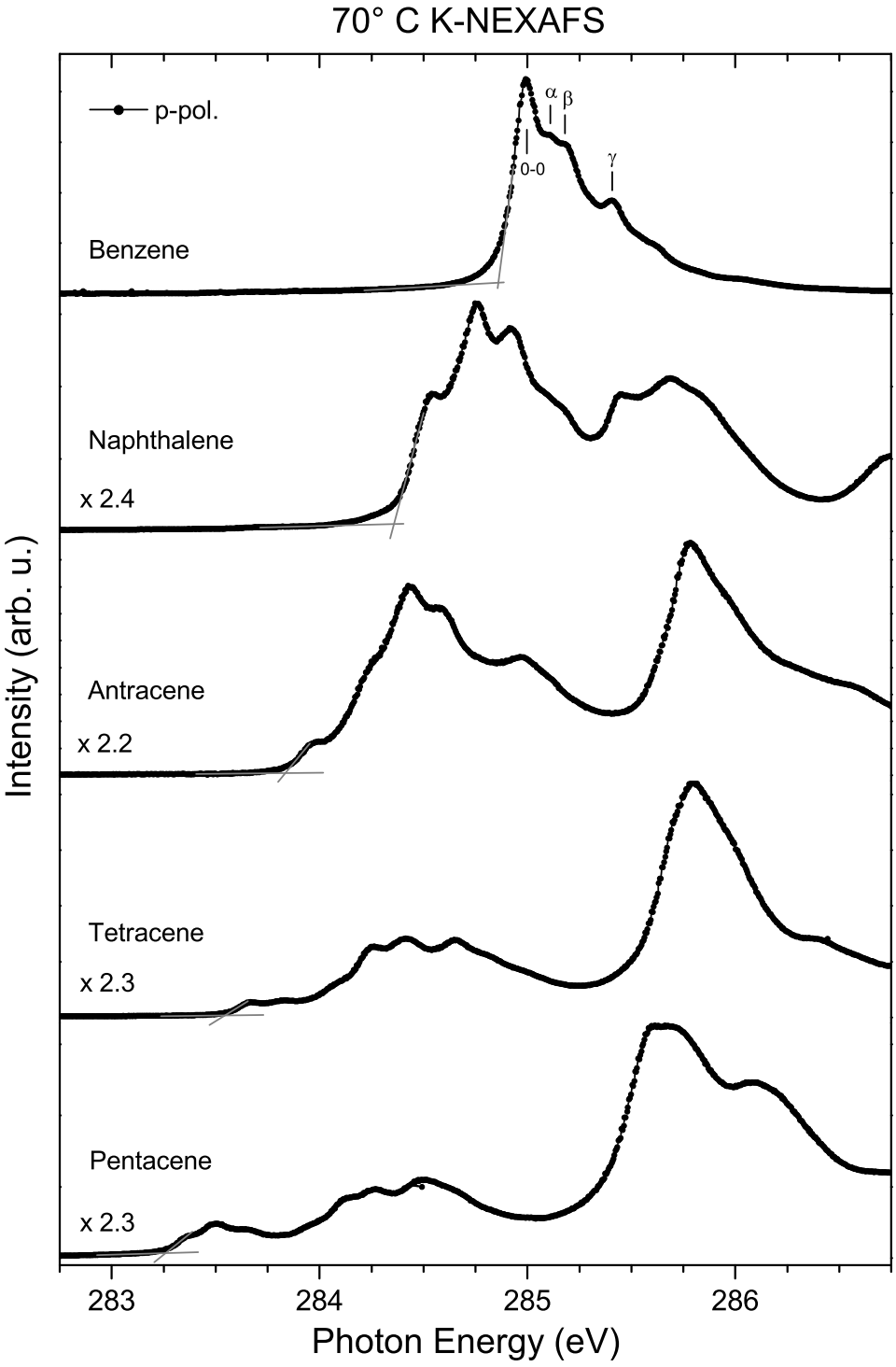

Figure 3.2: Blow–up of the pre–edge region of the C K–NEXAFS of benzene, naphthalene, anthracene, tetracene and pentacene from Fig. 3.1. The grey lines mark the NEXAFS onset – see also Tab. 3.1.

Furthermore, the prominent π^* signatures become spread out for larger molecules because of an increasing number of valence levels and inequivalent core hole sites with increasing molecular size. Additionally, the height of peak A with respect to the height of the absorption edge decreases for increasing molecular size, and the energy position of the onset of the resonance A decreases from 284.86 eV for benzene to 283.26 eV for pentacene, which is indicated in Fig. 3.2 and Tab. 3.1. As described above, the prominent feature A in the NEXAFS can be attributed to transitions into the LEMO and the resonance with the lowest energy corresponds to excitations at equivalent *mid–top* carbon sites for all investigated polyacenes – C_1 for an odd and C_2 for an even number of carbon rings, respectively. Consequently, a decrease in the matrix element and the excitation energy for the C_{mt} 1s $\rightarrow$ LEMO transition is observed with increasing molecular size.

3.2.5 Comparison between the energy of the NEXAFS onset and the C 1s and LUMO binding energy

In Fig. 3.3 the energy position of the NEXAFS onset, which was determined from Fig. 3.2, is plotted versus the size of the polyacene molecules. Additionally, the C 1s and the LUMO binding energies are indicated, which were measured by core level PES and IPES, respectively. [59, A3] Note that the authors mentioned explicitly that the IPES measurements were done at very thin molecular films (2 – 3 ML) in order to avoid charging and radiation damage. Therefore it can be assumed that these films are of high quality and that the measured LUMO binding energies are not biased by any defects.

The similarity between the trend in energy of the C K–NEXAFS onset and the LUMO binding energy is striking, while the trend in the C 1s binding energy differs significantly. Consequently, the excitation energy for the C_{mt} 1s $\rightarrow$ LEMO excitation decreases with increasing polyacene size by the same value as the LUMO binding energy. This suggests intuitively that the trend in the NEXAFS onset and the LUMO binding energy is dominated by effects in the ground state, namely the decrease of Koopmans' binding energy of the LUMO, and that in both cases the relaxation energy is only little affected by the polyacene size in contrast to core ionization, where the polyacene size influences the relaxation energy significantly [A3] as it is summarized at the beginning of *chapter 3*. Therefore it can be helpful to calculate the ground state energies of the respective orbitals and compare the trend in the orbital energies with increasing polyacene size to the experimental data.

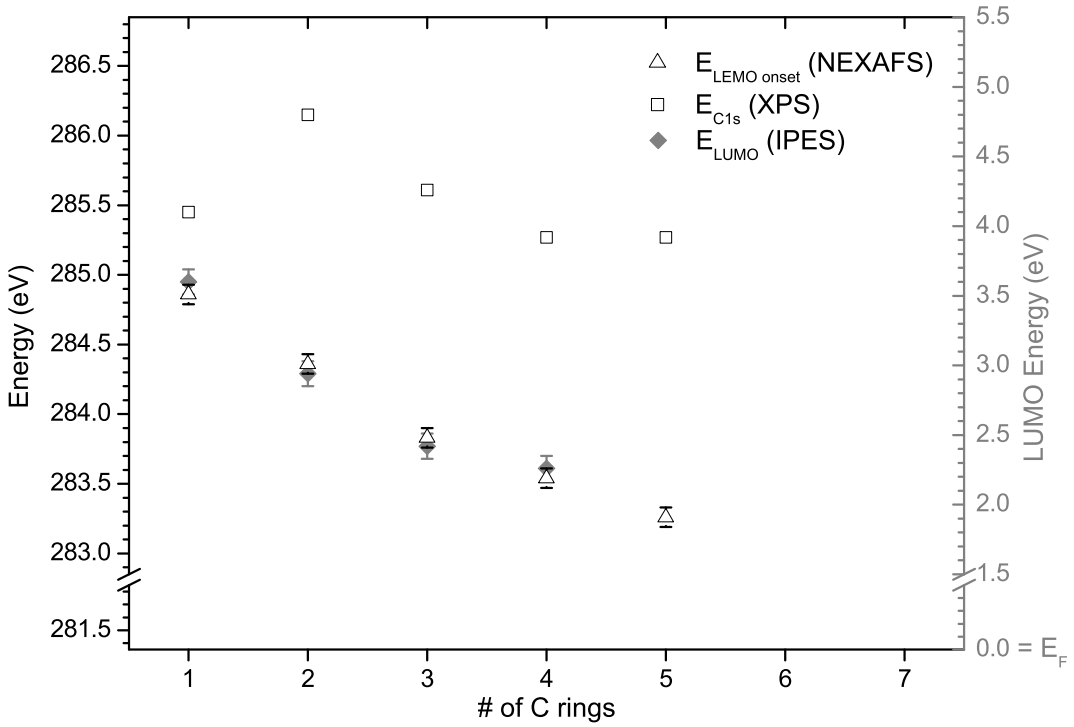

Figure 3.3: Comparison between the energy position of the NEXAFS onset (left energy axis), the C 1s (left energy axis) and the LUMO (right energy axis) binding energy from the PES and IPES data of [59, A3] over the number of benzol rings in the polyacene molecules.

3.3 The influence of the polyacene size

In the following the orbital energies of the LUMO and the C_{mt} 1s orbital at the *mid–top* carbon site are calculated for the different polyacene molecules. For the sake of computation time the calculations are carried out using **d**ensity **f**unctional **t**heory (DFT) with the B3LYP functional [60] and the 6-311G basis set. It is known that the DFT calculations do not provide Koopmans' binding energies and the "real" orbitals, but Kohn–Sham functions and energies instead, which in principle are only mathematical operants. However, it is demonstrated in *Appendix A* that it is sufficient for the polyacene series to consider the Kohn–Sham energies for the following discussion, because they follow the same trend as the Koopmans energies.

At first, the trend in the Kohn–Sham energy of the LUMO with increasing molecular size is compared to the trend in the LUMO binding energy, which was determined by IPES. [59] Secondly, the change in the Kohn–Sham energy of the C_{mt} 1s electrons at the *mid–top* carbon site with increasing polyacene size is compared to the change in the LUMO energy. This shows that the C_{mt} 1s energy decreases much less than the LUMO energy. Thirdly, the trend in the difference between the Kohn–Sham energy of the C_{mt} 1s level and the LUMO is compared to the trend in the C_{mt} 1s $\rightarrow$ LEMO excitation energy from the NEXAFS data.

3.3.1 The LUMO energy in IPES and DFT

The quality of the DFT calculations can be verified in Fig. 3.4 by the comparison of the calculated LUMO energies with the respective LUMO binding energies from the IPES experiments in [59]. Fig. 3.4 shows the energy position of the LUMO maximum in the IPES data of benzene, naphthalene, anthracene and tetracene [59] together with the calculated LUMO energies. For a better comparison the energy scale of all DFT calculations is compressed by 0.7025 and shifted by +3.79 eV in order to fit the experimental data. This established procedure accounts for inherent limitations of state–of–the–art DFT computations, e.g. underestimation of the electronic gap, better approximation of orbitals and energies for valence electrons than for core electrons, and shortcomings of the exchange–correlation Kohn–Sham potential. [61–68] The graph indicates that the trend in the calculated LUMO energies agrees well with the trend for the experimental data. Therefore the decrease in the LUMO binding energy in the IPES data with increasing polyacene size can be mainly attributed to the decrease in the ground state energy of the LUMO with increasing molecular size. Consequently, it is not surprising that the

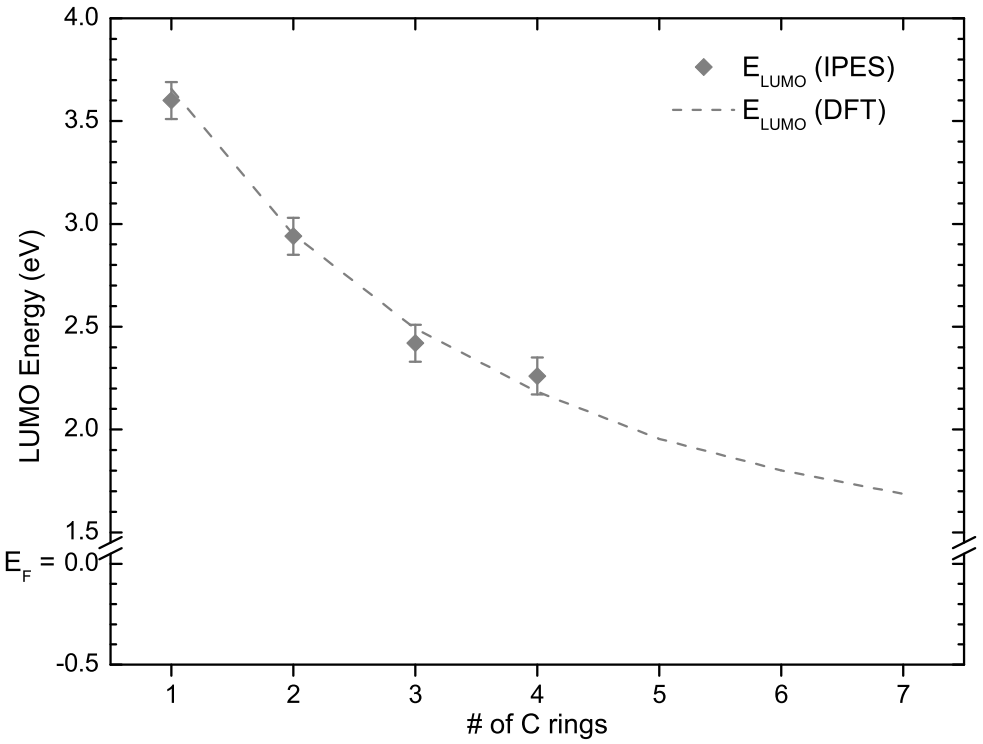

Figure 3.4: Comparison between the binding energy of the LUMO in the IPES data of [59] and the respective Kohn–Sham energy from DFT calculations for different polyacenes. These calculations were carried out with the B3LYP functional and the 6-311G basis set. The energy scale of the DFT calculations is compressed by 0.7025 and shifted by +3.79 eV.

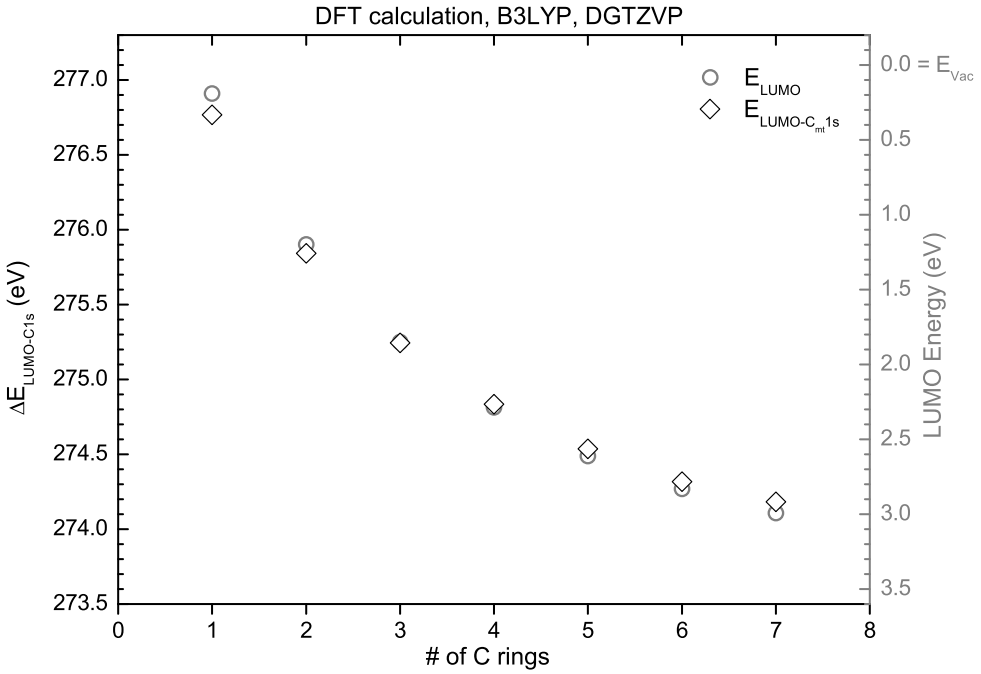

Figure 3.5: Comparison between the trend in the Kohn–Sham energy of the LUMO and the energy difference $\Delta E_{LUMO-C_{mt}1s}$ between the LUMO and the C_{mt} 1s level. The C_{mt} 1s energy corresponds to the orbital which is located at the *mid–top* atom according to section 3.2 and Fig. 3.1. The plotted energies are directly taken from DFT computations based on the B3LYP functional and the 6-311G basis set.

optical gap of the polyacene molecules decreases more than 2 eV from benzene to pentacene. [59, 69–72] Furthermore, this implies that the relaxation energy for the $C_{mt}^{\nu=0}$ 1s $\rightarrow$ LEMO$^{\nu'=0}$ transition in the C K–NEXAFS does not change significantly from benzene to tetracene because the energy of the C K–NEXAFS onset follows the same trend as the measured LUMO energy, which is due to an initial state effect.

3.3.2 Trend in the C_{mt} 1s and the LUMO energy

In the following the difference $\Delta E_{LUMO-C_{mt}1s}$ between the Kohn–Sham energies of the C_{mt} 1s level at the *mid top* carbon atom and the LUMO is studied as a function of polyacene size. In Fig. 3.5 $\Delta E_{LUMO-C_{mt}1s}$ (left scale) and the LUMO energy (right energy scale) is plotted over the molecular size. Both curves are very similar. The minor difference, namely the slightly larger curvature of the $\Delta E_{LUMO-C_{mt}1s}$

curve indicates that the C_{mt} 1s level decreases slightly less with increasing polyacene size — ca. 0.2 eV from benzene to pentacene. However, this effect is one order of magnitude smaller than the decrease in LUMO energy (-2.6 eV). As a consequence the trend in the energy difference $\Delta\ E_{LUMO-C_{mt}1s}$ is mainly determined by the LUMO energy.

3.3.3 Trend in the LEMO energy versus trend in the ground state

As discussed above the absolute value of the relaxation energy for the C_{mt} 1s $\rightarrow$ LEMO excitation cannot be determined because $\Delta E_{LUMO-C_{mt}1s}$ cannot be calculated accurately enough. However, it is possible to find out wether the relaxation energy depends on the molecular size by comparing the dependence of the C_{mt} 1s $\rightarrow$ LEMO excitation energy with the trend in $\Delta E_{LUMO-C_{mt}1s}$.

Due to electron–vibration coupling the electronic transitions are broadened by a vibronic fine structure, which is individual for the different polyacene molecules. Usually the energy spacing between the different vibronic levels is of the order of 100 meV for organic molecules [46], and several modes couple to a certain electronic transition, which leads to a rich vibronic fine structure. Therefore, it is necessary to consider only electronic transitions into the vibronic ground state ($\nu = 0 \rightarrow \nu' = 0$), when comparing the C_{mt} 1s $\rightarrow$ LEMO transition energies between the various polyacene molecules. If this transition is allowed it contributes to the leading edge of peak A. A detail Franck–Condon analysis of benzene, [51,53,73] and naphthalene [52] indicated that this is exactly the case for these molecules. As this is also the case for the C K–NEXAFS spectra of many other π–conjugated molecules [45,46] it can be assumed that for the larger polyacenes the leading edge of the C_{mt} 1s $\rightarrow$ LEMO excitation is also determined by the $\nu = 0 \rightarrow \nu' = 0$ transition. Therefore it is reasonable to compare the energy position of the onset of the first NEXAFS feature, which is marked in Fig. 3.2 and listed in Tab. 3.1.

Another approach is to determine the excitation energy of the $C_{mt}^{\nu=0}$ 1s $\rightarrow$ LEMO$^{\nu'=0}$ transition for larger polyacene molecules by fitting a benzene spectrum to the first NEXAFS feature. For the larger polyacenes the character of the core excitation at the *mid–top* carbon is supposed to be benzene–like to first order. [50,52] Consequently, when fitting a benzene spectrum to the first NEXAFS feature the maximum of the benzene signal indicates the $C_{mt}^{\nu=0}$ 1s $\rightarrow$ LEMO$^{\nu'=0}$ transition. Of course the vibronic fine structure changes for the different polyacenes, in particular the vibronic modes which are related to the C–C vibrations like peak β in the benzene spectrum in 3.6. However, it was shown, that these differences are comparatively small between benzene and naphthalene. [52] Consequently,

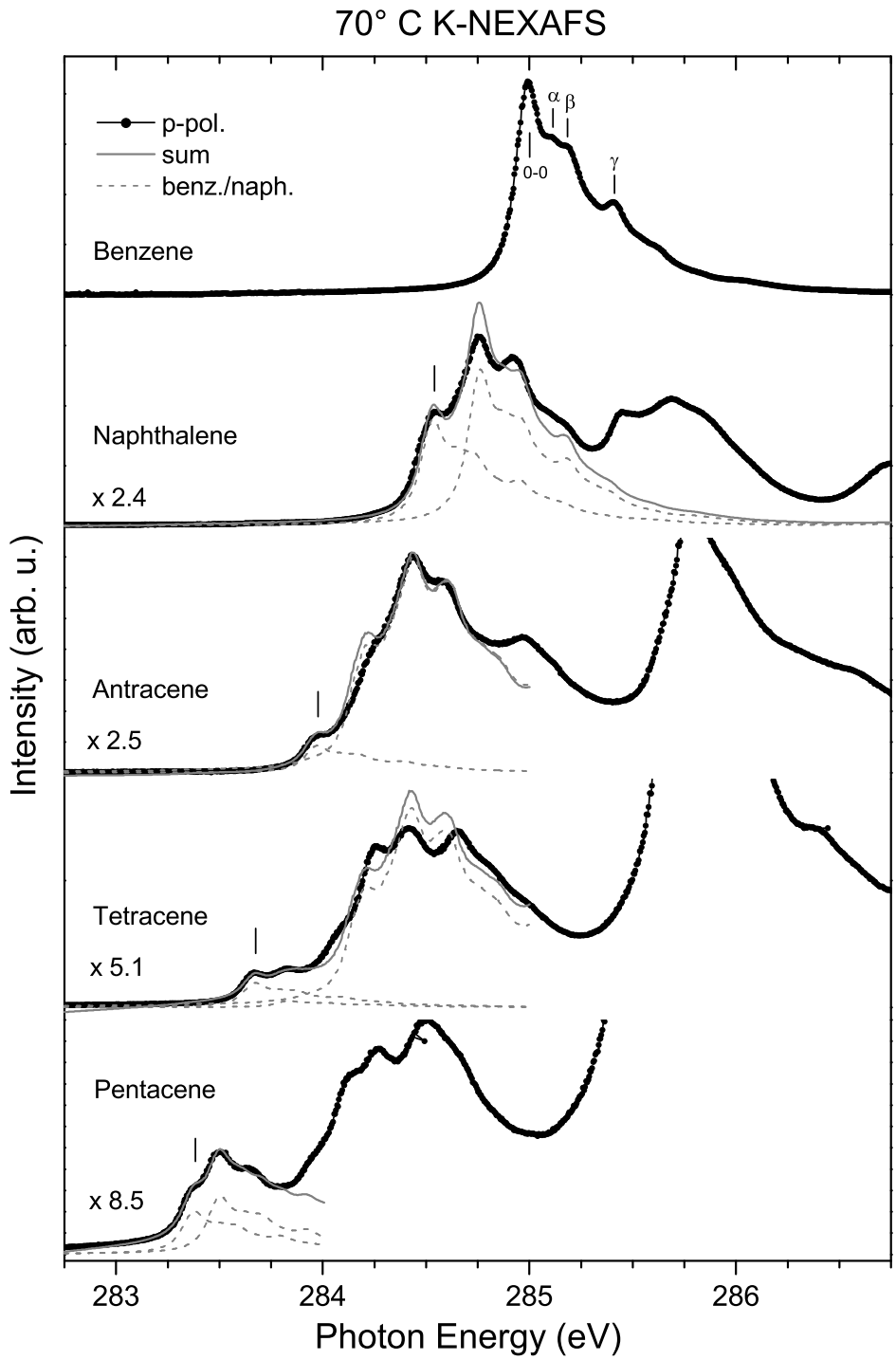

Figure 3.6: The first peak in the polyacene NEXAFS, which corresponds to C_{mt} 1s → LEMO transitions at the *mid–top* carbon site, can be reproduced by adding benzene and naphthalene signals (dashed lines). Each sum curve (solid line) was obtained by adding the respective two dashed curves and a linear background in the case of anthracene, tetracene and pentacene (not shown). The energy position of the maximum of the benzene component is indicated and additionally listed in Tab. 3.1.

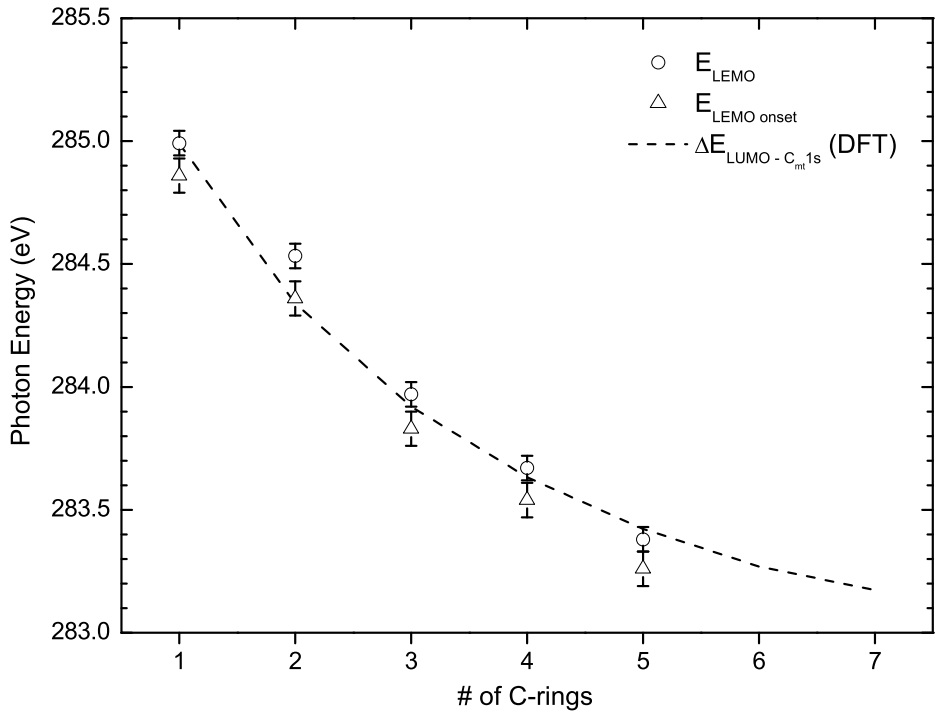

Figure 3.7: Comparison between the trend in the low–energy onset $E_{LEMOonset}$ in the C K–NEXAFS of benzene, naphthalene, anthracene, tetracene and pentacene with the trend in the excitation energy E_{LEMO} for the $C_{mt}^{\nu=0}$ 1s $\rightarrow$ LEMO$^{\nu'=0}$ transition and the difference in the Kohn–Sham energy $\Delta E_{LUMO-C_{mt}1s}$ between the C_{mt}1s orbital and the LUMO. The NEXAFS onset is determined according to Fig. 3.2 and the energy for the $C_{mt}^{\nu=0}$ 1s $\rightarrow$ LEMO$^{\nu'=0}$ excitations is obtained from the fit in Fig. 3.6. The DFT calculations were carried out as described before.

it can be assumed that these effects are also sufficiently small for larger polyacenes.

The signature of the first resonance in the NEXAFS of the polyacenes in Fig. 3.6 can be reproduced sufficiently well by superposing two benzene spectra or one benzene and one naphthalene spectrum in case of anthracene and tetracene, respectively. The good agreement between the sum curve and the measured data gives confidence in this approach. Hence, for the polyacene molecules the excitation energy for the $C_{mt}^{\nu=0}$ 1s $\rightarrow$ LEMO$^{\nu'=0}$ transition can be determined from the energy position of the maximum of the benzene spectrum. The corresponding excitation energies are shown in Fig. 3.8 and Tab. 3.1.

In Fig. 3.7 the energy position of the NEXAFS onset and the LEMO is plotted over the polyacene size. Additionally, the difference in the Kohn–Sham energies

Molecule	C 1s (PES)	LEMO onset	LEMO max.	E_{LUMO} (IPES)	E_{LUMO} (DFT)	$\Delta E_{LUMO-C_{mt}1s}$ (DFT)
Benzene	285.45	284.86	284.99	3.60	3.66	284.99
Naphthalene	286.15	284.36	284.53	2.94	2.95	284.34
Anthracene	285.61	283.83	283.97	2.42	2.49	283.92
Tetracene	285.27	283.54	283.67	2.26	2.18	283.63
Pentacene	285.27	283.26	283.38	–	1.95	283.42
Hexacene	–	–		–	1.80	283.27
Heptacene	–	–		–	1.69	283.17

Table 3.1: Comparison between the C 1s binding energy of different polyacenes in core level PES from [A3], the energy position of the C 1s → LEMO transition, the LUMO binding energy in the IPES data in [59], the trend in the LUMO ground state energy (DFT) and the trend in the energy difference $\Delta E_{LUMO-C_{mt}1s}$ between the LUMO and the C 1s level in the ground state (DFT). Note that the calculations are carried out with the B3LYP functional and a 6-311G basis set. The Kohn–Sham energies are rescaled according to *section 3.3.1*.

$\Delta E_{LUMO-C_{mt}1s}$ between the C_{mt}1s orbital and the LUMO is indicated (dashed line). The energy scale of the DFT calculations is compressed by 0.7025 and shifted in energy for better comparison, as it was described in *section 3.3.1*. The trend in the LEMO energy E_{LEMO} agrees well with that in $\Delta E_{LUMO-C_{mt}1s}$. Consequently, the decrease in the LEMO energy can be mainly attributed to an effect in the ground state, namely the decrease in the energy of the LUMO with increasing molecular size. This implies that the relaxation energy for the $C_{mt}^{\nu=0}$ 1s → $LEMO^{\nu'=0}$ transition does not change significantly with increasing polyacene size. Only for naphthalene the excitation energy is slightly higher (150 meV) than what is expected from the trend in the ground state. This may be a hint for a slightly smaller relaxation energy for naphthalene with respect to benzene, anthracene, tetracene and pentacene in analogy to the findings for core level PES, [A3] where the binding energy of the C 1s mainline increases by 0.7 eV from benzene to naphthalene and decreases by 0.9 eV from naphthalene to pentacene. This effect was mainly attributed to a significantly smaller relaxation energy for naphthalene due to the reduction of the molecular symmetry from D_{6h} for benzene to D_{2h} for naphthalene. For the $C_{mt}^{\nu=0}$ 1s → $LEMO^{\nu'=0}$ transition this effect seems to be one order of magnitude smaller.

3.3.4 The cross section for C_{mt} 1s → LEMO transitions

Furthermore, a significant decrease in intensity of the of the C $1s^{\nu=0}$ → $LEMO^{\nu'=0}$ excitation can be observed in Fig. 3.1 and 3.2 in addition to the shift to lower energy of the respective feature. From the fit of the x–ray absorption data with benzene and naphthalene spectra in Fig. 3.6 the intensity can be estimated for the

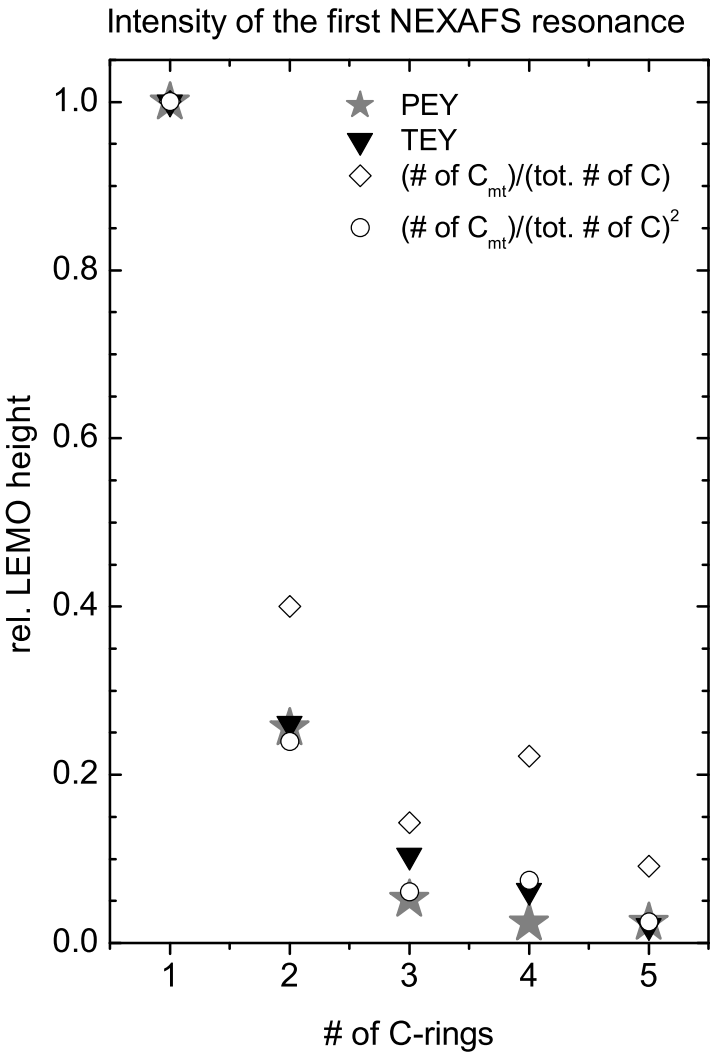

Figure 3.8: Comparison of the height of the first feature in the polyacene NEXAFS, which corresponds to C_{mt} 1s $\rightarrow$ LEMO transitions at the *mid–top* carbon site. The respective intensities are derived from the PEY and the TEY signal by fitting a Benzene spectrum to the respective NEXAFS signal as it is described in *subsection 3.3.3*. The respective intensities are corrected for the different molecular orientation of the polyacene moecules and normalized to the value of benzene. Furthermore, the expected tendency is indicated for two scenarios: the LEMO is not affected by an increase in polyacene size (◊) and delocalization of the LEMO over the entire molecule (○). – See the text for more details.

C_{mt} 1s $\rightarrow$ LEMO transition at the *mid–top* carbon site. The respective trend in the peak height can be compared to the expected trend for two extreme scenarios, namely to the case where the LEMO is completely delocalized over the entire molecule and to the case where the size of the LEMO is the same for the different polyacenes.

The transition intensity is influenced by the degeneracy of the excited state and the respective dipole matrix element, as it has been described in *subsection 3.1.2*. Taking both both aspects into account the trend with increasing polyacene size can be estimated in a rudimentary approximation:

Model 1: Same LEMO size for different polyacenes:

Assuming that the shape of the LEMO is the same for all polyacene molecules, the matrix element M_{fi} is also the same according to (3.21) in the one–electron view. Consequently, the intensity of the respective transition depends only on the degeneracy of the final state $\langle f|$, which corresponds to the number of equivalent C_{mt} core hole sites, namely 6 for benzene, 4 for naphthalene, 2 for anthracene, 4 for tetracene and 2 for pentacene. As the polyacene NEXAFS spectra are normalized to the height of the adsorption edge, which is proportional to the total number of C atoms in the probed volume, the LEMO intensity in the spectra should scale with the number of equivalent core hole sites over the total number of C atoms per molecule.

$$I_{LEMO} \sim \frac{\sharp \text{ of } C_{mt} \text{ atoms}}{\text{total } \sharp \text{ of C atoms per molecule}}. \tag{3.23}$$

Model 2: LEMO equally delocalized over the whole molecule:

If the LEMO is equally delocalized over the whole molecule, one can assume to first order that its density at each carbon site is equal. Consequently, its density at one carbon site is inversely proportional to the total number of C atoms per molecule. If the π–symmetry of the LEMO is conserved for all molecules without any additional nodal plane at the C_{mt} site which is perpendicular to the molecular plane the transition probability P_{fi} is also inversely proportional to the total number of C atoms per molecule. Therefore the intensity of the C_{mt} 1s $\rightarrow$ LEMO transition should scale with

$$I_{LEMO} \sim \frac{\sharp \text{ of } C_{mt} \text{ atoms}}{(\text{total } \sharp \text{ of C atoms per molecule})^2}. \tag{3.24}$$

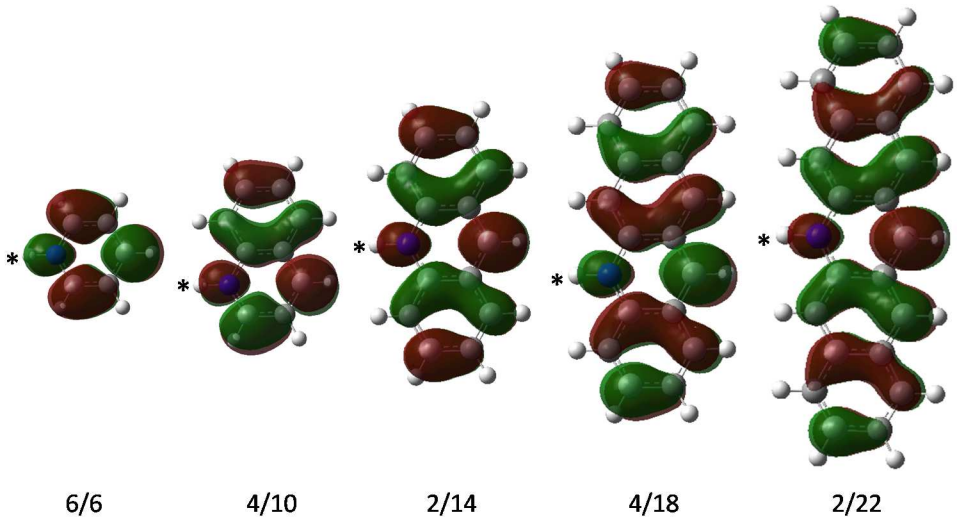

Figure 3.9: (Color online) The LEMO of different polyacenes for C_{mt} 1s $\rightarrow$ LEMO transitions at the *mid–top* carbon site – marked with an $*$. The orbitals are obtained from Z+1 DFT calcualtions with the B3LYP density functional and a 6-311G basis set. The graph shows the iso–density surface (0.02 e/bohr^3) with the phase of the wave function being indicated by red and green color. The number of core hole sites which contribute to the C_{mt} 1s $\rightarrow$ LEMO transition is given at the bottom together with the total number of carbon atoms.

The intensity of the C_{mt} 1s $\rightarrow$ LEMO(π^*) transition is plotted in Fig. 3.8 over the polyacene size for better comparison after correcting for the different average molecular orientations in the polyacene films and normalizing to the LEMO intensity in the benzene NEXAFS. Additionally, the expected values are indicated for two extreme scenarios, namely the same LEMO size for all polyacene molecules (*model 1*) and an equally distributed LEMO over the entire molecule (*model 2*).

The LEMO intensities in the NEXAFS spectra agree well with the expected values for *model 2*, where the LEMO is assumed to be delocalized over the entire molecule. This is corroborated by a comparison of the different polyacene LEMOs in Fig. 3.9 which are obtained from Z+1 calculations of the respective core excited states. Accordingly, the LEMO is completely delocalized over the entire molecule for all investigated polyacenes. Consequently, the results of the calculations are close to the assumptions for relation (3.24). Note that a strongly excitonic core excited state is often assumed to be closer to the assumptions for *model 1* than to those for *model 2*. This is discussed below in more detail.

3.4 Summary & Discussion

The C K NEXAFS investigation of polyacene thin films has demonstrated that the trend in the excitation energy for the C_{mt} 1s $\rightarrow$ LEMO(π^*) transition as a function of the polyacene size is very similar to the trend in the LUMO binding energy from IPES, while the trend in the C 1s binding energy in the core level PES data is different. The similar trends in NEXAFS and IPES data suggest that the decrease in the LEMO and the LUMO excitation energy with increasing polyacene size can mainly be attributed to an effect in the ground state. This has been further supported by DFT calculations. Consequently, the relaxation energy, which can be considered as a measure for the reorganization of the electronic structure in the excited state, is similar for the different polyacenes.

In contrast, for core ionization the relaxation energy differs strongly between the various polyacene molecules. This has been illustrated by the core level PES data of polyacene series. In particular the relaxation energy decreases by 0.7 eV from benzene to naphthalene and increases by 0.9 eV from naphthalene to pentacene. The decrease has been attributed to the reduction of the molecular symmetry, which

hinders the relaxation in the core ionized final state of naphthalene.[2] Moreover, the increase in the relaxation energy from naphthalene to larger polyacenes has been related to the increasing size of the π–system. [A3]

This effect is significantly weakened when the core electron is not emitted but still present in the LEMO. Consequently, the additional electron on the core excited molecule improves the relaxation of the electronic structure significantly, so that the change of the molecular symmetry between benzene and naphthalene as well as the increasing size of the π–system have only minor influence on the electronic relaxation. This effect is often considered as screening of the core hole by the excited electron. Consequently, in case of NEXAFS transitions the wave function $\Psi_f(N-1)$ of the remaining electrons is less modified with respect to the ground state ($\Psi_i(N-1)$) than in case of core ionization.

This finding has further consequences concerning the dipole matrix element and the transition probability for the respective core excitations. It has been discussed in *section 3.1.3* with respect to Koopmans' theorem that in PES the electronic relaxation leads to additional satellites above the main line. Analogously, satellite excitations contribute also to the NEXAFS spectra, but their overall cross section is smaller than in PES. Note that satellite excitations were studied extensively in the NEXAFS of argon and neon. [74–79] It is difficult to identify such multi–electron excitations in the NEXAFS of organic molecules because in general many transitions contribute to the overall signal, which overlap in energy. Nevertheless, one needs to keep in mind that satellite excitations also contribute to NEXAFS spectra.

Furthermore, a general statement about the core hole localization effect can be made. It is known that for core excitations into bound final states the relaxation energy depends strongly on the localization of the core hole with respect to the excited molecular orbital (EMO). As a rule of thumb, it is assumed that the transition probability is high and the electronic relaxation is large when the excited molecular orbital has a high density at the core hole (and appropriate symmetry). [35, 47, 55] The different relaxation energies between different core excited states of a certain molecule are often explained by this scenario. However, the NEXAFS investigation of the polyacene series has shown that the relaxation energy for C 1s $\rightarrow$ LEMO transitions at chemically similar carbon sites is the same, regardless of the delocalization of the LEMO, while the intensity decreases as expected. This demonstrates the many–body character of the NEXAFS transition. Apparently, the delocalization of the LEMO with increasing molecular size is compensated by the occupied valence states.

[2] Note that charging could be ruled out. Furthermore, it can be assumed that the interaction between neighboring molecules is similar for the benzene and the naphthalene film because of similar growth modes.

Considering all these aspects, the concept of a core exciton, which is often used in relation to NEXAFS spectroscopy, needs to be discussed briefly. In the classical sense an exciton is considered as an electron–hole pair due to Coulomb interaction. In general the exciton binding energy is defined as the energy, which is necessary to separate the electron from the hole or the energy for transferring the excited electron onto another molecule, respectively. Typically, it is small for delocalized excitons (Mott–Wannier type) and large for localized ones (Frenkel type).

For core excitations, the exciton binding energy is the energy difference between the C 1s $\rightarrow$ LEMO transition energy and the sum of the C 1s and the LUMO binding energy. With the values in Tab. 3.1 one finds that the exciton binding energy basically reflects the trend in the C 1s binding energy because of the different electronic relaxation. In particular it increases from benzene to naphthalene and decreases from naphthalene to pentacene. Consequently, a high exciton binding energy does not necessarily imply a high localization of the LEMO at the hole and a high transition probability. As this interrelation applies analogously for valence excitons it can be important for the electron–hole separation at interfaces as well as for electron–hole recombination, e.g. fluorescence decay.

4

Charge transfer satellites at metal–organic interfaces — PTCDI, PTCDA, BTCDI and BTCDA on Ag(111)

Charge transfer satellites have been intensively studied for various *transition metal compounds*, [80–89] e.g. for the divalent dihalides (CuF_2, $CuCl_2$, $CuBr_2$) and NiO. [8–12] In these materials transition metal atoms with a partially filled d or f shell, respectively, are embedded in a matrix of ligands. Due to the quite localized character of the d/f states many of the observed effects can be explained in a simple molecular orbital frame work, with only one metal atom and the surrounding ligands being considered. When a core hole is created at the metal atom, the energy of the initially unoccupied localized d/f states is lowered, so that it is similar to the energy of the occupied ligand valence levels, which can induce electron transfer from the ligands to the metal atom. Depending on the energy of the d/f levels in the core excited state with respect to that of the occupied ligand levels, the electron transfer can lower or raise the energy of the core excited state compared to core excitation without charge transfer, similar to shake–up or and shake–down transitions. Hence, a rich satellite structure can be observed in the core level spectra of these materials. As for transition metal compounds the intensity of the various spectroscopic features is often of the same order it is convenient to refer to the contribution with the lowest binding energy as the *main line* and the contributions at higher binding energy as the *satellites*. Moreover, it was found that charge transfer satellites can also be relevant for pure metals and alloys with localized d or f electrons. [90–95]

Furthermore, charge transfer satellites have also been observed for interfaces between adsorbate films of small molecules, e.g. CO and N_2 on various metal substrates [96–105] and carbonyl–transition–metal complexes. [106] Several core level PES studies and quantum chemical calculations of such interfaces indicate that the rich charge transfer contributions are very sensitive to the adsorbate–substrate coupling. [107] They particularly appear in case of covalent interface interaction. Moreover, it is suspected that charge transfer satellites also play an important role for adsorbate–substrate interfaces of large organic molecules. [108–111] The core level spectra of CO and N_2 monolayer films could be understood by comparing several

monolayer films on different substrates and by a theoretical approach developed by *Gunnarsson and Schönhammer*, which allows calculations of the core level spectra within the framework of the Anderson impurity model. [97,103,104,112,113] In this chapter an alternative and comparatively simple approach to the many–body effects in the core level spectra of adsorbates will be offered. It allows to model and understand the core level data qualitatively, and it improves the understanding of the fundamental physics at the adsorbate–substrate interface.

It will be shown that the concepts developed by *Sawatzky et al.* and *Kotani et al.* for charge transfer compounds [8,9,12,114–116] can be transferred to the situation for weakly chemisorbed molecules at the molecule–metal interface. The simplicity of the approach discussed in the following allows to model the PES data. Consequently, important parameters for the adsorbate–substrate interaction, e.g. the coupling strength, can be deduced from the PES data. It will be shown that these parameters are even quantitatively in a reasonable range, despite several approximations. In this scenario the molecule takes the role of the transition metal atom and the (metal) substrate surface can be considered as ligand with an infinite Fermi sea.

Several organic–metal interfaces are studied comprehensively and systematically in the following. The investigation of different molecular monolayers on the same metal surface gives information on the influence of the molecular properties on the interface interaction. For this study the Ag(111) surface was chosen because of its intermediate reactivity, which is in between that of Au and Cu. Furthermore, the (111) surface is a standard surface for many surface and interface investigations. Moreover, four different molecules are chosen, which are shown in Fig. 4.1 — 3,3',4,4'–**b**enzophenone **t**etra**c**arboxylic **di**a**n**hydride (BTCDA), 3,3',4,4'–**b**enzophenone **t**etra**c**arboxylic **di**i**m**ide (BTCDI), 3,4,9,10–**p**erylene **t**etra**c**arboxylic **di**a**n**hydride (PTCDA) and 3,4,9,10–**p**erylene **t**etra**c**arboxylic **di**i**m**ide (PTCDI). Consequently, the influence of the size of the π–system and the influence of the electronegativity of the functional group can be studied, which is lower for the diimide group than for the dianhydride group. As the energy of the valence levels is of interest for the charge transfer satellites, one should note that the HOMO–LUMO gap decreases from BTCDA to PTCDI. Moreover, PTCDA has become a standard molecule for studying organic thin films and interfaces, [117,118] and therefore the electronic thin film and interface properties can be discussed with respect to the PTCDA bench mark in the following.

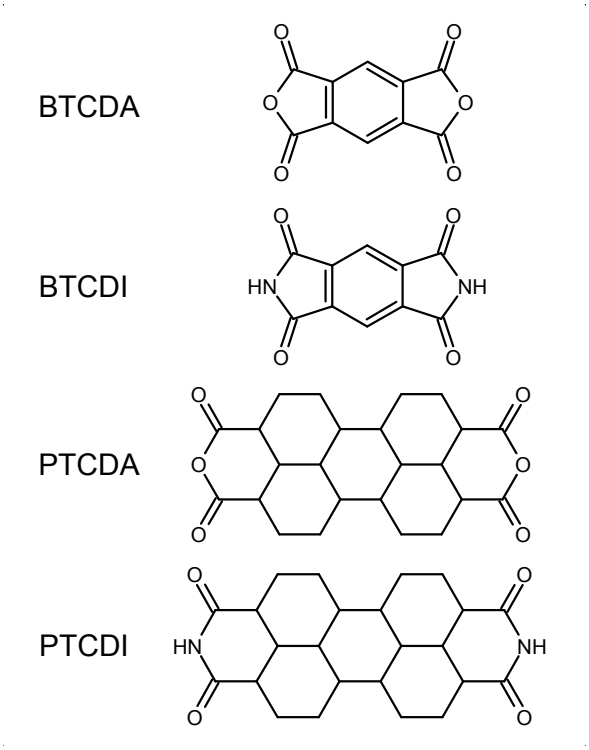

Figure 4.1: Structural formula of the aromatic molecules BTCDA, BTCDI, PTCDA, PTCDI.

4.1 General considerations for a two–level atom

Before dealing with the experimental data it is helpful to gain some insight into the interface properties by discussing the interaction of a single atomic adsorbate with a metal substrate. The effect of the interface interaction on the PES and NEXAFS signal is demonstrated by considering a free two–level atom at first, followed by switching on the coupling to the free electron gas of the metal substrate in the second step. It will be shown in *section 4.3* that the resulting effects are also relevant for molecular adsorbates on metal surfaces.

4.1.1 Valence configurations and core excited states without interface interaction

In a multilayer film of very weakly interacting atomic adsorbates, e.g. inert gas atoms, it is to first order sufficient to neglect the interatomic interaction when discussing the core excitation and to consider only the properties of the single atom instead. Two electronic levels are of interest in the following, one core level $|c\rangle$ with energy $\epsilon_c < 0$ and one valence level $|a\rangle$ with energy $\epsilon_a > 0$, which is initially unoccupied. The energies are given with respect to the chemical potential μ and the spin degeneracy is neglected for simplicity. Accordingly, the model Hamiltonian H which describes the creation of a core hole is given by

$$\begin{aligned} H &= H_0 + H_c \\ &= \epsilon_c n_c + [\epsilon_a - U_{ac}(1 - n_c)]n_a \end{aligned} \tag{4.1}$$

where the valence level is pulled down an energy U_{ac} due to the Coulomb interaction with the core hole, and electronic relaxation is neglected. [97, 112, 114–116, 119] Consequently, if the valence orbital is occupied ($n_a > 0$) and $U_{ac} > \epsilon_a$, the total energy of the core excited state is lower than for $n_a = 0$ and vice versa for $U_{ac} < \epsilon_a$ as indicated in Fig. 4.2. In analogy to the nomenclature for charge transfer compounds the core hole is described by c^{-1} and the occupation of the valence level is expressed by a^{+1}. On the left hand side in Fig. 4.2 the total energy of the ground state (a^0) and the first excited state a^{+1} are indicated. The creation of a core hole lowers the total energy of the configuration with an additional valence electron ($c^{-1}a^{+1}$) by U_{ac} with respect to the $c^{-1}a^0$ configuration. Assuming that the ground state corresponds to a pure a^0 configuration, the $c^{-1}a^{+1}$ configuration can be obtained by a direct electronic transition, as e.g. in NEXAFS spectroscopy, for appropriate

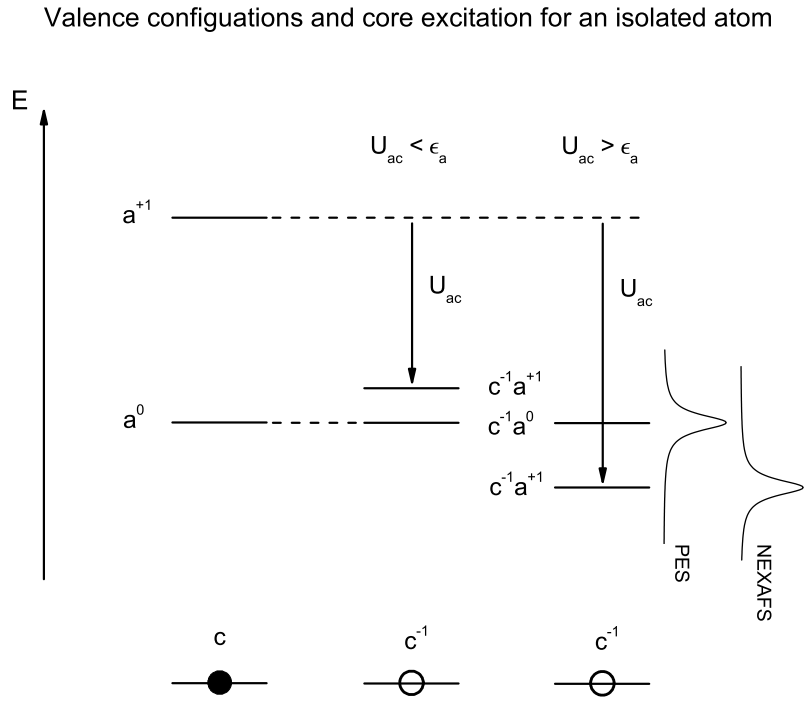

Figure 4.2: Comparison between different valence configurations in an isolated atom with core hole (c^{-1}) and without (c). For the case that no core hole is created the configuration where $|a\rangle$ is unoccupied corresponds to the ground state and the first excited state corresponds to $|a\rangle$ being occupied by an additional electron. Creation of a core hole lowers the total energy of the configuration with an additional valence electron ($c^{-1}a^{+1}$) by U_{ac} with respect to the $c^{-1}a^0$ configuration. Depending on the magnitude of U_{ac} with respect to ϵ_a the total energy of the $c^{-1}a^{+1}$ configuration is lower or higher than that for the $c^{-1}a^0$ configuration. Additionally, the contributions to the PES and NEXAFS signal is indicated for $U_{ac} > \epsilon_a$ under the assumption that $|c\rangle$ and $|a\rangle$ satisfy the dipole selection rule.

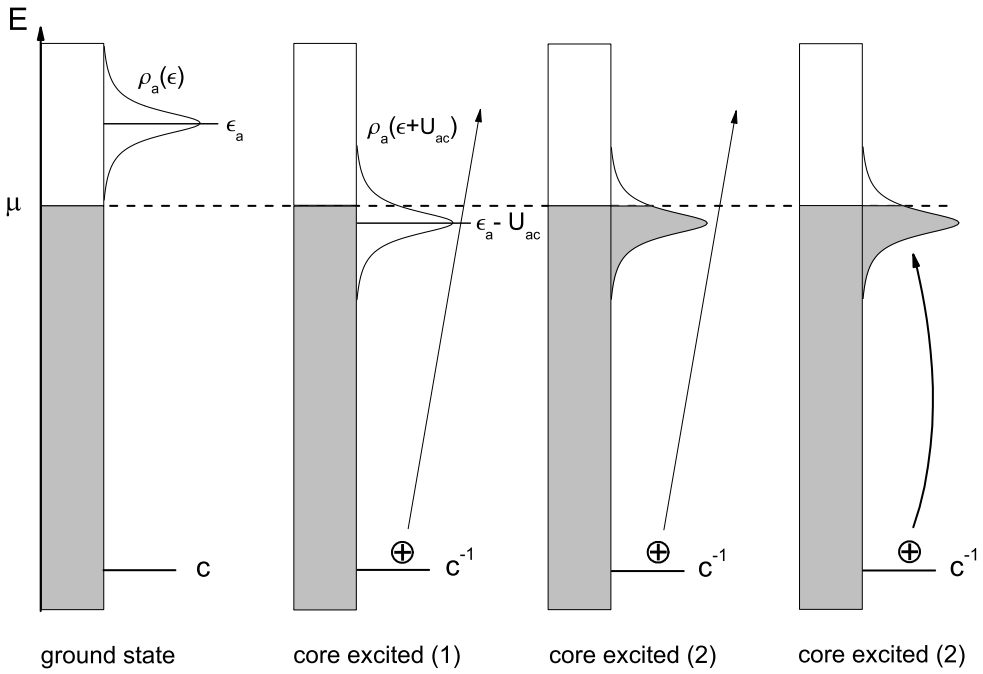

Figure 4.3: Schematic comparison between different valence configurations of core excited states for a two–level atom chemisorbed at a metal surface. Due to the coupling of the atomic valence level with the substrate states a density of adsorbate states $\rho_a(\epsilon)$ is formed. In the ground state (left) this DOS is centered at ϵ_a and unoccupied. In the core excited state adsorbate states can be pulled below the Fermi level and can now, in principle, accommodate an additional electron. *Core excited (2)* depicts the configurations for the core excited state of lowest energy, where all states below the Fermi level are occupied and all above are unoccupied. Either core ionization and electron transfer from the substrate into adsorbate valence states or a direct electronic transition can lead to the *core excited state (2)*.

orbital symmetries. The $c^{-1}a^0$ configuration corresponds to a core ionized state after photoemission of the core electron. Fig. 4.2 illustrates that it depends on U_{ac} whether the total energy of the final state after core ionization is higher or lower than the energy in the NEXAFS final state.

4.1.2 Chemisorption on a metal surface in the single impurity Anderson model for $U = 0$

Anderson [28] developed a description of the interaction between localized magnetic impurities with correlated d electrons, such as Fe, Co or Ni atoms, and a nearly

free electron gas. Accordingly, the coupling between the d state with energy E_a of the impurity and the states of the free electron gas leads to a density distribution of atom–substrate valence states. The density distribution of the impurity states can be described by

$$\rho_a(\epsilon) = \frac{1}{\pi}\frac{\Delta}{(\epsilon - E_a)^2 + \Delta^2} \tag{4.2}$$

with the width in energy Δ depending on the coupling parameter V and the electron density distribution of the free electron gas $\rho(\epsilon)$.

$$\Delta = \pi \langle V^2 \rangle_{av} \rho(\epsilon) \tag{4.3}$$

Furthermore, the eigenstates of the coupled two–level system can be described by linear combinations of the one–electron states. The mixing of these states is small if the correlation energy U is significantly larger than the width Δ and the mixing is large if both energies are of the same order.

The charge transfer at the interface upon core ionization can be treated in the same frame work. Considering weakly covalent interaction between the single atom from *section 4.1.1*, with negligible correlation energy U_{aa} between the two electrons in $|a\rangle$, and a metal substrate, the Anderson Hamiltonian [28, 120] for the interface problem has the form [97, 115, 116, 121]

$$H = \epsilon_c n_c + [\epsilon_a - U_{ac}(1 - n_c)]n_a + \sum_k \epsilon_k n_k + \sum_k (V_{ak} c_a^+ c_k + V_{ka} c_k^+ c_a), \tag{4.4}$$

with ϵ_k corresponding to the energy of the states $|k\rangle$ of the free electron gas, V_{ak} being the coupling parameter between $|k\rangle$ and the adsorbate level $|a\rangle$, and c_a^+ and c_k^+ being the respective creator operators. Consequently, the coupling between the adsorbate level $|a\rangle$ and the substrate induces a density distribution of adsorbate–substrate states, analogous to the findings for the coupling of magnetic impurity levels with the DOS of the free electron gas. Hence, the density distribution of adsorbate states $\rho_a(\epsilon)$ satisfies the relations (4.2) and (4.3). Note that it can be assumed that $E_a = \epsilon_a$ to first order, which implies that chemical shifts are neglected.

Consequently, the density distribution of adsorbate states $\rho_a(\epsilon)$ is centered at ϵ_a in the ground state and unoccupied as illustrated in Fig. 4.3. Hence, the charge transfer energy for full occupation of $\rho_a(\epsilon)$ is $\Delta_{CT} = \epsilon_a$. The interaction with the core hole lowers the energy of the adsorbate valence states by U_{ac}, so that

previously unoccupied states can be pulled below the Fermi level if U_{ac} is large enough. Consequently, the energy of the core excited state can be raised or lowered by occupying adsorbate valence states. If U_{ac} is so that $\rho_a(\epsilon + U_{ac})$ is centered close to the Fermi level as shown in Fig. 4.3, the core excited state which is lowest in energy corresponds to the configuration "core excited (2)" where all states below the Fermi level are occupied and all above are unoccupied. Inversion of the occupation of $\rho_a(\epsilon + U_{ac})$ leads to the highest core excited state.

The eigenfunctions of the Hamiltonian H can be expressed to first approximation in a two–fold basis containing the wave functions for two configurations in the uncoupled case, $\Psi(c^{-1}a^0)$, where a core hole is created, and $\Psi(c^{-1}a^{+1})$, where additionally an electron is transferred to the atom. Then the wave function for the core excited state can be written as

$$\Psi_{low} = (1- < n_a >)\Psi(c^{-1}a^0) \mp < n_a > \Psi(c^{-1}a^{+1}) \tag{4.5}$$

For the core excited state of lowest energy, which corresponds to "core excited (2)" in Fig. 4.3, the coefficient $< n(a) >$ can be determined by integrating the density of adsorbate–substrate states ρ_a from relation (4.2) up to the Fermi level ϵ_F.

$$\begin{aligned} < n_a > &= \int_{-\infty}^{\epsilon_F} \rho_a(\epsilon + U_{ac})\, d\epsilon \\ &= \frac{1}{\pi} \arctan\left(\frac{\epsilon_F - \Delta'_{CT}}{\Delta}\right) + 0.5 \end{aligned} \tag{4.6}$$

In the following it is referred to $\Delta'_{CT} = \epsilon_a - U_{ac}$ as charge transfer energy because it corresponds to the energy for transferring one electron from the substrate to the core excited adsorbate. As for the highest core excited state the occupation of $\rho_a(\epsilon + U_{ac})$ is just inverted, it follows immediately that

$$\Psi_{high} =< n_a > \Psi(c^{-1}a^0) \pm (1- < n_a >)\Psi(c^{-1}a^{+1}) \tag{4.7}$$

Consequently the configuration mixing depends on the parameter U_{ac} and the width Δ of the density distribution of adsorbate states. In particular for $U_{ac} = \epsilon_a$ the configuration mixing is 1:1 and it decreases with increasing or decreasing U_{ac}, respectively. Moreover, this decrease is steeper for smaller Δ.

Therefore, the charge transfer energy Δ'_{CT} plays a similar role as the correlation energy in the Anderson Impurity model in [28]. The mixing of the two configurations is very small if the charge transfer energy is much larger than the

width Δ of the density distribution of adsorbate states ($\Delta'_{CT}/\Delta >> 1$). However, the two configurations are strongly mixed if it is of the same order ($\Delta'_{CT}/\Delta \simeq 1$).

4.1.3 Satellite intensities and energies

As in core level PES the satellite transitions can be treated in the monopole approximation, [48, 49] strong mixing of the two configurations in the core excited state leads to a strong satellite intensity. In particular the intensity of the respective core excited states depends on the contribution of the ground state configuration to the wave function of the respective core excited state. Based on this interrelation the charge transfer satellites at the substrate–adsorbate interface can be modeled by the following formalism, which was developed by *Sawatzky* et al. [8] for the description of charge transfer satellites in core level photoelectron spectra of copper dihalides. It models the energy separation between the main and the satellite peak in the PES spectra and their relative intensity. This formalism can also be applied to the interface problem with minor modifications.

Assuming that the eigenstates for the Hamiltonian H without the core hole ($n_c = 1$ in (4.4)) are linear combinations of state $|m\rangle$ and $|n\rangle$ it is

$$\Psi = c_1|m\rangle + c_2|n\rangle \tag{4.8}$$

The eigenvalues for H can be obtained from

$$det \begin{pmatrix} H_{mm} - E & H_{mn} - S_{mn}E \\ H_{nm} - S_{nm}E & H_{nn} - E \end{pmatrix} = 0 \tag{4.9}$$

where the overlap integral $S_{mn} = \langle m|n\rangle$. For small overlap integrals ($S_{mn} \to 0$) the quadratic equation for the eigenvalues can be solved:

$$E_{1,2} = \frac{1}{2}(H_{mm} + H_{nn}) \pm \frac{1}{2}\sqrt{(H_{nn} - H_{mm})^2 + 4H_{mn}H_{nm}} \tag{4.10}$$

$$= E_0 + \frac{1}{2}\Delta_{CT} \pm \frac{1}{2}\sqrt{\Delta_{CT}^2 + 4T^2} \tag{4.11}$$

where $\Delta_{CT} = H_{nn} - H_{mm} = \langle n|H|n\rangle - \langle m|H|m\rangle$ and $T = H_{mn} = \langle m|H|n\rangle$. The corresponding eigenfunctions can be written for a positive value of T as

$$\Psi_1 = \sin\theta\ \Psi(a^0) + \cos\theta\ \Psi(a^{+1}) \quad (4.12)$$
$$\Psi_2 = \cos\theta\ \Psi(a^0) - \sin\theta\ \Psi(a^{+1}). \quad (4.13)$$

Moreover, from $\langle\Psi_1|H|\Psi_1\rangle - \langle\Psi_2|H|\Psi_2\rangle = \sqrt{\Delta_{CT}^2 + 4T^2}$ one obtains

$$\tan 2\theta = \frac{2T}{\Delta_{CT}} \quad (4.14)$$

where the value of θ is restricted to $0 < \theta < 45°$ for $\Delta_{CT} > 0$. For the core excited state the interaction of the core hole with the valence state $|a\rangle$ has to be taken into account additionally. Consequently, the energy difference between the $c^{-1}a^0$ and the $c^{-1}a^{+1}$ configuration is $\Delta'_{CT} = \Delta_{CT} - U_{ac}$. Accordingly, the eigenvalues are

$$E_{s,m} = E'_0 + \frac{1}{2}\Delta'_{CT} \pm \frac{1}{2}\sqrt{\Delta'^2_{CT} + 4T^2} \quad (4.15)$$

with the corresponding eigenfunctions

$$\Psi_l = \sin\theta'\ \Psi(c^{-1}a^0) + \cos\theta'\ \Psi(c^{-1}a^{+1}) \quad (4.16)$$
$$\Psi_m = \cos\theta'\ \Psi(c^{-1}a^0) - \sin\theta'\ \Psi(c^{-1}a^{+1}) \quad (4.17)$$

with

$$\tan 2\theta' = \frac{2T}{\Delta'_{CT}} \quad (4.18)$$

and with θ' restricted to $0 < \theta' < 45°$ for $\Delta'_{CT} > 0$. Hence, the core level spectrum consists of a main peak with intensity I_m which corresponds to the core excited state of lowest energy E_m and a satellite with intensity I_s which corresponds to the core excited state of energy E_s. With respect to (4.15) the energy separation between the main and the satellite peak is

$$W = E_s - E_m = \sqrt{(\Delta_{CT} - U_{ac})^2 + 4T^2} \quad (4.19)$$

In the sudden approximation the intensity ratio of the satellite and the main peak can be determined by the overlap of the wave functions in the ground state and in

the excited state. Assuming that $|a\rangle$ is unoccupied in the ground state ($\Delta_{CT} = \epsilon_a > 0$) and $0 < \theta < 45°$, the ground state corresponds to Ψ_2. According to the monopole selection rule for the satellite transitions [48, 49] the intensity ration follows from the direct overlap of the respective wave functions.

$$\begin{aligned} \frac{I_s}{I_m} &= \frac{|\langle\Psi_l|\Psi_2\rangle|^2}{|\langle\Psi_m|\Psi_2\rangle|^2} \\ &= \left(\frac{\sin\theta'\cos\theta - \cos\theta'\sin\theta}{\cos\theta'\cos\theta + \sin\theta'\sin\theta}\right)^2 = \tan^2(\theta' - \theta) \end{aligned} \tag{4.20}$$

From the choice of the wave functions it follows that $0° < \theta < 45°$ for $\Delta_{CT} > 0$ and $45° < \theta < 90°$ for $\Delta_{CT} < 0$ and $0° < \theta' < 45°$ for $\Delta_{CT} - U_{ac} > 0$ and $45° < \theta' < 90°$ for $\Delta_{CT} - U_{ac} < 0$. Consequently, the satellite intensity depends only on the difference in the configuration mixing between the ground state and the core excited state.

The effect of the configuration mixing is also depicted schematically in Fig. 4.4. The validity of this formalism can be checked by considering three extreme scenarios, where it is assumed that $\Delta_{CT} = \epsilon_a > 0$ and $\Delta'_{CT} = (\epsilon_a - U_{ac}) < 0$.

- **No coupling**

  For a free atom the coupling parameter V_{ka} vanishes and therefore $\Delta \to 0$ according to (4.3). Hence, it is $\Delta_{CT}/\Delta = \epsilon_a/\Delta \to \infty$ and $\Delta'_{CT}/\Delta = (\epsilon_a - U_{ac})/\Delta \to -\infty$, which implies no mixing of the configurations a^0, a^{+1} and $c^{-1}a^0$, $c^{-1}a^{+1}$, respectively. Thus, $\theta = 0°$ and $\theta' = 90°$, and therefore no charge transfer satellites are observed according to (4.20). Furthermore, as for this scenario $\Psi(c^{-1}a^0)$ and $\Psi(c^{-1}a^{+1})$ are the eigenstates of H it is $T^2 = |\langle\Psi(c^{-1}a^{+1})|H|\Psi(c^{-1}a^0)\rangle|^2 = 0$ in agreement with (4.18). Then the difference between the eigenvalues of H in (4.19) becomes $W = \Delta_{CT} - U_{ac}$, which corresponds to the energy difference of the one–electron states as it is indicated in Fig. 4.2.

- **Electronic coupling and $\epsilon_a >> 0$**

  In the case that $\epsilon_a >> \Delta$ there is no significant configuration mixing in the ground state and consequently $\theta = 0°$. If the coupling parameter V_{ka} is sufficiently large so that $(\Delta'_{CT}/\Delta \simeq 1)$, there is significant configuration mixing in the core excited state ($\theta' < 90°$), which leads to considerable satellite intensity according to (4.20). Additionally, $\Psi(c^{-1}a^0)$ and $\Psi(c^{-1}a^{+1})$ are not the eigenstates, which leads to $T^2 > 0$, and consequently according to (4.19) the difference of the eigenvalues of H is larger than for the non–interacting case.

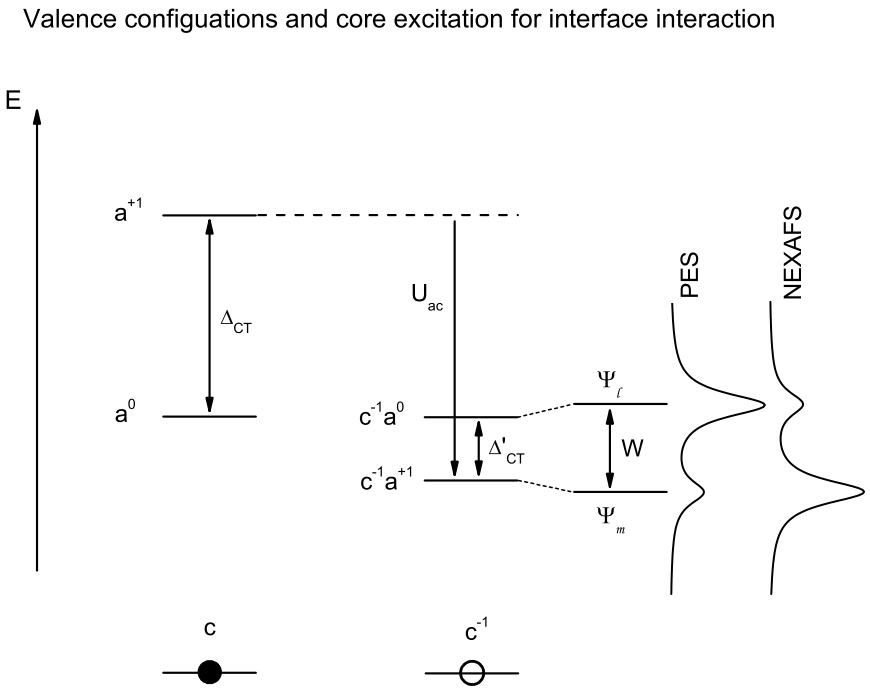

Figure 4.4: Configuration mixing in the core excited state for electronic coupling between unoccupied adsorbate valence states and the electronic states of a free electron gas. On the left hand side the energy diagram for two different electronic configurations is indicated for the ground state (c) and the core excited state (c^{-1}) without electronic adsorbate–substrate coupling. On the right hand side the influence of the coupling on the energy diagram for the core excited state is depicted together with the corresponding contributions in the respective core level photoelectron and NEXAFS spectrum. See also *section 4.1.4* for more details.

- **Electronic coupling and $\epsilon_a \to 0$**

  If ϵ_a is of the same order as Δ, there is significant configuration mixing in the ground state ($\theta > 0°$). If additionally $U_{ac} >> \Delta$, one can assume that the mixing in the core excited state is weak ($\theta' = 90°$). This would again lead to a significant satellite intensity with respect to (4.20).

Consequently, the adsorbate–substrate coupling can lead to significant satellite contributions in the core level photoelectron spectrum, which are related to substrate–adsorbate charge transfer. If the charge transfer energy is significantly larger than Δ, the configuration mixing is small, which results in a very large intensity ratio $I_s : I_m$ with the parameters assumed above, and the satellite and the main peak can be assigned to the scenario where charge transfer occurred or not. However, the configurations are strongly mixed if the correlation energy is of the same order as Δ. Therefore, the intensity ratio $I_s : I_m$ can be of the order of one, and each peak has significant contributions from both configurations.

4.1.4 The influence of the adsorbate–substrate coupling on NEXAFS spectroscopy

The aspect that the electronic coupling between the unoccupied adsorbate valence level with the substrate states leads to a density distribution of adsorbate valence states has significant influence on the NEXAFS. Consequently, a significant broadening of the electronic transitions can be expected with respect to the uncoupled case. Furthermore, relations (3.18), (4.12) and (4.16) suggest that many–body excitations play a significant role in the NEXAFS as well. Let's assume that for the free atom ($V_{ka} = 0 \to \theta = 0°$ and $\theta' = 90°$) the electronic transition from the core level to the unoccupied valence level contributes significantly to the NEXAFS signal. Then the following holds for the transition matrix element in the dipole approximation and the transition probability:

$$\begin{aligned} 0 &= |\langle \Psi_l | \epsilon \cdot \mathbf{p} | \Psi_2 \rangle|^2 \delta(E_l - E_2 \pm \hbar\omega) \\ &= |\langle \Psi(c^{-1}a^0) | \epsilon \cdot \mathbf{p} | \Psi(a^0) \rangle|^2 \delta(E_{c^{-1}a^0} - E_{a^0} \pm \hbar\omega) \qquad (4.21) \\ 0 &< |\langle \Psi_m | \epsilon \cdot \mathbf{p} | \Psi_2 \rangle|^2 \delta(E_m - E_2 \pm \hbar\omega) \\ &= |\langle \Psi(c^{-1}a^{+1}) | \epsilon \cdot \mathbf{p} | \Psi(a^0) \rangle|^2 \delta(E_{c^{-1}a^{+1}} - E_{a^0} \pm \hbar\omega) \qquad (4.22) \end{aligned}$$

Consequently, only one single resonance contributes to the NEXAFS signal from the free atom. Moreover, the coupling between the adatom and the substrate ($|V_{ka}|^2 >$

0) leads to configuration mixing ($0° < \theta < 45°$ and $45° < \theta' < 90°$) as it has been discussed above. Therefore the transition probability changes to

$$\begin{aligned} 0 &< |\langle\Psi_l|\epsilon\cdot\mathbf{p}|\Psi_2\rangle|^2\ \delta(E_l - E_2 \pm \hbar\omega) \\ &= (\sin^2\theta'\sin^2\theta|\langle\Psi(c^{-1}a^0)|\epsilon\cdot\mathbf{p}|\Psi(a^{+1})\rangle|^2 \\ &\quad + \cos^2\theta'\cos^2\theta|\langle\Psi(c^{-1}a^{+1})|\epsilon\cdot\mathbf{p}|\Psi(a^0)\rangle|^2 + ...)\ \delta(E_l - E_2 \pm \hbar\omega) \quad (4.23) \\ 0 &< |\langle\Psi_m|\epsilon\cdot\mathbf{p}|\Psi_2\rangle|^2\ \delta(E_m - E_2 \pm \hbar\omega) \\ &= (\cos^2\theta'\sin^2\theta|\langle\Psi(c^{-1}a^0)|\epsilon\cdot\mathbf{p}|\Psi(a^{+1})\rangle|^2 \\ &\quad + \sin^2\theta'\cos^2\theta|\langle\Psi(c^{-1}a^{+1})|\epsilon\cdot\mathbf{p}|\Psi(a^0)\rangle|^2 + ...)\ \delta(E_m - E_2 \pm \hbar\omega) \quad (4.24) \end{aligned}$$

This indicates that a second resonance appears in the NEXAFS when the electronic coupling is switched on. One is located at $E_m - E_2$ and the other one at $E_l - E_2$ as depicted in Fig. 4.4. For the limit $|V_{ka}|^2 \to 0$ the electronic transition $\Psi_2 \to \Psi_m$ becomes $\Psi_{a^0} \to \Psi_{c^{-1}a^{+1}}$, the single resonance for the free atom, and the signal which corresponds to $\Psi_2 \to \Psi_l$ vanishes, analogous to the findings for the core level photoelectron spectrum where the signal related to the core excited state Ψ_m disappears.

4.1.5 Additional effects for covalent molecule–metal interaction

In general, the adsorption of atoms and molecules leads to a rearrangement of the electronic structure beyond what is taken into account by the simple Anderson Hamiltonian in *section 4.1.2*. These effects can be comparatively small for physisorption with weak, non–covalent interface interaction, e.g. for inert gases on noble metals surfaces, [122–124] and comparatively strong for covalent interface interaction. [125–127, A4] It has been observed that PES core level spectra of ideally physisorbed atoms and molecules on noble metal surfaces resemble the multilayer spectra, except for an overall energy shift which is attributed to the formation of an image potential in the metal as a reaction on the core hole. [128, 129] However, for chemisorbed atoms and molecules with covalent interface interaction considerable (differential) chemical shifts are observed, which indicate a reorganization of the electronic structure between the adsorbate and the metal substrate in both, the ground state and the core excited state. [119] Particularly, adsorbate–substrate hybrid orbitals, which have been neglected so far in the present discussion, play a significant role. In addition to the rearrangement of the electronic structure in the ground state, the adsorbate–substrate hybrid orbitals can contribute significantly to the electronic relaxation in the core excited state, which can lead to differential

chemical shifts between satellites and the main line as well as to changes in the relative intensities due to substrate–adsorbate charge transfer. This is corroborated by the findings in *chapter 3* where it was demonstrated that the electronic relaxation can be significantly different for core ionized states and core excited states with an additional electron in a previously unoccupied level.

In the formalism described in *section 4.1.3* a two–fold basis set was assumed for relation (4.12) and (4.16) consisting of the wave functions for two configurations without adsorbate–substrate coupling. Therefore, the influence of covalent adsorbate–substrate interaction is neglected. However, *Bagus et al.* have recently shown for the CeO_2 transition metal compound that the covalent interaction between the metal and the ligand atoms contributes significantly to the relaxation energy. [130, 131] Moreover, calculations for CO/Cu(001) and PES investigations of the core levels of N_2 and CO on various metal substrates indicate that the relative energy position of the charge transfer satellites is similar for different metal substrates and different coupling parameter V_{ak}, respectively, but their relative intensities vary significantly. [96–100, 132] (and references in [98]) Consequently, the contribution of the adsorbate–substrate hybrid orbitals seems to be similar for these different interfaces and dominated by the same π–orbitals. It can assumed that the simplified model which has been introduced in this section can be well applied to such interfaces. It is particularly suited in case of weakly covalent interface interaction, where the redistribution of the adsorbate–substrate hybrid orbitals contributes comparatively little to the electronic relaxation in the core excited state.

Furthermore, in case of molecules there can be various electronic states near the Fermi level, and consequently several different electronic configurations can mix instead of two. This can lead to broad multi–peak signatures in core level PES and NEXAFS spectroscopy. Then the eigenstates in 4.1.3 can be expressed as a linear combination of several electronic configurations, and the eigenvalue problem has to be solved for a larger basis set. Additionally, the electron–vibration coupling plays a significant role for molecules. In particular the NEXAFS and **h**igh–**r**esolution **e**lectron **e**nergy **l**oss (HREELS) spectra can contain a rich vibronic fine structure, as shown in *chapter 3* and [133–136]. Because the vibronic fine structure is sensitive to the charge distribution in the molecule, it is different for different electronic configurations. When considering the total wave function for the electronic and vibronic states in relation (4.8) and (4.16) it becomes evident that the mixing of various electronic configurations leads also to a mixing of vibronic states. As a consequence the configuration interaction between various electronic transitions and vibronic progressions can lead to significant broadening of the fine structure in the respective NEXAFS spectrum. [133, 134]

Consequently, in case of covalent adsorbate–substrate interaction (differential) chemical shifts can be expected, which can however be neglected to first order. Furthermore, for molecules the mixing of several molecular configurations might be relevant, including the electronic and the vibronic wave functions. Accordingly, the number of electronic and vibronic transitions in a certain energy interval can increase with increasing coupling strength, which can lead to a significant broadening of the spectral fine structure, particularly in the NEXAFS signal.

4.2 Characterization using PES and NEXAFS spectroscopy

PTCDA multi- and monolayer films have been studied in detail with various techniques so that PTCDA films have been established as a standard for studying surface and interface properties of organic semiconductors. [117, 118, 124, 137–150] As the investigated molecules have a similar structure, the multi- and monolayer spectra of the PTCDI, BTCDI and BTCDA thin films can be understood by comparison to the PTCDA bench mark. Therefore, the current state of knowledge with respect to the interpretation of the PES and NEXAFS data of the PTCDA/Ag(111) films is reviewed at first according to [126, 134, 151–153] including hints to aspects which still need to be investigated further. Afterwards, the PTCDI, BTCDI and BTCDA data are discussed.

4.2.1 PTCDA/Ag(111)

In Fig. 4.5 the core level and valence PES data for the multilayer and 1 ML film are plotted in black and grey, respectively. In the valence spectrum of the multilayer film in Fig. 4.5 (a) the HOMO at $E_B = 2.49$ eV can be distinguished well from the lower lying molecular levels. In the spectrum of the 1 ML PTCDA/Ag(111) film the adsorbate signal contributes considerably at the Fermi level. As this signal is absent in the multilayer spectrum, it can be attributed to charge transfer into the lowest unoccupied molecular orbital (LUMO). With respect to *section 4.1.2* its metallic character can be attributed to electronic coupling between the LUMO and the DOS distribution of the metal substrate and partial occupation, which is interpreted as significant indication for a covalent molecule–substrate interaction. [117, 126, 155, 156] Recent k–space tomography PES investigations of this signal indicate a high molecular orbital character with substantial substrate admixture. [150] This is in agreement with recent investigations of a Shockley–type metal–organic interface

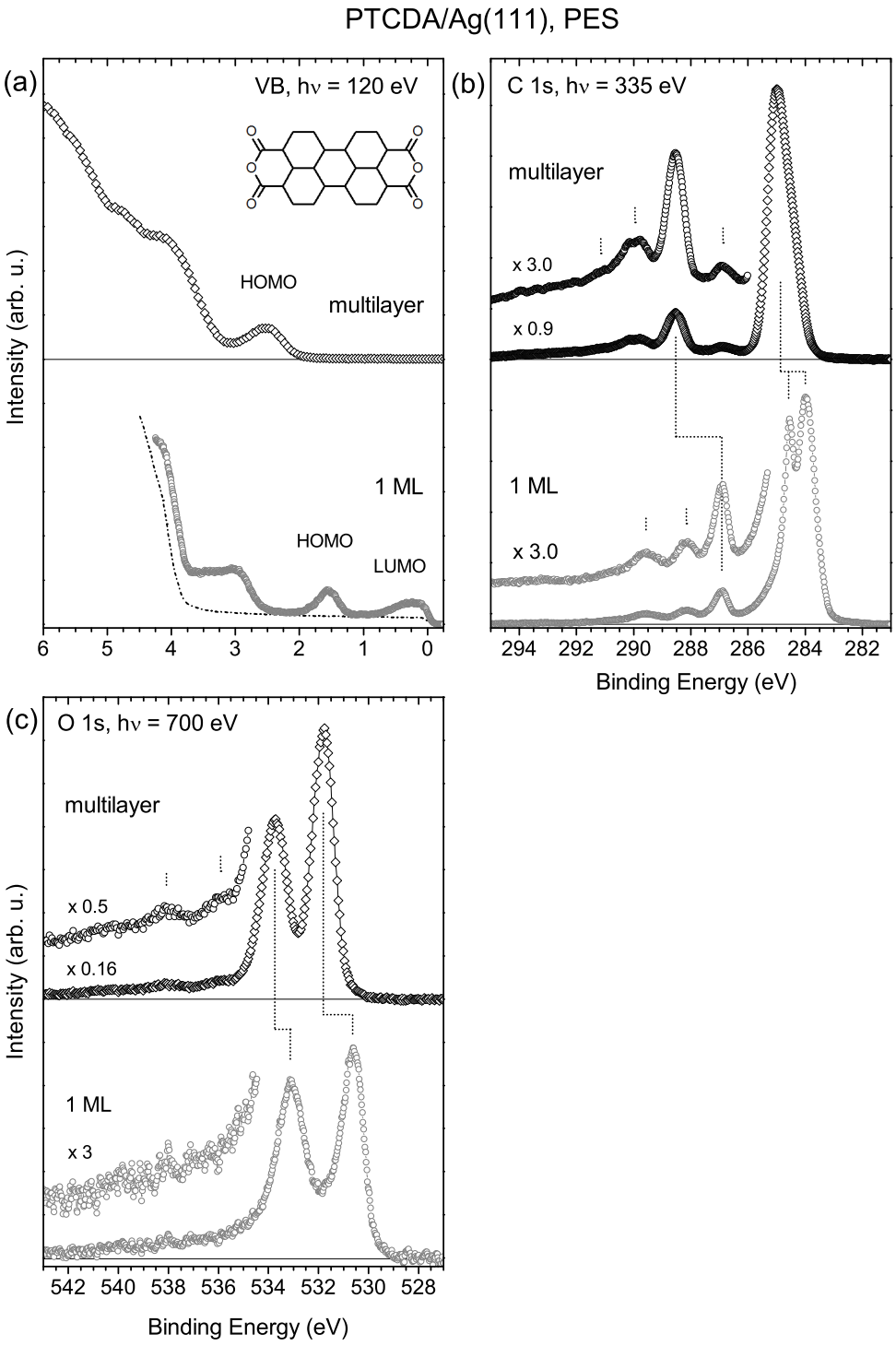

Figure 4.5: Valence and core level photoelectron spectra of a multilayer (black) and a 1 ML PTCDA/Ag(111) film (grey). The angle integrated valence spectrum of a clean Ag(111) substrate (dotted line) is indicated additionally to the valence spectrum of the 1 ML PTCDA/Ag(111) film. For better comparison the satellite structure in the core level spectra is additionally plotted on an expanded scale. Note that the VB and C 1s spectrum for the multilayer film was recorded by S. Krause, Y. Zou and A. Schöll, respectively, and published in [126, 154].

state in the unoccupied valence regime, which have provided additional indications for a covalent molecule–substrate interaction. [157–159] Furthermore, the highest occupied molecular orbital (HOMO) at $E_B = 1.54$ eV is shifted by 0.95 eV to lower binding energy and the signal of the contribution from lower lying MOs is also significantly altered, which indicates differential shifts in the respective electronic levels. For the sake of simplicity the terms LUMO and HOMO are also used for the respective orbitals of the adsorbed molecule in the following, even though the LUMO is not unoccupied anymore.

The C 1s multilayer spectrum in Fig. 4.5 (b) consists of two main peaks. The one which is located at $E_B = 285.00$ eV can be assigned to the various perylene carbon species, which explains its asymmetric shape, and the other one, which is located at $E_B = 288.52$ eV originates from the carboxylic carbon species in the anhydride group. Additionally, small shake–up satellites are observed at $E_B = 286.94$ eV and 289.96 eV, which belong to the perylene main peak and to the carboxylic main peak, respectively.

The C 1s spectrum of the 1 ML PTCDA/Ag(111) film is significantly modified by the interface interaction with respect to the multilayer spectrum. The fact that all features are shifted to lower binding energy and the appearance of a double peak structure in the perylene contribution at $E_B = 283.97$ eV and 284.54 eV, respectively, which is accompanied by a strong change in signature are the most prominent differences. Particularly the trailing edge of the high–energy perylene peak is extremely broadened, which suggests a drastic change in the satellite structure and metallic character. This is in agreement with the observation of further modifications in the satellite structure corresponding to the asymmetric carboxylic main peak at $E_B = 286.94$ eV, namely two well separated satellite peaks at $E_B = 288.16$ eV and 289.59 eV, respectively, with a broad trailing edge.

In the O 1s spectrum of the multilayer film two main peaks can be distinguished, which correspond to the terminal oxygen ($E_B = 531.81$ eV) and the bridging oxygen species ($E_B = 533.73$ eV), and at least three satellites at $E_B = 535.9$ eV, 537.9 eV and 540.6 eV are observed. From a fit taking the stoichiometric ratio 2:1 into account according to [151, 152] one finds that a relatively intense shake–up is located at $E_B = 533.8$ eV which corresponds to the terminal oxygen peak. In the O 1s spectrum for 1 ML PTCDA/Ag(111) both main peaks are located at lower binding energy. The terminal oxygen peak at $E_B = 530.62$ eV is shifted even more than the contribution from the bridging oxygen at $E_B = 533.12$ eV. Furthermore, the peak shape and the satellite structure are modified significantly, in particular the trailing edge of the bridging oxygen peak is broadened and goes over into a broad, featureless satellite contribution, similar to the findings for the C 1s signal.

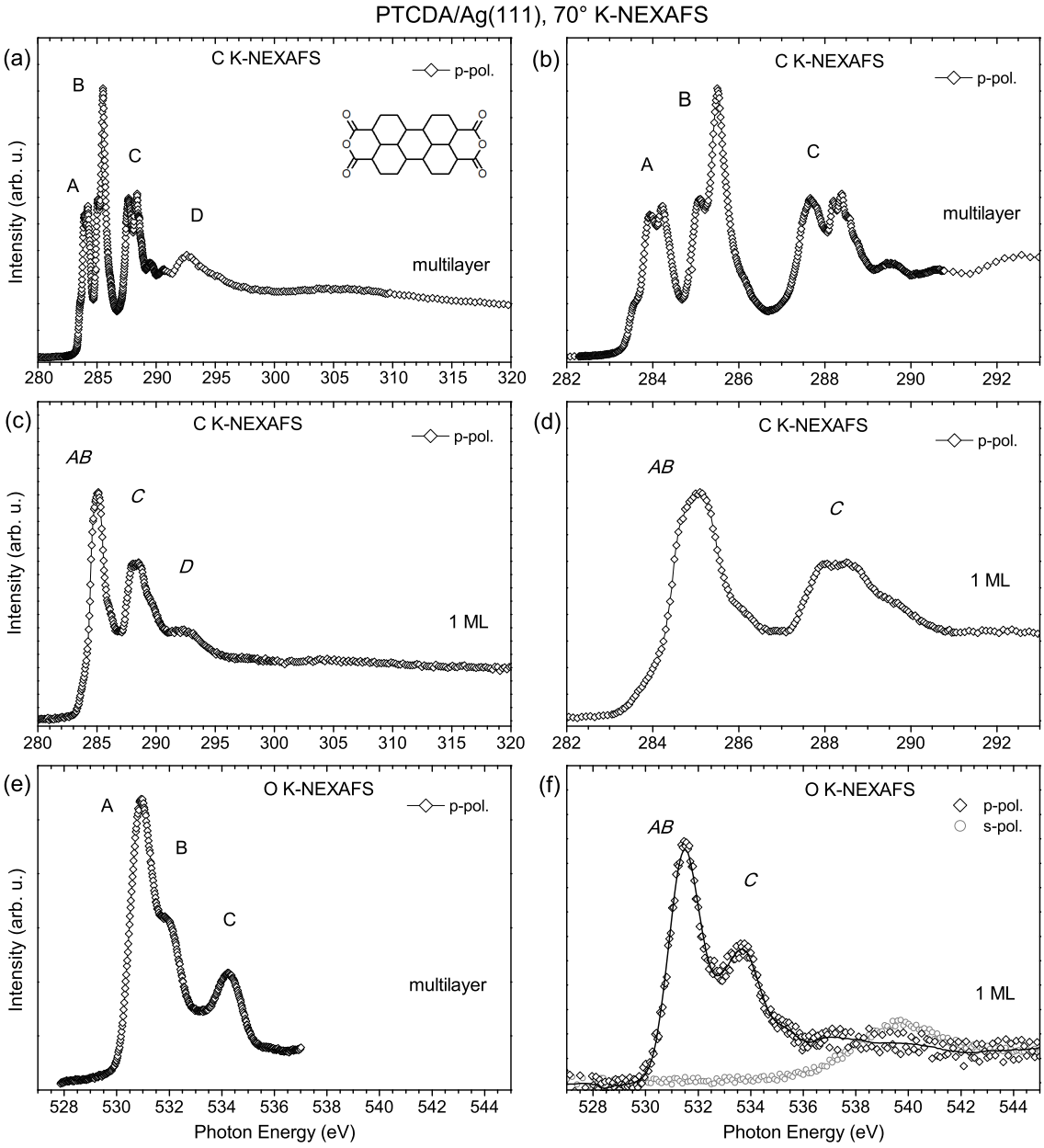

Figure 4.6: C K–NEXAFS (a, b) and O K–NEXAFS (e) of the multilayer (left) and the 1 ML PTCDA/Ag(111) film (c, d, f) at 70° angle of incidence from the surface normal. The partial electron yield signal was recorded with 150 V retarding field at the C K–edge and 300 V retarding field at O K–edge. All spectra are normalized to the height of the absorption edge. The multilayer data were measured by A. Schöll and F. Holch.

In Fig. 4.6 the C and O K–NEXAFS data of the multilayer and the monolayer film are shown. It is known that PTCDA forms well ordered monolayer and multilayer films of perfectly flat lying molecules for up to 1000 ML. [126, 160, 161] so that the C 1s $\rightarrow \pi^*$ transitions can be best excited with p–polarized x-ray light. The C K–NEXAFS of the multilayer film has four prominent peaks in the energy region below the absorption edge, A, B, C, and D in Fig. 4.6 (a) with a rich fine structure, which is mainly due to contributions from various C 1s $\rightarrow \pi^*$ excitations and electron–vibration coupling. [46, 133, 134, 152] The signature of the resonance A and B at 284 eV and 285.5 eV, respectively, suggests that several electronic transitions at the perylene carbon sites into π^* states contribute to the signal. Particularly the signal in the foot of the first NEXAFS feature at 283.6 eV corresponds to excitations into the *lowest excited molecular orbital* (LEMO) at the perylene ring. The signal at 288 eV can be mainly attributed to excitations at the carboxylic carbon site at the functional group into the LEMO+1 and LEMO+2. [46, 126, 134]

The C K–NEXAFS of the 1 ML PTCDA/Ag(111) film is very different from the multilayer NEXAFS. Only three prominent peaks *AB, C* and *D* are observed at 285.1 eV, 288.3 eV and 292.1 eV, which are very broad and lack a sharp fine structure as it has been observed for the multilayer film. This suggests a strong influence of the adsorbate–substrate interaction with significant differential chemical shifts. Accordingly, peak *AB* corresponds to excitations at the perylene carbon sites into the LEMO(π^*) and higher excited states. The foot at 283.6 eV which is due to C 1s $\rightarrow$ LEMO(π^*) transitions, is significantly broadened with respect to the multilayer spectrum, but its onset is located at 283.3 eV for both, the monolayer and multilayer spectrum. An interesting aspect is the finding that the C K–NEXAFS spectrum is comparatively similar for the PTCDA/Ag(111) and PTCDA/Ag(110) 1 ML film, respectively, [126] which will be commented in *section 4.4*. Note that for the sake of simplicity the term LEMO is also used in case of the ML films although it was discussed in *section 4.1.4* that the electronic adsorbate–substrate coupling can lead to a density distribution of adsorbate–substrate states.

The O K-NEXAFS of the multilayer film consists of three dominant peaks in the pre–edge region at 530.9 eV, 531.8 eV and 534.2 eV, denominated A, B and C in Fig. 4.6. Signals A and B originate from transitions at the terminal oxygen site into the LEMO and LEMO+1, respectively. [46] The main contribution to peak C can be assigned to the O 1s $\rightarrow$ LEMO+1 transition at the bridging oxygen. Note that transitions from the bridging oxygen into the LEMO are symmetry forbidden and consequently not observed in the NEXAFS spectra.

The dichroism in the O K–NEXAFS of the 1 ML PTCDA/Ag(111) film confirms that the molecules are perfectly flat lying at the Ag surface and that all excitations below the absorption edge correspond to electronic transitions into π^* states. The

observed differences between the mono- and the multilayer spectrum are in principle the same as for the C K–edge. The number of spectral features below the absorption edge is reduced by one, namely to peak *AB* at 531.5 eV and peak *C* at 533.7 eV. Because peak *AB* is located at an energy which is in between the energy position of peak A and B in the multilayer spectrum and its leading edge is significantly broader than that of peak A, it can be assigned to excitations at the terminal oxygen atom into the LEMO and higher excited states. Accordingly, peak *C* originates from excitations at the bridging oxygen species. It is shifted by 0.5 eV to lower energy and lies on top of the signal from the terminal oxygen.

Summarizing the most prominent aspects, striking differences are observed in the PES and NEXAFS spectra between the multilayer and the monolayer data due to the covalent molecule–substrate interaction. Particularly the PES spectra show (differential) chemical shifts to lower binding energy, e.g. the C 1s signal of the perylene contribution splits into two peaks. Furthermore, the features in the NEXAFS data and the core level spectra of the monolayer films are significantly broadened or smeared out, and featureless, continuous satellite contributions are observed above the core level peaks. Both aspects can be explained by the metallic character of the film.

4.2.2 PTCDI/Ag(111)

In Fig. 4.7 the valence and the C 1s, N 1s and O 1s core level photoelectron spectra of a PTCDI/Ag(111) multilayer film are shown together with the respective data for a 1 ML film. As the PES and the NEXAFS data of the PTCDI thin films in Fig. 4.8 is very similar to the corresponding PTCDA data, which is also evident from the direct comparison in Fig. 4.14, only the differences to the PTCDA data are emphasized in the following.

In the valence spectrum of the PTCDI multilayer film the contribution from the HOMO at E_B = 2.16 eV with FWHM= 0.62 eV is well separated from the lower lying valence orbitals. Consequently, the HOMO is located at ca. 0.4 eV lower binding energy than for the PTCDA film, as it is expected from the finding that for the PTCDI multilayer film the HOMO–LUMO gap is smaller than for PTCDA. [153] Note that no signal from the Fermi edge of the Ag sp valence band is observed, which indicates that a closed PTCDI multilayer film is grown. For the 1 ML PTCDI/Ag(111) film the valence spectrum is significantly altered. A new density distribution of adsorbate–substrate states is observed, which is cut by the Fermi level, equivalent to the finding for the PTCDA monolayer film. Hence this feature can be attributed analoguously to electronic coupling between the LUMO and substrate states, which implies covalent molecule–substrate interaction. Moreover,

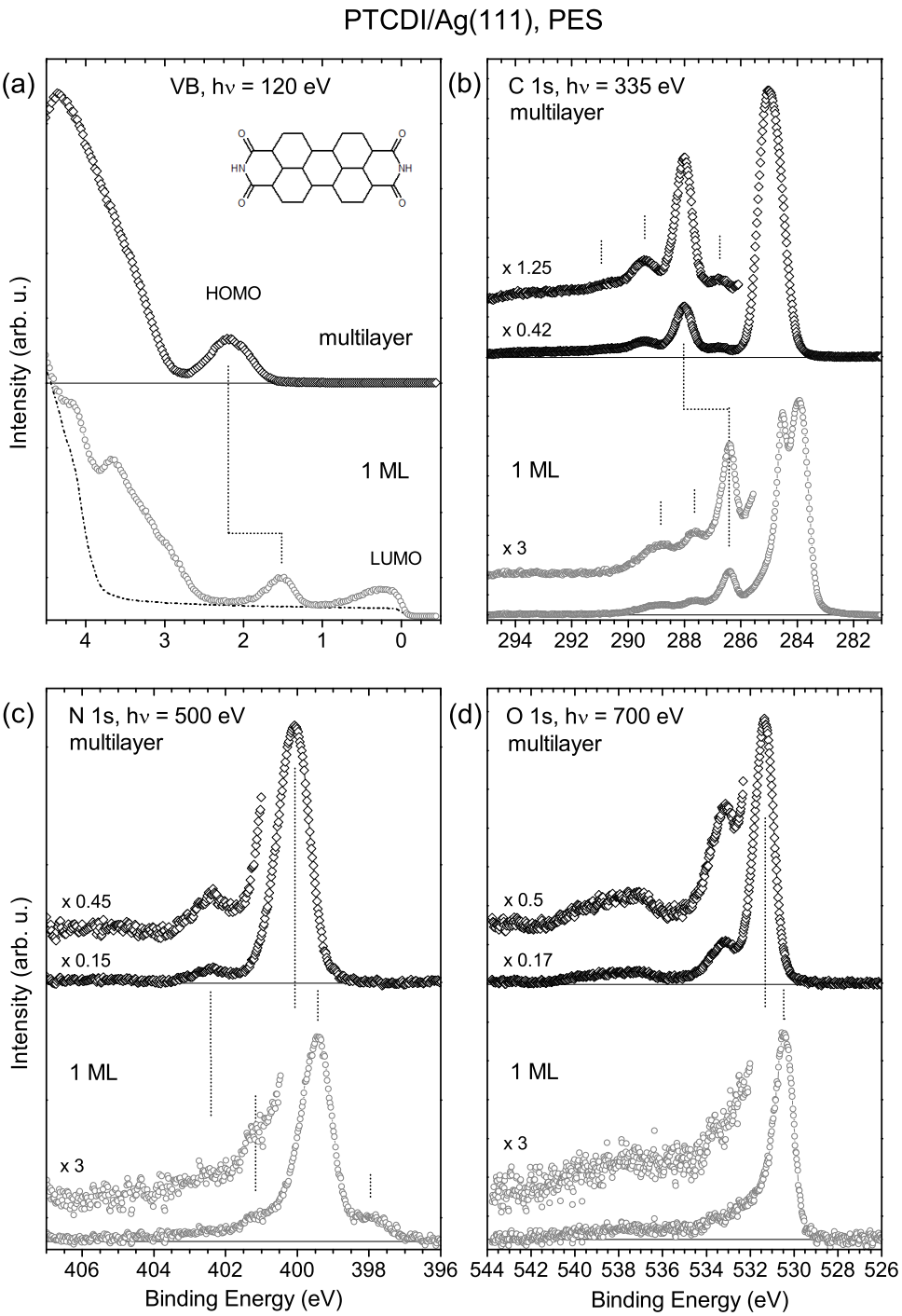

Figure 4.7: Core level and valence photoelectron spectra of a multilayer (black) and a 1 ML PTCDI/Ag(111) film (grey). The angle integrated valence spectrum of a clean Ag(111) substrate (dotted line) is indicated additionally to the valence spectrum of the 1 ML PTCDA/Ag(111) film. For better comparison the satellite structure in the core level spectra is additionally plotted on an expanded scale.

the HOMO maximum is located at E_B = 1.51 eV, which is close to the energy position of the HOMO in the PTCDA monolayer film (1.54 eV). Consequently, the chemical shift of the HOMO is 0.3 eV smaller for the PTCDI (0.64 eV) than for the PTCDA monolayer (0.95 eV). The similarity between the valence spectra of the PTCDI and the PTCDA thin films suggests a good quality of the PTCDI thin films.

In the PTCDI C 1s multilayer spectrum in Fig. 4.7 (b) the prominent perylene peak is located at E_B = 285.0 eV, similar to its position in the PTCDA spectrum, and the contribution from the imide carbon is located at E_B = 288.03 eV, which is 0.5 eV lower than the contribution of the anhydride carbon in the PTCDA spectrum. While the perylene peak is comparatively asymmetric in the PTCDA data it is nearly symmetric for PTCDI. This can be explained by the smaller electronegativity of the imide groups compared to the anhydride groups, which can lead to chemical shifts and to a difference in electron–vibration coupling. Furthermore, the first shake–up satellite which is related to the perylence peak is located at E_B = 286.82 eV and consequently located 0.1 eV closer to the main line than for PTCDA. The same applies for the shake–up satellites related to the main peak of the imide carbon at E_B = 289.39 eV. The lower satellite energies might be related to the smaller HOMO–LUMO gap in the PTCDI film compared to the PTCDA film.

The C 1s spectrum of the 1 ML PTCDI/Ag(111) film is also very similar to that of the PTCDA monolayer film. Particularly the contribution of the perylene carbon forms a double peak structure and is shifted to the same binding energy position as for the PTCDA monolayer, namely E_B = 283.97 eV and 284.53 eV, respectively. This is also accompanied by a broad foot at the trailing edge, which extends several eV and suggests various satellite excitations and metallic character. Moreover, the main peak of the imide carbon is shifted by 1.6 eV with respect to the multilayer film to E_B = 286.43 eV. Additionally, two satellites with respect to the main line of the imide carbon are observed at E_B = 287.6 eV and 288.9 eV, respectively, equivalent to the satellites related to the main line of the anhydride group in the PTCDA monolayer spectrum.

The N 1s signal of PTCDI multilayer film in Fig. 4.7 (c) originates from only one single nitrogen species. The contributions of the main line at 400.05 eV (FWHM= 1.05 eV) and the small shake–up satellite at 402.35 eV can be distinguished well. In the monolayer spectrum the main peak is located at E_B = 399.46 eV with similar width compared to the multilayer data (FWHM=1.07 eV). Furthermore, additional signals are observed at the leading and and the trailing edge of the main peak at E_B = 397.91 eV and at 401.01 eV. Moreover, the trailing edge is relatively broad with significant intensity at up to 4 eV above the main peak, similar to what has been observed for the perylene peaks in the C 1s monolayer spectrum. All these

indications of a strong change of the satellite structure need to be discussed in detail in *section 4.4*.

The PTCDI O 1s multilayer spectrum in Fig. 4.7 (d) originates from only one single oxygen species as well. The O 1s main line is located at E_B = 531.36 eV with FWHM= 1.05 eV. Additionally, shake–up satellite contributions are observed at E_B = 533.09 eV and 537.84 eV, which confirms the assumption of a satellite contribution at 533 eV in the O 1s spectrum of the PTCDA monolayer. In the PTCDI monolayer spectrum the main peak is located at E_B = 530.44 eV with an asymmetric signature. The trailing edge is considerably broadened and the satellite structure is smeared out, which is consistent with all other core level data of the PTCDI/Ag(111) and PTCDA/Ag(111) monolayer films.[1]

In Fig. 4.8 the O, N and C K–NEXAFS data of the PTCDI/Ag(111) multilayer and the monolayer film are shown. In the O K–NEXAFS of the PTCDI multilayer film in Fig. 4.8 (a) two peaks can be observed at 530.9 eV and 532.1 eV with a broad trailing edge. As their energy position is similar to that of peak A and B in the O K–NEXAFS of the PTCDA multilayer film in Fig. 4.6, this finding supports their assignment in the PTCDA data to transitions at the terminal oxygen into the LEMO, LEMO+1 and higher excited states.

The N K–NEXAFS spectrum of the PTCDI multilayer film in Fig. 4.8 (b) contains a large peak at 401.1 eV, a smaller peak at 402.5 eV and a broad structure above 404 eV. Taking into account that for PTCDA electronic transitions from the bridging oxygen into the LEMO are symmetry forbidden, the 402.5 eV can be assigned to transitions into the LEMO+1 accordingly and the remaining features are due to transitions into higher excited states.

It has been described in detail in chapter 3, that the dichroism for linear polarized x–ray light gives information on the molecular orientation. As the excitations below the absorption edge correspond to transitions into π–symmetric states, the C K–NEXAFS in Fig. 4.8 (c) indicates that for the multilayer film the PTCDI molecules are lying perfectly flat on the substrate, similar to what has been found for PTCDA. Furthermore, the pre–edge region of the C K–NEXAFS in Fig. 4.8 (d) is very similar to that of the PTCDA multilayer film, particularly the energy position and the signature of features A and B. Therefore, it is referred to the discussion of the PTCDA data in *section 4.2.1* for a detailed assignment of peak A — D. Minor differences are: The low energy foot in the PTCDI spectrum which is located at the leading edge of peak A between 283.3 eV and 283.7 eV and attributed to

[1] The integration of the spectra as well as a peak fit analysis (not shown here) indicate a slight increase of the overall satellite intensity for the O 1s spectra of the PTCDI and the PTCDA ML film. Note that for an accurate analysis of the satellite intensities the back ground needs to be subtracted from the raw data very carefully, which has been done here to the best of knowledge.

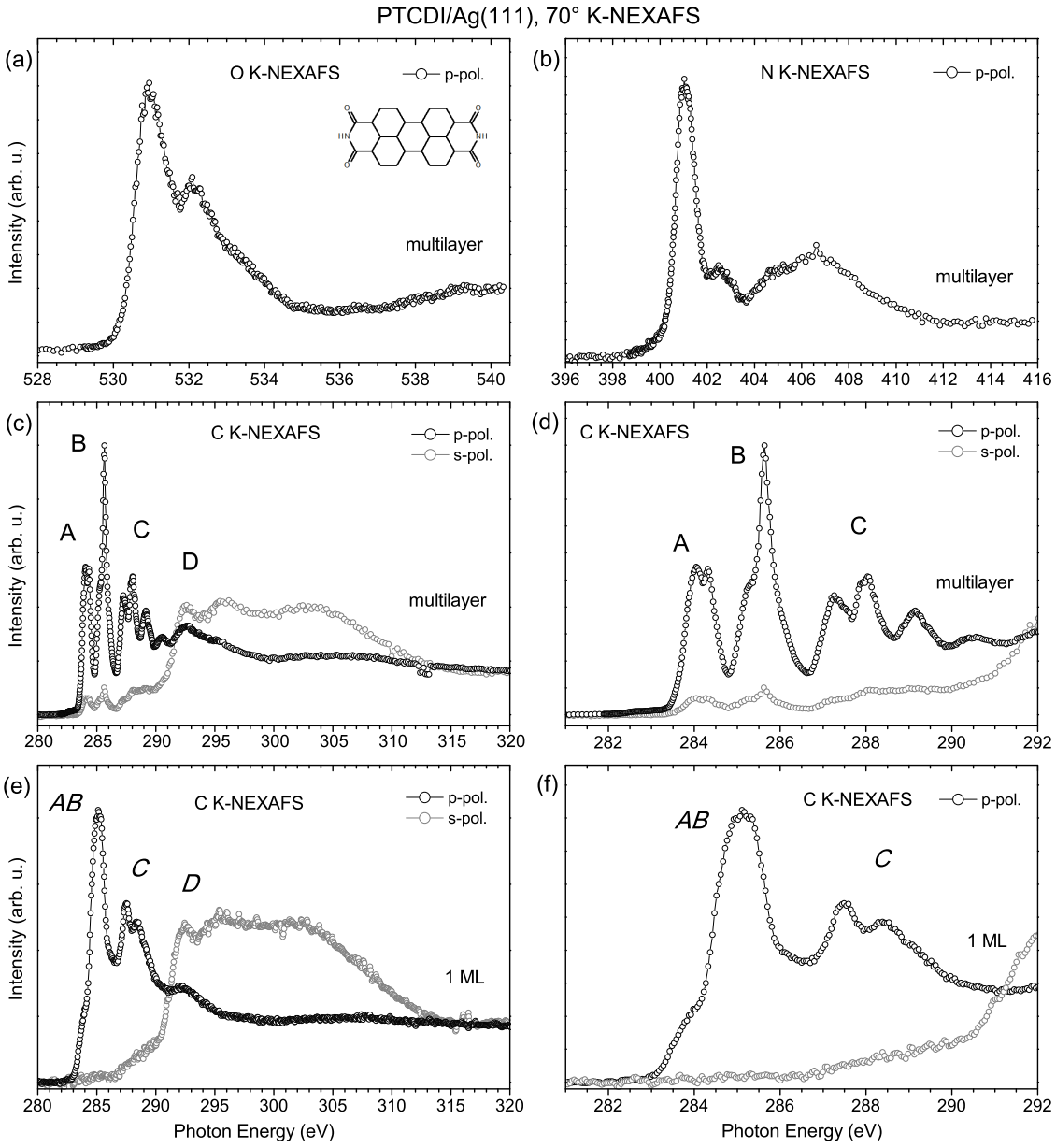

Figure 4.8: (a) O K–NEXAFS, (b) N K–NEXAFS and (c,d) C K–NEXAFS of a PTCDI/Ag(111) multilayer film as well as (e, f) C K–NEXAFS of a 1 ML PTCDI/Ag(111) film. The spectra are recorded with 70° angle of incidence from the surface normal. The partial electron yield detector was run with 150 V retarding field at the C K–edge and 300 V retarding field at the N and O K–edges.

the signal from C 1s → LEMO transition is less distinct than for the PTCDA monolayer. Furthermore, for the PTCDI film the signal C from the functional group is shifted by 0.4 eV to lower energy with respect to the PTCDA film, the peak at 288.0 eV has a different fine structure and the 289.2 eV peak is more intense.

In the PTCDI/Ag(111) monolayer film the molecules are lying perfectly flat according to the C K–NEXAFS in Fig. 4.8 (e) and (f), similar to what is observed for the PTCDA monolayer film. Furthermore, the C K–NEXAFS spectrum is changed drastically with respect to the multilayer spectrum from four main peaks to only three, and the distinct fine structure which is observed for the multilayer film is washed out, similar to the observations for the PTCDA monolayer. The signature of the feature *AB* is nearly identical to that for the PTCDA monolayer film, except that the low–energy foot between 283 eV and 284 eV is more intense for the PTCDI film than for the PTCDA film. Moreover, the contribution *C*, which originates mainly from the functional group, differs from that for the PTCDA film. In particular for the PTCDI monolayer film the signal is again shifted by ca. 0.4 eV to lower energy and its signature is modified.

Summing up, the PES and NEXAFS data of the PTCDI multilayer film show that well defined PTCDI/Ag(111) films can be prepared, with flat lying molecules forming a closed molecular layer. The spectral features of the PTCDI/Ag(111) multilayer and monolayer film agree very well with the findings for the corresponding PTCDA film, which supports the given interpretation of the data. For both molecules the interface interaction changes the electronic structure drastically with respect to the multilayer film. The LUMO–derived DOS becomes partially occupied which indicates metallic character. Furthermore, the interface interaction leads to chemical shifts and multi–peak structures in the core level PES data, even for the single nitrogen species, and to a drastic change in the satellite structure towards metallic character. Moreover, the chemical shifts are also evident in the NEXAFS spectra. This is accompanied by a loss of the distinct fine structure which is observed for the multilayer NEXAFS. The following BTCDI and BTCDA investigation can illuminate, whether these effects are particular PTCDA and PTCDI interface properties or whether they are generally relevant for covalent molecule–metal interaction.

4.2.3 BTCDI/Ag(111)

In Fig. 4.9 (a) the PES valence data of a BTCDI/Ag(111) multilayer film is shown. The HOMO signal is not separated from that of the lower lying electronic states in contrast to the findings for the PTCDA and PTCDI multilayer films. Therefore its

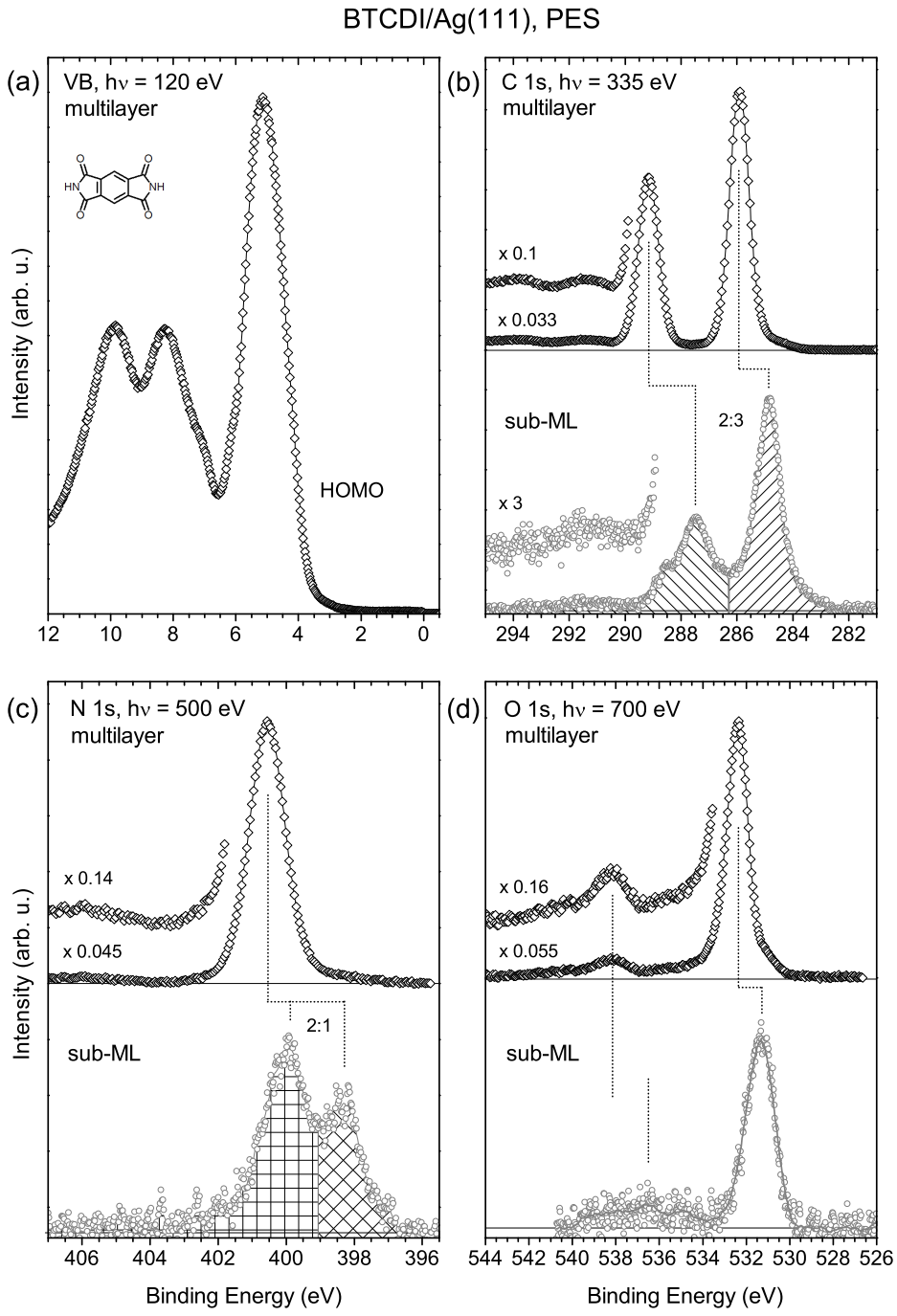

Figure 4.9: Core level and valence photoelectron spectra of a multilayer (black) and a sub–ML BTCDI/Ag(111) film (grey). During the preparation of the multilayer film and the acquisition of the multilayer data the sample temperature was kept at $-70°$ C. For better comparison the satellite structure in the core level spectra is additionally plotted on an expanded scale. (b, c) The hatched areas indicate the surface areas of the monolayer spectra. The exact ratio is indicated on top of each spectrum. See the text for more details.

energy position can only be estimated to be between $E_B = 3.5$ eV and 4 eV in the leading edge of the broad peak which is centered at $E_B = 5.1$ eV. Consequently, the BTCDI HOMO is located at ca. 1.3 eV lower binding energy than that of PTCDA. Note that a tiny signal of the substrate Fermi edge might contribute to the valence spectrum, which could be a hint to an enhanced roughness of the film, compared to that of PTCDA and PTCDI multilayer films.

The C 1s signal of the BTCDI multilayer film in Fig. 4.9 (b) consists of two prominent peaks at $E_B = 285.91$ eV (FWHM= 0.83 eV) and 289.17 eV (FWHM= 0.88 eV), and two small satellites, probably shake–ups, at $E_B = 291.4$ eV and 293.7 eV. The main peak at high energy can be assigned to the carbon species in the imide group and the low energy peak to the carbon species in the benzene ring. The intensity ratio of the two peaks is close to the stoichiometric ratio of 2:3. The small signal at $E_B = 284.9$ eV may originate from the first monolayer, which corroborates the assumption that the multilayer film has a comparatively large surface roughness.

For a sub–ML coverage of ca. 0.2 ML BTCDI/Ag(111) the C 1s signal is strongly modified with respect to that of the multilayer film. The two main peaks at $E_B = 284.82$ eV and 287.48 eV, which are related to the benzene and the imide carbon species, are shifted by 1.09 eV and 1.69 eV to lower binding energy, respectively. Note that the width of the benzene peak is increased significantly to FWHM= 1.10 eV and the tail of the leading edge is considerably broader than in the multilayer spectrum. Moreover, the peak which is related to the imide carbon has a distinct shoulder at $E_B = 288.60$ eV and is also broader than in the multilayer film. Additionally, the satellite structure above 290 eV is modified so that there is one broad signal at $E_B = 291.5$ eV. These differences with respect to the multilayer spectrum are significant for a covalent molecule substrate interaction with differential chemical shifts, similar to the findings for PTCDA and PTCDI. Moreover, the spectral signature was observed to be sensitive to the conditions during sample preparation, in particular to the annealing temperature. It is shown in *appendix B* that different preparations can alter the relative intensity of the shoulder at $E_B = 288.60$ eV and change the signature of the peak related to the benzene carbon so that spectral weight is shifted to higher or lower binding energy, which can lead to a variation in the energy position of the peak maximum by up to 0.3 eV. This observation suggests different adsorption phases for a sub–ML coverage of BTCDI, which should be studied in detail elsewhere. Nevertheless, the general effect of the interface interaction can be studied by considering the data set for one particular sub–ML film, because the spectral differences between the various sub–ML films are significantly smaller than the differences between the monolayer and the multilayer films.

The N 1s signal in Fig. 4.9 (c) originates from one single nitrogen species. The multilayer spectrum contains a single main peak which is located at $E_B = 400.55$ eV with FWHM= 1.26 eV and a weak satellite at $E_B = 406.0$ eV. In the sub–ML spectrum a broad double peak structure is observed with the respective peak maxima being located at $E_B = 398.37$ eV and 399.93 eV. Moreover, with FWHM= 1.2 eV the low energy peak is considerably narrower than the high energy peak (FWHM= 1.8 eV). It will be shown during the discussion of the NEXAFS data that for a sub–ML coverage of BTCDI the molecules are not standing upright but are oriented flat on the surface. Furthermore, it was particularly checked that the data is not disturbed by effects from radiation damage and impurities.

At first glance, the peak at $E_B = 398.37$ eV might be interpreted as indication of atomically bound nitrogen species and dissociation of the BTCDI molecules, similar to what has been previously discussed for CO and NO monolayer films on different metal surfaces. [100, 113, 162] Such a scenario would also be reflected in the C 1s spectrum. In particular, the ratio between the signal from the carbon species in the functional group to that of the carbon species in the molecular core would not meet the stoichiometric ration 2:3. However, the hatched areas in Fig. 4.9 (b), which are adjusted to meet this stoichiometric ratio, agree well with the given interpretation of the C 1s spectrum of the monolayer film. This shows that the ratio between the signal from the carbon species in the functional group and that of the carbon species in the benzene–like ring meets the stoichiometric ratio very well. Consequently, it is unlikely that the relatively large N 1s peak at $E_B = 398.37$ eV is due to dissociation of the BTCDI molecules. This is further supported by the fact that in case of the PTCDI monolayer film the low–energy peak ($E_B = 397.91$ eV) is located at 0.46 eV lower binding energy than in BTCDI. If both signals were due to atomically bound nitrogen species they should appear at the same binding energy. Note that the N 1s signal of atomic nitrogen adsorbed on W(110), Ru(0001) and Ni(001) contributes between $E_B = 396.5$ eV and 397.1 eV [100, 163–165], which is more than 1 eV below the low–energy peak in the N 1s spectrum of the BTCDI monolayer film.

Moreover, if the double peak structure in the N 1s spectrum was due to the coexistence of different nitrogen species in case of intact molecules, e.g. from different adsorption phases, the shoulder and the main peak of the C_N 1s signal would meet the same intensity ratio as the two N 1s peaks in Fig. 4.9 (c), namely 2:1. This is obviously not the case. Therefore it is unlikely that this N 1s double peak signature is due to the presence of chemically different nitrogen species. Additionally, the energy splitting of 1.56 eV between the two peaks is nearly identical to the energy splitting between the two low–energy signals in the N 1s spectrum of the PTCDI monolayer spectrum in Fig. 4.7 (c). These findings rather suggest that the double peak signature in N 1s and C_N 1s signal from the BTCDI monolayer film is due to satellite excitations. This could also explain the different intensity

ratios between the BTCDI and the PTCDI monolayer film as it is discussed in *section 4.4*.

The O 1s signal of the BTCDI multilayer film in Fig. 4.9 (d) originates from the terminal oxygen species. Therefore, only one main peak is observed at $E_B = 532.38$ eV with FWHM= 1.17 eV and a satellite at $E_B = 538.20$ eV. The small signal at 531 eV in the low energy tail of the main peak probably originates from the first monolayer. Its relative intensity is slightly higher than in the C 1s multilayer spectrum because of the higher kinetic energy of the photoelectrons in case of the O 1s spectrum, which leads to a larger electron mean free path. For a sub–ML coverage the main peak is shifted to $E_B = 531.2$ eV and considerably broadened (FWHM= 1.50 eV). Additionally, the satellite is significantly broadened as well in agreement with the findings for the C 1s data. Moreover, for the BTCDI monolayer the O 1s peak is comparatively symmetric, and no significant intensity contribution to a broad featureless tail at the high–energy edge is observed in contrast to the findings for the PTCDA and PTCDI monolayer films. Consequently, the satellite excitations have less metallic character for the BTCDI monolayer film. Note that the O 1s signal of atomic oxygen on W(110), Ru(0001) and Ni(001) after dissociation contributes between $E_B = 529.0$ eV and 530.3 eV [100, 113, 163–167], and in particular on Ag(111) it contributes at $E_B = 530.3$ eV. [168, 169] The O 1s peak in the spectrum of the BTCDI monolayer film is located at 0.9 eV higher binding energy, which indicates the absence of dissociated molecules in the BTCDI sub–ML film.

In Fig. 4.10 the N, O and C K–NEXAFS of the BTCDI/Ag(111) multilayer and the monolayer film are shown. The dichroism in the N K–NEXAFS in Fig. 4.10 (a) indicates that in the multilayer film the molecules are lying nearly perfectly flat on the substrate. For p–polarized light two prominent peaks are observed at 401.0 eV and 403.5 eV, which correspond to electronic transitions into π–symmetric states. The excitations above 405 eV are predominantly due to transition into σ–symmetric states according to the linear dichroism. The peak at 401.0 eV can be assigned to N 1s $\rightarrow$ LEMO+1 transitions and the second peak at 403.5 eV to transitions into higher EMOs with respect to the N K–NEXAFS of the PTCDI multilayer film. The latter is shifted by 1.0 eV to higher photon energy and considerably enhanced compared to the PTCDI NEXAFS.

The assignment of the peak at 398.9 eV is not unambiguous. As the PES data indicate a comparatively rough multilayer film, it is not clear if the peak at 398.9 eV in the NEXAFS spectrum originates from the first monolayer or from higher molecular layers. In the latter case it must be due to transitions into the LEMO, which in principle should be symmetry forbidden in analogy to the O and N K NEXAFS spectra of the PTCDA and PTCDI multilayer films. However, the finite transition

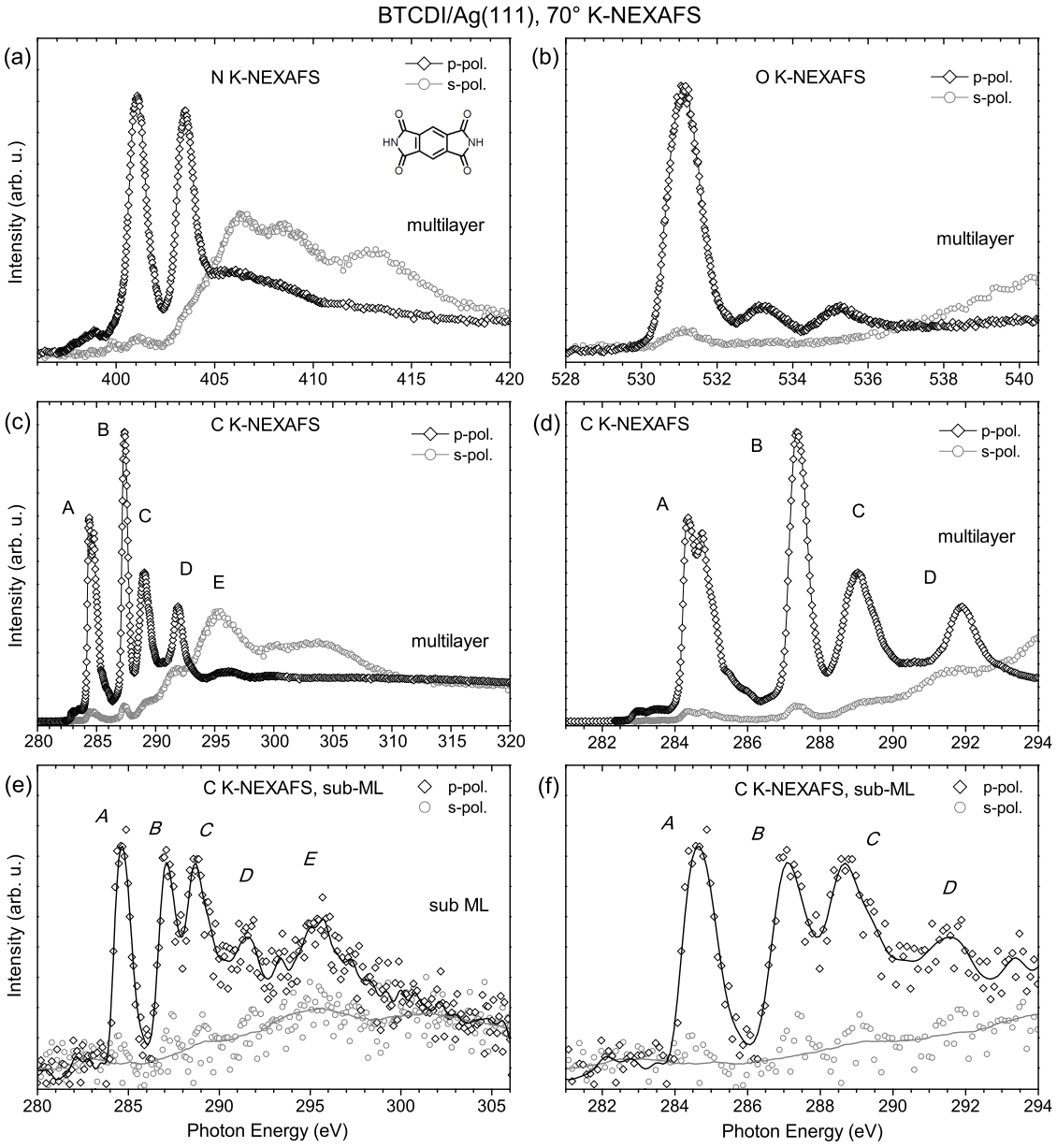

Figure 4.10: (a) N K–NEXAFS, (b) O K–NEXAFS and (c, d) C K–NEXAFS of a BTCDI/Ag(111) multilayer film. (e, f) For the C K–NEXAFS of a sub–ML film (ca. 0.2 ML coverage) the data points and a smoothed curve are shown. The spectra are recorded with 70° angle of incidence from the surface normal. The partial electron yield signal was run with 150 V retarding field at the C K–edge and 300 V retarding field at the N and O K–edge. During the preparation of the multilayer film and the acquisition of the multilayer spectra the sample temperature was kept at −70° C.

probability for BTCDI could be explained by symmetry breaking due to electron–vibration coupling. [170] If the signal originated from the first monolayer it could be associated either with atomically adsorbed nitrogen species [171, 172] due to dissociation of the BTCDI molecules or with electronic transitions into the LUMO derived density of adsorbate–substrate states. As the dissociation scenario is unlikely with respect to the core level data of the monolayer film the latter might be the case. A finite N 1s → LEMO transition probability would not be surprising, considering that the hybridization between molecular states and the substrate DOS can modify the symmetry of the electronic states significantly as it has been recently shown for the LUMO of PTCDA/Ag(111) monolayer films. [150] Despite the origin of the peak at 398.9 eV cannot be clarified unambiguously it is likely that it is related to transitions into the LEMO, either in the first or in higher adsorbate layers.

The dichroism in the O K–NEXAFS data in Fig. 4.10 (b) confirms the conclusion that the BTCDI molecules are lying flat on the substrate. For p–polarization three well separated peaks can be identified at 531.1 eV, 533.2 eV and 535.2 eV. As the first peak is located at a nearly identical energy position as the first resonance in the PTCDI and PTCDA O K–NEXAFS this peak can be assigned to electronic transitions into the LEMO. The second and the third peak originate from transitions into the LEMO+1 and higher excited states.

In Fig. 4.10 (c) and (d) the C K–NEXAFS spectra for the BTCDI/Ag(111) multilayer film are shown. The same dichroism is observed as for the N and O K–edge. The spectrum for p–polarization contains four prominent features (A — D) at 284.6 eV, 287.4 eV, 289.0 eV and 291.9 eV. Feature A has a double peak signature, similar to what has been found for PTCDI and PTCDA, where the respective feature is located at ca. 0.6 eV lower energy. Therefore, A can analoguously be attributed to transitions into the LEMO and LEMO+1 in the benzene ring. The maximum of peak B is shifted by ca. 1.8 eV to higher energy with respect to the PTCDA and PTCDI spectrum. Its signature suggests that it is governed by a single electronic transition into the LEMO+1 at the benzene ring and some additional contributions at the trailing edge similar to the findings for BTCDA. [46] Feature C corresponds to transitions at the imide carbon site into the LEMO and the LEMO+1 in analogy to the assignment for PTCDI, PTCDA and BTCDA in [46].

For the sub–ML coverage of BTCDI/Ag(111) the dichroism in the C K–NEXAFS indicates that the molecules are lying flat on the surface. Moreover, the spectrum is significantly modified compared to the multilayer data. Despite the relatively poor statistics as a result of the low coverage (ca. 0.1 ML) four prominent features (A—D) can be resolved with their maximum being located at 284.6 eV, 287.1 eV,

288.7 eV and 291.5 eV. Accordingly, peak *A* is located at the same energy as contribution A in the multilayer spectrum where the signals *B*–*D* are shifted by 0.3–0.4 eV to lower energy. Additionally, the intensity of *B* is decreased considerably. Consequently, the chemical shifts in the C K–NEXAFS between the multilayer and the monolayer film are less drastic in relation to the findings for PTCDI and PTCDA, where differential chemical shifts of more than 1 eV are observed, e.g. features A and B merge to a single feature *AB*, and the fine structure is washed out. This may be related to the indications for less metallic character in the satellite excitations in the O 1s core level spectrum.

Taking all findings together the BTCDI/Ag(111) films can be characterized well with PES and NEXAFS spectroscopy. A well ordered multilayer film of flat lying molecules can be prepared. The core level and NEXAFS data can be interpreted in analogy to the PTCDI and PTCDA data. The core level data of the BTCDI sub–ML film show effects which are typical for a covalent molecule–substrate interaction, e.g. chemical shifts, broadening of peaks and a change in the satellite structure. Particularly the single nitrogen species contributes to a broad signal with a double peak singature in the N 1s spectrum with nearly identical energy splitting to what is observed for the N 1s data of the PTCDI/Ag(111) monolayer but considerably different intensity ratio and absolute energy position. These findings and the differences to the PES signal of atomic oxygen and nitrogen after dissociation on different noble metal surfaces suggest that these signals are due to satellite excitations. Additionally, there are indications for less metallic character for the satellite contributions to the O 1s and the C 1s spectrum of the sub-ML film. Moreover, the benzene–like carbon species contributes to a single peak in the C 1s monolayer spectrum with a broad leading edge in contrast to the perylene contribution in the PTCDI/Ag(111) and the PTCDA/Ag(111) monolayer spectrum, where a double peak signature is observed with a steep leading edge. Furthermore, the C K–NEXAFS of the BTCDI sub–ML film is less altered with respect to the multilayer NEXAFS than in case of PTCDI and PTCDA. All these aspects can be interpreted as indications for a weaker molecule–substrate interaction for BTCDI with less covalent character than for PTCDI and PTCDA.

4.2.4 BTCDA/Ag(111)

In Fig. 4.11 the valence and core level spectra of the BTCDA/Ag(111) multilayer and monolayer films are shown. In the multilayer valence spectrum in Fig. 4.11 (a) the electronic state with lowest binding energy is observed at $E_B = 3.5$ eV. One could argue that the signal in the multilayer spectrum at $E_B = 3.5$ eV originates from the first layer, because there is some signal at the same binding energy in the

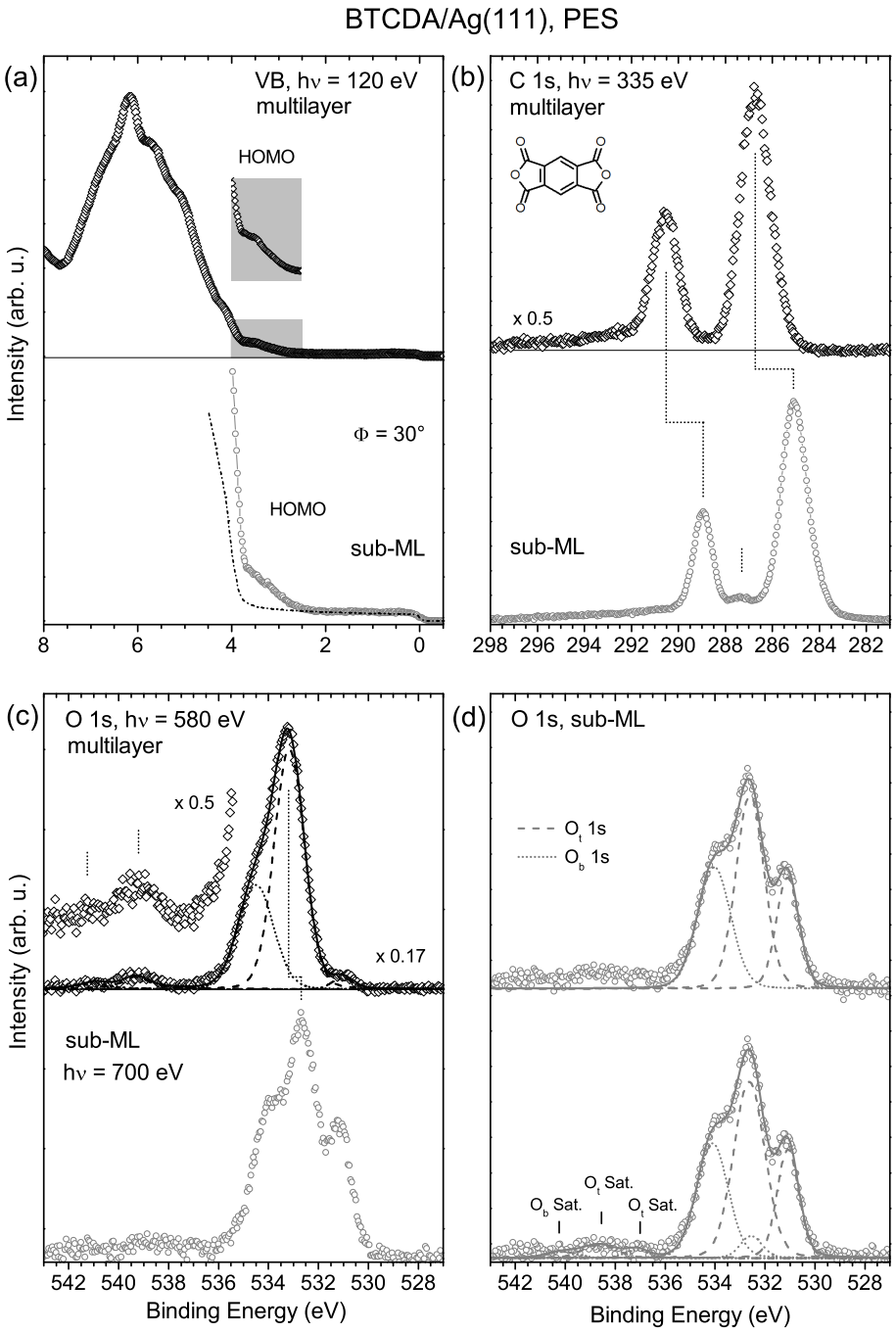

Figure 4.11: (a – c) Valence and core level photoelectron spectra of a BTCDA/Ag(111) multilayer film (black) and a sub–ML film at 300 K (grey). In case of the multilayer film the sample was cooled to 170 K during preparation and measurements. The inset in (a) shows the grey shaded part of the spectrum on an expanded intensity scale. For the valence spectrum of the monolayer film the emission angle was adjusted to $\phi = 30°$ in order to maximize the signal from the molecular orbitals. [150, 173, 174] (d) Two fits of the O 1s spectrum of the sub–ML film with the contributions from the bridging oxygen species O_b (dotted) and from the terminal oxygen species O_t (dashed) being represented by Voigt profiles. The solid curve shows the sum of all peaks. See the text for more details.

monolayer spectrum. However, the inset shows that its signature differs from that of the monolayer signal. Consequently, for both, the multilayer and the monolayer film, the HOMO is located at approximately the same binding energy. Additionally, no signal is observed which can be assigned to a LUMO derived DOS distribution in contrast to what has been observed for PTCDI and PTCDA monolayer films, where the molecule–substrate interaction leads to a chemical shift in the HOMO and a partially occupied LUMO derived DOS.

In the C 1s multilayer spectrum in Fig. 4.11 (b) two prominent peaks are located at $E_B = 290.55$ eV (FWHM= 1.38 eV) and 286.71 eV (FWHM= 1.58 eV), respectively, which can be assigned to the carboxylic and the benzene–like carbon species, and the signal at $E_B = 292.7$ eV can be attributed to satellite excitations. Moreover, the relative intensities of the main peaks are close to the stoichiometric ratio 2:3. The peaks are considerably broader than those in the BTCDI multilayer spectrum, ΔFWHM = 0.7 eV and 0.5 eV. As this applies for both peaks this effect might be due to inhomogeneous broadening.

In the monolayer spectrum both peaks are shifted by 1.6 eV to lower binding energy, namely to $E_B = 288.97$ eV and 285.09 eV. The satellite structure is similar to that in the multilayer film, except for an additional satellite at $E_B = 287.3$ eV. This parallel shift and the minor modification of the satellite structure is in contrast to the differential chemical shifts and the metallic character of the satellite structure for the PTCDI and PTCDA monolayer films. These differences compared to what has been found for the PTCDA and PTCDI monolayer films might be related to the partial occupation of the LUMO derived DOS distribution in case of PTCDA and PTCDI. Furthermore, the decrease in the peak width (FWHM= 1.00 eV and 1.33 eV) compared to the multilayer spectrum supports the assumption that inhomogeneous broadening contributes significantly to the width in the multilayer spectrum. Note that there are minor temperature dependent modifications of the monolayer spectrum which are indicated in Fig. B.3. However, they are significantly smaller than the differences between the multilayer and the monolayer data, similar to the finding for the BTCDI monolayer film.

In the O 1s multilayer spectrum in Fig. 4.11 (c) the signal of the carboxylic and of the bridging oxygen overlap as indicated by the result of a peak fit analysis, where the ratio of the peak areas was kept constant according to the stoichiometric ratio 1:2. The terminal oxygen peak is centered at $E_B = 533.2$ eV with FWHM= 1.44 eV and the bridging oxygen peak is centered at $E_B = 534.5$ eV with FWHM= 1.67 eV. The satellites at $E_B = 539.3$ eV and 541.0 eV can also be taken into account by two peaks with the ratio of the areas being 1:2. Consequently, the 539.3 eV satellite can tentatively be attributed to the terminal oxygen species and the 541.0 eV satellite to the bridging oxygen species. Furthermore, the small signal at $E_B = 531.1$ eV probably originates from the first layer. This is an indication for a comparatively

rough surface considering the fact that the total BTCDA coverage was considerably higher than 10 ML.

The O 1s spectrum of the BTCDA/Ag(111) sub–ML in Fig. 4.11 (c) shows two peaks and a prominent shoulder at E_B = 531.1 eV, 532.6 eV and 534.0 eV, respectively, and two broad features contribute to the signal at E_B = 538.5 eV and 441.5 eV. Note that the low–energy peak is located at 0.8 eV higher binding energy than what is expected for dissociated oxygen, [100, 113, 163–169] This corroborates the assumption that the BTCDA molecules are not dissociated.

The sub–ML spectrum was also fitted with respect to several models. The simplest fit is shown which can reproduce the O 1s spectrum below 536 eV well is shown in Fig. 4.11 (d, top). It is composed of three Voigt profiles with the peak areas being constrained so that the area of the peak at highest energy and the sum of the area of the two peaks at lower energy satisfy the ratio 1:2. This result suggests that the peak at E_B = 534.0 eV can be attributed to the bridging oxygen species O_b and the two remaining peaks at E_B = 531.1 eV and 532.6 eV to the terminal oxygen O_t. Their area ratio is 0.46, which is significantly different from what is expected for the coexistence of chemically different terminal oxygen species — 1:3, 2:2 or 3:1, respectively. Therefore it is likely that these two peaks are due to strong satellite excitations, similar to the finding for the N 1s signal of the BTCDI monolayer film. Note that the separation in energy between the satellite and the main peak is similar to that for the N 1s signal of the BTCDI monolayer spectrum. Moreover, the energy difference between the satellite and the signal from the bridging oxygen is 1.4 eV, which is similar to the 1.3 eV separation of the two contributions in the multilayer spectrum.

Considering this interpretation another fit was applied in Fig. 4.11 (d, bottom) based on a more sophisticated model. If the two peaks at E_B = 531.1 eV and 532.6 eV were related to charge transfer satellite excitations at the terminal oxygen species, this would be also relevant for the bridging oxygen species. Therefore the signal below E_B = 536 eV is fitted by four Voigt profiles, two for the O_b 1s signal and two for O_t 1s contribution. The energy separation between the satellite and the main line is 1.55 eV for both contributions in order to match the splitting between the N 1s peaks in the BTCDI sub–ML spectrum in Fig. 4.9 (c). Moreover, both main peaks and both satellite peaks are constrained to the same width. Additionally, three peaks, labeled "O_b Sat." and "O_t Sat." are placed 6.06 eV above the three largest peaks. The two "O_t Sat." peaks are forced to the same intensity ratio and peak width ratio as the two O_t peaks below 536 eV. The overall peak areas of the three O_b peaks and the four O_t peaks satisfy the stoichiometric ratio 1:2. Fig. 4.11 (d, bottom) illustrates that this fit reproduces the O 1s spectrum very well, even the satellite contributions above 536 eV.

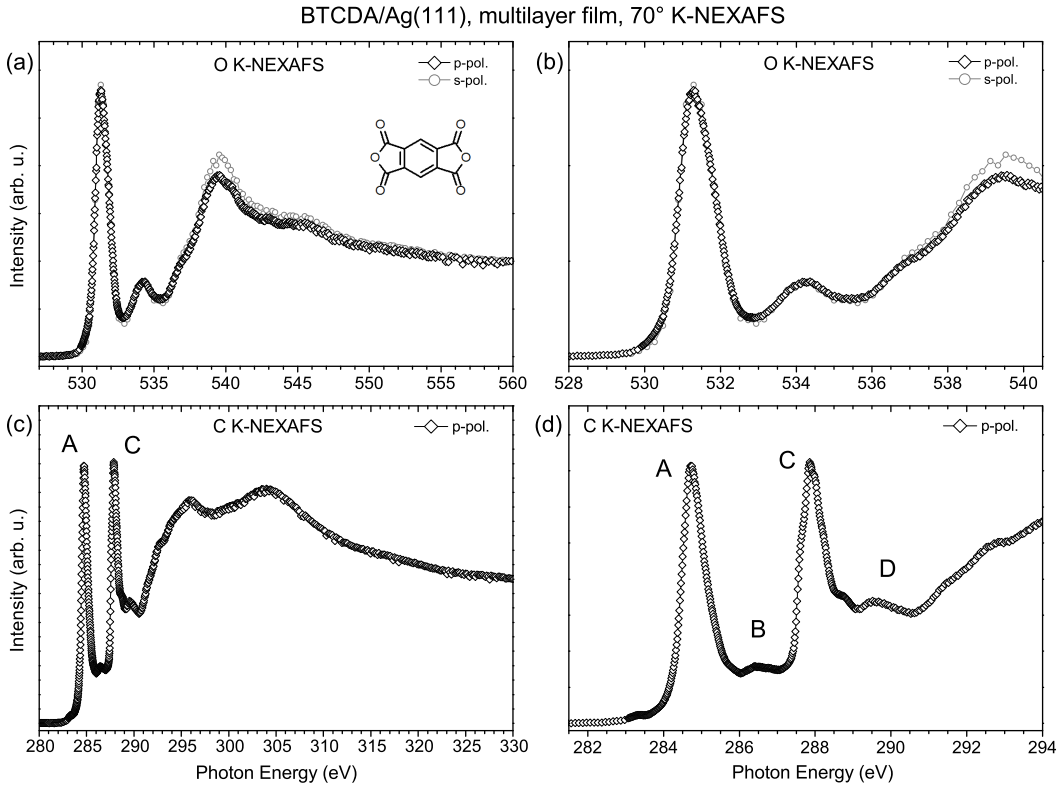

Figure 4.12: O K–NEXAFS (top) and C K–NEXAFS (bottom) of a BTCDA/Ag(111) multilayer film with 70° angle of incidence from the surface normal. The partial electron yield signal was recorded with 150 V retarding field at the C K–edge and 300 V retarding field at the O K–edge. The sample was cooled to 170 K during the preparation and the measurements.

For both fit approaches the energy separation between the two O_t (and the two O_b) peaks at lowest energy agrees well with the splitting of the two peaks in the N 1s spectrum of the BTCDI sub–ML film. It is not very straightforward that dissociation of the molecules leads to the same chemical shift in all three cases. Therefore this finding can be considered as indication for the interpretation of these peaks as main peaks and satellite peaks.

Fig. 4.12 shows the O and C K–NEXAFS for the BTCDA/Ag(111) multilayer film. The very small dichroism in the O K–NEXAFS in Fig. 4.12 (a) and (b) suggests that the molecules have nearly no preferential order, which is typical for an amorphous thin film. This may explain the comparably large inhomogeneous broadening in the core level spectra of the multilayer film. In the spectrum in Fig. 4.12 (b) three peaks can be observed at 531.3 eV, 534.3 eV and 539.6 eV. Additionally, the leading edge of the high–energy peak has a shoulder at 536.6 eV. The energy position of the first

three features is similar to that of the first three peaks in the O K–NEXAFS of the BTCDI multilayer film. Accordingly, the first feature at 531.3 eV originates from transitions at the terminal oxygen into the LEMO. The 534.3 eV peak corresponds to excitations at the terminal oxygen into the LEMO+1 and LEMO+2. [46] It can be assumed that transitions at the bridging oxygen site into the LEMO are to first order symmetry forbidden, similar as for the BTCDI, PTCDI and PTCDA multilayer films. The transitions at the bridging oxygen into the LEMO+1 are probably located around 535.5 eV according to previous calculations, and the broad leading edge including the shoulder at 536.6 eV is due to transitions into higher excited states. [46]

The C K–NEXAFS in Fig. 4.12 (c) shows two distinct π–resonances (A and C) and a structure between 295 eV and 310 eV which is mainly due to excitations into σ–symmetric states according to the findings for BTCDI, PTCDA and PTCDI. The pre–edge region in Fig. 4.12 (d) is dominated by the two distinct peaks A and C at 284.7 eV and 287.8 eV, and additional features B and D are observed at 286.5 eV and 289.6 eV. In analogy to the BTCDI, PTCDI and PTCDA NEXAFS data peak A can be assigned to transitions at the benzene ring into the LEMO and peak C corresponds mainly to transitions at the carboxylic carbon sites into the LEMO. Consequently it is straightforward to assign feature B to transitions at the benzene ring into the LEMO+1. The intensity of this transition is decreased significantly compared to the BTCDI multilayer spectrum. Moreover, the feature D can be predominantly assigned to transitions at the benzene–like carbon sites into higher excited states. [46]

Combining the results of the PES and NEXAFS data the BTCDA/Ag(111) can be characterized well. The NEXAFS data of the multilayer film suggests that BTCDA forms an amorphous multilayer film. The various spectral signatures in the NEXAFS and the photoelectron spectra can be understood with respect to the BTCDI, PTCDI and PTCDA data. Moreover, the HOMO is located at similar energy for the multilayer and the monolayer film, and significant differential chemical shifts are not observed in the C 1s data of the monolayer film. Furthermore, the satellite structure is only little modified in the C 1s spectrum of the monolayer film. All this suggests that the interface interaction is weak for BTCDA with less covalent character than for the remaining molecules. Moreover, the O 1s signal suggests strong satellite excitations in relation to the terminal oxygen species, similar to what is found for the N 1s data for the BTCDI/Ag(111) monolayer film. Note that the weaker interface interaction for BTCDA and BTCDI compared to PTCDA and PTCDI may be related to the fact that the LUMO is not occupied in case of the small molecules, whereas it contributes to the bonding of the large molecules.

4.3 Direct comparison of the core level PES data

In the previous section the various molecular thin films have been characterized with PES and NEXAFS spectroscopy. It was shown that the multilayer and the monolayer data are understood so that a consistent picture of the molecule–substrate interaction can be drawn. In the following some general aspects of the interface interaction will be reviewed and some trends will be pointed out for this series from BTCDA/Ag(111) to PTCDI/Ag(111).

Fig. 4.13 shows that in the multilayer spectra the energy position of the main peak from the terminal oxygen species shifts considerably to lower binding energy from E_B = 533.2 eV for the BTCDA multilayer to 531.4 eV for the PTCDI multilayer. This is accompanied by a decrease in width of the terminal oxygen peak from FWHM = 1.44 eV for the BTCDA multilayer film to FWHM = 1.02 eV for the PTCDI multilayer film. The energy shift can be attributed to two effects, namely to the increase in size of the π–system and to the lower electronegativity of the nitrogen atom compared to the bridging oxygen atom. The decrease in peak width might be related to a decrease of the inhomogeneous broadening with increasing order of the molecular films and to a change in the electron–vibration coupling.

Moreover, (differential) peak shifts to lower binding energy are observed for all O 1s monolayer spectra, the peak width is more or less modified and the satellite structure is altered. These aspects are significant indications for a molecule–substrate interaction with covalent character. Furthermore, the maximum position of the terminal oxygen peak in the monolayer spectrum decreases from E_B = 531.1 eV for the BTCDA monolayer film to 530.4 eV for the PTCDI monolayer film.[2] Concurrently, the leading edge becomes narrower from the BTCDA to the PTCDI monolayer film. Moreover, in all monolayer spectra the satellite structure is broadened, particularly the prominent shake–up satellite which is observed in the PTCDI multilayer spectrum has disappeared in the monolayer data. Additionally, a broad tail at the high energy side of the peaks is observed for the PTCDA and PTCDI monolayer films, which can be interpreted as an indication of metallic character comparable to Doniach–Mahan–Sunjic line profiles in case of metals and transition metal compounds. [88, 175–178] As the change in the satellite structure together with the chemical shifts can be considered as a good indicator of the interface interaction, the findings in Fig. 4.13 suggest a stronger interface interaction for PTCDA and PTCDI with more covalent character than for BTCDI and BTCDA. There

[2] As dissociated oxygen species contribute at E_B = 530.3 eV [168, 169] it is unlikely that the low–energy peaks in the O 1s spectra of the BTCDA and BTCDI sub–ML films are due to dissociation of the molecules.

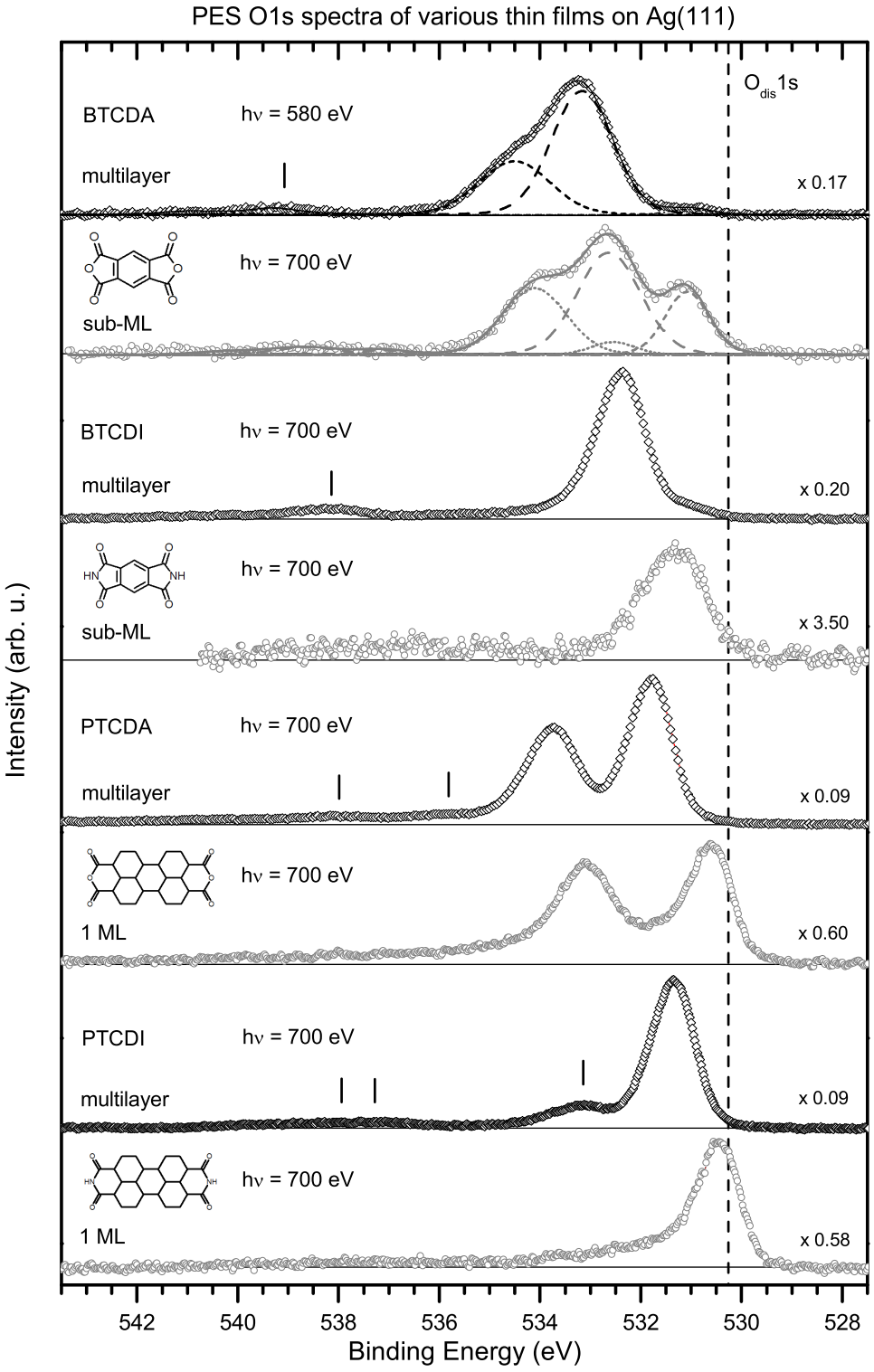

Figure 4.13: Comparison of multilayer (black) and monolayer O 1s spectra (grey) of BTCDA, BTCDI, PTCDA and PTCDI films on Ag(111) from *section 4.2*. For the BTCDA spectra the dominant contributions from the bridging (short dots) and the terminal oxygen species (dashes) are also indicated. The energy position of dissociated oxygen on Ag(111) is marked by a vertical line. [168,169]

are further hints in the NEXAFS data which support this interpretation. While the general signatures of the multilayer and the monolayer C K–NEXAFS spectrum are comparatively similar for BTCDI, strong differences are found in case of the PTCDA and PTCDI films, where peak shifts of more than 1 eV are observed accompanied by strong changes in intensity. Furthermore, the rich fine structure, which is found in the NEXAFS spectra of the PTCDA and PTCDI multilayer films, is completely washed out as it is expected for considerable coupling to the metal. These effects might be related to the partial occupation of the LUMO derived DOS distribution in case of the PTCDI and PTCDA monolayer films as it will be discussed in *section 4.5*. Furthermore, the signal of the terminal oxygen species in the BTCDA monolayer spectrum has a comparatively intense satellite contribution 1.5 eV above the main peak. Moreover, the main peak with FWHM = 1.06 eV is located at similar binding energy as the O 1s signal for the BTCDI monolayer film, which is asymmetric and significantly broader (FWHM= 1.50 eV). This might indicate that two peaks contribute to the O 1s signal from the terminal oxygen atom for the BTCDI monolayer film as well even though their energy separation is considerably smaller than in the BTCDA monolayer spectrum, which will be discussed in *section 4.4.1*.

In the C 1s spectra in Fig. 4.14 the trends are similar to those in the O 1s data. In the multilayer spectra all peaks shift to lower binding energy from BTCDA to PTCDI. This shift is larger for the carbon species in the functional group than for the benzene–like or perylene–like carbon species. Furthermore, the peak which corresponds to the benzene or perylene carbon atoms is asymmetric for BTCDA and PTCDA. This can be explained by the higher electronegativity of the functional group, which leads to larger chemical shifts for the different carbon species in the benzene and perylene group compared to the diimide molecules.

In the monolayer spectra all peaks are shifted to lower binding energy with respect to the multilayer spectra. The chemical shift is largest for the carbon species in the functional group. Moreover, the maximum position of the first peak decreases within this series of monolayer films from $E_B = 285.1$ eV for the BTCDA/Ag(111) monolayer to 283.9 eV for the PTCDI/Ag(111) monolayer and its leading edge becomes narrower. This change in signature gives the impression that for all monolayer films the low–energy tail of the first C 1s peak extends down to similar energy. Furthermore, in the PTCDA/Ag(111) and the PTCDI/Ag(111) monolayer spectra a several eV broad tail is observed at the high energy side of the double peak signature of the perylene contribution and the satellite structure is significantly broadened. Both aspects are indications of considerable metallic character, analogous to the interpretation of the O 1s data.

Furthermore, it can be speculated about the difference in the signal from the carbon species in the functional group between the BTCDI and the BTCDA mono-

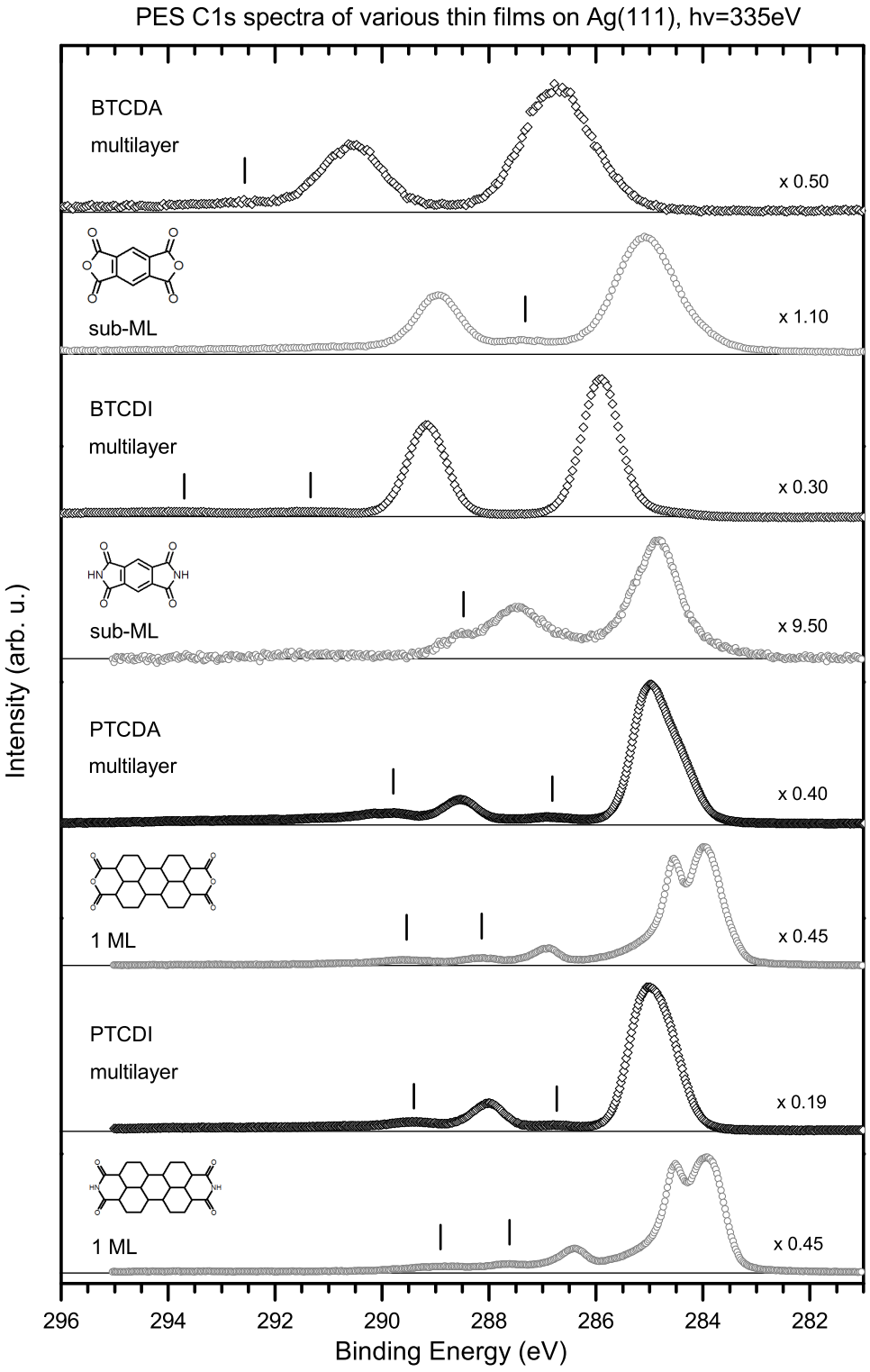

Figure 4.14: Comparison of multilayer (black) and monolayer C 1s spectra (grey) of BTCDA, BTCDI, PTCDA and PTCDI films on Ag(111). All spectra are normalized to the background and an exponential background was subtracted. In case of the 1 ML data a Shirley background was subtracted additionally.

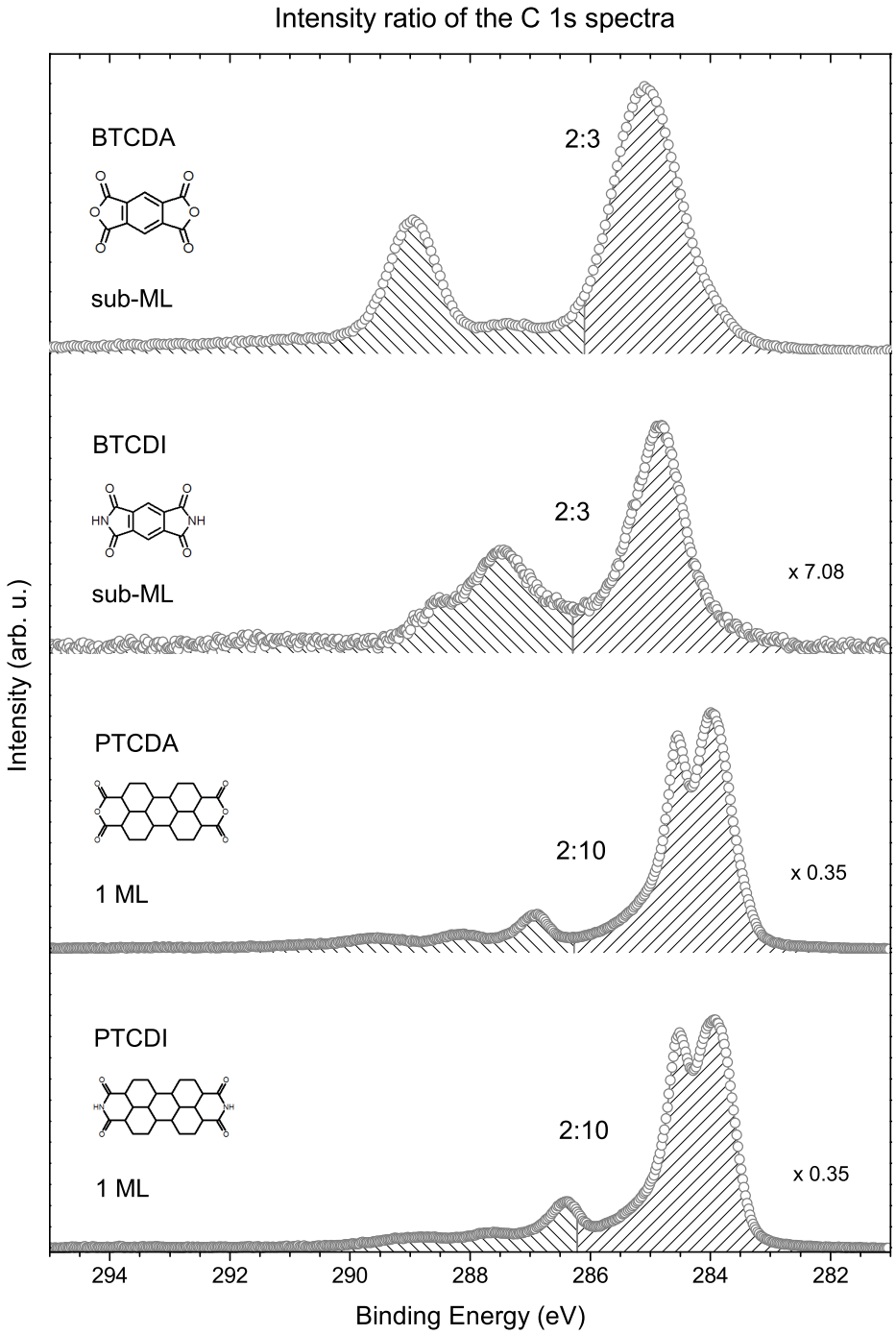

Figure 4.15: Comparison of the intensities of the monolayer C 1s spectra of BTCDA, BTCDI, PTCDA and PTCDI films on Ag(111). The ratio of the hatched areas corresponds to the stoichiometric ratio between the carbon species in the functional group and those in the molecular core. The respective ratio is indicated on top of each spectrum. The spectra plotted here are the same as those shown in Fig. 4.14.

layer film. For the BTCDI/Ag(111) monolayer spectrum the maximum of the contribution of the imide carbon species is located at E_B = 287.5 eV with a distinct shoulder at E_B = 288.6 eV, which has been attributed to satellite excitations in *section 4.2.3*. The energy difference of 0.4 eV between the C_N 1s satellite in the BTCDI monolayer spectrum and the C_O 1s peak in the BTCDA monolayer spectrum is similar to the energy difference between the C_N 1s and the C_O 1s contribution in the PTCDI and PTCDA monolayer spectrum, respectively, which is ΔE = 286.9 eV − 286.4 eV = 0.5 eV. Additionally, there is some signal in the BTCDA monolayer spectrum at E_B = 287.3 eV and hence at similar energy as the C_N 1s main peak in the BTCDI monolayer spectrum. Considering that the main peak of the O 1s signal from the terminal oxygen species in Fig. 4.13 is located at similar binding energy for the BTCDI and the BTCDA monolayer film, it can be speculated whether the contribution at E_B = 287.3 eV is related to the C_O 1s main peak and the signal at 289.0 eV to satellite excitations. Then the relative intensity of the satellite contribution would be significantly higher for the BTCDA monolayer film than for the BTCDI monolayer film. Moreover, it could be speculated whether the double peak signature in the contribution of the perylene carbon atoms in PTCDA and PTCDI monolayer spectra is related to satellite excitations as well. However, the latter can also be explained by the presence of chemically different carbon species.

Moreover, the ratios of the relative intensities in the C 1s spectra of the monolayer films can provide additional information about the stoichiometry. In Fig. 4.15 the respective C 1s spectra are plotted and the overall surface areas are subdivided into two areas according to the stoichiometric ratio between carbon atoms in the functional group and those in the molecular core, 2:10 or 2:3. For all spectra the two areas meet at E_B = 286.1 ± 0.1 eV, and the areas agree well with the previously given peak assignment. This brief check of the relative intensities supports the assumption that the molecules in the first layer are intact and not dissociated.

Fig. 4.16 shows the N 1s spectra of the BTCDI/Ag(111) and the PTCDI/Ag(111) multilayer and monolayer films. As the molecules contain only one single nitrogen species, only one single main peak is observed in the N 1s multilayer spectra, and a small satellite in case of the PTCDI spectrum. For the molecule with the larger π–system the N 1s main line is located at lower binding energy in agreement with the O 1s and C 1s data.

Moreover, a chemical shift and a strong change of the spectral signature is observed for the monolayer films. Particularly the BTCDI/Ag(111) monolayer spectrum shows a double peak structure with the maximum positions at E_B = 399.9 eV and 398.3 eV, respectively, and with a broad leading and trailing edge. The PTCDI/Ag(111) monolayer spectrum contains a small signal at E_B = 397.9 eV,

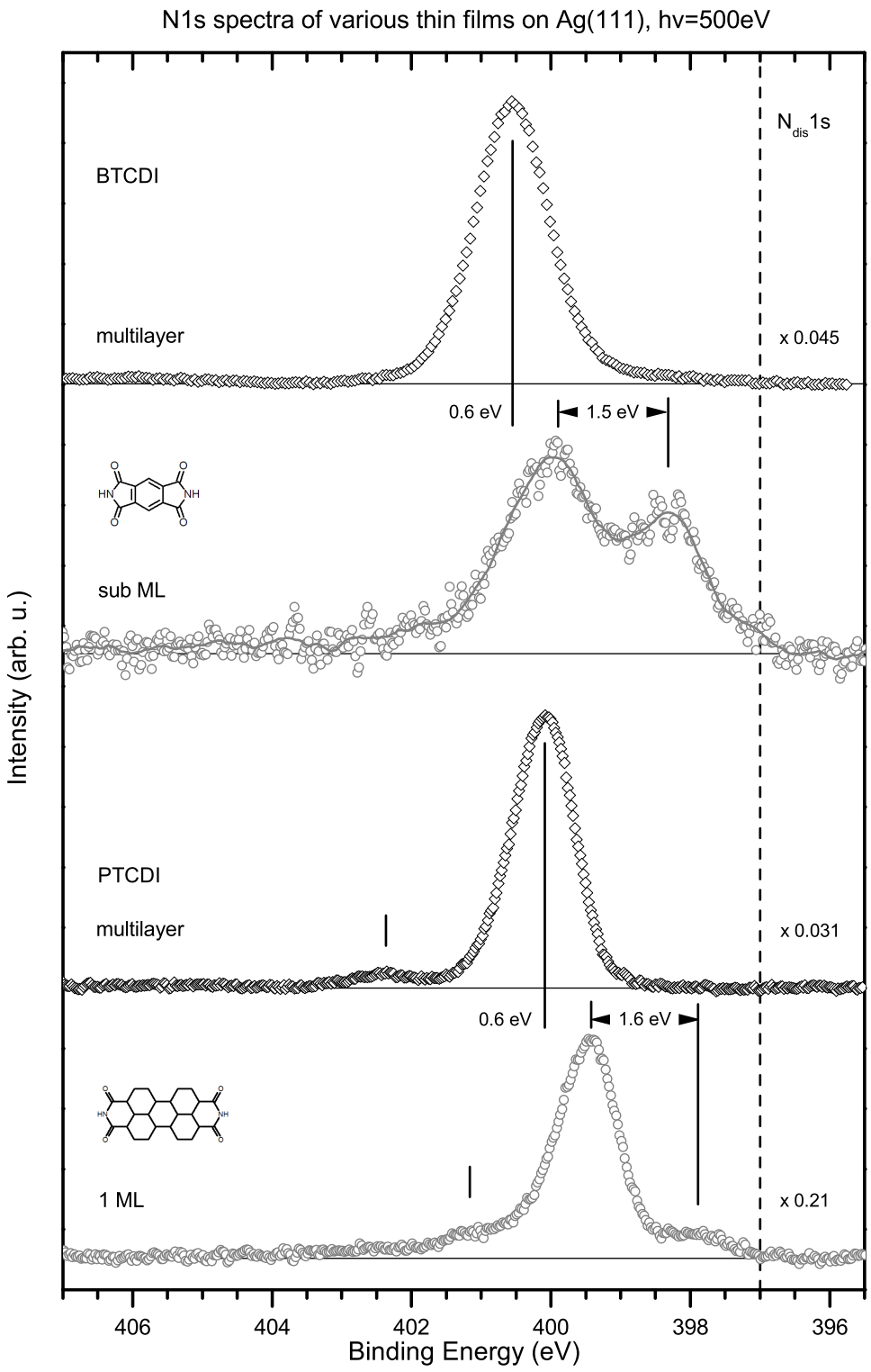

Figure 4.16: Comparison of the multilayer (black) and monolayer N 1s spectra (grey) of BTCDI and PTCDI films on Ag(111) from *section 4.2*. The energy position of dissociated nitrogen on different noble metal surfaces is marked by a vertical line. [100, 163–165]

a prominent main peak at $E_B = 399.4$ eV, and a broad tail at the high energy side with a weak, washed out satellite peak on top at $E_B = 401.2$ eV in agreement with the O 1s and C 1s data of the PTCDI/Ag(111) monolayer data. It has already been pointed out in *section 4.2.3* that impurities, radiation damage and the coexistence of different absorption phases are very unlikely the reasons for this double peak signature. The low–energy features are located at ca. 1 eV higher binding energy than the signal of dissociated nitrogen. [100,163–165] Furthermore, in case of dissociation one would expect that the low–energy peaks in the BTCDI and in the PTCDI spectra are located at the same energy in contrast to the observed separation by 0.4 eV. The comparison of the N 1s and C_N 1s signal rather suggested that the different peaks in the N 1s spectra of the BTCDI/Ag(111) and PTCDI/Ag(111) monolayer films are not due to the coexistence of chemically different nitrogen species but due to satellite excitations or different core excited (final) states, respectively. It is an interesting aspect that the chemical shift of the two low–energy features in the PTCDI monolayer spectrum with respect to the multilayer spectrum is nearly the same as for the two peaks in the BTCDI monolayer spectrum — $\Delta E = 0.6$ eV and 2.1 eV, respectively. A similar chemical shift is observed for the signal of the bridging oxygen species of the BTCDA and PTCDA monolayer film, namely 0.5 eV and 0.6 eV, respectively. Therefore it can be assumed that the satellite contribution dominates the signal from the bridging oxygen species in the BTCDA and PTCDA monolayer O 1s spectra.

The comparison of the core level data shows that there are considerable chemical shifts in all monolayer spectra and that satellites with extra ordinarily high intensity contribute to the signal. Furthermore, these distinct *giant satellites* can predominantly be identified in the BTCDI and BTCDA monolayer spectra. The (differential) chemical shifts and the metallic character in the satellite structure suggest that the adsorbate–substrate interaction is stronger with more covalent character for the PTCDA and PTCDI monolayer films than for the BTCDA and BTCDI monolayer films. This might be related to the partial occupation of the LUMO derived density of substrate–adsorbate states, which contributes to the adsorbate–substrate bonding and the interface interaction in case of PTCDA and PTCDI. For the BTCDA monolayer film, where the interface interaction can be assumed to be weakest according to *section 4.2.4*, charge transfer satellite excitations are mainly observed for the signal of the terminal oxygen. For the BTCDI monolayer film charge transfer satellites also contribute significantly to the C_N 1s and to the N 1s signal. In the O 1s signal the satellite contribution seems to be shifted close to the mainline so that only a single broad peak is observed instead of two separate peaks, as it has been discussed above. Consequently differential chemical shifts play an important role for the charge transfer satellites.

This is directly related to the covalent character of the adsorbate–substrate interaction. In particular, as it has been discussed in *section 4.1.5*, adsorbate–substrate

hybrid orbitals contribute significantly to the electronic relaxation in the core excited state, which can influence the energy position of the satellites significantly with respect to the main line. In *section 4.1* a simplified model for the charge transfer satellites has been introduced where the charge transfer was only considered in terms of occupation of previously unoccupied adsorbate–derived valence states. However, the reorganization of the adsorbate–substrate hybrid orbitals in the core excited state can additionally contribute significantly to the charge transfer and the electronic relaxation. Therefore, the characteristic giant satellites, as they are observed in the BTCDA and the BTCDI monolayer spectra, appear only for covalent interface interaction of intermediate strength — strong enough that charge transfer can occur and so weak that the reorganization of the adsorbate–substrate hybrid orbitals in the core excited state contributes only little to the charge transfer, so that the differential chemical shift between the satellite and the mainline is comparatively small. Accordingly, the small energy separation between the satellite and the mainline in the O 1s spectrum of the BTCDI monolayer film can be attributed to more covalent character for the BTCDI/Ag(111) interface interaction than for the BTCDA/Ag(111) interface. The data discussed in *section 4.2.1* and *4.2.1* indicate an even stronger interface interaction for PTCDA and PTCDI with more covalent character, which is probably due to the LUMO derived interface states. This would explain, why the signal of the respective oxygen species in the PTCDA and PTCDI O 1s monolayer spectra is dominated by only one single peak instead of two.

4.4 Covalent molecule–metal interaction

In the formalism for the charge transfer satellites in *section 4.1.2 and 4.1.3* the assignment of the satellite and main peak to the respective charge transfer states depends on the parameter U_{ac} for the Coulomb potential of the core hole with respect to the energy ϵ_a of the relevant unoccupied electronic adsorbate level $|a\rangle$. In particular if $U_{ac} > \epsilon_a$ the main peak can be predominantly associated with electron transfer from the substrate to the adsorbate in contrast to the satellite, and it is vice versa for $U_{ac} < \epsilon_a$. Moreover, it was also indicated that a comparison between the core level PES and NEXAFS data can provide information on the relation between U_{ac} and ϵ_a because core ionization and direct electronic transitions of a core electron into an unoccupied valence state can result in the same core excited state in case of covalent interface interaction with substrate–adsorbate charger transfer. In the following it will be shown that the lowest core excited state in the core level and NEXAFS spectra have the same energy for the investigated monolayer films,

which indicates that the interface interaction plays a significant role. Moreover, the assignment of the satellite and main peaks to the respective charge transfer states will be discussed in this context. Furthermore, the formalism which has been described in *section 4.1.3* will be discussed with respect to the PES data. Additionally, the metallic character of the satellite structure in the core level data of the PTCDA/Ag(111) and PTCDI/Ag(111) monolayer film will be discussed together with the loss of the fine structure in the NEXAFS spectra of the monolayer films compared to the multilayer data.

4.4.1 Comparison of photoelectron and NEXAFS spectra

It was demonstrated in *section 4.1.4* that charge transfer satellites are also relevant for the NEXAFS spectra. In particular it was shown that in case of charge transfer satellites in the core level spectra due to adsorbate–substrate coupling the dipole matrix element for a direct electronic (NEXAFS) transition into the respective core excited eigenstates can be finite. As a result satellite excitations can appear in the NEXAFS spectra as well. As the lowest unoccupied molecular orbitals of the investigated molecules are of π–symmetry, the dipole matrix element for the electronic transition of a core electron into the EMOs is large. It can therefore be expected that the electronic coupling of the relevant molecular orbitals with the distribution of substrate states leads to significant charge transfer satellite contributions in the NEXAFS as it is depicted in Fig. 4.4. Furthermore, it has been demonstrated that the energy position of the respective contributions and eigenstates, respectively, is identical in the core level and in the NEXAFS spectra, but their relative intensities can vary considerably.

In Fig. 4.17 (a) the C K–NEXAFS and the C 1s spectrum of a PTCDA/Ag(111) multilayer and monolayer film are compared as well as the respective data of the PTCDI/Ag(111) and the BTCDI/Ag(111) monolayer film. Additionally, the O 1s and the O K–NEXAFS signal of the PTCDA/Ag(111) multilayer and monolayer film are plotted in (b), and the N 1s spectrum of the BTCDI/Ag(111) sub–ML film as well as the N K–NEXAFS of the BTCDI/Ag(111) multilayer film are shown in (c). The energy position of the energetically lowest contribution to the respective signal can be estimated by determining the onset with straight lines, as it is indiciated in Fig. 4.17. Accordingly, the onset of the C 1s signal for the PTCDA multilayer film in Fig. 4.17 (a) is located 0.5 eV above the onset of the C K–NEXAFS signal at 283.3 eV. Additionally, the low–energy onset in the O 1s data in (b) is located 0.9 eV above the O K–NEXAFS onset at 530.1 eV. According to the discussion above this indicates that for the PTCDA multilayer film the best relaxed core excited $c^{-1}LEMO^{+1}$ state has a significantly lower energy than the

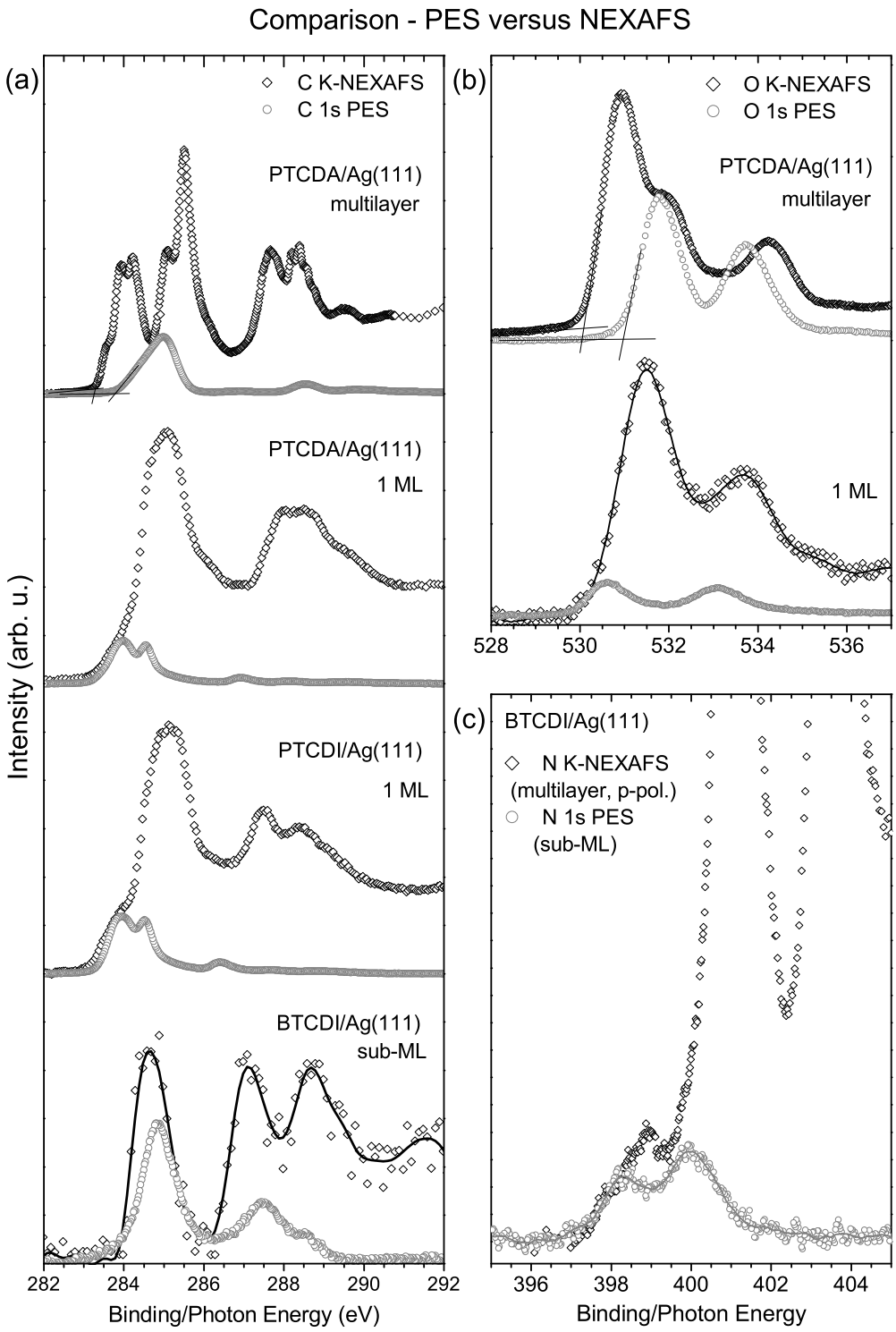

Figure 4.17: (a) C 1s PES and C K–NEXAFS spectrum for the PTCDA/Ag(111) multilayer and monolayer film on Ag(111), as well as for the PTCDI monolayer film and the BTCDI sub–ML film. (b) O 1s PES and O K–NEXAFS data for the PTCDA monolayer and multilayer film. (c) N 1s spectrum for the BTCDI sub–ML film and the spectrum for the BTCDI multilayer N K–NEXAFS, where the LEMO signal might originate from the first ML.

best relaxed core ionized (c^{-1}) state. This implies that the core hole lowers the energy of previously unoccupied molecular orbitals so that the LEMO is pulled below the Fermi level which implies $U_{LUMO\,c} > \epsilon_{LUMO}$ according to the notation in *section 4.1*. Note that this is observed for all PTCDI, BTCDI and BTCDA multilayer data except for the N K–NEXAFS, where electronic transitions into the LEMO are symmetry forbidden.

For the PTCDA/Ag(111) monolayer the leading edge of the C 1s signal with lowest binding energy in Fig. 4.17 (a) is located at the same energy as the onset of the C K–NEXAFS. The same applies for the O 1s and O K–NEXAFS data. According to the previous discussion this implies that the signals at the lowest energy in the PES and in the NEXAFS spectra correspond to the same core excited eigenstate. Therefore this is an indication of covalent interface interaction with significant substrate–adsorbate charge transfer. As the energy position of the onset in the NEXAFS data from the monolayer film is very similar to that of the multilayer film, it can be assumed that the respective core excited eigenstate has considerable $c^{-1}LEMO^{+1}$ character. Consequently, the coincidence of the leading edge of the core level and the NEXAFS signal suggests the scenario that the core hole pulls the LEMO below the Fermi level and in case of core ionization negative charge is transferred from the substrate to the core excited molecule.

Furthermore, the double peak signature in the perylene contribution to the C 1s spectrum of the PTCDA/Ag(111) monolayer might be due to charge transfer satellite excitations. Then the low energy peak at $E_B = 284.0$ eV could be attributed to the well relaxed main line with considerable $c^{-1}LEMO^{+1}$ character and the peak at $E_B = 284.5$ eV corresponds to satellite excitations. — It is an interesting aspect that the satellite energy is similar to the maximum of the perylene contribution in the C 1s spectrum of a 1 ML PTCDA/Au(111) film, where the PTCDA molecules are physisorbed and no charge transfer satellites occur. [126] This may be an indication that the signal at $E_B = 284.5$ eV can be associated with $c^{-1}LEMO^{0}$ character.

The O 1s spectrum of the PTCDA/Ag(111) monolayer film can be interpreted analoguously. Accordingly, the signal at $E_B = 530.6$ eV from the terminal oxygen species can also be related to substrate–adsorbate charge transfer. The fact that only one prominent peak is observed for each oxygen species can be attributed to the formation of molecule–substrate hybrid states, which contribute significantly to the electronic relaxation in the core excited state as has been discussed in *sections 4.1.5* and *4.3*.

A similar agreement of the energy position of the leading edge in the C 1s and the C K–NEXAFS spectrum can be observed for the PTCDI/Ag(111) monolayer film in Fig. 4.17 (a). However, the situation is different for the respective data of the BTCDI/Ag(111) monolayer film. Despite the poor statistics of the C K–NEXAFS

spectrum one can see that the maximum of the first feature in the C 1s spectrum is located at the trailing edge of the first NEXAFS peak and the C 1s signal has only little spectral weight at energies close to the onset in the NEXAFS spectrum. Consequently, the low energy tail of the first feature in the C 1s spectrum of the BTCDI/Ag(111) monolayer film can be attributed to well relaxed core excited states and the peak maximum to higher excited states.

In this context the differences in the signature of the first peak in the C 1s data in Fig. 4.14 can be understood. As the interface interaction is weaker and less covalent for the BTCDA and BTCDI monolayer film only little spectral weight is on the well relaxed excited states and most weight is on the higher excited states. Whereas for the PTCDA and PTCDI monolayer film the interface interaction is stronger, and consequently the probability for charge transfer is higher, which shifts spectral weight to lower binding energy.

In Fig. 4.17 (c) the N 1s spectrum of the BTCDI/Ag(111) monolayer film is compared to the N K–NEXAFS data of the BTCDI multilayer film. It was pointed out in *section 4.2.3* that it cannot be completely ruled out that the NEXAFS signal at 399 eV, which is due to transitions into the LEMO, originates from the first monolayer. Apart from that, it can be assumed that for the sub–ML film the onset of the signal from transitions into the LEMO is located at similar energy as for the multilayer film, similar to the finding for the PTCDA and PTCDI NEXAFS data. The comparison of the N K–NEXAFS signal of the multilayer with the N 1s monolayer signal shows that the leading edge of the first feature is located at the same energy in both spectra. This suggests that the first peak in the N 1s spectrum at $E_B = 398.4$ eV can be associated with significant charge transfer from the substrate to the adsorbate and considerable $c^{-1}LEMO^{+1}$ character and the satellite peak at $E_B = 399.9$ eV with less charge transfer and considerable $c^{-1}LEMO^{0}$ character.

Consequently it can be shown by a comparison of core level PES and NEXAFS data that the covalent interaction at the molecule–metal interface can lead to charge–transfer satellites in the core level photoelectron spectra. For the studied molecular thin films the main line can be associated predominantly with charge transfer from the substrate to the adsorbate in contrast to the satellites which can be associated with little charge transfer. Furthermore, the data implies for the parameters in the formalism for charge transfer satellites in *section 4.1* that $U_{LUMO\,c} > \epsilon_{LUMO}$.

4.4.2 Analysis of charge transfer satellites

In the formalism for substrate–adsorbate charge transfer satellites in *section 4.1* the eigenstates of the system are considered for a two–fold basis set for simplicity, which consists of the wave functions for two different electronic configurations. Consequently the electronic relaxation is neglected, particulary the influence of the adsorbate–substrate hybrid states. The satellite intensity depends only on the admixture of the respective configurations in the ground state and in the core excited state. It was also pointed out that not only two configurations are relevant for molecules, as in the example in *section 4.1*, but several. However, in the simplest approach for the molecule–substrate interface the two most relevant configurations are the ground state configuration and that, where an additional electron is transferred into the LUMO. This approach may be sufficient to first order because the most prominent contributions to the monolayer spectra which are associated with charge transfer satellites have a double peak structure as it would be the case for a two–configuration scenario. Consequently, the intensity ratio and the energy separation of the satellite and the main peak can be evaluated with respect to (4.20), (4.18) and (4.19), which provides information on the configuration mixing and the charge transfer energy Δ'_{CT}.

The respective formalism is strictly applied to all core level signals and the corresponding parameters are listed in Tab. 4.1, e.g. the energy position of the satellite and the main peak. The difference in the mixing parameter of the wave functions for the two configurations $\theta' - \theta$ is estimated with relation (4.20) from the intensity ratio I_s/I_m, where the peak areas were determined by a peak fit analysis (see also *appendix B*). As the charge transfer energies are $\Delta_{CT} > 0$ and $\Delta'_{CT} < 0$ the range for θ and θ' is $0° < \theta < 45°$ and $45° < \theta' < 90°$, respectively. From a comparison of $\theta' - \theta$ for different charge transfer satellites for the same molecular film the range of θ and θ' can be narrowed down. Moreover, the charge transfer energy Δ'_{CT} and the off–diagonal element T of the Hamiltonian can be estimated from the energy separation of the satellite and the main peak using the relations (4.18) and (4.19). As it cannot be distinguished between the satellite and the main line in the O 1s spectra of the PTCDA and PTCDI monolayer film, as discussed in *section 4.3*, only the energy position of the main line is given. Furthermore, the parameters for the C_C 1s signal of PTCDA and PTCDI in Tab. 4.1 are based on the speculation that the double peak signature in the C 1s contribution of the perylene ring is related to charge transfer satellite excitations. Moreover, the intensity ratio of the C_N contribution to the C 1s spectrum of the BTCDI monolayer film can only be roughly estimated because the signal from the C_N carbon species at $E_B = 287.5$ eV overlaps with contributions from the C_C carbon species. The same can be assumed for the C_O contribution to the C 1s spectrum of the BTCDA monolayer film.

Monolayer	level	$E_s(eV)$	$E_m(eV)$	ΔE_{sm} (eV)	I_s/I_m	$\theta' - \theta$	θ	θ'	Δ'_{CT} (eV)	T (eV)
PTCDI	C_C 1s	284.5	284.0	0.5	0.8 – 1	42° – 45°		$45° < \theta' < 59°$	$-0.24 < \Delta'_{CT} < 0$	$0.22 < T < 0.25$
	N 1s	399.5	397.9	1.6	17	76°	$0° < \theta < 14°$	$76° < \theta' < 90°$	$-1.60 < \Delta'_{CT} < -1.41$	$0 < T < 0.38$
	O 1s	–	~ 530.5	–	–	–				
PTCDA	C_C 1s	284.5	284.0	0.5	0.5 – 0.75	35° – 41°	$4° < \theta$	$45° < \theta' < 86°$	$-0.50 < \Delta'_{CT} < 0$	$0.03 < T < 0.25$
	O_t 1s	–	~ 530.6	–	–	–				
BTCDI	C_C 1s	284.8	284.0	0.8	≥ 7	$\geq 69°$		$82° < \theta' < 90°$	$-0.80 < \Delta'_{CT} < -0.77$	$0 < T < 0.11$
	C_N 1s	288.6	287.5	1.1	≥ 0.4	$\geq 32°$	$13° < \theta < 21°$	$45° < \theta' < 53°$	$-0.30 < \Delta'_{CT} < 0$	$0.53 < T < 0.55$
	N 1s	399.9	398.4	1.5	1.7	53°		$66° < \theta' < 74°$	$-1.27 < \Delta'_{CT} < -1.00$	$0.40 < T < 0.56$
	O 1s	531.7	531.0	0.7	0.8	42°		$55° < \theta' < 63°$	$-0.41 < \Delta'_{CT} < 0.24$	$0.28 < T < 0.33$
BTCDA	C_C 1s	285.1	284.1	1.0	11	73°		$73° < \theta' < 86°$	$-0.99 < \Delta'_{CT} < -0.83$	$0.07 < T < 0.28$
	C_O 1s	289.0	287.3	1.7	≥ 3	$\geq 60°$	$\theta < 13°$	$60° < \theta' < 73°$	$-1.41 < \Delta'_{CT} < -0.85$	$0.48 < T < 0.74$
	O_b 1s	534.0	–	–	≥ 20	$\geq 77°$		$77° < \theta' < 90°$		
	O_t 1s	532.7	531.1	1.6	2	55°		$55° < \theta' < 68°$	$-1.15 < \Delta'_{CT} < -0.55$	$0.56 < T < 0.75$

Table 4.1: Parameters for the formalism for charge transfer satellites in *section 4.1* for PTCDI, PTCDA, BTCDI and BTCDA monolayer films on Ag(111). It is indicated from the left to the right: The core level, the energy position of the satellite E_s and the main peak E_m together with the respective energy difference ΔE_{sm} and the intensity ration I_s/I_m from the peak areas according to a peak fit analysis (see also *appendix B*). The difference in configuration mixing $\theta' - \theta$ was calculated with relation (4.20) where $0° < \theta < 45°$ and $45° < \theta' < 90°$. From the comparison of $\theta' - \theta$ for different core levels the range of θ and θ' can be narrowed down, respectively. The charge transfer energy Δ'_{CT} and the off–diagonal element T of the Hamiltonian can be estimated from θ' using the relations (4.18) and (4.19).

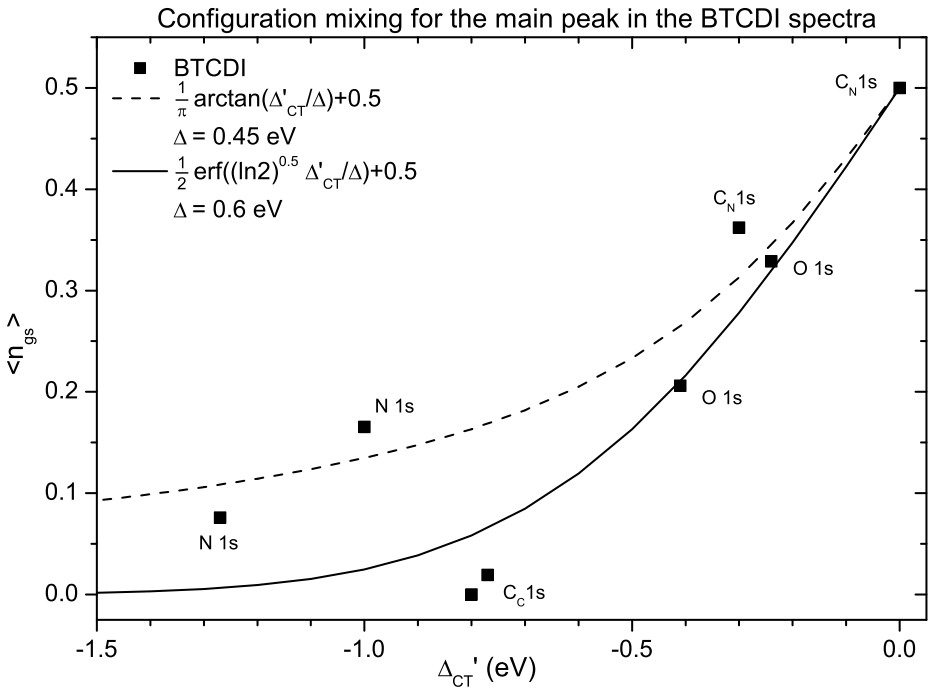

Figure 4.18: Configuration mixing for the main peak of different core level signals from the BTCDI sub–ML films. The contribution of the ground state configuration $< n_{gs} > = \cos^2\theta'$ to the eigenstate which is related to the main peak is plotted over the charge transfer energy Δ'_{CT} for the minimum and maximum values given in Tab. 4.1. See the text for more details.

Tab. 4.1 shows that θ is small in the ground state and consequently the configurations are mixed very little. It has been pointed out in *section 4.1.3* that this indicates that Δ_{CT} is significantly larger than the hybridization energy Δ due to the substrate–adsorbate coupling. Furthermore, one can even assume that for all monolayer films the mixing parameter θ is close to its lower limit. For the core excited states values for $\theta' \rightarrow 45°$ can be found. Consequently, the configuration mixing can be large, e.g. for the C_C 1s signal from the PTCDI and PTCDA monolayer film and for the N 1s and O 1s signal of the BTCDI and BTCDA monolayer film, respectively. Moreover, one finds for this data that $\theta' \rightarrow 45°$ for $\Delta'_{CT} \rightarrow 0$. Additionally, $\theta' \rightarrow 90°$ for large values of Δ'_{CT} between 1 and 2 eV, as it is the case for the N 1s signal of PTCDI and BTCDI and the C 1s signal of BTCDA. Consequently, the parameters are consistent so far.

For the BTCDI monolayer film the interrelation between the configuration mixing and the charge transfer energy Δ'_{CT} is also shown in Fig. 4.18. The contribution of the ground state configuration $< n_{gs} >= \cos^2\theta'$ to the eigenstate which is related to the main peak is plotted over Δ'_{CT} for the minimum and maximum values of

Tab. 4.1. Accordingly, the configuration mixing decreases clearly with increasing Δ'_{CT}. Consequently, the further the core hole pulls the density distribution of unoccupied adsorbate states below the Fermi level, the larger is the charge transfer energy Δ'_{CT}, and the smaller is the configuration mixing and the contribution from the main line to the signal. Furthermore, the decrease in $< n_{gs} >$ allows to estimate roughly the coupling parameter Δ as it was discussed in *section 4.1.2*. If the interaction of the LEMO with the substrate states induces a density distribution of adsorbate states of Lorentzian shape then relation (4.6) holds and $< n_{gs} >$ should decrease with larger Δ'_{CT} according to

$$< n_{gs} >= \frac{1}{\pi} \arctan\left(\frac{\Delta'_{CT}}{\Delta}\right) + 0.5 \; . \tag{4.25}$$

In Fig. 4.18 an example curve is plotted for $\Delta = 0.45$. It fits to the data, except for the C_C 1s data points $\Delta_{CT} = -0.77$ eV and -0.80 eV, respectively. However, considering that for the PTCDA and the PTCDI monolayer film the HOMO and the partially occupied LUMO peak in Fig. 4.5 and 4.7 resemble to first approximation a Gaussian instead of a Lorentzian function, the appropriate relation for the configuration mixing is

$$< n_{gs} >= \frac{1}{2} \operatorname{erf}\left(\frac{\sqrt{\ln 2}\,\Delta'_{CT}}{\Delta}\right) + 0.5 \tag{4.26}$$

instead of relation (4.25). The respective curve is also indicated in Fig. 4.18 for $\Delta = 0.6$ eV, which is reasonable with respect to the fact that in the valence data in Fig. 4.5 and 4.7 the LUMO width is of the order of HWHM = 0.5 eV. It agrees well with the BTCDI data points except for those of the N 1s signal. The exceptional role of the N 1s data becomes even more evident in Fig. 4.19, where the coupling parameter T, which corresponds to the off–diagonal element of the Hamiltonian H in (4.10), is plotted over the charge transfer energy Δ'_{CT}. According to relation (4.18) one expects that T decreases with decreasing configuration mixing and consequently with increasing charge transfer energy Δ'_{CT}. Moreover, Fig. 4.19 shows that exactly this trend is observed for the C 1s and O 1s signal, so that it can be assumed that T decreases from $T \simeq 0.6\ eV$ for $\Delta'_{CT} = 0$ eV to $T \simeq 0$ eV $\Delta'_{CT} = -1.0$ eV. However, the values for the N 1s satellites are significantly off, so that for a comparatively large charge transfer energy Δ'_{CT} considerable configuration mixing is implied. These deviations indicate the limits of this simple model, which takes only two electronic configurations into account and neglects the electronic relaxation of the core excited states and the resulting chemical shifts and intensity modifications as it has already been pointed out in *section 4.1.5*.

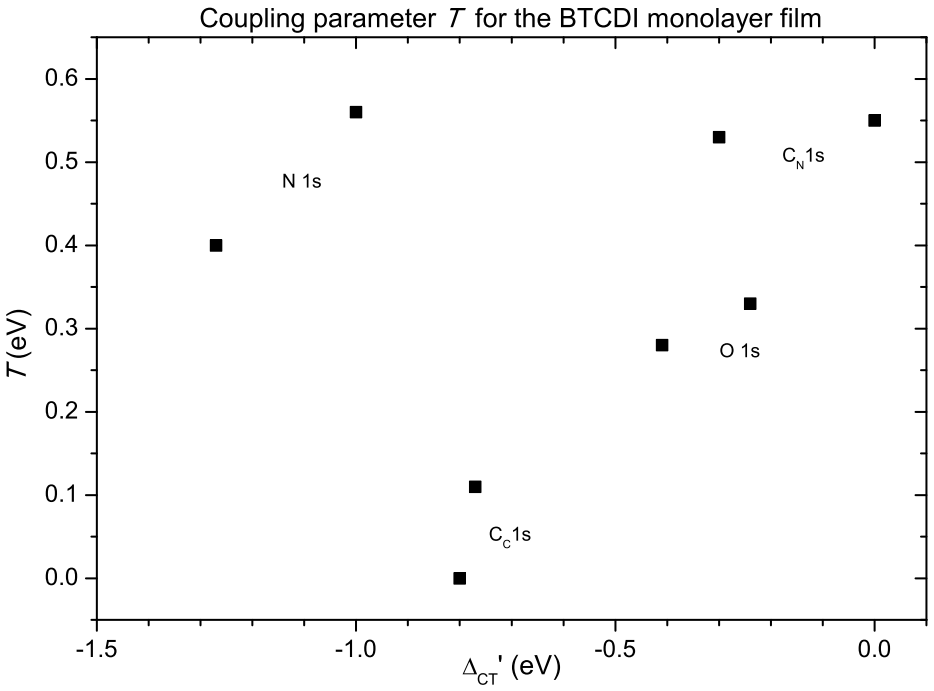

Figure 4.19: The values of the coupling parameter T in Tab. 4.1 for the BTCDI sub–ML film, which corresponds to the off–diagonal element of the Hamiltonian H, are plotted over the charge transfer energy Δ'_{CT}. Note that for each core level two data points are indicated, which correspond to the minimum and the maximum value of T, respectively.

Accordingly, not only one particular unoccupied molecular state may be relevant for the charge transfer at the molecule–substrate interface but several, which implies then the mixing of these electronic configurations. This may for example be relevant for the N 1s spectrum of the BTCDI monolayer film, where the satellite contribution has a similar energy as the contribution in the N K–NEXAFS which corresponds to direct electronic transitions into the LEMO+1. Furthermore, it has been shown in *chapter 3* that the electronic relaxation can be different for different core excited states, e.g. $c^{-1}LEMO^0$ and $c^{-1}LEMO^{+1}$ due to many–body effects. The reorganization of adsorbate–substrate hybrid orbitals can contribute significantly to the electronic relaxation and to differential energy shifts between the satellite and the main line, respectively, and it can also influence the relative intensities. *Bagus* et al. for example showed very recently that these effects are in particular relevant for the CeO_2 transition metal complex, where the covalent interaction between the metal and the ligand atoms has considerable influence on the charge transfer satellites. [130, 131] These effects need be taken into account for covalent adsorbate–substrate interaction as well. Moreover, they can be differently

distinct, depending on the covalent character of the interface interaction and the core hole site. This is supported by the BTCDA data in Fig. B.4 and B.5 where a deviation of the charge transfer parameters for the O 1s and C_O 1s signal is observed, similar to what is found for the N 1s signal of the BTCDI sub–ML film. This indicates that the covalent interface interaction plays a significant role for the respective charge transfer satellites.

In this context there are indications that the covalent character of the interface interaction is larger for the PTCDA and PTCDI monolayer films than for the BTCDA and BTCDI sub–ML films. The charge transfer satellite and the main peak cannot be separated in the O 1s spectra of the PTCDA and PTCDI monolayer films but each core level contributes to a single peak as it has been pointed out in *section 4.3* whereas in the O 1s spectrum for the BTCDA monolayer film the charge transfer satellite from the terminal oxygen is significantly separated from the main line and a significant asymmetry can be observed in the O 1s peak for the BTCDI monolayer film.

4.4.3 Metallic character in the core level and NEXAFS spectra

It has been discussed that the satellite structures in the core level spectra of the monolayer films are significantly broadened and washed out with respect to the multilayer data. Particularly for the PTCDA and the PTCDI monolayer film a broad tail is observed above the main peaks, which is typical for metallic character, in contrast to the satellite structure in the multilayer data, e.g. see the O 1s data in Fig. 4.5 and 4.7. This can be understood within the framework of the Anderson model. Due to the covalent adsorbate–substrate coupling the originally discrete molecular levels contribute to a density of adsorbate–substrate states $\rho_{as}(\epsilon)$ as it is demonstrated in Fig. 4.3. Hence, it cannot be distinguished between shake–up and charge transfer satellites, but both are interrelated. Therefore, it is straightforward that the satellite structure is broadened significantly for the monolayer films, and the continuous loss feature above the main peaks in the spectra of the monolayer PTCDA and PTCDI films, which is typical for metallic solids is not surprising. [88, 175–178] The appearance of this continuous tail indicates that the electronic coupling between the molecular states and the density of valence states distribution of the substrate is comparatively strong, which implies considerably covalent interface interaction.

Furthermore, the adsorbate–substrate interaction leads to chemical shifts, to broadening and to a loss of fine structure in the NEXAFS spectra. The simplified model of the interface interaction in *section 4.1* gives an idea about the relevant effects.

Moreover, it has been shown in *section 4.1.4* that the configuration mixing approach, which models the charge transfer satellites in the PES data sufficiently well, also predicts satellite contributions to the NEXAFS. As many different electronic transitions contribute to the NEXAFS signal and overlap in energy, the various satellites cannot be resolved but lead to broad NEXAFS structures. Furthermore, it has been pointed out in *section 4.1.5* that the configuration mixing involves not only the electronic wave function but that it also leads to the mixing of vibronic states because of electron–vibration coupling. This implies an additional loss of vibronic fine structure compared to the NEXAFS of multilayer films. Consequently it can be understood that the NEXAFS of the PTCDI and PTCDA monolayer films is modified more with respect to the multilayer films than in case of BTCDI, where the covalent interface interaction is weaker than for the perylene derivatives.

4.5 Summary & Conclusion

Different molecular thin films have been investigated systematically with core level PES and NEXAFS spectroscopy in particular with respect to the adsorbate–substrate interaction. The interaction between organic molecules and the Ag(111) substrate is known generally to be of intermediate strength, in between that for Au and Cu substrates. Nevertheless, strong differences are observed between the monolayer and the multilayer data which are beyond what is commonly understood as a chemical shift. In particular multi peak signatures are observed in the N 1s and C 1s spectra which cannot be explained by effects in the ground state. Moreover, it can be shown that these multi peak features can be attributed to satellites which involve substrate–adsorbate charge transfer, similar to the charge transfer satellite excitations in transition metal complexes or for CO and N_2 adsorbed on transition metal and noble metal surfaces.

Furthermore, the interface interaction can be described by the *single impurity Anderson model* where electronic coupling between a single adsorbate level and the substrate DOS is taken into account, and electronic relaxation upon core hole creation is neglected. Accordingly, a density of adsorbate–substrate states is formed for finite coupling. Moreover, a distribution of previously unoccupied electronic states can be pulled below the Fermi level upon core hole creation by the Coulomb interaction with the core hole. Consequently, these states can be occupied by charge transfer from the substrate which leads to core excited states of different energy. Moreover, it is shown that it depends on the energy position of this DOS distribu-

tion with respect to the Fermi level whether it is completely or partially occupied by charge transfer, or unoccupied, respectively.

In a further simplification this scenario can be described by a formalism developed by *Sawatzky* et al. for transition metal compounds, which is an alternative to the *Gunnarsson and Schönhammer* approach. Due to its simplicity it illustrates the charge transfer mechanism and it improves the understanding of the interface interaction. It even allows to obtain model parameters directly from the PES data. The core excited states are described by the mixing of only two molecular configurations, namely that for no and that for one electron being transferred onto the adsorbate, respectively. Consequently, the relative intensities of the main and the satellite peak can be obtained from the overlap of the ground state configuration with that of the core excited states, which simply corresponds to the contribution of the no–charge-transfer configuration to the excited state. It is demonstrated that this model cannot only describe the influence of the interface interaction qualitatively, but that it even allows to deduce direct information from the PES data, e.g. the charge transfer energy, the strength of the configuration mixing and a parameter for the coupling strength. Despite the above described approximations the respective values are in a reasonable range, e.g. the parameter for the interaction strength indicates a width for the distribution of adsorbate–substrate states which is in agreement with the width of the partially occupied LUMO derived DOS of the PTCDA and PTCDI monolayer films. Therefore, the discussed approach can provide even a semiquantitative estimate of the relevant parameters for the interface interaction.

Moreover, significant deviations of the coupling parameters from the expected trends are observed for some core level data. This indicates the limits of the applied model. Particularly for molecules several unoccupied molecular electronic states may be of interest, which implies that the mixing of not only two but several configurations needs to be considered. Furthermore, the adsorbate–substrate hybrid orbitals contribute significantly to the electronic relaxation in the core excited state, which results in chemical shifts and modifies the relative intensities of the satellite and main lines. The relaxation of the respective orbitals also contributes to the substrate–adsorbate charge transfer. This effect can be so strong that the model described above breaks down and only one single peak is observed in the respective core level spectra instead of a satellite and a main peak. Therefore charge transfer satellites could only be identified for covalent adsorbate–substrate interaction of intermediate strength — strong enough that charge transfer occurs, and weak enough that the adsorbate–substrate hybrid orbitals contribute only little to the electronic relaxation.

Furthermore, the validity of this model implies that core excitations at such adsorbate–substrate interfaces cannot be understood in the single particle picture but only in

the framework of clear many–body excitations. This becomes particularly evident in core level PES by the fact that the shake–up satellite structure which is observed for the multilayer film is strongly washed out, and broad high–energy tails are observed, which are typical for metallic character. This is a further indication for the many–body character, because it shows that both, shake–up and charge transfer satellite excitations, are interrelated. The many–body excitations are also evident in the NEXAFS data of the monolayer films. For PTCDA and PTCDI, for example, the signature is completely changed and the sharp fine structure which is observed in the multilayer NEXAFS is completely washed out in the monolayer spectra. The modification of the general spectral signature and the broadening can be explained by chemical shifts and charge transfer satellite contributions in the NEXAFS, similar to what is observed in core level PES. The loss of vibronic fine structure can be attributed to configuration mixing, which also involves the vibronic states due to electron–vibration coupling. Note that a modification of the life time of the excited states due to the interface interaction may also be relevant. Altogether these many–body effects can lead to strong modifications in the NEXAFS with respect to the multilayer data.

Consequently, the interpretation of the data is not straightforward due of the break down of the single particle picture in case of significant covalent adsorbate–substrate interaction. The same holds for electronic transitions in NEXAFS spectroscopy. However, comprehensive quantum chemical calculations of high quality and systematic comparison data from different interfaces can help in analyzing and interpreting such data in detail. Moreover, the many–body character of the core excited states has also implications for the various decay channels. It can be expected that it is also reflected in the Auger and fluorescence decay as well. Furthermore, it can be interesting to study these many–body effects in the time domain. In this context RIXS and resonant Auger spectroscopy can provide important information for the understanding of the interaction at adsorbate–substrate interfaces as it will be demonstrated in *chapter 5*.

5

Resonant Auger Raman spectroscopy of metal–organic interfaces

The results of the previous chapters demonstrated that PES and NEXAFS spectroscopy are powerful techniques for studying the electronic properties of surfaces and interfaces. The decay of core excited states can provide additional site specific information about the electronic structure. In this context two decay channels are of interest, namely fluorescence and Auger decay, which correspond to the emission of a photon or an electron, respectively. In case of light elements and shallow core levels the cross section for Auger decay is considerably larger than for fluorescence decay. Additionally, the relatively short electron mean free path leads to high surface sensitivity compared to the fluorescence signal. Therefore, Auger electron spectroscopy (AES) is the method of choice for studying thin adsorbate films of organic molecules. It has been successfully applied for studying the composition of molecular thin films and their electronic structure. [179–181]

Moreover, for many materials x–ray emission and Auger electron spectroscopy show a dependence on the excitation energy, particularly for energies close to an absorption edge, where core electrons can be excited into different unoccupied bound states. This photon energy dependence is made of use by *resonant inelastic x-ray scattering* (RIXS) spectroscopy, and *resonant PES* and *AES*, which have been established during the last decades due to the development of high brilliance synchrotron beamlines. The dependence of the emission spectra on the excitation energy can provide further information about the electronic structure. The branching ratio of the various decay channels, for example, can vary with the excitation energy as well as the life time of the core excited state, which can lead to sophisticated interference effects as it is briefly discussed in section 5.1.1. These effects can even provide access to dynamic aspects which occur on the fs time scale during the life time of the core excited state, e.g. atomic motions which couple to the electronic structure and charge transfer phenomena. [182–186] In this context this method is often referred to as core hole clock spectroscopy. It has the advantage of site specific excitations in contrast to laser based pump–probe experiments with visible light. [187, 188] This can provide valuable information about the electronic structure, e.g. about the localization and symmetry of valence states. [189–193]

These aspects are particularly interesting when studying adsorbate layers, interfaces and surfaces. During recent decades the adsorbate–substrate interaction has predominantly been studied for "simple" model systems consisting of atomic or small molecular adsorbates [194–198]. The following investigation will focus on thin film model systems of organic dye molecules and organic–metal interfaces which are considered to be of interest for various applications.

The interest in phthalocyanines as catalyst and as dye molecule for applications in OLEDs and organic solar cells has driven research on these molecules with respect to applications and fundamental aspects. [199–204] In this context the electronic and structural properties of phthalocyanine thin films are of interest with respect to the bulk, organic–metal interfaces and organic–organic interfaces. Moreover, it has been shown that well ordered thin films can be prepared from these molecules which allows to study their structural, optical, and electronic properties in detail. [205–220] However, RIXS and photon energy dependent AES investigations have been comparatively scarce on molecular thin films. [221–224] Furthermore, as tin–phthalocyanine (SnPc) thin films deposited on a Ag(111) surface have been well characterized with low energy electron diffraction, x–ray standing wave method and PES, [214, 225, A4] such molecular films are suitable model systems for studying the properties of bulk, organic–metal interfaces and organic–organic interfaces. All three aspects are addressed in this chapter by means of NEXAFS spectroscopy and resonant AES.

The comparison of the core level PES and NEXAFS data in section 5.2.1 indicates that the adsorbate–substrate interaction is so strong that many–body excitations involving adsorbate–substrate charge transfer play a significant role. It is expected that these effects are also significant in the photon energy dependent AES data. Their spectral features can be identified when comparing data between different molecular adsorbate films, where these effects are absent or dominant, respectively. Therefore a SnPc/Ag(111) multilayer film will be investigated at first, for which the intermolecular interaction is considerably weaker than the adsorbate–substrate coupling. Secondly, a SnPc/Ag(111) monolayer film will be studied and systematic differences to the multilayer data will be discussed with respect to many–body excitations involving substrate–adsorbate charge transfer. Moreover, some implications of many–body effects will be discussed in section 5.4 with respect to the common tunneling approach of the adsorbate–substrate charge transfer, in which the intensity of certain spectral features is directly related to an average tunneling probability and charge transfer time, respectively. [183–186]

Thirdly, the influence of the interface interaction on the second adsorbate layer will be addressed. Therefore a hetero–molecular adsorbate film will be studied, where 1 ML SnPc is deposited on top of a PTCDA/Ag(111) monolayer film. Recent PES and NEXAFS investigations have shown that well defined thin films can be prepared

with SnPc forming a wetting layer on top of the PTCDA monolayer. [226, A6] Additionally, the SnPc contribution to the valence and C K–NEXAFS spectra can be clearly distinguished from the PTCDA signal making the interpretation of the autoionization spectra easier than for a 2 ML SnPc/Ag(111) film, for which the signal from the first and the second monolayer is very similar. Furthermore, recent PES investigations of this hetero–molecular thin film indicate a rigid level shift of 0.4 eV to lower binding energy for the SnPc monolayer on top of the PTCDA/Ag(111) monolayer film with respect to the SnPc/Ag(111) multilayer film. [A6, A7] A comparison of the photon energy dependent AES data of the hetero–molecular film to that of the SnPc/Ag(111) multilayer and that of the monolayer film can provide further information about the influence of the interface interaction on the second monolayer.

5.1 Some aspects of core excitation and de–excitation

Some fundamental aspects of resonant AES will be introduced briefly in the following as far as they are relevant to the discussion of the data in *section 5.2*. It has already been mentioned above that interference effects between different transition amplitudes can alter the spectra considerably. Therefore the conditions for which these effects are relevant will be discussed briefly in *section 5.1.1*. Afterwards, a time–dependent description of the autoionization spectra is introduced in *section 5.1.2*, which improves the understanding of dynamic aspects as electron–vibration coupling in *section 5.1.3*. Moreover, different excitation and decay channels will be introduced in *section 5.1.4* in a simplified view. Finally, it is shown in *section 5.1.5* and 5.1.6 that resonant excitation can enhance CIS valence signals. This offers the possibility of studying satellites in the valence band spectra, which are typically very weak for organic films. This is particularly of interest when studying interface interaction.

5.1.1 Resonant Photoelectron spectroscopy versus resonant Auger spectroscopy

Electronic states of atoms and molecules are usually classified in terms of electronic configurations, according to the independent–particle approximation. Particularly the actual (stationary) states may be represented by a linear combination of different electronic configurations, e.g. when modeling the charge transfer satellites in

section 4.1.3 the respective electronic states have been expressed by a linear combination of two different electronic configurations. Configuration mixing is important for the phenomenon of autoionization as well. In this context one needs to consider the mixing of a discrete configuration with a continuum of configurations, e.g. in case of resonant photoemission the mixing of one final state configuration, which is discrete in photon energy, with the continuous spectral configurations of direct photoemission channels. According to the formalism developed by *Fano* and *Rice* such a scenario leads to interference effects between the various spectrum configurations, which results in asymmetric line shapes because of destructive and constructive interference in case of strong configuration mixing. Only the crucial relations for the description of such Fano profiles will be briefly discussed in the following, and it is referred to [227–229] for more details.

We consider one discrete state φ and the unperturbed continuum states ψ_E. The elements of the energy matrix are

$$(\varphi|H|\varphi) = E_\varphi \tag{5.1}$$
$$(\psi_{E'}|H|\varphi) = V_{E'} \tag{5.2}$$
$$(\psi_{E''}|H|\psi_{E'}) = E'\delta(E''-E') \tag{5.3}$$

with the coupling parameter $V_{E'}$. The eigenvectors can be written as a linear combination of the discrete state and the continuous states.

$$\Psi_E = a\varphi + \int dE'\, b_{E'}\psi_{E'} \tag{5.4}$$
$$\Phi = \varphi + P\int dE'\, \frac{V_{E'}\psi_{E'}}{E-E'} \tag{5.5}$$

Consequently, the continuum states are modified by an admixture of the discrete state φ and vice versa. Then the ratio of the transition probabilities between electron transitions from the initial state i into the (continuous) eigenstates Ψ_E and transitions into the unperturbed continuum states ψ_E can be expressed as a function of energy ϵ

$$\frac{\left|(\Psi_E|T|i)\right|^2}{\left|(\psi_E|T|i)\right|^2} = \frac{(q+\epsilon)^2}{1+\epsilon^2} \tag{5.6}$$

$$q = \frac{(\Phi|T|i)}{\pi V_E^*(\psi_E|T|i)} \tag{5.7}$$

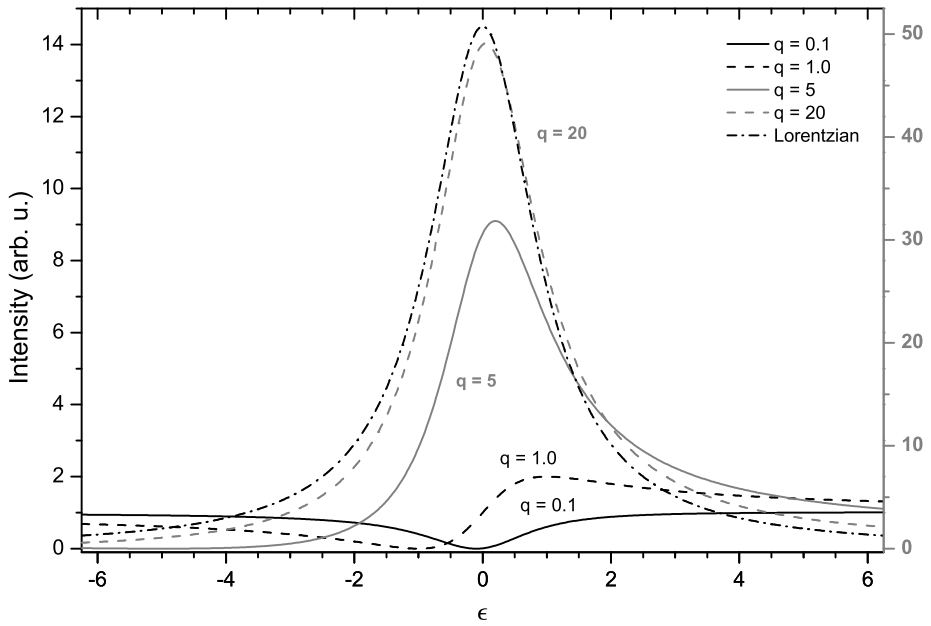

Figure 5.1: Fano profiles for the parameter $q = 0.1$, 1.0, 5 and 20. Additionally a Lorentzian profile is plotted which is equivalent to $q \to \infty$.

with T being the appropriate transition operator. [229] The parameter q depends on the coupling parameter V_E for the strength of the configuration mixing and the ratio between the amplitudes of transitions into the discrete spectrum configuration Φ and transitions into the unperturbed continuum states ψ_E.

Some Fano profiles are plotted in Fig. 5.1 for different values of the parameter q. For small q the Fano profile is very asymmetric while it resembles a Lorentzian profile for large q. This asymmetry can be understood when considering the amplitude of transitions into the eigenstate Ψ_E from relation (5.4):

$$(\Psi_E|T|i) = a(\varphi|T|i) + \int dE'\, b_{E'}(\psi_{E'}|T|i) \tag{5.8}$$

One realizes intuitively that interference effects can play an important role for the superposition of $(\varphi|T|i)$ and the continuum of transition amplitudes $(\psi_{E'}|T|i)$. These interference effects are large for small values of q and vanish with increasing q so that the Fano profile results in a Lorentzian profile for $q \to \infty$, which becomes also evident from relation (5.6).

Note that q is small if the transition amplitudes $(\Phi|T|i)$ and $(\psi_E|T|i)$ are of the same order of magnitude and the coupling parameter V_E is sufficiently large. Then

interference effects appear in the autoionization spectra. Such effects are strong, for example, when the hole in the core excited state and in the final state is located in the same electronic shell, so that Coster–Kronig or super Coster–Kronig decays are dominant, which results in a short life time τ of the excited state. [33,183,230–235] As the coupling parameter V_E is directly related to τ, so that $|V_E|^2$ will be large if the life time is short, the Fano parameter q is small for such quickly decaying states. Consequently, the interference between the amplitudes of transitions into the discrete Auger final state and continuous transitions into the direct photoemission final states will be significant if the transition probabilities of both channels are comparable. Such a scenario is related to the term *resonant PES* in the following. Resonant PES of nickel at the M–edge is a typical example for which Coster–Kronig decay plays an important role. Particularly transitions into the Ni $3p^5 3d^{10}$ core excited state lead to resonant enhancement of a satellite at 6 eV higher binding energy with respect to the Ni $3d^9$ main line, which can be predominantly related to the Ni $3d^8 4s^1$ configuration. Moreover, analysis of the peak shape suggests considerable interference effects. [33,91,194] Analogous resonant enhancements of satellites have been studied for other metals as well, e.g. copper, calcium, manganese, [236–239] alloys [95] and transition metal compounds as CuO, NiO, V_2O_3. [86,240–242]

As for the following investigation of organic thin films the core hole is located in the K–shell, and in the final state the holes are located in the L–shell, one can assume that the coupling parameter V_E is comparatively small and hence q becomes comparatively large. This suggests only minor interference between the amplitudes of the discrete autoionization transition and the continuum of direct photoemission transitions amplitudes. Hence, it can be assumed that the total signal is just a superposition of the direct photoemission and the autoionization signal. Another aspect which supports this assumption is the intensity ratio between the autoionization signal at resonance ($\epsilon = 0$) and off resonance. For the data of the SnPc multilayer film in section 5.2 this ratio is $I(\epsilon = 0) : I_0 \sim 100$ which is even higher than for the profile in Fig. 5.1 where $q = 20$. Consequently, the interference effects discussed above can be neglected for the following investigation. Hence, the total transition probability P_{f0} can be considered as superposition of the transition probability of direct photoemission and that of the Auger like autoionization process, which can be described as photon scattering event according to *Kramers–Heisenberg* relation. [243]

$$P_{fi} \sim \left(\left| \langle f | \epsilon \cdot \mathbf{p} | i \rangle \right|^2 + \left| \sum_k \frac{\langle f | O_c | k \rangle \langle k | D | i \rangle}{\hbar\omega - E_k + E_i + i\Gamma_k} \right|^2 \right) \delta(E_f - E_i - \hbar\omega) \qquad (5.9)$$

Here D is the dipole operator and O_c is the Coulomb operator. The energies E_x with $x = 0, j, f$ correspond to the eigenvalues of the system in the ground state, excited state and the final state. As the autoionization contribution dominates the total photoemission signal, it is sufficient to consider only the matrix element

$$T_{fi} = \sum_k \frac{\langle f|O_c|k\rangle\langle k|D|i\rangle}{\hbar\omega - (E_k - E_i) + i\Gamma_k} \,. \tag{5.10}$$

It is referred to this scenario as *resonant Auger spectroscopy* or *resonant Auger Raman spectroscopy* in case of detuning of the energy of the incident x–ray beam ($\hbar\omega \neq E_k - E_i$) so that transitions in the Raman regime contribute significantly.

5.1.2 Time–dependent approach

The autoionization spectra can be either interpreted in the energy picture, which has been introduced above, or in the time–dependent picture. Both are equivalent to each other and lead to the same result. The combination and comparison of these two pictures can improve the understanding of the autoionization spectra in this chapter. Therefore, the time–dependent approach will be introduced here before discussing aspects like electron–vibration coupling and charge transfer within both pictures.

5.1.2.1 "Duration time" of the scattering process

One important aspect of the resonant x–ray Raman scattering is its "duration time". Principally this is a physical concept which corresponds to the time between absorption and emission. It has been shown that the duration time can be varied by detuning the photon energy $\hbar\omega$ of the incident x–ray beam from the energy difference between the exact eigenstates $E_k - E_i$. [196, 244–246] As this is related to modifications of the emission spectrum, it gives access to dynamical aspects of the excited states on the time scale of the scattering even, e.g. nuclear and electron dynamics. This allows to study vibrations, dissociation and charge transfer. The principle aspects of the duration time of x–ray Raman scattering are briefly discussed in the following by deducing the correlation time, or duration τ_c, of the scattering process from the time–dependent representation of T_{fi}. [196, 244–246]

The T matrix (5.10) can be written in the time representation as

$$T_{fi} = \int_0^\infty dt\; e^{i\hbar(\omega-\overline{\omega_{ki}})t} < f|\Psi_i(t) > \tag{5.11}$$

with some average resonant frequency $\overline{\omega_{ki}}$ of the x–ray absorption transition from $|i\rangle$ to $|k\rangle$ and the state $\Psi_i(t)$, which is an electro–vibronic wave packet that describes the time evolution of the initial wave packet $|i>$. These states are interrelated by the exact time–dependent retarded *Green's function* $G = -ie^{-i(H-\hbar\overline{\omega}_{ki}-i\Gamma)t}$:

$$\Psi_i(t) = O_c G D|i> . \tag{5.12}$$

Under off–resonant conditions the exponent in (5.11) oscillates strongly if the detuning $\omega - \overline{\omega_{ki}}$ is large and is quickly attenuated when the lifetime broadening Γ is large. Consequently, the contribution of this exponent to the integral over time in (5.11) is small for $t \neq 0$ and the main contribution originates from $t \approx 0$. Then the matrix element can be written as

$$T_{fi} =< f|\Psi_i(0) > \int_0^\infty dt\; e^{i\hbar(\omega-\overline{\omega_{ki}})t-\Gamma_k t} . \tag{5.13}$$

Relation (5.11) shows that a strong correlation of moments of absorption and emission with the correlation time τ_c exists, which is caused by two mechanisms. The first is the finite lifetime of the core excited state. The correlation, or the delay time, τ_c, between absorption and emission cannot exceed the life time $1/\Gamma_k$. The second is the phase difference between the amplitude of sudden decay and decay after time t. As strong interference of scattering amplitudes occurs for large times, it must be $t < \hbar|\omega - \overline{\omega_{ki}}|^{-1}$. Therefore

$$\tau_c = \sqrt{(\omega - \overline{\omega_{ki}})^2 + \Gamma_k^2}^{-1} \tag{5.14}$$

can be interpreted as the correlation time or *duration time* of the scattering process. This relation indicates that τ_c becomes shorter for large detuning of $\hbar\omega$ of the incident photons than the natural lifetime $1/\Gamma_k$ of the core excited state for resonant excitation.

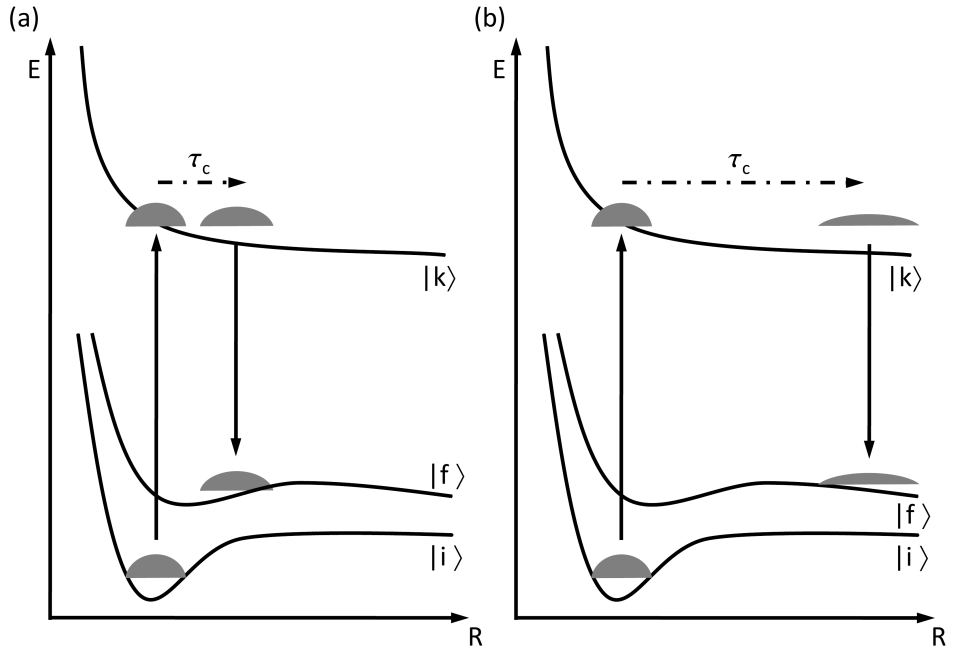

Figure 5.2: Schematic representation of dissociation in resonant Auger Raman spectroscopy for (a) detuned excitation and short duration time τ_c, and (b) resonant excitation and long duration time τ_c.

5.1.2.2 Propagation of wave packets

The physical concept of time–dependent electro–vibronic wave packets and duration time τ_c of the scatter process has already been indicated in *section 5.1.2.1*. The dependence of the spectral signature on τ_c can be attributed to the time–dependence of the excited state, namely to the propagation of the electro–vibronic wave packet Ψ_t in time. This illustrative concept allows to describe the photon energy induced changes in the scattering amplitude by interference suppression of large time contributions to the scattering amplitude. Particularly for comparatively short duration time τ_c the scattering amplitude T_{fi} can mainly be described by the wave packet $\Psi(t = 0)$, while for comparatively long τ_c time contributions for $\Psi(t > 0)$ are also relevant. This is an important relation for the discussions in this chapter.

The wave packet character of $\Psi(t)$ is shown in [196] by separating the transition probability T_{if} from relation (5.11) into a time–dependent and a time–independent component.

$$T_{fi}(\tau) \simeq \text{const} - e^{-(\Gamma/\hbar)\tau} \sum_k \frac{\langle f|Q_c|k\rangle\langle k|D|i\rangle}{\hbar(\omega-\omega_{ki})+i\Gamma}\, e^{-i(\omega-\omega_{ki})\tau} \tag{5.15}$$

Accordingly, the wave packet $\Psi(t)$ has contributions from different states $|k\rangle$. The principal concept can be understood best by considering the dissociation of molecules upon core excitation as it is illustrated in Fig. 5.2. It was found in RIXS data and resonant Auger Raman spectra of several molecules, e.g. HCl, H_2O or H_2S [196, 247–252], that the spectral signature can be reproduced by a linear combination of a spectrum for intact and dissociated molecules. The relative intensity of the contribution from intact molecules increased and that from dissociated molecules decreased when detuning the photon energy $\hbar\omega$. This can be directly related to the propagation of the wave packet as it is illustrated in Fig. 5.2 — small τ_c $\rightarrow$ short propagation, large $\tau_c \rightarrow$ long propagation. A long propagation leads to dissociation for the suggested potential curves in Fig. 5.2. Note that the dynamics of the wave packet is determined by the group velocity and the phase velocities of the different Fourier components as discussed in detail in [196]. The effective width Δ of the envelope of excited state vibronic levels, for example, can be related to the deformation time $\tau_{wp} \sim 1/\Delta$ of the wave packet. [196,246,253,254] This aspect is illustrated in Fig. 5.2 by the broadening of the wave packet.

5.1.3 Electron–vibration coupling

Electron–vibration coupling can broaden the valence, core level and NEXAFS spectra of molecular adsorbates significantly [133, 134, 204, 219] as it has already been discussed in section 3.1.2 and 4.1.5. Moreover, investigations of electro–vibronic coupling with resonant Auger Raman spectroscopy and RIXS are subject to current research. Particularly small molecules have been studied in this context, e.g. CO, H_2O, H_2S, ethylene and benzene. [196, 198, 247, 253–257] These investigations show a strong dependence of the vibronic fine structure on excitation energy, particularly differences between resonant and off–resonant excitation. These effects can be either understood in the time–dependent picture or in the energy picture. Both descriptions are equivalent as it will be shown in the following.

5.1.3.1 Time–dependent approach

The vibronic fine structure in the resonant Auger Raman spectra can be understood along the same line of arguments as the dissociation of molecules in *section 5.1.2.2*. This interrelation is illustrated in Fig. 5.3, where harmonic potentials

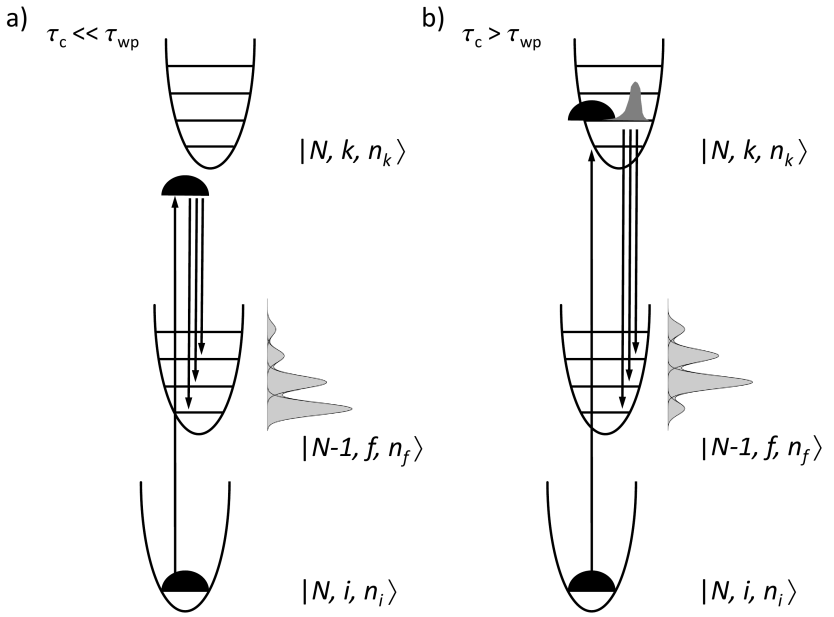

Figure 5.3: Schematic representation of vibronic excitations in resonant Auger Raman spectroscopy. (a) Detuned excitation and short duration time τ_c. (b) Resonant excitation and long duration time τ_c. The wave packet is indicated for different times, $|\Psi(t=0)|^2$ (black) and $|\Psi(t>0)|^2$ (grey). Each eigenstate depends on the number of bound electrons N, and the electronic and vibronic quantum numbers i, k, f and n_i, n_k, n_f of the initial state, core excited state and final state. Note that decay of the core excited state reduces the number of bound electrons from N to $N-1$.

are assumed for the vibronic states. If the duration of the x–ray scattering process τ_c is short compared to the time scale of the propagation of the wave packet $\Psi(t)$, the scattering amplitude is essentially determined by $\Psi(t=0)$ as it is depicted in Fig. 5.3 (a). In this case the vibronic fine structure resembles that of the direct photoemission signal. This is the case for large detuning of the photon energy of the incident x–rays according to relation (5.14). For resonant excitation the "duration" of the x–ray scattering becomes longer ($\tau_c \to 1/\Gamma_k$) so that the propagation of the wave packet $\Psi(t>0)$ plays a role. This can lead to significant modifications of the vibronic fine structure compared to that off resonance and that of the direct photoemission signal. Note that detuning the photon energy at the C K edge by 1 eV reduces τ_c from $\sim$ 7 fs (on resonance) to $\sim$ 0.7 fs with respect to relation 5.14.

5.1.3.2 Energy–dependent approach

The time–independent transition matrix T_{fi} (5.10) needs to be considered for the total wave functions of the electrons and the nuclei ($|I\rangle$, $|K\rangle$, $|F\rangle$). These wave functions can be separated into a product of the electronic wave functions ($|i\rangle$, $|k\rangle$, $|f\rangle$) and the nuclear wave functions ($|n_i\rangle$, $|n_k\rangle$, $|n_f\rangle$) under the assumption that the Born–Oppenheimer approximation holds, which yields the Franck–Condon factors for the various vibronic transitions. Consequently, it is

$$\begin{aligned} T_{fi} &= \sum_K \frac{\langle F|O_c|K\rangle\langle K|D|I\rangle}{\hbar\omega - (E_K - E_I) + i\Gamma_K} \\ &= \sum_{k,n_k} \frac{\langle f, n_f|O_c|k, n_k\rangle\langle k, n_k|D|i, n_i\rangle}{\hbar\omega - (E_{kn_k} - E_{in_i}) + i\Gamma_k} \\ &= \sum_k \left(\langle f|O_c|k\rangle\langle k|D|i\rangle \sum_{n_k} \frac{\langle n_f|n_k\rangle\langle n_k|n_i\rangle}{\Omega - \hbar(\omega_k n_k - \omega_i n_i) + i\Gamma_k} \right), \end{aligned} \tag{5.16}$$

where $\Omega = \hbar\omega - (E_k - E_i + \hbar(\omega_k - \omega_i)/2)$ corresponds to the detuning of the absorbed photon $\hbar\omega$, and E_x, ω_x and n_x are the equilibrium electronic energy, the vibronic frequency and the vibronic quantum number of the electronic state $x = i, k, f$. Note that in the ground state it is $n_i = 0$. If only one particular electronic state $|k\rangle$ is relevant, the overlap of the vibronic states $|n_x\rangle$ will determine the amplitude T_{fi} of transitions into different vibronic final states $|n_f\rangle$. Consequently, the resonant Auger Raman spectrum is broadened by a vibronic fine structure which is determined by both, the core excited and the final state. This is the case for resonant excitation ($\Omega - \hbar\omega_k n_k = 0$). In case of large detuning compared to the effective width Δ of the envelope of excited state vibronic levels ($\Delta/|\Omega| < 1$) the transition amplitude T_{fi} is not dominated by one particular vibronic state n_k but all n_k contribute significantly. [196, 246, 253, 254] Hence, the summation in relation (5.16) needs to be carried out over all vibronic levels and therefore it is $\sum_{n_k} |n_k\rangle\langle n_k| \simeq 1$. The transition amplitude then becomes

$$\lim_{\Delta/|\Omega|<<1} T_{fi} \sim \frac{\langle n_f|n_i\rangle}{\Omega + \Gamma} \tag{5.17}$$

This shows that for large detuning the vibronic fine structure of the resonant Auger Raman spectra only depends on the Franck–Condon factor $\langle n_f|n_i\rangle$ between vibronic states in the initial and in the final state. Consequently, the vibronic fine structure resembles that of the direct photoemission signal. It is modified with decreasing detuning since then the vibronic states $|n_k\rangle$ become important for the transition

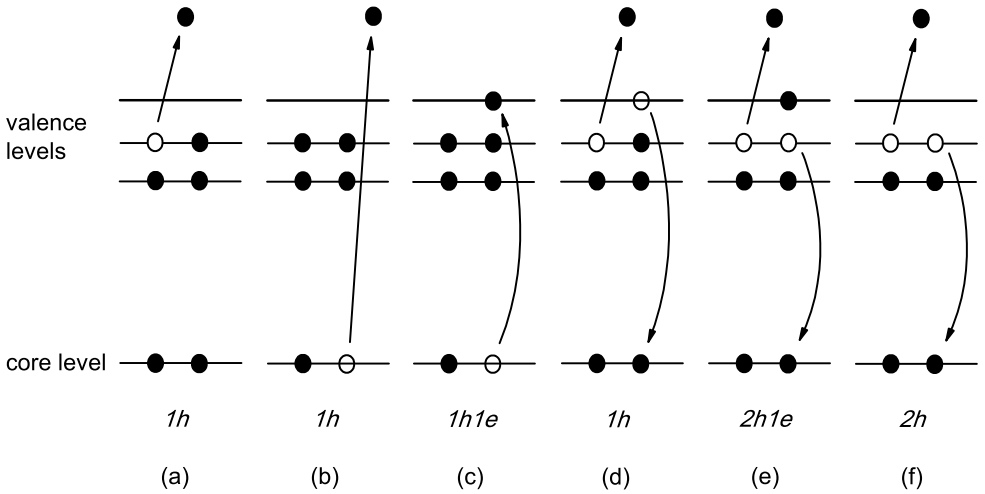

Figure 5.4: Schematic illustration of various excitation and decay channels for excitation energies in the soft x–ray regime: (a) photoemission of a valence electron, (b) photoemission of a core electron, (c) core excitation into a bound unoccupied state (NEXAFS spectroscopy), (d) participant decay of such a core excited state, (e) spectator decay of such a core excited state, (f) regular Auger decay after core ionization. The number of holes and electrons in previously unoccupied states is indicated additionally.

amplitude T_{fi}. In the adiabatic limit only one particular state $|n_k\rangle$ dominates. Consequently, considerations in the energy picture agree with those in the time–dependent picture.

5.1.4 Decay channels for a free atom or molecule

The core excited state can decay via different channels. Fig. 5.4 gives an overview of various excitation and decay channels for resonant excitation. After photoemission of a core electron the *1h* core excited can be filled by various *regular Auger* decay channels, where an electron from an upper shell fills the core hole and kicks out another electron due to Coulomb interaction as it is indicated in Fig. 5.4 (b) and (f). Accordingly, the kinetic energy of the Auger signal is independent of the excitation energy and therefore it is often referred to as constant final state (CFS) signal. Moreover, a core hole state where a core electron is excited into a previously unoccupied bound state, as depicted in Fig. 5.4 (c), decays via *autoionization*. It is distinguished between (d) *participant* decay, where the excited electron fills the core hole and emits another electron, and (e) *spectator* decay, where the respective electron is passive ("spectator"). The spectator electron can influence the cross

section for different decay channels and the kinetic energies of the emitted electron compared to the regular Auger decay channels. These energy shifts are also known as *spectator shift*.

5.1.5 Enhancement of CIS signals in the valence regime

The scheme in Fig. 5.4 illustrates that autoionization can enhance constant initial state (CIS) signals. Participant decay (Fig. 5.4 (d)), for example, can result in the same $1h$ final state as direct photoemission of one valence electron (Fig. 5.4 (a)). Moreover, the electronic configuration after spectator decay (Fig. 5.4 (e)) matches that of a shake–up excitation by direct photoemission. Consequently, certain CIS signals might be enhanced at resonant excitation energies, in analogy to the enhancement of the 6 eV satellite with respect to the Ni $3d^9$ peak. [91,194,240,258,259] The matrix element T_{fi} for the respective transitions can be determined from relation (5.10).

In general it is assumed for organic thin films of π–conjugated molecules with delocalized valence orbitals that the direct photoemission cross section for (shake–up) satellite excitations is small in the valence regime, so that they do not contribute significantly to the direct photoemission signal. However, as certain CIS valence signals can be selectively enhanced by autoionization, such satellites can be investigated at resonant excitation.

5.1.6 Adsorbate–substrate coupling at a metal surface

The investigation of several organic–metal interfaces in *section 4.2* indicated significant adsorbate–substrate coupling. Satellite contributions with significantly metallic character were observed, which have been related to many–body excitations and adsorbate–substrate charge transfer, particularly for the core level spectra of the PTCDA/Ag(111) and the PTCDI/Ag(111) monolayer films. The fact that no satellites were found in the valence spectra is not very surprising, because the direct photoemission cross section for satellite excitations in the valence spectra is generally small for such molecules, as already pointed out above. However, it was demonstrated in *section 5.1.5* that autoionization and direct photoemission can lead to the same final states. Therefore, the autoionization signal can contribute to satellite signals in the valence regime so that they are significantly enhanced. This offers the possibility of studying such satellites at resonant excitation energies.

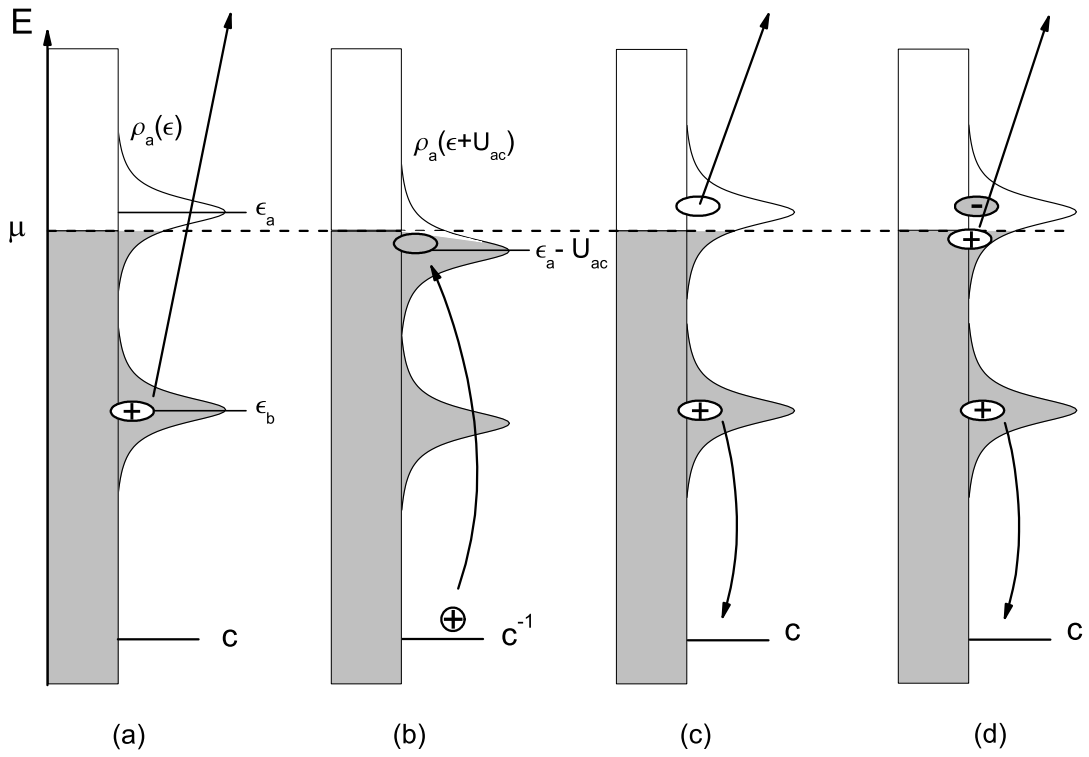

Figure 5.5: Schematic illustration of direct valence photoemission and autoionization for strong substrate–adsorbate coupling. The many–body excitations are classified into scenarios which are comparable to those illustrated in Fig. 5.4 for the limit of no coupling. — (a) photoemission of a valence electron, (b) core excitation into a bound unoccupied state (NEXAFS spectroscopy), (c) "1h" final state and (d) "2h1e" final state. The grey fill color indicates the occupied density of substrate and adsorbate states.

It is straightforward that the many–body effects must be reflected in the autoionization signal as well. The essential aspects will be discussed in the following in the context of a simplified, descriptive and more phenomenological picture, which brings the concepts of charge transfer satellites and autoionization together. Fig. 5.5 is an attempt to illustrate the dominant effects for weak adsorbate–substrate coupling according to the understanding and the picture which has been developed in *chapter 4*. The many–body excitations are classified in Fig. 5.5 into scenarios which are comparable to those illustrated in Fig. 5.4 for the free molecules despite the concepts of participant and spectator electrons are not appropriate in case of strong adsorbate–substrate coupling.[1] Moreover, one has to be aware of the fact that an excitation drives the interface into a non–equilibrium state.

[1] See *section 5.2.3* for a discussion of this aspect.

Fig. 5.5 (a) illustrates the situation after direct photoemission of a valence electron with the distribution of adsorbate–substrate states ρ_a being partially occupied. In Fig. 5.5 (b) a previously unoccupied distribution of substrate–adsorbate states has been occupied by a NEXAFS transition. One can imagine several relevant final states after decay of this core excited state in analogy to the participant and spectator decays in Fig. 5.4 for a free atom or molecule. One possible "$1h$" final state is illustrated in Fig. 5.5 (c). It resembles the final state after direct photoemission in Fig. 5.5 (a) and therefore this process can be considered as pendant to participant decay. One possible "$2h1e$" final state is depicted Fig. 5.5 (d). This process can be considered as pendant to spectator decay or satellite excitation with respect to scenario (a). It can be expected that such satellites have considerable metallic character as they correspond to excitations within the continuum of adsorbate–substrate states. In this case continuous satellite features may contribute to the valence spectra, similar to what has been observed for the core level spectra in *chapter 4*. The enhancement of satellite features at resonant excitation energies is known for the autoionization signal of metals, alloys and transition metal compounds. [33, 86, 91, 95, 194, 236–242, 260]

Furthermore, it can be shown with respect to the matrix element (5.10)

$$T_{fi} = \sum_k \frac{\langle f|O_c|k\rangle\langle k|D|i\rangle}{\hbar\omega - (E_k - E_i) + i\Gamma_k}$$

that the formation of a distribution of substrate–adsorbate states ρ_a can lead to interference effects in the autoionization signal. In this case the sum has to be carried out over all states $|k\rangle$ in the energy interval of relevance. This sum over transition amplitudes can result in constructive and destructive interference, and consequently in asymmetric line shapes ($\sigma(\omega) \sim |T_{fi}|^2$). In the Fano picture described in *section 5.1.1* this scenario corresponds to the interaction of one discrete autoionization spectrum configuration φ with a continuum of autoionization spectrum configurations ψ_E. Particularly, φ can be associated with a final state after autoionization of the uncoupled adsorbate, which is discrete in excitation energy ($\hbar\omega = E_{c\to a}$), e.g. a hole in state b after participant decay of the core excited $c^{-1}a^{+1}$ state. Furthermore, one can imagine that there are continuous transitions of the core electron into the unperturbed density of unoccupied substrate states. "Participant decay" of these continuous core excited states can also lead to a final state with a hole in state b. This can be associated with the continuous spectrum configurations ψ_E. The Fano parameter q is sufficiently small if the transition amplitudes are of similar magnitude and V_E is large. Then considerable interference effects appear. Note that excitations into a continuum of metallic states was already suggested for the NEXAFS spectra of C_{60}/Al(110) and C_{60}/Al(111) monolayer films. [184, and refs therein]

It has been shown in *section 5.1.5* for free atoms and molecules that autoionization can lead to the same finale states as direct photoemission, which enhances the CIS signal at resonant excitation. This allows to study "satellites" in the valence regime at resonant excitation. Moreover, it has been illustrated that this may also be valid for interfaces with significant adsorbate–substrate coupling and a distribution of adsorbate–substrate states. It can be expected that many–body effects involving adsorbate–substrate charge transfer are relevant in this context, in analogy to the investigation of core level satellites in *chapter 4*.

5.2 Resonant Auger spectra of different SnPc films

The following proceeding is helpful for a detailed understanding of the effects at the adsorbate–substrate interface: At first a multilayer film will be studied, where the intermolecular interaction is comparatively weak, so that it can be assumed that the intramolecular effects are dominant. The next step will focus on the adsorbate–substrate interface by investigating a SnPc/Ag(111) monolayer film and comparing the observed effects to those of the multilayer film. SnPc multilayer and sub–ML films have been studied recently by UPS, core level PES, electron diffraction and the x–ray standing wave method. [214, 225, 261, A4] Accordingly, closed multilayer films of high quality can be prepared with flat lying molecules which form molecular dimers. [A4] Moreover, various adsorption phases are found in the sub–ML regime. The valence and core level spectra of these films indicate a partially occupied LUMO derived density of substrate–adsorbate states and significant changes in the core level spectra similar to what has been discussed for the PTCDA/Ag(111) and PTCDI/Ag(111) monolayer films in *chapter 4*. Consequently, it can be assumed that many–body excitations play an important role for PES and NEXAFS spectroscopy, and interference effects may contribute to the autoionization signal according to the considerations in *section 5.1.6*.

Furthermore, it is an interesting question how the second adsorbate layer is effected by the substrate. It has been shown recently that well defined hetero–molecular adsorbate layers can be prepared by depositing 1 ML SnPc on top of a PTCDA/Ag(111) monolayer film; a closed wetting layer of flat lying SnPc molecules is formed. [226, A6] In a further UPS and core level investigation it has been found that the spectral features of the signal from the SnPc monolayer of this hetero–molecular film are comparable to those of the SnPc/Ag(111) multilayer film. However, a rigid level shift of 0.4 eV to lower binding energy is observed for the SnPc monolayer in the hetero–molecular film with respect to the SnPc/Ag(111) multi-

layer film. Consequently, the interface interaction effects the second (SnPc) monolayer significantly but the similarity of its spectral features to those of the (SnPc) multilayer film suggests that its interaction with the first (PTCDA) layer is considerably weaker than the direct adsorbate–substrate interaction of the first molecular layer. This aspect and the fact that the signal from the SnPc HOMO and HOMO-1 can be well separated from the valence contributions of the PTCDA/Ag(111) monolayer make this hetero–molecular film well suited for the resonant Auger spectroscopy investigation in the following.

In this context resonant Auger spectroscopy measurements at the N K absorption edge were theoretically a good choice because in this case the autoionization signal originates explicitly from the SnPc layer. However, it turned out that the autoionization is at the N K–edge considerably lower than at at the C K–edge due to fewer N atoms per molecule than C atoms. Additionally, the cross section for direct photoemission of the delocalized valence electron is smaller at the N K–edge than at the C K–edge and vice versa for the Ag 4d bands. Hence a discussion of the measurements at the C K–edge is more promising. Nevertheless some data for the N K–edge are also shown in the appendix D as they provide additional information. However, before analyzing the resonant Auger spectra it is helpful to discuss briefly the corresponding NEXAFS data.

5.2.1 Comparison of NEXAFS and core level PES spectra

In Fig. 5.6 the C K–NEXAFS spectra are plotted for (a) a SnPc/Ag(111) multilayer film, (b) a SnPc/Ag(111) monolayer film, (c) a PTCDA/Ag(111) monolayer film and (d) a hetero–molecular film, where 1 ML SnPc was deposited on top of a PTCDA/Ag(111) monolayer film. Note that for Fig. 5.6 (b – d) only the spectra for p–polarized light are shown as for these films the molecules are lying flat on the surface, and hence the signal for s–polarization is weak and featureless for photon energies below the absorption edge. For the SnPc multilayer film with 12–14 ML thickness, according to the attenuation of the Ag 3d PES signal, the NEXAFS pre–edge region in Fig. 5.6 (a) exhibits five distinct peaks (A – E) at $h\nu = 284.42$ eV, 285.28 eV, 287.18 eV, 289.12 eV and 290.86 eV. Peak A is probably dominated by transitions at the various phenyl carbon atoms into the LEMO, and peak B can predominantly be attributed to transitions at the porphyrine carbon species into the LEMO. [262, 263] Note that the vibronic fine structure could not be resolved even when recording spectra with smaller steps in photon energy, which might be a hint that several electronic transitions and vibronic progressions contribute to the NEXAFS peaks, respectively.

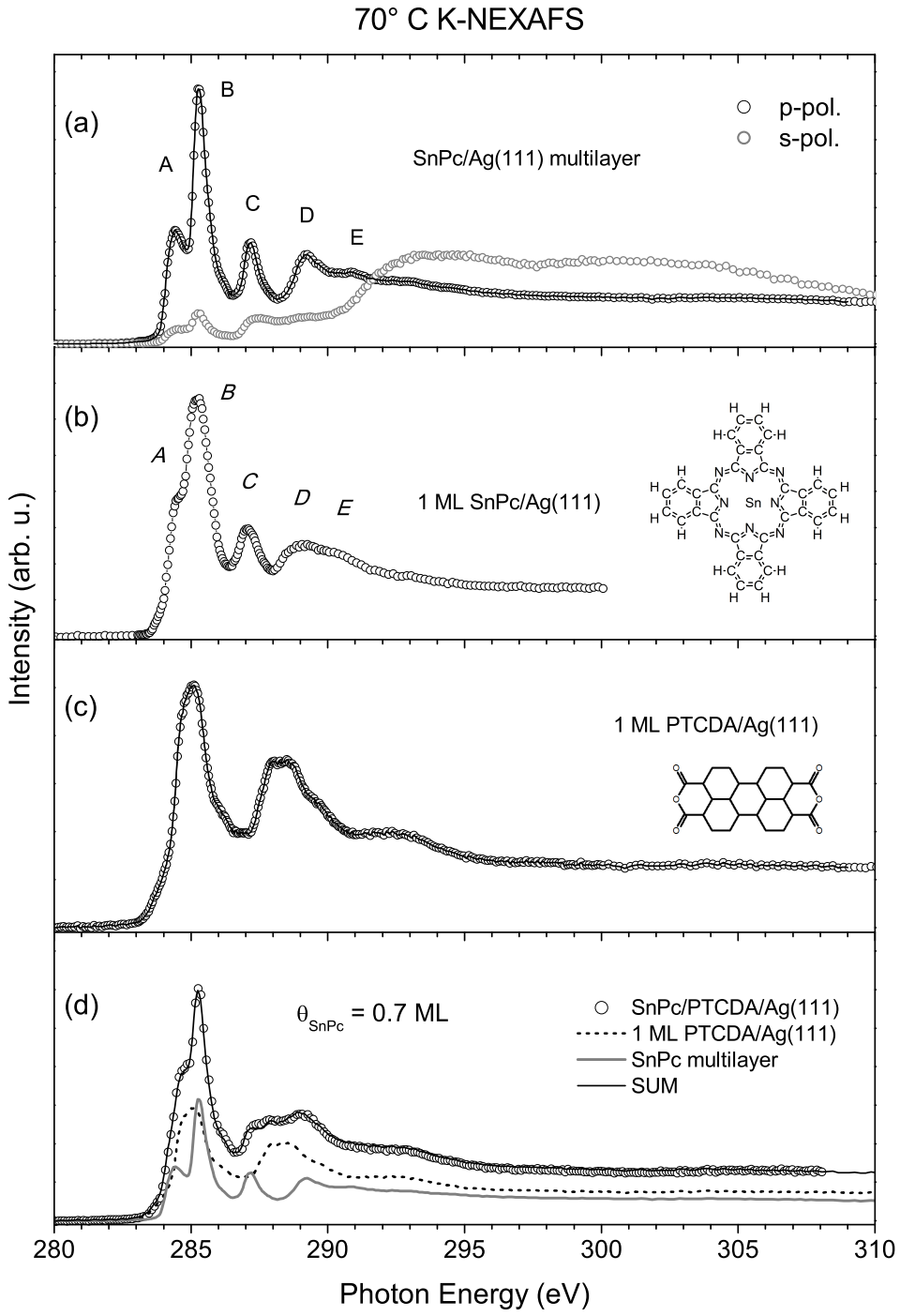

Figure 5.6: C K–NEXAFS spectra for a (a) multilayer and (b) 1 ML film of SnPc/Ag(111), as well as for (c) 1 ML PTCDA/Ag(111) and (d) a SnPc/PTCDA/Ag(111) film with $\theta_{SnPc} = 0.7$ ML. The C K–NEXAFS in (d) can be well reproduced by a linear combination of a PTCDA/Ag(111) monolayer spectrum and a SnPc multilayer spectrum. For all measurements linearly polarized light was used with s– or p–polarization and 70° angle of incidence with respect to the surface normal. The signal was recorded using a partial electron yield detector with 150 V retarding field.

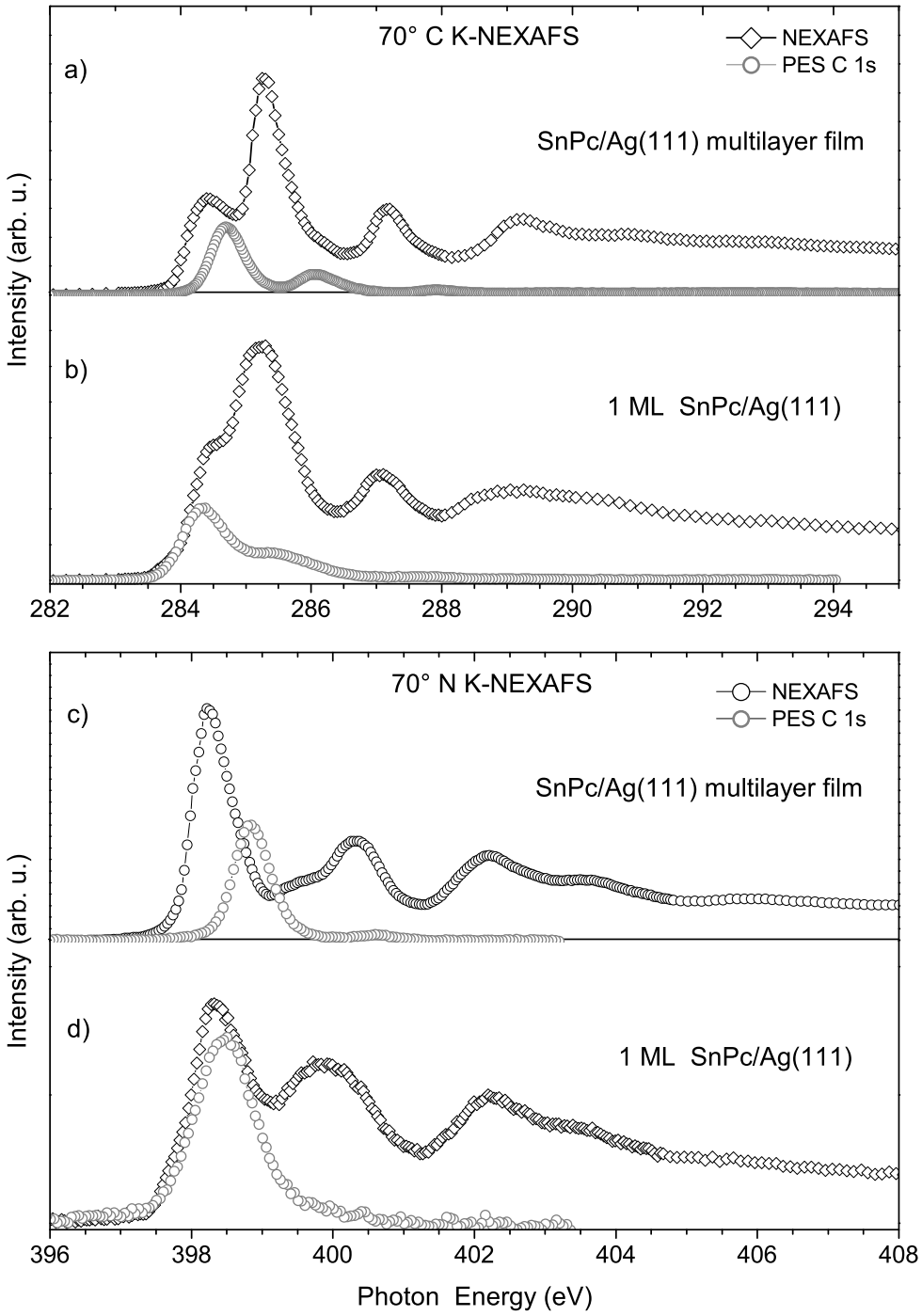

Figure 5.7: Upper half: C 1s PES and C K–NEXAFS spectra for (a) a SnPc/Ag(111) multilayer film and (b) a SnPc/Ag(111) monolayer film. Lower half: N 1s PES and N K–NEXAFS spectra for (c) a SnPc/Ag(111) multilayer film and (d) a SnPc/Ag(111) monolayer film. The data were recorded at 70° angle of incidence with p–polarized light and 150 V/300 V retarding field for the C K/N K–edge.

Moreover, for the SnPc/Ag(111) monolayer film Fig. 5.6 (b) the signature of the pre–edge region is considerably altered, in agreement with the chemical shifts in the core level and valence spectra. [A4] In particular the maxima of the first peaks $A - E$ are slightly shifted to $h\nu = 284.3$ eV, 285.21 eV, 287.06 eV, 289.2 eV and 290.5 eV, and considerably broadened compared to the multilayer spectrum. — Note, for example, the broadening of the leading edge of the shoulder A. — This finding is analogous to what is observed for the PTCDA/Ag(111) monolayer spectrum in Fig. 5.6 (c), which was already discussed in detail in *section 4.4.3* together with the data for the PTCDI/Ag(111) monolayer films. Accordingly, the modifications of the NEXAFS spectrum for the SnPc monolayer film with respect to the multilayer film can be interpreted as hint for many–body excitations involving substrate–adsorbate charge transfer. This is corroborated by the comparison between the NEXAFS and the core level spectra for the multilayer and the monolayer film in Fig. 5.7. The onsets of the C 1s and N 1s signals of the multilayer spectra in Fig. 5.7 (a) and (c) are located at significantly higher energy than the respective onsets of the NEXAFS signal, but for the monolayer film in Fig. 5.7 (b) and (d) both onsets are located at the same energy, identical to the findings for PTCDA and PTCDI in *section 4.4.3*. Note that this comparison in Fig. 5.7 (b) supports the suggested assignment of the peaks A and B, because the peaks at $E_B = 284.32$ eV and 285.45 eV in the C 1s spectrum for the SnPc monolayer film correspond to excitations at the phenyl carbon species and the C_N species next to the nitrogen atoms, respectively. [261, 263, A4]

Furthermore, the C K–NEXAFS spectrum in Fig. 5.6 (d) can be reproduced well by a linear combination of the spectrum of the PTCDA/Ag(111) monolayer film from Fig. 5.6 (c) and the multilayer spectrum from Fig. 5.6 (a). This indicates that the interaction between the SnPc layer and the PTCDA/Ag(111) monolayer film is comparable to the intermolecular interaction in the SnPc multilayer film and consequently considerably weaker than the adsorbate–substrate interaction in case of the SnPc/Ag(111) monolayer film. This is discussed in more detail in [226, A6, A7]. Moreover, the differences in the absorption spectra between the PTCDA and the SnPc contribution allow to associate photon energy dependent changes in the autoionization spectra with the corresponding monolayer.

5.2.2 SnPc/Ag(111) multilayer film

The photon energy dependence of the autoionization spectra of the SnPc multilayer film for p–polarized light is depicted in the surface plot in Fig. 5.8. Note, that such spectral maps are carefully normalized in order to be able to compare the intensities of the various signals as described in *section 2.2.3*. The inset shows the surface plot

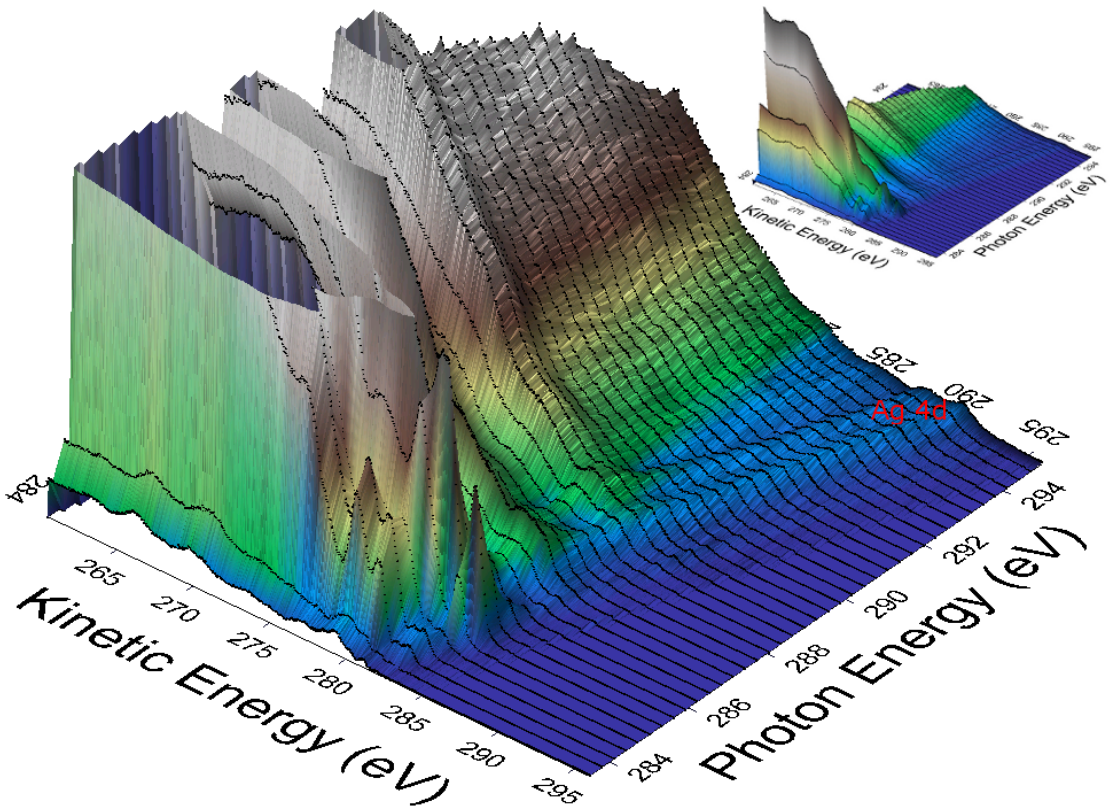

Figure 5.8: (Color online) Surface plot for a series of autoionization spectra of a SnPc/Ag(111) multilayer film with ca. 12 ML thickness for different photon energies. The inset depicts the surface plot on the total intensity scale, whereas it is four times expanded for the enlarged image. The black lines correspond to the actual data points. Note that the intensity of the dominant contribution to the CIS signal, which originates from the Ag 4d substrate states, is very small compared to the maximum of the autoionization signal.

on the total intensity scale whereas it is four times expanded for the large image. The autoionization signal is broad in the kinetic energy direction and increases towards lower kinetic energies, comparable to the typical KVV for such organic molecules. [184] Moreover, some comparatively narrow and distinct features can be observed in Fig. 5.8 between 284 eV and 286 eV photon energy. The sharp peak at hν = 285.3 eV and E_{kin} = 283.8 eV is due to resonant enhancement of the CIS signal from the SnPc HOMO. As its intensity is two orders of magnitude higher than the CIS signal from the SnPc HOMO off resonance the Fano parameter q is larger than 20 with respect to Fig. 5.1 where it is shown that the peak maximum is only 50 times as high as the signal off resonance for $q = 20$. Hence, interference effects between the direct photoemission and the Auger signal can be neglected. The EDCs can therefore be considered as a superposition of the direct photoemission contribution and the Auger–like autoionization signal. The peaks at lower kinetic energy are superposed by the CIS signal from the Ag 4d substrate bands which however is comparatively weak due to Franck–van der Merwe growth and a layer thickness of ca. 12 ML.

The energy position of the different features in the autoionization spectrum can be better identified on the right hand side of Fig. 5.9, where the data from Fig. 5.8 is depicted as 2D intensity plot. On the left hand side of Fig. 5.9 the respective C K–NEXAFS spectrum is indicated additionally. Note, that for kinetic energies lower than 275 eV the autoionization signal reflects the intensity variation in the NEXAFS spectrum well, which is an indication that the PY signal in the NEXAFS measurements, is dominated by the signal for kinetic energies lower than 275 eV kinetic energy. For higher kinetic energies intense spots are observed in the 2D intensity plot which coincide with the CIS signal of the SnPc HOMO, HOMO-1 and lower molecular orbitals. Therefore, these features can be attributed to participant decay. Moreover, they are most prominent for the lower NEXAFS resonances, particularly for excitations at hν = 284.4 eV and 285.3 eV, which correspond to transitions into the LEMO. Furthermore, it seems that for higher excited states participant decay contributes less to the autoionization signal. This could be interpreted as a hint that the autoionization signal resembles more and more the regular Auger signal with increasing photon energy. Certain selected autoionization spectra (A – G) are investigated in more detail in Figs. 5.10 and 5.11 in order to study this aspect in more detail.

The autoionization signals (grey) in Fig. 5.10 are obtained by subtracting the CIS contribution from the respective EDCs, which was recorded separately with hν = 280.5 eV and consequently with a photon energy far below the energies where autoionization plays a role. Before subtracting the CIS contribution the EDCs are normalized to the Sn 4d CIS contribution at E_B = 25 eV, which turned out to be consistent with the normalization of the series of EDCs in Fig. 5.8 and 5.9. The signal of the Ag 4d bands changes with photon energy due to energy dis-

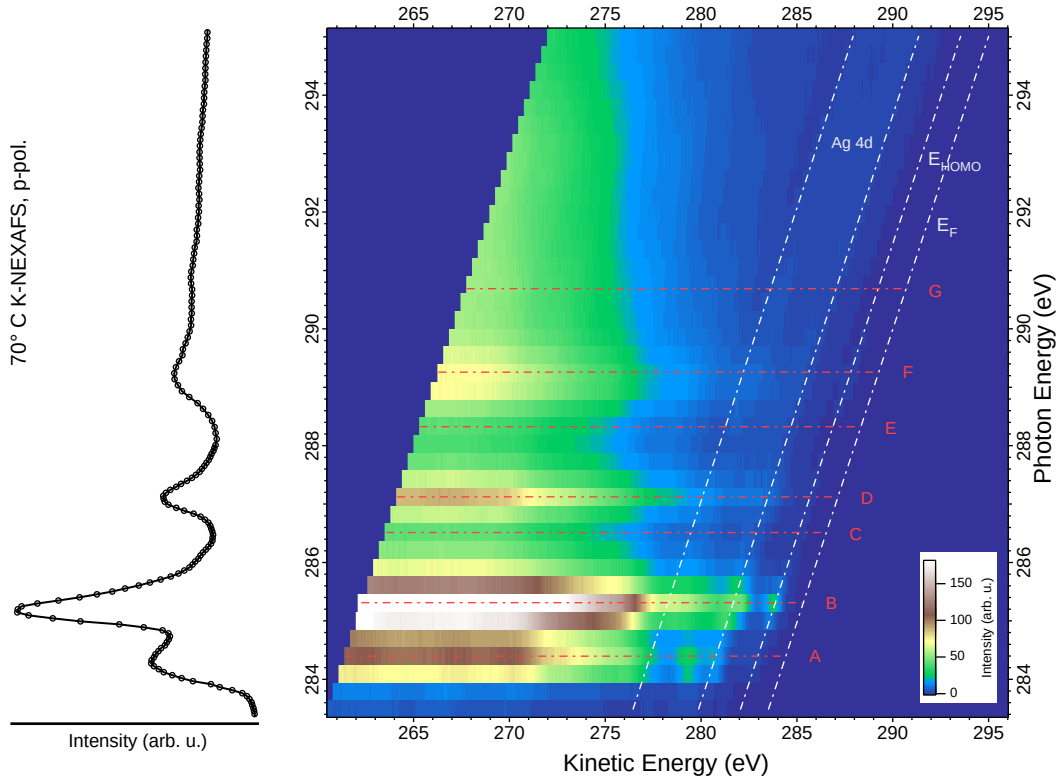

Figure 5.9: (Color online) Photon energy dependence of the autoionization spectra at the C K–absorption edge for a SnPc/Ag(111) multilayer film recorded at 70° angle of incidence with respect to the surface normal and p–polarized light. The diagonal lines mark the energy position of some CIS contributions, namely the Fermi level (E_F), the Ag 4d contribution of the substrate, and the SnPc HOMO (E_{HOMO}) of the adsorbate layer. The horizontal lines (A – H) indicate the autoionization spectra which are further evaluated in Fig. 5.10. Additionally, the corresponding C K–NEXAFS spectrum is shown on the left hand side for better orientation.

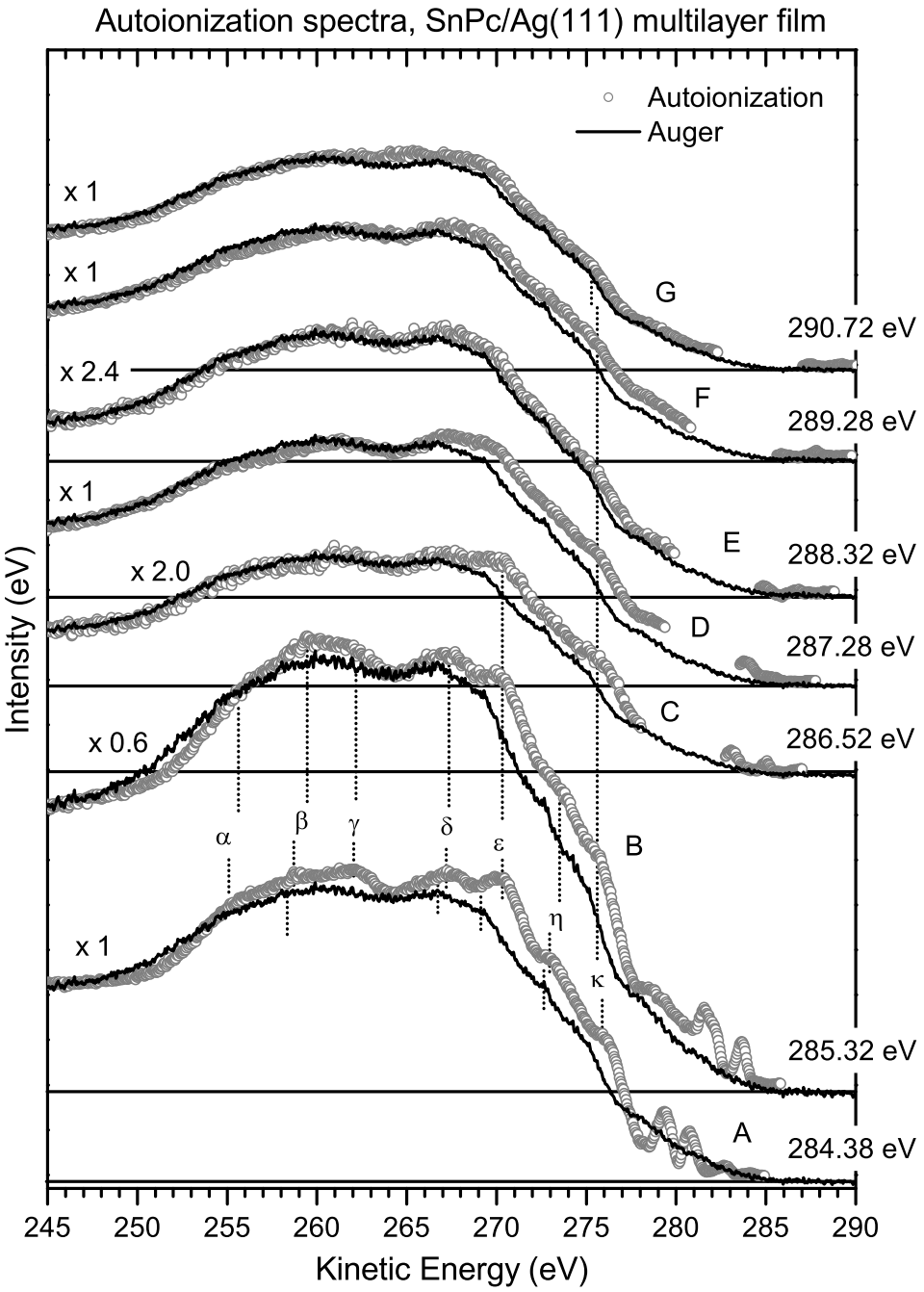

Figure 5.10: C K–autoionization spectra of a SnPc/Ag(111) multilayer film for the photon energies indicated in Fig. 5.9. The autoionization spectra are obtained from the EDCs by subtracting the PES contribution, which was recorded separately with hν = 280.5 eV. Additionally the regular Auger signal, which was recorded at hν = 320.04 eV, is plotted above each autoionization spectrum for better comparison.

persion, and therefore it cannot be subtracted properly. Therefore, the respective part of the spectrum where the Ag 4d signal contributes significantly is cut out in Fig. 5.10, so that the grey curves do not show any bias from the data processing.

The comparison of the autoionization signal (grey) with the regular Auger signal for hν = 320 eV (black) indicates significant differences for the EDCs A – D, whereas the curves E – F, which were recorded at photon energies close to the absorption edge, are similar to the regular Auger signal. Particularly the autoionization spectra for hν = 284.4 eV (A) and 285.3 eV (B) develop a distinct fine structure. The total spectral weight of A and B is shifted ca. 1 eV to higher kinetic energy compared to the regular Auger signal. Moreover, it appears as if the distinct peaks and shoulders $\alpha - \eta$ in the autoionization spectra A and B have a less distinct pendant in the regular Auger signal. Hence, these contributions can be associated with spectator decay or $2h1e$ final states with two valence holes and an additional electron being located in a previously unoccupied orbital. Accordingly, the shift of these features to higher kinetic energy in the autoionization spectrum with respect to the regular Auger signal can be attributed to the spectator electron.

Furthermore, one finds differential spectator shifts and variations in the relative intensity of the different contributions when comparing the features $\alpha - \eta$ between the autoionization spectrum A and the regular Auger signal as well as when comparing the spectra A and B to each other. For spectrum A, for example, the maximum of the features $\alpha - \kappa$ are located at E_{kin} = 255.1 eV, 258.7 eV, 262.0 eV, 267.2 eV, 270.4 eV, 273.0 eV and 275.9 eV, whereas for spectrum B these features are located at E_{kin} = 255.7 eV, 259.5 eV, 262.2 eV, 267.3 eV, 270.3 eV, 273.6 eV and 275.7 eV and for the regular Auger signal they are located at 254.5 eV (α), 258.3 eV (β), 266.7 eV (δ), 269.2 eV (ε), 272.6 eV (η) and 275.3 eV (κ). Consequently, different decay channels are altered differently by the spectator electron, depending on the symmetry of the wave functions of the core excited state and the final state. This is analogous to the findings for the NEXAFS investigation of the polyacene molecules, where the energy lowering of the $1h1e$ core excited state due to an additional electron in the LEMO can be different with respect to the core ionized state, depending on where the core hole site is located.

For the analysis of the participant contributions to the autoionization spectra the EDCs of interest are plotted in Fig. 5.11 as black curves over the binding energy scale for better comparison with the CIS signal (grey). The data was recorded in the fixed mode of the electron analyser, where the kinetic energy of the photoelectrons is not swept but only a certain range of their energy distribution is directly imaged on the CCD camera of the analyser. The raw data is divided by the detector response function in order to account for the spatial dependence of the detector sensitivity, as described in *section 2.2.4*. Moreover, the respective spectra

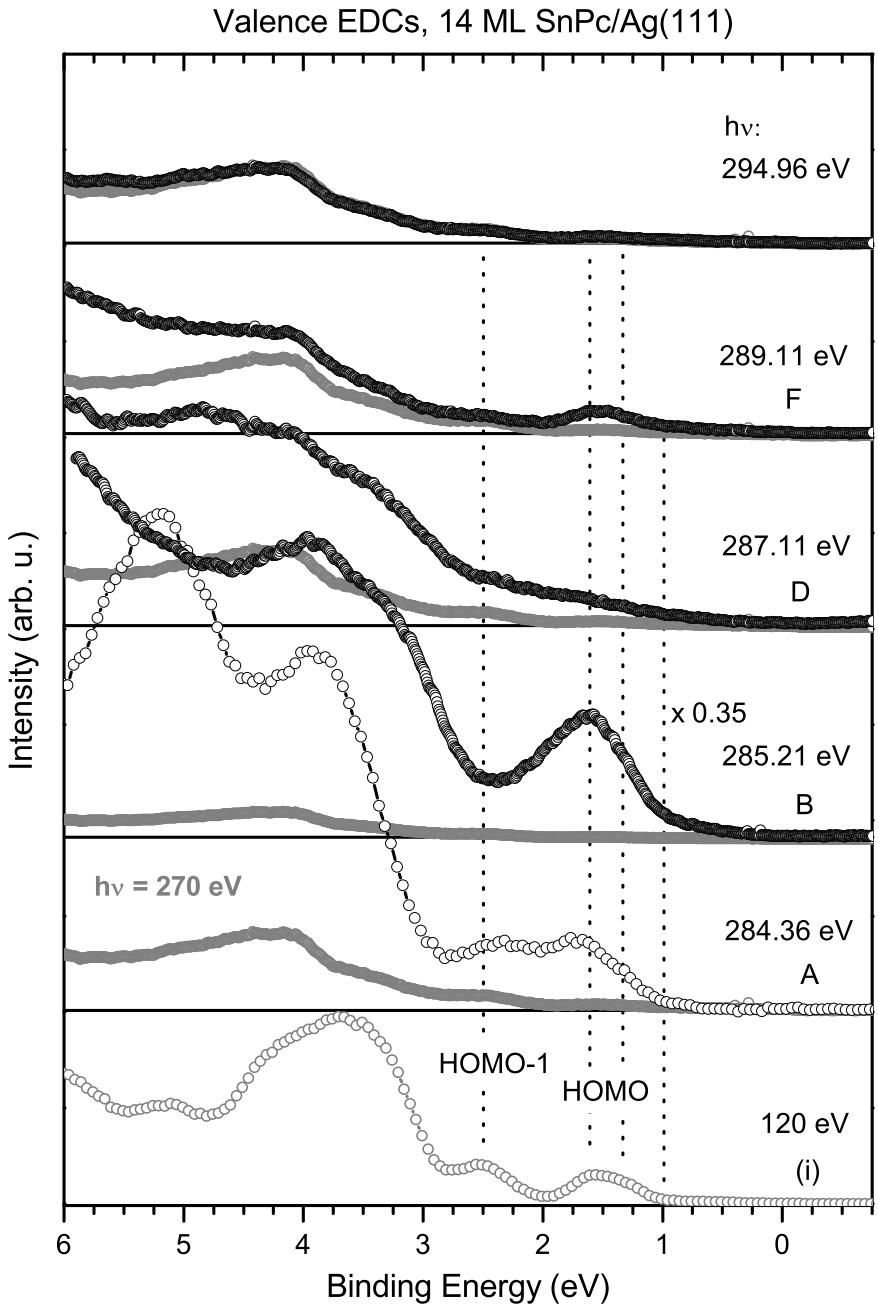

Figure 5.11: Comparison of valence EDCs for a SnPc/Ag(111) multilayer film for the photon energies indicated in Fig. 5.9. The EDCs for photon energies higher than 284 eV (black) are plotted over the photoelectron spectra recorded at hν = 270 eV (grey) for better comparison. The photoelectron spectrum (i) for hν = 120 eV is depicted at the bottom.

are normalized to the EDCs from Fig. 5.8 and 5.9 in order to be able to compare the absolute intensities. The contributions of the delocalized molecular valence states can hardly be identified in the EDC for hν = 270 eV because the photoemission matrix element is low for such energies. Therefore the valence spectrum (i), which was recorded with 120 eV photon energy, is provided additionally at the bottom of Fig. 5.11.

As for binding energies larger than 3 eV a continuum of molecular states contributes to the PES signal (i) it is difficult to assign the respective autoionization signal to a particular final state. However, the signal from the HOMO at E_B = 1.5 eV and the HOMO-1 at E_B = 2.5 eV can be well distinguished. Note the comparatively large peak width and the asymmetry of the HOMO signal in (i). Its signature might be an indication for an increase in surface roughness for coverages higher than 10 ML, because a well defined double peak signature is observed (E_B = 1.4 eV and 1.7 eV) for a SnPc coverage below 10 ML due to the formation of dimers and a bonding–antibonding scenario. [A4] Comparing the autoionization spectra A – F one finds that in A and B the signals from the HOMO and the HOMO-1 are strongly increased compared to the direct photoemission signal for hν = 270 eV and 294.96 eV. The additional intensity can be attributed explicitly to the participant autoionization channel considering that interference effects between the direct photoemission signal and the autoionization signal can be neglected with respect to the discussion at the beginning of this section and in *section 5.1*. Moreover in spectrum A both peaks, the HOMO and the HOMO-1 signal, are of similar intensity, where the HOMO contribution is considerably larger in spectrum B. Taking into account that for 284.36 eV photon energy C_C $1s$ $\rightarrow$ LEMO transitions at the carbon rings are induced and that for hν = 285.21 eV C_N $1s$ $\rightarrow$ LEMO transitions at the carbon species next to the nitrogen atoms are dominant, one can assume to first order with respect to the Coulomb term in (5.9) that for the excitation at the C_N species the HOMO wave function is more localized at the core hole than the HOMO-1 wave function. Moreover, for excitations at the C_C species both, the HOMO and the HOMO-1, seem to be similarly localized at the core hole site.

Furthermore, for higher core excited states, e.g. those associated with the spectra D and F, the relative intensities of the respective participant channels decrease. For example for spectrum F the intensity of the participant channel associated with the HOMO is more than 10 times lower than in spectrum B, whereas the total intensity of the autoionization signal is only reduced by a factor of 2. Accordingly, the Auger matrix element and consequently the Coulomb interaction between the excited electron and those in the HOMO decreases for higher core excited states. Moreover, the autoionization signal between E_B = 3 eV and 4 eV in the spectra A, B and D can also be associated with participant decay and $1h$ final states, respectively, which are related to lower lying molecular orbitals. If these signals corresponded

to spectator decay and $2h1e$ final states, respectively, the respective contributions would not be located at the same binding energy in all three spectra but they would be shifted to 2.75 eV higher binding energy in spectrum D. Moreover, the participant signal related to lower lying orbitals is in D significantly stronger than in F, while the overall HOMO intensity between $E_B = 1.0$ eV and 1.8 eV is comparable. This illustrates that the intensity for the respective decay channels depends on the localization of the core hole site and the symmetry of the wave function of the core excited and the final state, respectively.

Furthermore, one finds significant differences between the autoionization signal and the direct PES spectrum (i) when considering the signature of the participant contributions in Fig. 5.11. In spectrum B, for example, the participant signal at $E_B = 1.6$ eV, which is related to the SnPc HOMO, is significantly broader than the respective photoemission signal for $h\nu = 120$ eV. Particularly the trailing edge extends to higher binding energy above $E_B = 2.0$ eV. Moreover, the autoionization signal in spectrum A does also not drop to zero at $E_B = 2.0$ eV as it is expected with respect to spectrum (i). Monitoring the respective participant signal when tuning the photon energy through the respective NEXAFS resonance can provide further insight into this effect.

Fig. 5.12 shows the $h\nu$–dependence of the EDCs of the upper valence regime when tuning the photon energy form 283.50 eV to 285.62 eV in 0.3 eV steps. Note that these EDCs are plotted over the kinetic energy scale, so that the CIS contributions shift linearly with photon energy. The participant signal at $E_{kin} = 283.8$ eV in spectrum (g), which is related to the SnPc HOMO, can be identified clearly, as well as feature γ, which is probably due to a participant signal related to the states between 3 eV and 4 eV binding energy. One finds significant differences in the peak shape of the HOMO signal between the spectra (e) – (h) when tuning the photon energy through the peak B of the C K–NEXAFS spectrum in Fig. 5.6 (a). In spectrum (e) the HOMO is only little enhanced with its maximum being located at $E_{kin} = 283.2$ eV, while in spectrum (f) the autoionization signal is significantly higher and the peak is shifted 0.3 eV to $E_{kin} = 283.5$ eV as it is expected for a participant signal. Moreover, a weak shoulder can be observed at the tail to higher kinetic energies, where for the spectrum (g) the low energy tail is considerably broadened. In (h) the maximum of the HOMO peak is located at $E_{kin} = 284.1$ eV with a relatively intense shoulder at 283.3 eV, so that the low energy edge of the respective signal is located at similar kinetic energy in all spectra (e) – (h). Consequently, the participant signal related to the HOMO has at least two contributions, one with a pseudo CFS character and another one with a CIS behavior. The latter becomes evident from the inset where the spectra of interest are plotted over the binding energy scale. The situation seems to be similar for the spectra (a) to (e) where the autoionization signal does not drop to zero in between the CIS contributions from the HOMO and the HOMO-1.

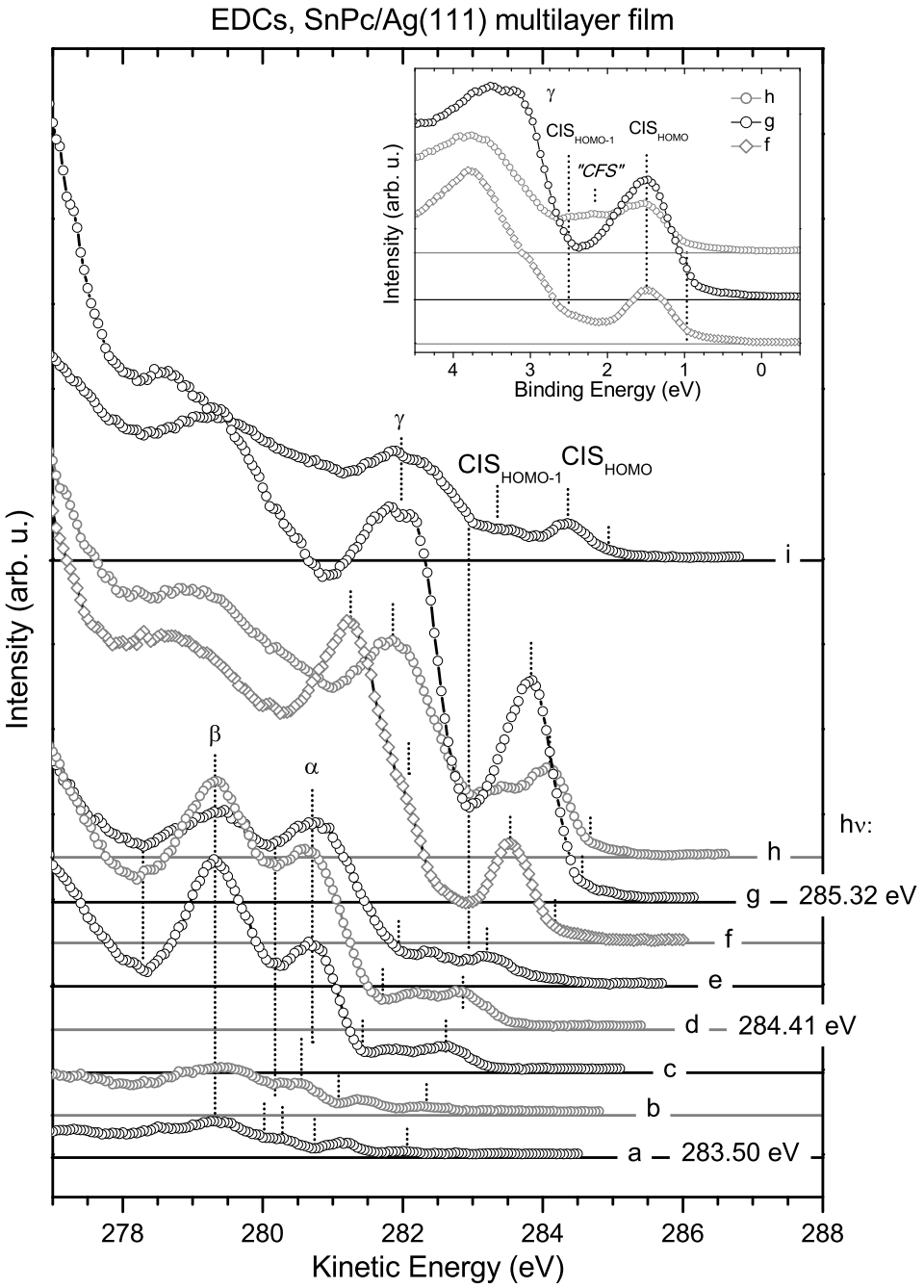

Figure 5.12: Comparison of the EDCs of the upper valence regime of a SnPc/Ag(111) multilayer film for photon energies corresponding to the first and the second peak in the C K–NEXAFS spectrum, which has been shown in Fig. 5.6 (a). The excitation energy is tuned from hν = 283.50 eV to 285.62 eV in 0.3 eV steps. The EDCs (f – h) are plotted in the inset on a binding energy scale.

This finding can be interpreted as indication for electron–vibration coupling with respect to the discussion in section 5.1.3. The same trend was found for the elastic peak in the RIXS spectra of N_2, ethylene, benzene and C_{60}. [198, 256, 264, 265] Namely a shoulder develops at the low–energy tail of the elastic peak for photon energies corresponding to the low–energy tail of the peak in the absorption spectrum which is related to resonant excitation into the unoccupied π^* orbitals. This shoulder can appear at constant emission energy, when hν is tuned through the resonance to higher photon energies. It could be explicitly shown that this pseudo CFS behavior can be explained by variation of the of the duration of the scattering process τ_c with respect to the time scale for the propagation of the electro–vibronic wave packet τ_{wp} in analogy to the discussion in *section 5.1.3*. [198, 256]

The photon energy dependent variation of the participant signal which is related to the SnPc HOMO can be explained along the same line of arguments. In the time–dependent picture introduced in *section 5.1.3* large detuning of the photon energy into the Raman regime corresponds to short duration τ_c of the x–ray scattering process in contrast to resonant excitation. If τ_c is short compared to τ_{wp}, which is the case in the Raman regime, the vibronic fine structure of the autoionization signal will resemble that of the direct photoemission signal. τ_c increases when tuning the photon energy into the NEXAFS resonance, and the propagation of the electro–vibronic wave packet modifies the vibronic fine structure of the autoionization signal compared to the direct photoemission signal. Exactly this behaviour is observed for the signal of the SnPc HOMO in Fig. 5.12. This effect can analogously be explained in the energy–dependent approach, which has also been discussed in *section 5.1.3*.

A similar behavior can also be found for the signals α and β in the spectra (a) – (e) for photon energies corresponding to peak A of the C K–NEXAFS spectrum in Fig. 5.6 (a). In particular the maximum of the peak β is located at constant kinetic energy in all of these spectra, namely at E_{kin} = 279.3 eV. Moreover, in spectrum (a) the peak α is centered at E_{kin} = 280.2 eV and in (b) at E_{kin} = 280.5 eV, as it is expected for a CIS signal. However, in each spectrum (c) – (e) the maximum of the peak α is located at E_{kin} = 280.7 eV, whereas the leading edge shifts to higher kinetic energies so that this contribution can be attributed to a CIS signal. Accordingly the trend for the signal α and β in the spectra (a) – (e) is analogous to what is observed for the HOMO related participant signal in the spectra (e) – (h), but for α and β the pseudo CFS contribution is considerably higher than the CIS contribution. This suggests that for these electronic transitions interference effects might be weaker than for the HOMO participant signal.

5.2.3 Adsorbate–substrate coupling — 1 ML SnPc/Ag(111)

The SnPc/Ag(111) interface is studied in the following by investigating a SnPc monolayer film. Moreover, it has been shown in *section 5.2.1* that many–body excitations involving substrate–adsorbate charge transfer contribute significantly to the core level and NEXAFS spectra of the SnPc/Ag(111) monolayer film. The data suggests that these effects are comparable to what has been discussed for the PTCDA/Ag(111) and the PTCDI/Ag(111) monolayer films in *chapter 4*. Consequently it is expected that these effects are also important for the Auger and the autoionization signal.

In Fig. 5.13 a surface plot is shown of a series of EDCs of a 1 ML SnPc/Ag(111) film for different photon energies close to the C K absorption edge with p–polarized light. The data is carefully normalized according to the description in *section 2.2.3*. The Ag 4d CIS signal dominates the spectra at first glance due to the high photoemission cross section of these states at such photon energies, and the Fermi edge can be observed at a few eV higher kinetic energy. Despite the intense Ag 4d contribution the autoionization signal from the adsorbate layer can be clearly identified on top of the contributions from the sp valence bands of the substrate. A broad and relatively intense autoionization signal is observed for h$\nu \sim$ 285 eV for example, which extends up to the Fermi level. Moreover, a weak CFS signal with a double peak signature contributes at the change over between the greenish and blue area at 280 eV kinetic energy. As these features have not been observed for the multilayer film they are a significant indications for a comparatively strong adsorbate–substrate coupling.

A 2D intensity plot of the data from Fig. 5.13 is shown in Fig. 5.14, where the maximum of the color scale is set to 25% of the highest signal in order to improve the contrast in the regions of interest. The autoionization signal reflects the intensity variation of the C K–NEXAFS spectrum on the left hand side well for kinetic energies below 275 eV, analogous to the finding for the multilayer film. Furthermore, the CFS contribution at E_{kin} = 279.1 eV and 280.3 eV becomes evident in this plot as well. Moreover, the autoionization signal contributes considerably to the intensity at kinetic energies between the Ag 4d signal and the Fermi level in the EDCs A and B, which were recorded at photon energies corresponding to the maxima positions of the peaks *A* and *B* of the C K–NEXAFS spectrum in Fig. 5.7 (b). Whereas for the EDC C the autoionization seems to contribute only little to the signal at E_{kin} = 284 eV, and no significant contribution to the upper valence signal is observed for the EDCs D and E.

In Fig. 5.15 the regular Auger signal and the autoionization spectra A – E are depicted for the photon energies corresponding to the maxima of the C K–NEXAFS signal as indicated in Fig. 5.14. These EDCs were recorded separately for a wider

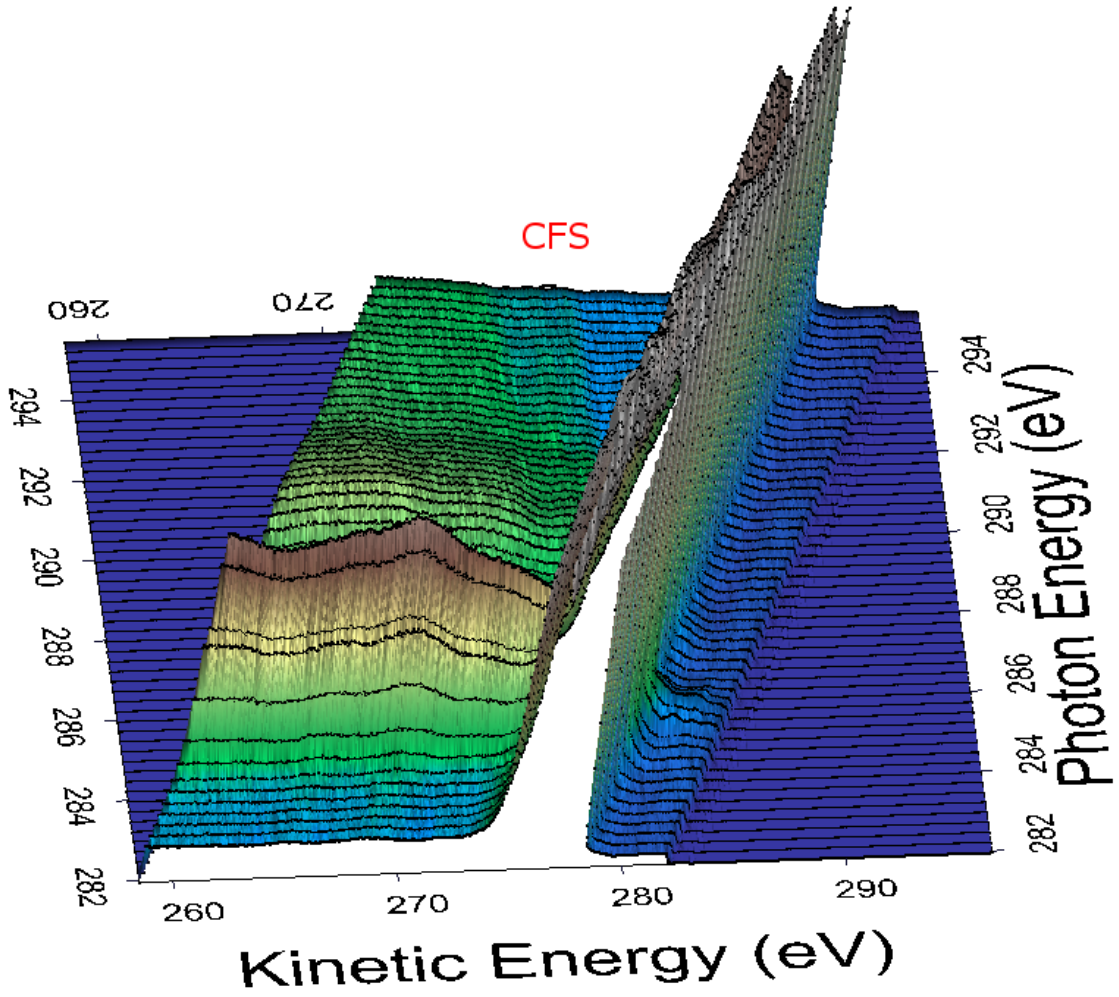

Figure 5.13: (Color online) Surface plot of a series of EDCs of a 1 ML SnPc/Ag(111) film for different photon energies, recorded at 70° angle of incidence with respect to the surface normal and p–polarized light. Note that the dominant CIS signal originates from the Ag 4d states of the substrate. Moreover, two CFS contributions appear at E_{kin} = 279.1 eV and 280.3 eV, which have not been observed in the multilayer data.

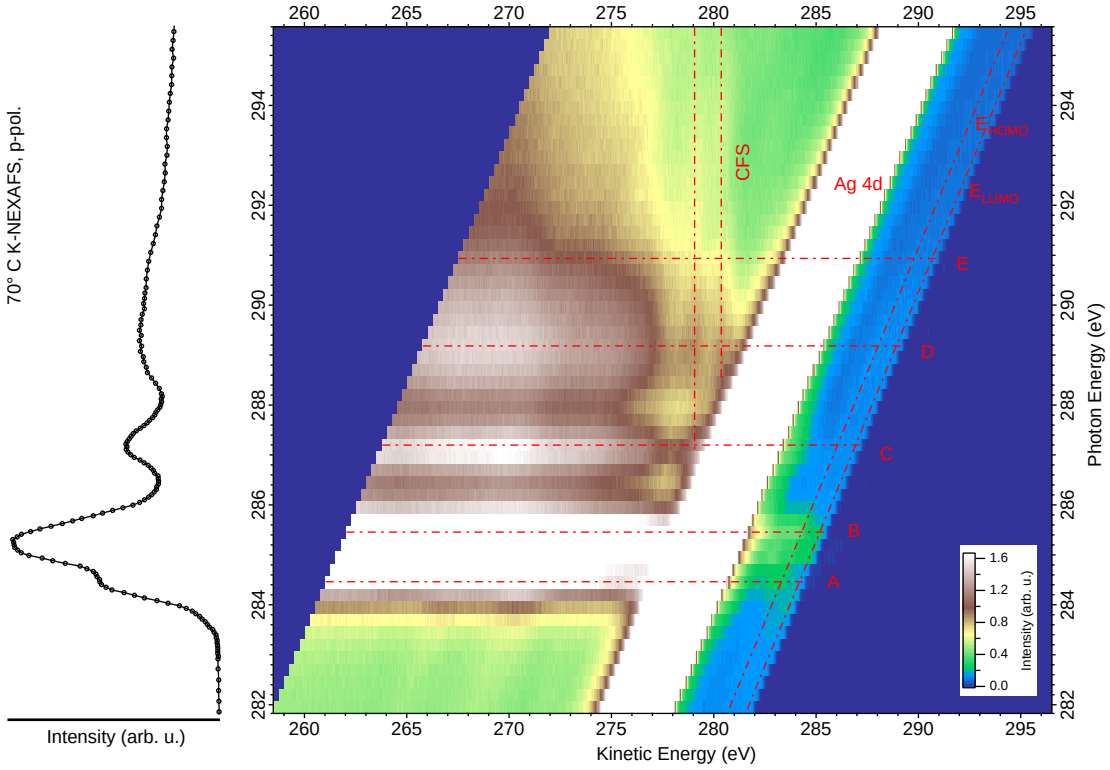

Figure 5.14: (Color online) Photon energy dependence of the EDCs of a 1 ML SnPc/Ag(111) film, recorded at the C K–absorption edge with 70° angle of incidence with respect to the surface normal and p–polarized light. The maximum of the color scale corresponds to 25% of the highest signal intensity. The diagonal lines mark the CIS contributions in particular the relative intense Ag 4d signal from the substrate as well as the signal of the SnPc HOMO (E_{HOMO}) and LUMO (E_{LUMO}). The vertical lines indicate CFS contributions to the signal at E_{kin} = 279.1 eV and 280.3 eV, which are absent in the multilayer spectrum. The horizontal lines (A – F) indicate the EDCs which are further evaluated in Figs. 5.15 and 5.16. Additionally, the corresponding C K–NEXAFS spectrum is shown on the left hand side for better orientation.

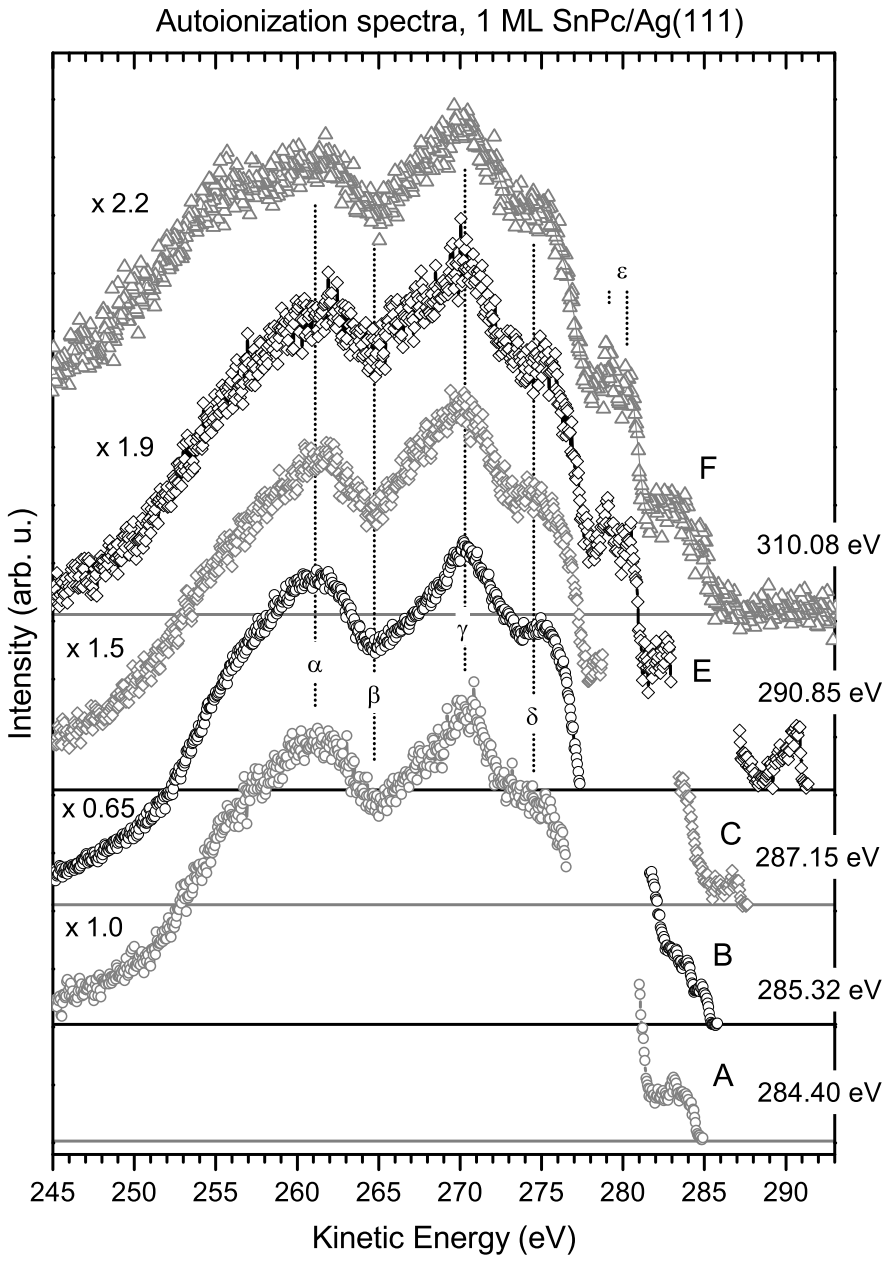

Figure 5.15: C K–autoionization spectra of a 1 ML SnPc/Ag(111) film for the photon energies indicated in Fig. 5.9. The curves were obtained by subtracting the PES contribution from the EDCs, which was recorded separately with $h\nu = 280.08$ eV. Additionally, the regular Auger signal (F) for $h\nu = 310.08$ eV is shown.

kinetic energy range than those in Fig. 5.14. These spectra were normalized to the Sn 4d signal, and the CIS signal for hν = 280 eV was subtracted. This comparison shows that all spectra are nearly identical for kinetic energies below 280 eV, even the autoionization signal and the regular Auger spectrum. Particularly the energy positions and the relative intensities of the features $\alpha - \varepsilon$ at E_{kin} = 261.1 eV, 264.2 eV, 270.3 eV, 274.6 eV, 279.1 eV and 280.3 eV are very similar for all spectra in contrast to what has been found for the SnPc/Ag(111) multilayer film, where significant differences have been observed between the various autoionization spectra as well as between the autoionization spectra and the regular Auger signal due to the spectator electron. Consequently, the similarity between the different autoionization spectra of the monolayer film is a further indication for a comparatively strong adsorbate–substrate coupling.

Furthermore, indications for many–body excitations and substrate–adsorbate charge transfer have been pointed out in *section 5.2.1* with respect to the C K–NEXAFS and the core level spectra of the SnPc/Ag(111) monolayer film. It has been demonstrated in *section 4.1.2* and *4.4.1* with respect to Fig. 4.4 that a direct transition of a core electron into the unoccupied density of adsorbate–substrate states can result in the same core excited states as direct photoemission of the core electron because of substrate–adsorbate charge transfer. Only the cross section for the respective transitions may be different. Therefore, the same continuum of core excited states can be expected in case of strong adsorbate–substrate coupling for both, direct photoemission of the core electron and a direct transition of the core electron into the unoccupied DOS, except for different cross sections or spectral weight of the different core excited states. In particular in the simple model which is schematically depicted in Fig. 4.4 only two core excited states Ψ_l and Ψ_m contribute to the photoelectron spectrum and the NEXAFS spectrum, respectively. In case of strong substrate–adsorbate coupling both contributions I_s and I_m are of similar intensity. If the energy separation W is similar or even smaller than the life time broadening of these peaks both states Ψ_l and Ψ_m have to be considered in the sum of relation (5.10). This may lead to interference effects between transition amplitudes as it has been discussed in *section 5.1*. It is straightforward from Fig. 4.4 that these effects are similar for direct photoemission of the core electron and for a direct transition of the core electron into the unoccupied density of adsorbate–substrate states. As a consequence the various autoionization spectra and the regular Auger spectrum are similar. Exactly this is observed for the autoionization spectra of the SnPc/Ag(111) monolayer film in Fig. 5.15. Consequently, the similarity between the different autoionization spectra and the regular Auger spectrum in Fig. 5.15 is a strong indication for many–body excitations involving substrate–adsorbate charge transfer.

Moreover, the double peak signature of the CFS contribution ε at E_{kin} = 279.1 eV and 280.3 eV is clearly observed in the autoionization spectrum E and it can be

assumed, that this signal also contributes to the autoionization spectra A–C. As this contribution is absent for the SnPc multilayer film it is likely that it is related to the (partial) occupation of the LUMO derived DOS. This is supported by the energy splitting of 1.2 eV between the two peaks which is compatible with the energy splitting between the maxima of the C_C 1s and the C_N 1s contributions to the C 1s core level spectrum in Fig. 5.7 and [A4], which are located at E_B = 284.32 eV and 285.45 eV, respectively. Accordingly, the peak in the autoionization curve at E_{kin} = 280.3 eV might result from an Auger decay of a C_N 1s core hole state into a 2h final state where an electron from the Fermi level fills the C_N 1s core hole and emits another electron from a lower lying orbital at E_B = 5.1 eV. Then the second peak at E_{kin} = 279.1 eV would be due to the decay of the C_C 1s core hole state into the same final state. In a simplified illustration one can compare this scenario to the situation in Fig. 5.5 (c). Consequently, the appearance of the double peak signature ε in all autoionization spectra and regular Auger spectra at the C K absorption edge is an additional manifestation of the many–body character of the core excitation, which involves substrate–adsorbate charge transfer, in analogy to the discussion above.

The EDCs of the SnPc/Ag(111) monolayer film to which the autoionization contributes significantly are plotted in Fig. 5.16 (black curves) over the photoelectron spectra at hν = 270 eV and 120 eV (grey curves). In spectrum (i) several spectral features of the adsorbate layer can be identified, which lie on top of the signal from the substrate sp–bands, namely the LUMO related density of adsorbate–substrate states at E_B = 0.3 eV, which is cut by the Fermi level and hence partially occupied, the signal from the HOMO at E_B = 1.3 eV and contributions from several adsorbate states around 3 eV. [A4] Comparing the various EDCs one finds that for all spectra A – D the CIS signal related to the HOMO and the LUMO is more or less enhanced. In curve A, for example, which was recorded at a photon energy corresponding to C_C 1s $\rightarrow$ LEMO transitions at the phenyl rings, the HOMO is strongly enhanced, whereas the LUMO signal is only little increased. Moreover, the autoionization signal contributes continuously from E_B = 1.0 eV to higher binding energies, so that the signature of this autoionization signal does not reflect that of the HOMO signal in spectrum (i) but suggests an intense, several eV broad tail at the high energy side of the HOMO peak. Furthermore, in spectrum B both the LUMO and the HOMO contributions are strongly enhanced by the autoionization. And again their spectral signature does not reflect that of spectrum (i) but it seems as if a several eV broad high energy tail is associated to each peak. Note, that for the EDCs C and D the autoionization signal contributes considerably less to the HOMO and the LUMO signal than in B. This is similar to what is observed for the multilayer film, where the cross section for the respective participant decay channels decreases with increasing excitation energy. Moreover, in C and D the spectral signature of the autoionization signal resembles the signature observed in the curve (i) better and

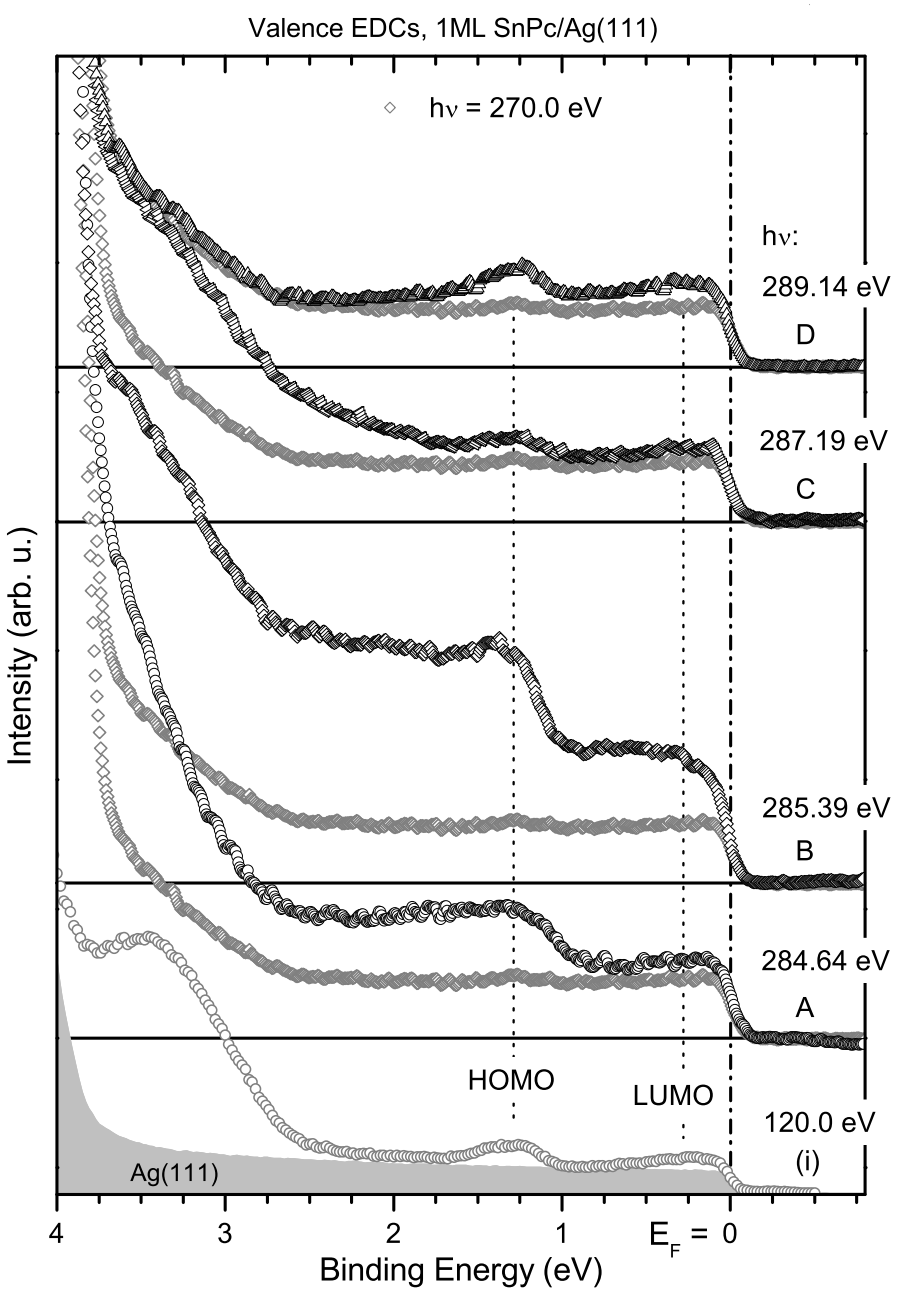

Figure 5.16: Comparison of the valence EDCs of a 1 ML SnPc/Ag(111) film recorded at the photon energies indicated in Fig. 5.14. The EDCs of photon energies higher than 284 eV (black) are plotted above the photoelectron spectra recorded at hν = 270 eV and 120 eV (grey) for better comparison. The angle integrated valence spectrum of the clean Ag(111) surface for hν = 120 eV is indicated by the grey area.

the contributions from the high energy tail appear to be smaller. Consequently, the continuous autoionization signal dominates in particular for photon energies corresponding to the first two peaks *A* and *B* in the C K–NEXAFS spectrum from Fig. 5.6 (b), which has been attributed to transitions of core electrons into the density of unoccupied adsorbate–substrate states at the Fermi level. This agrees with the scenario discussed with respect to Fig. 5.5 (d), namely that the charge transfer satellites are expected to contribute significantly to the autoionization signal. A detailed investigation of the photon energy dependence of the autoionization signal when tuning hν through these NEXAFS resonances can provide further information about this high energy tail.

Fig. 5.17 shows the EDCs of the upper valence regime when tuning the photon energy in 0.25 eV steps through the first two peaks *A* and *B* of the C K–NEXAFS spectrum in Fig. 5.6 (b). Note that these EDCs are plotted over the kinetic energy scale, so that the CIS contributions shift linearly with photon energy. The first three spectra are nearly identical and therefore these signals can be (explicitly) attributed to the direct photoemission contribution. However, one can observe significant changes in the EDCs from spectrum (a) to (j) which must be due to autoionization. In all these spectra the HOMO and the LUMO peaks are more or less enhanced, particularly in the EDCs (e) and (f), which are recorded with photon energies close that of the maximum of the C K–NEXAFS signal. A comparison between (e) and (f) shows, that the signature of (f) is very different to that of (e). In (e), for example, one can clearly identify three maxima at E_{kin} = 284.68 eV, 283.92 eV and 283.10 eV, whereas in (f) the signal increases continuously from the Fermi edge to lower kinetic energies with a step like increase at E_{kin} = 284.15 eV, comparable to the signature of spectrum B in Fig. 5.16. As for the EDC (d) these three peaks are shifted to E_{kin} = 284.48 eV, 283.70 eV and 282.86 eV, so that the difference in their kinetic energy between (d) and (e) is similar to the difference in photon energy, these signals can be assigned to CIS contributions. This is further corroborated by the spectra (a), (b) and (c), where significant contributions of the autoionization signal can be observed at the respective energies. Moreover, the peak in (d) at E_{kin} = 284.48 eV and E_B = 0.50 eV, respectively, can be attributed to the decay of the core excited state into a final state with a hole in the LUMO derived DOS (CIS_{LUMO} in Fig. D.5 in *appendix D*), and the peak at E_{kin} = 283.70 eV and E_B = 1.28 eV, respectively, can be related to the participant decay into final states with a hole in the HOMO (CIS_{HOMO}). Note, that in spectrum (i) in Fig. 5.16 the maximum of the LUMO signal is located at E_B = 0.3 eV and consequently at 0.2 eV lower binding energy than in the autoionization spectra. A plot of the valence EDCs over the binding energy scale in Fig. D.5 in *appendix D* illustrates the CIS character of these features even better. Furthermore, Fig. D.5 indicates that the autoionization signal contributes in all spectra (a) to (j) at E_B = 2.1 eV and 0.5 eV. Additionally, these contributions are particularly intense at photon

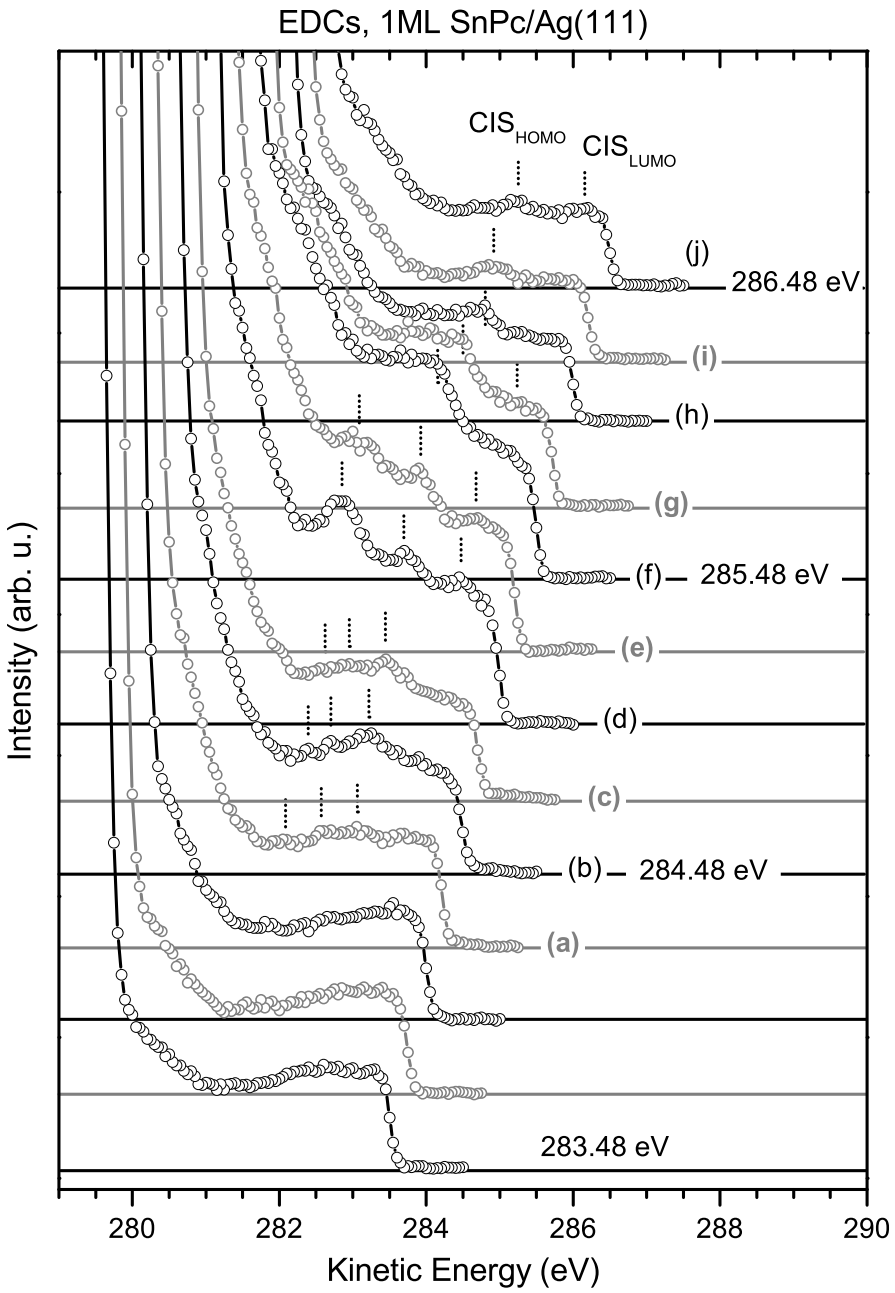

Figure 5.17: Comparison of various valence EDCs of a 1 ML SnPc/Ag(111) film when tuning the photon energy in 0.25 eV steps through the first two peaks *A* and *B* of the C K–NEXAFS spectrum in Fig. 5.6 (b). The spectra are the same as those shown in Figs. 5.13 and 5.14.

energies corresponding to the low–energy side of the C K–NEXAFS peaks A and B in Fig. 5.6 (b), respectively. This is in contrast to what has been observed for the electron–vibration coupling in the SnPc multilayer film in *section 5.2.2*, where a shoulder has developed at the high binding energy side of the HOMO peak for increasing photon energy with a pseudo CFS character. Consequently, the CIS contribution to the autoionization signal of the SnPc/Ag(111) monolayer film at E_B = 2.1 eV and 0.5 eV is probably not primarily related to vibronic energy losses.

From this point of view it is straightforward to associate these CIS signals with predominantly electronic energy loss features with respect to the main peak at E_B = 1.28 eV and 0.3 eV. Their signatures are similar to the several eV broad metallic satellite features which have been discussed for the core level spectra of the PTCDI/Ag(111) and PTCDA/Ag(111) monolayer films in section 4.2 and 4.3. Note, that such contributions have been observed in the core level data of the SnPc/Ag(111) monolayer film as well. [A4] Furthermore, it has been shown in chapter 4 that many–body excitations contribute to a continuum of core excited states for strongly coupled adsorbate monolayer films, which are comparable to the SnPc/Ag(111) monolayer film, due to charge transfer satellites. Moreover, it has been demonstrated in section 5.1.6 that interference between transition amplitudes can be expected for the autoionization signal as a consequence, which can lead to asymmetric peak shapes. Note that the relative intensities of the satellites at E_B = 2.1 eV and 0.5 eV are largest for $h\nu$ = 284.98 eV and decrease with increasing photon energy in opposite to the trend for the main peaks at E_B = 1.28 eV and 0.3 eV. This may be related to interference of transition amplitudes.

The autoionization spectra can be understood in the framework of a time–dependent approach in analogy to the discussion of the electron–vibration coupling in *sections 5.1.3* and *5.2.2*, where the propagation of a wave packet was considered within the duration τ_c of the x–ray scattering process. In case of excitations in the Raman regime (detuned photon energy) τ_c is significantly shorter than for resonant excitation. The deformation time of the wave packet τ_{wp} can be related to the effective width Δ_k of the distribution of core excited states, in analogy to the concept of electro–vibronic wave packets in *section 5.1.3* ($\tau_{wp} \sim 1/\Delta_k$). For short τ_c (Raman regime) the wave packet does not propagate within the duration of the scattering event, which means that the electronic structure does not rearrange, in contrast to long τ_c (resonant excitation). Therefore satellites at higher binding energy are particularly increased for excitation energies corresponding to the leading edge of the respective NEXAFS resonances, whereas the well relaxed main peaks are particularly enhanced for resonant excitation.

Note that it is established to deduce the average charge transfer time at a weakly interacting substrate–adsorbate interface from resonant AES data by a simple tun-

neling approach in the single particle picture, where certain spectral features are directly related to a particular electronic configuration after a charge transfer or a non–charge transfer scenario. [183–186] However, this approach is questionable in case of strong adsorbate–substrate coupling because particular spectral features cannot be directly related to particular electronic configurations where charge transfer occurred or not due to many–body excitations. Calculations of the excitation spectra may provide more insight into the excitation process and the adsorbate–substrate charge transfer.

5.2.4 The coupling between the first and the second adsorbate monolayer — SnPc/PTCDA/Ag(111)

A hetero–molecular film is investigated in the following consisting of 1 ML SnPc adsorbed on a 1 ML PTCDA/Ag(111) film in order to study the interaction between the first and the second adsorbate layer. The contribution if this SnPc layer to the C K–NEXAFS spectrum and the photoelectron spectra has an individual signature which can be well distinguished from the signal of the PTCDA interlayer, as discussed in detail in [226, A6, A7]. This is illustrated in Fig. 5.6 and in Fig. 5.21 additionally. Moreover, it has been shown that well defined hetero–molecular films can be prepared with a closed SnPc wetting layer on top of the PTCDA/Ag(111) monolayer film. Furthermore, the interaction at the hetero–molecular interface leads to a rigid shift of 0.4 eV for the SnPc levels with respect to the SnPc/Ag(111) multilayer film. Nevertheless, the signature of the SnPc contribution to the C and N K–NEXAFS spectra in Fig. 5.6 (d) as well as the signature of the SnPc contribution to the core level spectra in [A7] is comparable to the signature of the respective spectra of the SnPc/Ag(111) multilayer film, except for small deviations. Altogether this suggests that the electronic coupling between the first and the second adsorbate layer is considerably weaker as the coupling between the first adsorbate monolayer and the substrate.

Furthermore, it is expected that the PTCDA autoionization signal is driven by many–body effects similar to what was discussed for the SnPc/Ag(111) monolayer film in section 5.2.3 because of the similarities in the NEXAFS and PES data between the SnPc/Ag(111) and the PTCDA monolayer film. For both monolayer films, for example, a partially occupied LUMO derived DOS is observed, considerable chemical shifts are observed in the valence and core level spectra, accompanied by metallic satellite features. For both monolayer films the energy position of the C and N K–NEXAFS onset coincides with that of the respective core level signal, which is a strong indication for many–body excitations involving adsorbate–substrate charge transfer according to the findings in *chapter 4*.

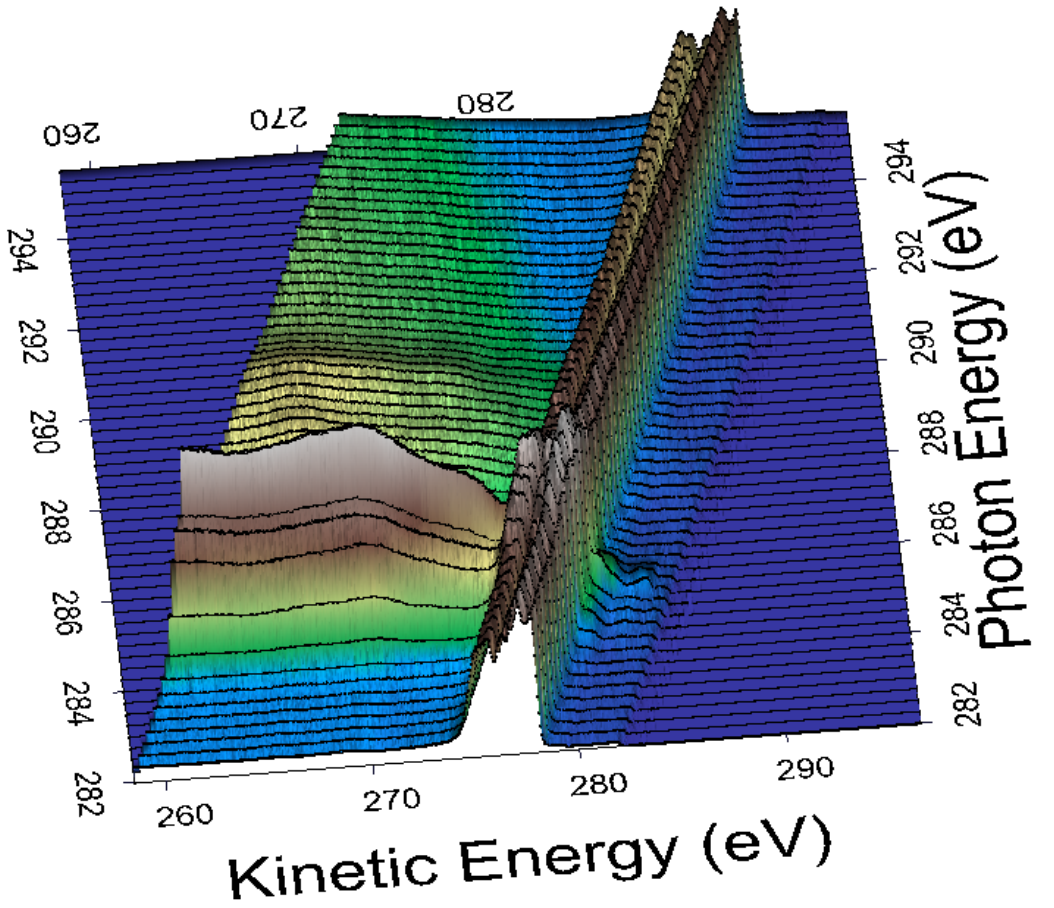

Figure 5.18: (Color online) Surface plot of a series of autoionization spectra of a hetero–molecular film with 1 ML SnPc on top of 1 ML PTCDA/Ag(111), recorded with 70° angle of incidence with respect to the surface normal and p–polarized light. The black lines correspond to the actual data points. Note that the CIS signal of the Ag 4d substrate states dominates the spectrum.

A surface plot of a series of EDCs of the SnPc/PTCDA/Ag(111) film for different photon energies is shown in Fig. 5.18. The data is carefully normalized according to the description in *section 2.2.3*. In this data set the autoionization signal is more intense with respect to the Ag 4d signal from the substrate than for the 1 ML SnPc/Ag(111) film because of the higher adsorbate coverage. However, the Fermi edge of the substrate is still clearly visible. Again the most prominent autoionization feature appears at 285 eV photon energy with significant enhancement of the valence signal in the energy range of the Ag 4d contributions and higher kinetic energies up to the Fermi level. Furthermore, no CFS signal is observed around 280 eV kinetic energy with the double peak signature which is characteristic for the SnPc/Ag(111) monolayer film, neither in Fig. 5.18 nor in Figs. 5.19 and 5.20. This can be interpreted as a further indication for a well ordered hetero–molecular film, so that the SnPc molecules are not directly in contact with the Ag(111) surface. Vice versa this finding supports the suggestion in section 5.2.3, namely that in case of the SnPc/Ag(111) monolayer film the double peak CFS signal at $E_{kin} = 279.1$ eV and 280.3 eV is caused by the adsorbate–substrate interaction.

The 2D intensity plot of the series of EDCs on the right hand side of Fig. 5.19 shows again that the intensity variation of the autoionization signal for $E_{kin} < 275$ eV reflects the intensity variation of the C K–NEXAFS signal on the left hand side of Fig. 5.19 well. Furthermore, it can be seen that for $h\nu = 285$ eV the valence signal above 280 eV kinetic energy is considerably enhanced with respect to the photoelectron spectrum for $h\nu = 283$ eV. Moreover, a comparison between the C K–NEXAFS spectra and the autoionization signal suggests that this enhancement of the valence signal is not only due to the SnPc contribution but the PTCDA signal contributes considerably as well. Considering the NEXAFS spectra one can expect additionally that the PTCDA layer contributes significantly to the autoionization signal for 287 eV $< h\nu <$ 290 eV.

The SnPC/PTCDA/Ag(111) autoionization spectra A – E are plotted in Fig. 5.20 as well, together with the regular Auger signal on top of the graph. The autoionization signal for the SnPc multilayer film from section 5.2.2 is shown additionally for better comparison (black line) as well as the regular Auger signal for a PTCDA/Ag(111) monolayer film (grey line). Moreover, the maxima of the PTCDA autoionization signal are indicated by the grey bars according to the data of a PTCDA/Ag(111) monolayer film, which is shown in Fig. D.7 in *appendix D*. A comparison of the regular Auger signal at the top of Fig. 5.20, shows that the general signature of the signal of the SnPc/PTCDA/Ag(111) film, the SnPc multilayer film and the PTCDA monolayer film is relatively similar, e.g. for all films the regular Auger signal is highest around 260 eV and 270 eV kinetic energy with a small local minimum at 264.4 eV for the SnPc multilayer signal and 265.9 eV for the PTCDA monolayer signal. This can be understood with respect to the fact that the signal

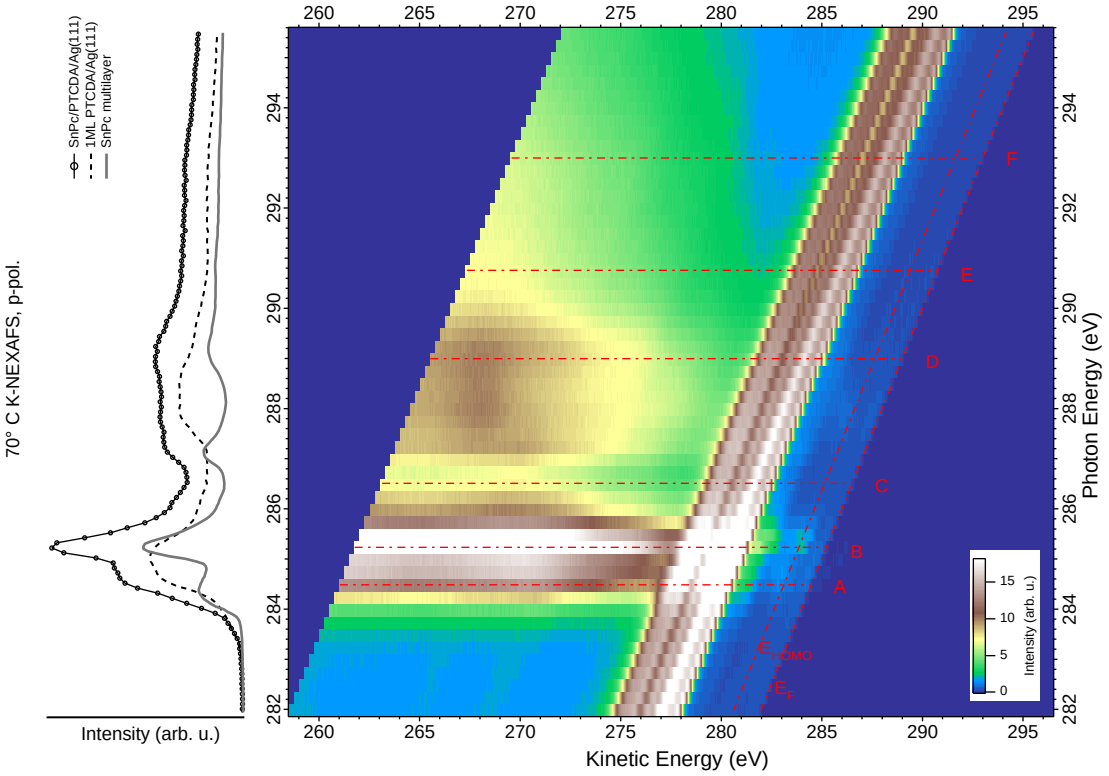

Figure 5.19: (Color online) Photon energy dependence of the EDCs at the C K–absorption edge for a hetero–molecular film with 1 ML SnPc on top of 1 ML PTCDA/Ag(111) recorded at 70° angle of incidence with respect to the surface normal and p–polarized light. The maximum of the color scale corresponds to 75% of the maximum intensity. The diagonal lines mark the CIS contributions, in particular the Ag 4d signal and the Fermi edge (E_F) of the substrate as well as the SnPc HOMO signal (E_{HOMO}). The horizontal lines (A – F) indicate the EDCs which are further evaluated in Fig. 5.20 and 5.21. The corresponding C K–NEXAFS spectra are shown on the left hand side for better orientation.

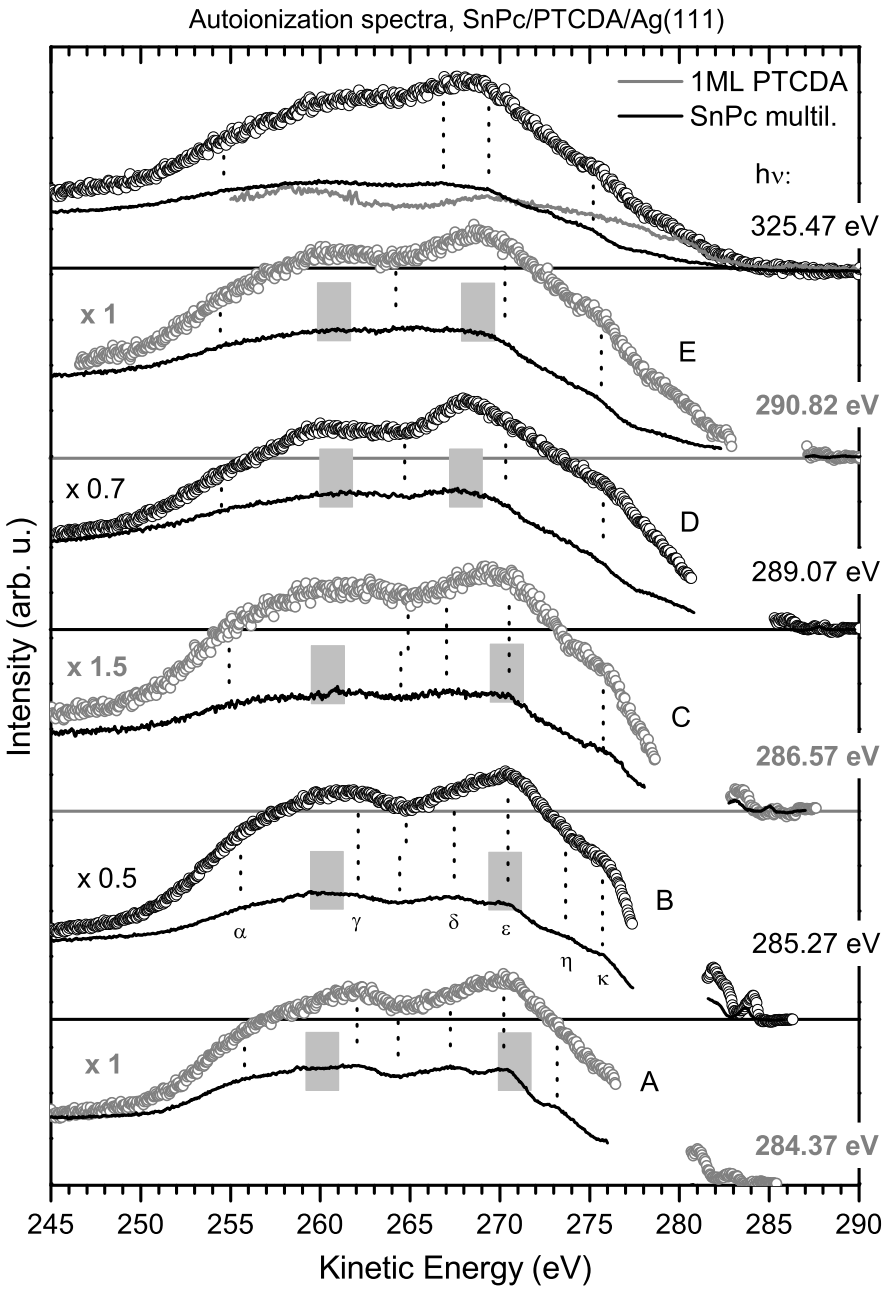

Figure 5.20: C K–autoionization spectra of a hetero–molecular film with 1 ML SnPc on top of a 1 ML PTCDA/Ag(111) film. The curves A – E are obtained by subtracting the PES contribution from the EDCs indicated in Fig. 5.19, which was recorded separately with hν = 280 eV. The same applies for the Auger signal. Additionally, the autoionization signal of the SnPc multilayer film is plotted (black line) and the regular Auger contribution of the PTCDA/Ag(111) monolayer film (grey line). Furthermore, the peaks and shoulders in the SnPc/PTCDA/Ag(111) autoionization signal which are similar to the features in the SnPc multilayer spectrum are marked by dotted lines, and the energy positions of the maxima of the PTCDA monolayer signal according to Fig. D.7 are indicated by grey bars.

originates predominantly from carbon species in a similar chemical environment, namely from the phenyl and the perylene ring system. However, significant differences in the fine structure of the autoionization spectra can be observed between the SnPc multilayer film and the PTCDA monolayer film in Fig. 5.10 and Fig. D.7, respectively. Consequently, one will be able to identify characteristic features of the SnPc multilayer signal in the autoionization signal of the SnPc/PTCDA/Ag(111) film if the electronic properties of the SnPc layer in the SnPc/PTCDA/Ag(111) film are similar to that of the SnPc multilayer film.

It will be briefly shown in the following that some contributions to the features $\alpha - \kappa$ in the autoionization data of the SnPc multilayer film, which were discussed in *section 5.2.2*, can also be identified in the autoionization signal of the SnPc/PTCDA/Ag(111) film. Particularly the shoulder in spectrum B at E_{kin} = 275.7 eV, which appears in each autoionization spectrum B – F as well, can be associated with the shoulder κ of the SnPc multilayer signal in Fig. 5.20. For the regular Auger signal of the SnPc/PTCDA/Ag(111) this shoulder is shifted to E_{kin} = 275.1 eV in agreement with the SnPc multilayer data. Furthermore, the shoulder at 267.4 eV and 255.5 eV in spectrum B can be associated with the peak δ and the shoulder α in the respective SnPc multilayer spectrum. Accordingly, the SnPc contribution to the SnPc/PTCDA/Ag(111) autoionization spectrum is similar to the respective signal for the SnPc multilayer film. For higher photon energies the comparison of the respective spectra becomes more difficult since the fine structure in both, in the SnPc multilayer data and in the SnPc/PTCDA/Ag(111) data becomes less distinct. However, in spectrum E and in the regular Auger signal the features α and κ can still be identified. Note that for spectrum D the maximum of the SnPc/PTCDA/Ag(111) signal is located at E_{kin} = 257.5 eV, which is ca. 2 eV lower than for the remaining spectra. It is indicated in Fig. 5.20 that this shift can predominantly be attributed to the PTCDA contribution with respect to Fig. D.7. In particular for $h\nu = 289.07$ eV the excitations at the carbon species in the carboxyl group contribute significantly to the signal. Therefore the observed differences in the autoionization signal demonstrate the sensitivity of the Auger and autoionization signal to the local chemical environment.

All these findings suggest, that the SnPc and the PTCDA contributions to the SnPc/PTCDA/Ag(111) autoionization spectra are similar to the respective signals for the SnPc multilayer film and for the pure PTCDA/Ag(111) film, which is in agreement with the findings from the core level PES and NEXAFS investigations. [A7] Consequently the autoionization data suggest as well that the interaction between the SnPc monolayer and the PTCDA/Ag(111) monolayer film is considerably weaker than the coupling between the first adsorbate monolayer and the substrate. For further detailed analysis of the SnPc contribution to the total signal by means of difference spectra it is necessary to record PTCDA/Ag(111) data of higher quality as that shown in the appendix D.

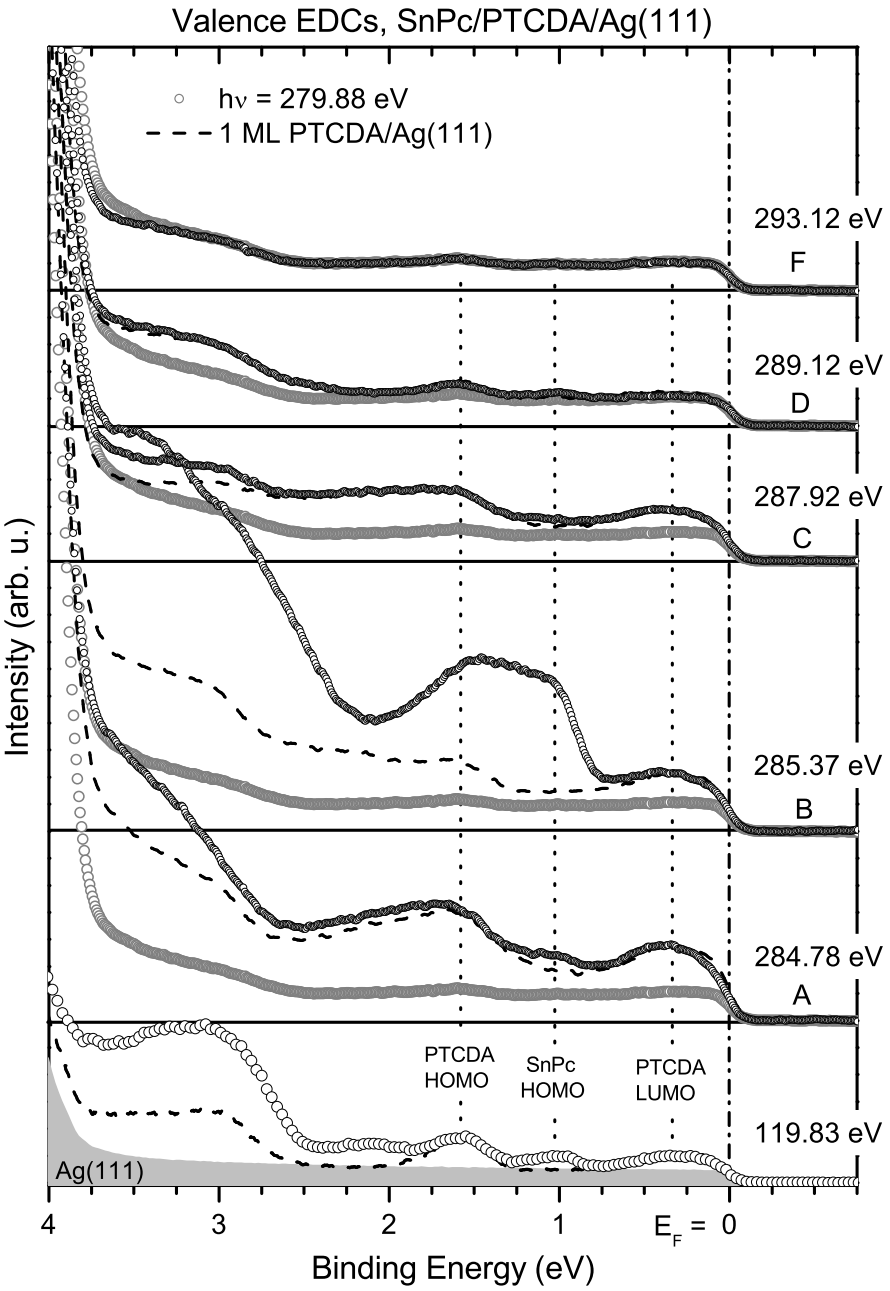

Figure 5.21: Comparison of the valence EDCs of a hetero–molecular film with 1 ML SnPc on top of 1 ML PTCDA/Ag(111) for the photon energies indicated in Fig. 5.19. The EDCs for photon energies higher than 284 eV (black) are plotted above the photoelectron spectra recorded at hν = 279.88 eV and 119.83 eV (grey) for better comparison. The angle integrated valence spectrum of the clean Ag(111) surface for hν = 119.83 eV is shown additionally as grey area.

The EDCs A – F of the upper valence regime, which were recorded with photon energies corresponding to the NEXAFS resonances as indicated in Fig. 5.19, are plotted in Fig. 5.21 on a binding energy scale for better comparison to the direct PES signal. Additionally to each SnPc/PTCDA/Ag(111) curve the direct PES spectrum is shown, which was recorded with hν = 280 eV, and the respective signal from a PTCDA/Ag(111) monolayer film, which was recorded separately at the same photon energy as the spectrum for the hetero–molecular film. At the bottom of the graph the respective data is depicted for hν = 120 eV. The direct PES signal of the SnPc layer can be well distinguished from that of the PTCDA monolayer. In particular the PTCDA layer contributes to the signal in the range of 0 eV $< E_B <$ 0.8 eV, 1.3 eV $< E_B <$ 2.0 eV and $E_B >$ 2.5 eV, which can be attributed to the LUMO derived DOS, the HOMO and stronger bound states, where the SnPc signal contributes predominantly for 0.8 eV $< E_B <$ 1.3 eV binding energy (HOMO) and 1.7 eV $< E_B <$ 2.5 eV (HOMO-1). For higher binding energies the signal from several SnPc states overlaps with the PTCDA contribution. Moreover, the energy position of the SnPc contribution indicates a shift of 0.4 eV to lower binding energies compared to the energy positions for the multilayer film in [A4], which agrees well with recent findings. [A7].

Comparing the SnPc contribution to the autoionization signal between the spectra A – F, in particular the difference between the black curves, one finds that the trend in the enhancement of the signal is similar to the trend for the SnPc multilayer film. In spectrum A, for example, which was recorded for a photon energy that allows in the SnPc molecule only C_C 1s $\rightarrow$ LEMO transitions, the SnPc signal at $E_B = 3$ eV is significantly enhanced and the HOMO and the HOMO-1 signal is only slightly increased. This enhancement can be attributed to participant decay of the core excited state, e.g. where the electron in the LEMO fills the core hole and emits another electron from the HOMO, HOMO-1 or lower lying orbitals. In spectrum B both, the autoionization signal from the SnPc HOMO and at $E_B = 3$ eV is very intense, whereas the contribution from the HOMO-1 at $E_B = 2$ eV is quite small. Moreover, the autoionization signal contributes in spectrum C predominantly at $E_B = 3$ eV and little to the signal from the SnPc HOMO at $E_B = 1.0$ eV. The SnPc contribution to the autoionization signal in spectrum D is so weak that spectrum D can hardly be distinguished from that for the PTCDA monolayer, and no significant autoionization signal can be observed in curve F, only the direct photoemission signal. This trend is in principal similar to what has been observed for the SnPc multilayer film in Fig. 5.11.

Moreover, Fig. 5.21 suggests that the SnPc signal contributes significantly to the broad feature in spectrum B between 0.7 eV and 2.2 eV. This is also illustrated in Fig. 5.22 (a) where the difference between the autoionization signal for the SnPc/PTCDA/Ag(111) film and the PTCDA monolayer film is plotted. Additionally the photoelectron spectra of these films is shown in Fig. 5.22 (c) for 120 eV

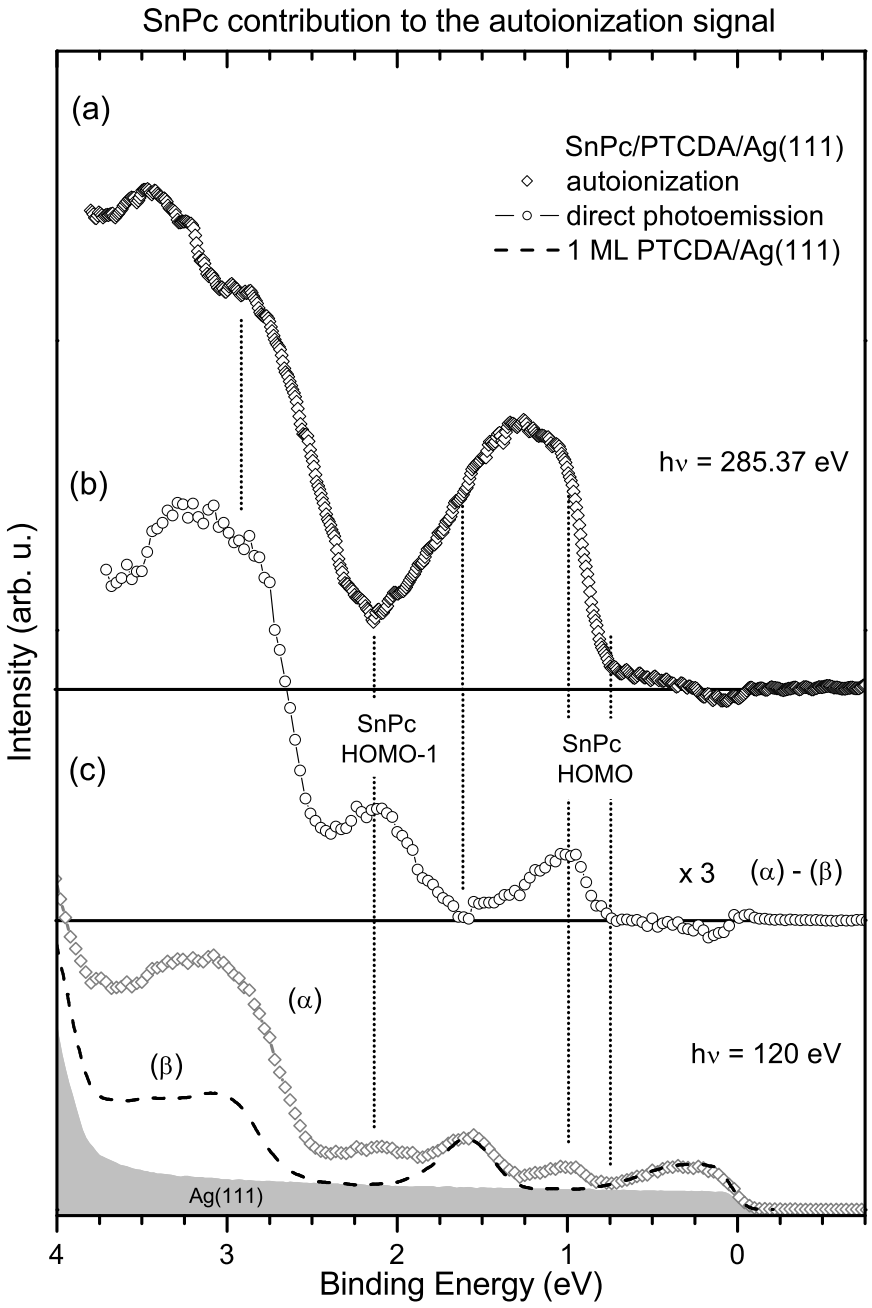

Figure 5.22: Comparison between the direct photoemission signal and the autoionization signal of the SnPc contribution of the hetero–molecular SnPc/PTCDA/Ag(111) film: (a) difference between spectrum B in Fig. 5.21 and the respective PTCDA/Ag(111) signal, (b) difference between the SnPc/PTCDA/Ag(111) and the PTCDA/Ag(111) photoelectron spectra shown in (c).

photon energy, and the difference between these spectra is depicted in Fig. 5.22 (b). This curve indicates clearly that the direct photoelectron signal from the SnPc HOMO contributes only to the EDC between 0.7 eV and 1.6 eV binding energy. However, the autoionization signal from the SnPc layer in Fig. 5.22 (a) is very intense in the range of 0.7 eV $< E_B <$ 2.1 eV, where the maximum is located at E_B = 1.27 eV. Its signature suggests that at least two peaks contribute to this signal. Considering that indications for electron–vibration coupling and interference effects have been found for the SnPc multilayer film, which give rise to a shoulder with respect to the CIS signal from the HOMO, one can assume that this interrelation also plays a role for the SnPc/PTCDA/Ag(111) film. Studying the photon energy dependence of the autoionization signal from the SnPc monolayer can provide further insight.

The autoionization spectra of the SnPc/PTCDA/Ag film (dots) and the PTCDA monolayer film (solid lines) are plotted in Fig. 5.23 over the kinetic energy scale when tuning the photon energy through peak B of the C K–NEXAFS signal of the SnPc layer, which has been shown in Fig. 5.6 (d). Additionally, in the inset the respective data is also plotted over the binding energy scale for better identification of the CIS contribution. In the spectrum recorded with 284.98 eV photon energy a small contribution from the SnPc layer to the autoionization signal can be observed at E_{kin} = 284.0 eV and E_B = 1.0 eV, respectively, which can be attributed to participant decay of the core excited state. This signal increases considerably with increasing photon energy. One can identify at least two components of this signal. One contributes at 1.0 eV binding energy and shifts with increasing photon energy to higher kinetic energies, respectively, as it is expected for a CIS signal. The other component contributes at 283.9 eV kinetic energy which leads to the broad tail at the side to lower kinetic energies and higher binding energies, respectively. This is similar to what as been observed for the SnPc multilayer film in *section 5.2.2*, where this pseudo CFS contributions has been discussed with respect to RIXS investigations of smaller molecules. [198, 256] Hence, this effect can be attributed analogously to electron–vibration coupling. Additionally, in case of the hetero–molecular film the intensity of the pseudo CFS signal is significantly higher with respect to the CIS contribution than for the multilayer film. Furthermore, for the spectrum recorded with 285.73 eV photon energy one can observe significant signal from the SnPc film from 285.0 eV down to 283.2 eV kinetic energy and in the range 0.7 eV $< E_B <$ 2.5 eV, respectively. This can be interpreted as indication for a modification of the electron–vibration coupling for the hetero–molecular film with respect to the SnPc/Ag(111) multilayer film. This would also explain the minor differences in the signature of the SnPc contribution to the core level spectra compared to the multilayer spectra. Consequently, the broadening of the HOMO peak can be explained by electron–vibration coupling and interference effets, in analogy to the findings for the SnPc multilayer film.

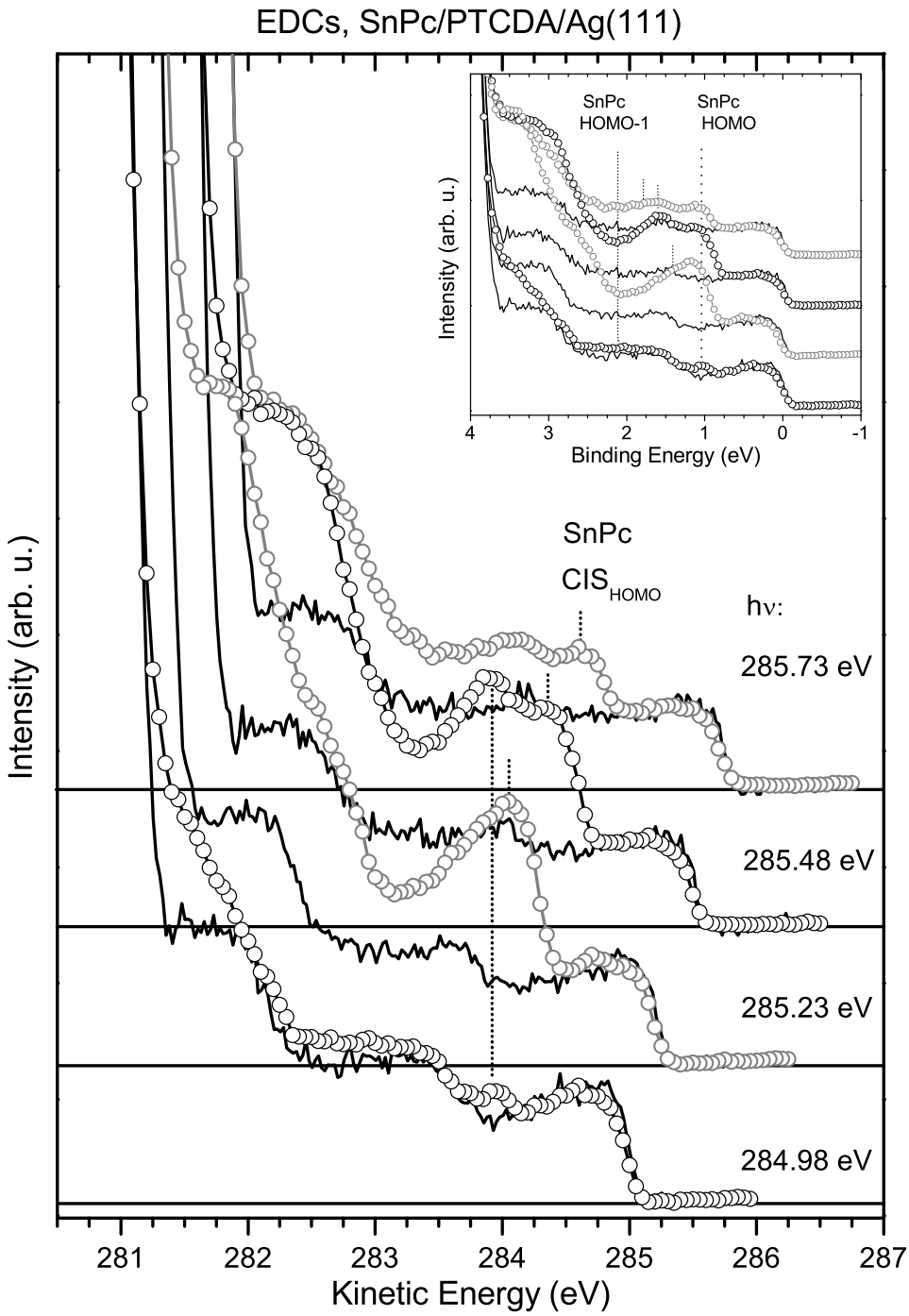

Figure 5.23: Comparison of EDCs of the upper valence regime for a hetero–molecular film with 1 ML SnPc deposited on a PTCDA/Ag(111) monolayer film for photon energies corresponding to the second resonance of the SnPc C K–NEXAFS signal. The spectra of the SnPc/PTCDA/Ag(111) film are show (dots) together with the spectra of PTCDA/Ag(111) monolayer film (solid lines).

Summing up, the resonant AES investigation of the SnPc/PTCDA/Ag(111) film indicates that the interaction between the SnPc layer and the PTCDA/Ag(111) monolayer film is considerably weaker than the adsorbate–substrate interaction for the SnPc/Ag(111) monolayer film and comparable to the intermolecular interaction for the SnPc multilayer film. Particularly the SnPc contribution to the autoionization spectra of the hetero–molecular film is similar to the data for the SnPc multilayer film, e.g. a fine structure is observed in the autoionization spectra of the hetero–molecular film below 280 eV kinetic energy which is equivalent to that for the SnPc multilayer film. Furthermore, a strong enhancement of the CIS signal from the SnPc HOMO and HOMO-1 is observed for the SnPc/PTCDA/Ag(111) film due to participant decay of the core excited state, particularly for photon energies corresponding to transitions into the LEMO. Moreover the dependence of these contributions to the autoionization signal on the photon energy is comparable to what has been observed for the multilayer film. The interference effects between different vibronic states namely contribute to the autoionization signal in analogy to what is found for the SnPc multilayer film in section 5.2.2. Consequently the coupling strength between the SnPc monolayer and the PTCDA/Ag(111) monolayer film is comparable to the intermolecular interaction in the multilayer film.

5.3 Electron–electron correlation energy

In section 4.1.2 it was assumed for the description of the adsorbate–substrate interaction in the single impurity Anderson model that the correlation energy U between two electrons can be neglected to first order when considering delocalized frontier orbitals, e.g. π–orbitals in a conjugated molecular ring system like for benzene and perylene derivatives or phthalocyanines. A comparison of the regular Auger spectra with the core level and valence PES data can provide information on the electron–electron correlation energy U as it will be demonstrated in the following.

When considering a free atom with one core level (c) and one valence level (a) which is occupied by two electrons with spin $\uparrow$ and spin $\downarrow$, respectively, the Hamiltonian from (4.1) needs to be extended by a term for the correlation energy U_{cc} of the core electrons and by a term for the correlation energy U_{aa} of the valence electrons:

$$H = \epsilon_c(n_{c\uparrow}+n_{c\downarrow})+U_{cc}\, n_{c\uparrow}n_{c\downarrow}+[\epsilon_a-U_{ac}(2-n_{c\uparrow}-n_{c\downarrow})](n_{a\uparrow}+n_{a\downarrow})+U_{aa}\, n_{a\uparrow}n_{a\downarrow} \quad (5.18)$$

As it is assumed that both spin directions are equivalent, the notation for the electronic configuration where one spin ↑ or one spin ↓ electron is missing in the core level is simplified to $(c^{-1}a^{0})$. Accordingly, the following relation holds for the kinetic energy E_{kin} of the Auger electron after decay of the core hole state $\Psi(c^{-1}a^{0})$ into the $2h$ final state $\Psi(c^{0}a^{-2})$:

$$\begin{aligned} E_{kin} &= \langle\Psi(c^{-1}a^{0})|H|\Psi(c^{-1}a^{0})\rangle - \langle\Psi(c^{0}a^{-2})|H|\Psi(c^{0}a^{-2})\rangle \\ &= E_c - 2E_a - U_{aa} \ , \end{aligned} \tag{5.19}$$

where the energy E_c and E_a correspond to the energy for creating one core or one valence hole, respectively, as it is measured by PES.

$$\begin{aligned} E_c &= \langle\Psi(c^{-1}a^{0})|H|\Psi(c^{-1}a^{0})\rangle - \langle\Psi(c^{0}a^{0})|H|\Psi(c^{0}a^{0})\rangle \\ &= -\epsilon_c - U_{cc} - 2U_{ac} \end{aligned} \tag{5.20}$$

$$\begin{aligned} E_a &= \langle\Psi(c^{0}a^{-1})|H|\Psi(c^{0}a^{-1})\rangle - \langle\Psi(c^{0}a^{0})|H|\Psi(c^{0}a^{0})\rangle \\ &= -\epsilon_a - U_{aa} \end{aligned} \tag{5.21}$$

In case of the SnPc multilayer film the intermolecular interaction is comparatively weak. The regular Auger signal with the highest kinetic energy can therefore be related to a decay of the C_N 1s core excited state where a HOMO electron fills the core hole and emits the second HOMO electron. Consequently the correlation energy between the two electrons in the HOMO can be determined with (5.19) from the energy positions of the onset of the regular Auger signal, and the energy position of the C_N 1s and the HOMO signal in the photoelectron spectra. As for the SnPc/Ag(111) monolayer film the LUMO derived DOS is partially occupied the regular Auger signal with the highest kinetic energy corresponds to a decay of the C_N 1s core excited state where an electron from the LUMO derived DOS distribution right at the Fermi level fills the core hole and emits another electron from this DOS distribution.

The leading edge of the regular Auger spectrum of the SnPc multilayer film from Fig. 5.10 is plotted at the top of Fig. 5.24 and labeled (i). The spectrum of the SnPc/Ag(111) monolayer film from Fig. 5.15 is plotted at the bottom and labeled (ii). As even for the 12–14 ML thick SnPc film a weak signal from the first monolayer contributes to the regular Auger signal it is necessary to subtract this contribution

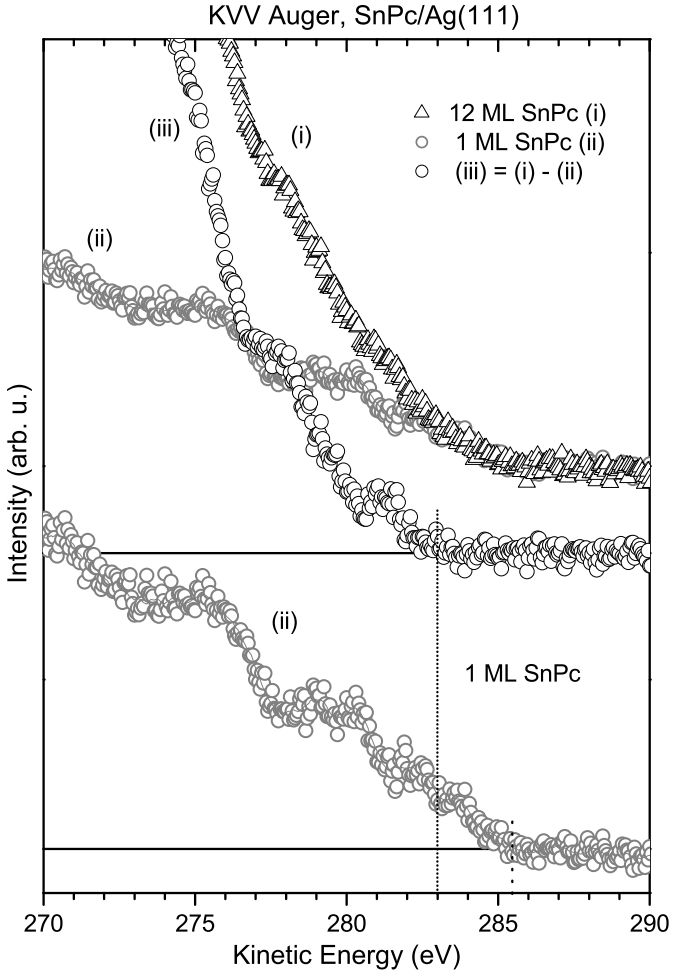

Figure 5.24: High–energy tail of the KVV Auger spectra of a SnPc/Ag(111) multilayer film (i) and a 1 ML film (ii) recorded with hν = 320 eV and 325 eV, respectively. Additionally, the difference spectrum (iii) is shown, where the 1 ML contribution has been subtracted from the multilayer spectrum. The dotted line indicates the energy position of the onset of the Auger signal.

first. The respective difference spectrum corresponds to curve (iii). Its onset is located at $E_{kin} = 283.0 \pm 0.3$ eV. The maximum of the C_N 1s peak in the C 1s core level spectrum for the multilayer film in Fig. 5.7 (a) can be determined with high accuracy to be $E_B = 286.00 \pm 0.03$ eV. Note that for the multilayer film the HOMO contributes to a double peak signature due to the formation of SnPc dimers and a bonding–antibonding scenario. [217, A4] The Auger signal with the highest kinetic energy is related to a final state with two holes in the lower bound HOMO orbital, which is located at $E_B = 1.30 \pm 0.03$ eV. According to (5.19) this leads to $U_{HH} = 0.4 \pm 0.3$ eV correlation energy of the HOMO electrons.

If one assumes that vibronic broadening plays a significant role for the photoelectron spectra of the SnPc multilayer film the energy position of the C_N 1s and HOMO signal needs to be considered which corresponds to the vibronic ground state. Accordingly, the correlation energy U_{HH} can be estimated analogously from the leading edge of the C_N 1s peak ($E_B = 285.5 \pm 0.05$ eV) and the HOMO peak ($E_B = 1.10 \pm 0.05$ eV). Altogether, both approaches provide an estimate of the electron–electron correlation energy for the HOMO of $0.1 < U_{HH} < 0.7$ eV. This value is in between those for delocalized sp states in the upper valence regime of metals, where the correlation energy is close to zero, and the values of quite localized orbitals, where the correlation energy can be much higher, e.g. from several eV for d and f states of transition metals [33, 266–268] up to several tens eV for the F 2s and the He 1s orbitals. [269]

The onset of the regular Auger spectrum (ii) of the SnPc/Ag(111) monolayer film in Fig. 5.24 is located at $E_{kin} = 285.45 \pm 0.05$ eV and consequently at significantly higher kinetic energy than in case of the multilayer film. Moreover, the maximum of the C_N 1s peak in the C 1s core level spectrum of the SnPc/Ag(111) monolayer film is located exactly at the same energy position as illustrated in Fig. 5.25. This corroborates the assignment of the signal to a decay of the C_N 1s core excited state where an electron of the LUMO derived DOS right at the Fermi level fills the core hole and emits another LUMO electron. Furthermore, this finding suggests that the correlation energy U_{LL} between electrons in the LUMO derived DOS is close to zero, similar to what is found for the delocalized sp states in the upper valence regime of metals. This implies that many body effects play a role for the SnPc monolayer film. Consequently, the agreement of the energy position of the core level signal and the onset of the regular Auger signal can be considered as further indication for strong (electronic) adsorbate– substrate coupling so that a joint density of substrate–adsorbate states is formed, which leads to many–body excitations in the PES, NEXAFS and resonant Auger spectroscopy with metallic character as it has been shown in *chapter 4* and *section 5.2.3*.

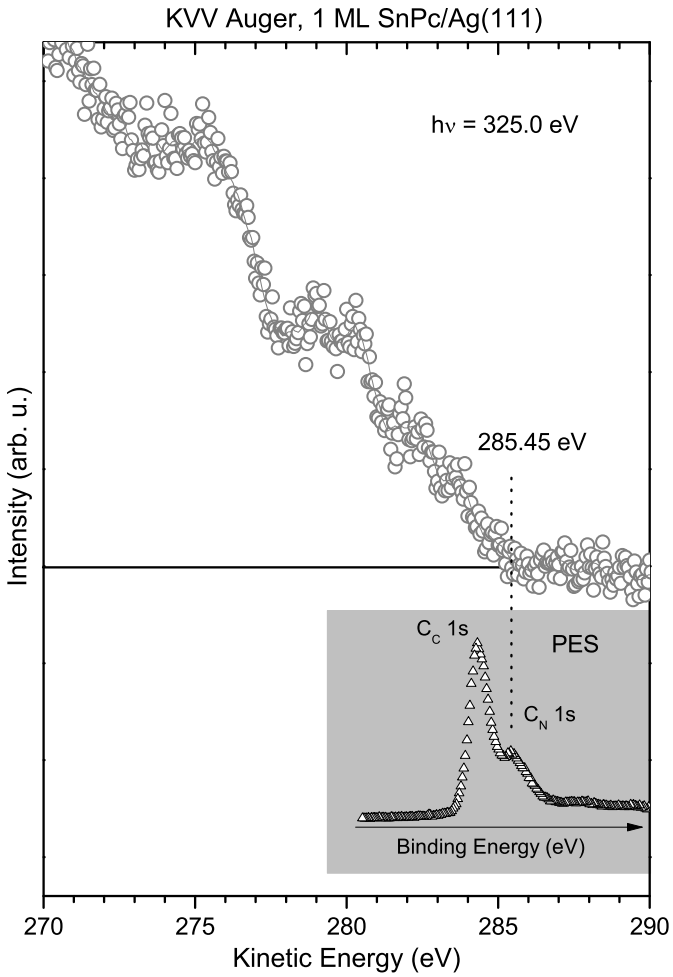

Figure 5.25: Comparison between the high–energy tail of the KVV Auger spectrum of a 1 ML SnPc/Ag(111) film (top) and the respective C 1s photoelectron spectrum (bottom) at the same energy scale.

5.4 Discussion & Conclusion

In has been demonstrated in *section 5.2.1* that the 1 ML SnPc/Ag(111) film is representative for molecular adsorbate films which react strongly with a metal substrate. Moreover, the investigation of the SnPc films demonstrates that resonant Auger spectroscopy is a sensitive method for studying the electronic structure of organic thin films and surfaces. Due to site specific core excitations the resonant enhancement of certain spectral features can be related to the localization of orbitals as it has been discussed, for example, for the SnPc multilayer film with respect to the HOMO and HOMO-1 contribution. Additionally, interference effects can provide information about dynamical aspects, e.g. nuclear motion and substrate–adsorbate charge transfer as it has been demonstrated for the SnPc multilayer and the monolayer film as well as for the hetero–molecular film. Furthermore, autoionization spectra can be a significant indicator for many–body excitations, which becomes evident by the comparison of the data of the SnPc/Ag(111) multilayer film with that of the monolayer film. For the multilayer film in *section 5.2.2* certain features in the autoionization signal can be well explained by the simplified concept of a spectator decay, where a core electron is excited into an unoccupied state where it remains "passive" during the subsequent Auger decay. However it was shown in *section 5.2.3* that the spectator and participator concept breaks down for the monolayer film for which many–electron excitations dominate.

The study in *chapter 4* indicates that the NEXAFS and the core level spectra of molecular monolayer films which are strongly coupled to a metal substrate need to be discussed in the frame work of many–body excitations involving substrate–adsorbate charge transfer. In this context the asymmetric peak profiles in the core level spectra are due to a continuum of core excited states comparable to Doniach–Mahan–Sunjic line profiles. [88, 175–178] This implies that many–body excitations and interference effects between different core excited states play a significant role for the autoionization of such films considering the Kramers–Heissenberg relation (5.10) and the Fano approach. As a result, charge transfer satellites can contribute considerably to the autoionization spectra. Their contributions may change when tuning the excitation energy through a resonance. Moreover, these effects can be related to the duration τ_c of the x–ray scattering process — the satellites are large for short τ_c. Consequently the variations in the autoionization spectra can be attributed to a difference in the reaction of the electronic structure for different life times of the excited state. This can be considered as if the reaction of the electronic structure on the radiation field occurred on the time scale of the core hole life time.

In the autoionization data of the SnPc/Ag(111) monolayer film in *section 5.2.3* the relative intensity of the charge transfer satellite contribution with respect to the

CIS signal from the HOMO has been higher for shorter duration τ_c of the x–ray scattering process. In the context of what has been discussed above this can be interpreted in the way that the electronic structure reacts on a similar time scale as the core hole life time and consequently within a few fs. Furthermore, the particular spectral features of the monolayer data cannot be related explicitly to particular electronic configurations in the single electron frame work because of many–body effects. Hence a certain peak cannot be assigned to a particular electronic configuration after a substrate–adsorbate charge transfer scenario or a non–charge transfer scenario. As a consequence the well established tunneling approach in the single particle picture, where the decrease or increase of a spectator or participant signal is directly related to the tunneling rate of one electron between the adsorbate and the substrate is only suitable in case of weak adsorbate–substrate interaction. [183–186] However, quantum chemical calculations of the autoionization spectra may be helpful in case of strong adsorbate–substrate coupling, comparable to the calculations of photoemission spectra for transition metal compounds with charge transfer satellites. [87, 130]

Furthermore, the investigation of the hetero–molecular film in *section 5.2.4* can provide fundamental information on the interaction of the second monolayer with the first one for molecular thin films of flat lying π–conjugated molecules. As the general signature of the autoionization contribution from the SnPc monolayer is similar to that for the SnPc/Ag(111) multilayer film it can be assumed that the strength of the interaction between the first and the second molecular monolayer is comparable to the intermolecular interaction in the multilayer film and charge transfer satellites do not contribute to the autoionization spectra. Moreover, the autoionization data suggest a modification of the electron–vibration coupling for the SnPc layer, which is in agreement with the signature of the SnPc signal in the core level spectra. [A7] Consequently, a reactive metal surface can in general be capped by adsorbing only one single densely packed adsorbate monolayer. Accordingly, significant hybridization is only observed between the electronic states of the first layer and the metal substrate.

However, a rigid level shift of 0.4 eV is observed for the SnPc monolayer with respect to the SnPc/Ag(111) multilayer and bilayer film. Moreover, it has been shown in [A7] that this shift agrees well with the work function difference between the PTCDA/Ag(111) monolayer film and the SnPc/Ag(111) multilayer film. Consequently the rigid level shift can be attributed to an increase of the interface dipole by the PTCDA interlayer. In this context the rigid level shift can be interpreted as an indication for vacuum level alignment due to the weak interaction between the second (SnPc) monolayer and the first (PTCDA) monolayer as it has been discussed in more detail in [A7].

Consequently, resonant Auger spectroscopy is a powerful method which can provide important information about the interface interaction. Due to the high cross section for the light elements and the high surface sensitivity compared to RIXS it is particularly suitable for studying organic thin films and surfaces. This spectroscopy technique is of interest because it is site selective and it provides access to nuclear and electronic dynamics at the interface. These properties are very important for all kinds of applications where charge transport, [270–273] the life time of excited states and reaction dynamics play a role. [188, 274–276] This can be illustrated by the following examples: The interfaces are often the bottle neck which limit the carrier mobility in electronic devices. The efficiency of solar cells and LEDs depends on the relation between the life time of excited states and the charge carrier mobility at the interfaces. Catalytic reactions often occur at surfaces due to a complex interplay between the life time of excited states and the molecular and atomic dynamics. Moreover, heterogeneous catalysis is driven by only a few highly reactive hot spots at the surface where the conditions for a certain reaction path are optimal. These conditions need to be understood in order to improve such catalysts systematically.

6

Concluding remarks

It has been demonstrated that PES, NEXAFS spectroscopy and resonant AES can provide important information about the electronic structure with high surface sensitivity, and hence theses methods are suitable for studying thin adsorbate films and interfaces. It has been shown in the *chapters 3 – 5* and additionally in the *appendix C* that many–body effects can contribute significantly to the spectra of the bulk and the substrate–adsorbate interface, in particular in the case of strong adsorbate–substrate coupling. Moreover, in *chapter 5* indications for weak electron–electron correlation in the frontier orbitals of π–conjugated organic molecules are found. Consequently, it may be necessary to take such correlation effects into account for a proper description of the interface interaction. Consequently, the intermolecular interaction, which can be mediated by the substrate, can induce electron hopping between different molecules in a densely packed film of adsorbates with a partially occupied LUMO derived DOS.

These effects, the adsorbate–substrate coupling, the electronic correlation and the intermolecular interaction, can be described by the Hubbard model. [277–281] This description has been successfully applied to various transition metal compounds, e.g. transition metal oxides, halides, sulfides and alloys. [116] In this model a lattice is considered in which electrons can hop between the different sites and a Coulomb energy U has to be payed for double occupation of one site. For the discussed adsorbate monolayer films, where the molecules are lying flat at the substrate, one can assume that the direct coupling between different adsorbates is comparatively weak and that the adsorbate–substrate coupling is the dominant effect which mediates the intermolecular interaction. It has been shown that for such a scenario it is convenient to project the Hubbard approach onto the single impurity Anderson model, so that only the interaction of a single impurity with an electron reservoir is considered, which covers also the interactions between different sites in the Hubbard lattice. This simplification is one key aspect of dynamical mean–field theory. [282] In combination with DFT it allows to model the dependence of the quasi–particle DOS distribution on the correlation energies U and the substrate–adsorbate coupling. The latter can be related to the width W of the density distribution of substrate–adsorbate states in the limit $U = 0$. The general trend of this interrelation which

is found for various materials is schematically indicated in Fig. 6.1 for zero temperature and a half filled DOS which corresponds in the Hubbard model to the same number of electrons as lattice sites. [7, 33, 282–285]

Accordingly, Fig. 6.1 (a) illustrates the case in which the electrons are entirely independent ($U = 0$) as it was assumed in *chapter 4*. In the weakly correlated regime of Fig. 6.1 (b) the quasi–particle DOS distribution resembles still that of independent electrons. However, the peak becomes narrower with increasing electron–electron correlation and two shoulders develop at the high and low–energy side. Fig. 6.1 (c) illustrates the characteristic Hubbard bands for the strongly correlated regime with the distinct, narrow quasi–particle peak at the Fermi level. When the correlation is sufficiently strong the Mott metal–insulator transition happens and the quasi–particle peak vanishes in Fig. 6.1 (d). In this context the data from the previous chapter allows to classify the SnPc/Ag(111) monolayer film in terms of correlation strength.

One can assume for the SnPc/Ag(111) monolayer film that in case of correlation effects being absent ($U = 0$) the width W of the LUMO derived DOS distribution was similar to that of the HOMO peak in spectrum Fig. 5.16 (i), namely of the order of 0.4 eV. Furthermore, in section 5.3 the correlation energy U_{HH} between the electrons in the delocalized HOMO was estimated to be $U_{HH} = 0.4 \pm 0.3$ eV for the multilayer film, where the intermolecular interaction is weak enough to be neglected. As the LUMO orbital is similarly delocalized one can assume a similar value for the LUMO. Consequently, the ratio $U/W \sim 1$ which implies that the SnPc/Ag(111) monolayer film is somewhere in between the weak and the strongly correlated regime in Fig. 6.1 (b) and (c).[1] Accordingly if these described many–body and correlation effects are a realistic scenario for this molecular monolayer film one should find spectral features in the photoelectron data, which are similar to what is illustrated in Fig. 6.1.

However, in the valence PES data in Fig. C.2 in the *appendix C* no evidence can be found for such spectral features, which might be due to comparatively high sample temperature and the circumstance that these measurements were carried out with comparatively poor energy resolution and statistics. However, for CuPc/Ag(111) monolayer films such a Hubbard like signature has been observed for the LUMO contribution. These spectra were measured at 80 K sample temperature with high energy resolution. [286] It was also shown for these films that the sharp peak at the Fermi level which might correspond to the quasiparticle peak in between the lower and the upper Hubbard becomes narrower and more distinct when decreasing the temperature to 10 K. Moreover, a similar spectral signature has been found recently

[1] Note that there has been an intense debate with respect to transition metal compounds wether the Hubbard U can be directly related to the correlation energy for a free atom, where hybridization and screening does not contribute. [18, 22]

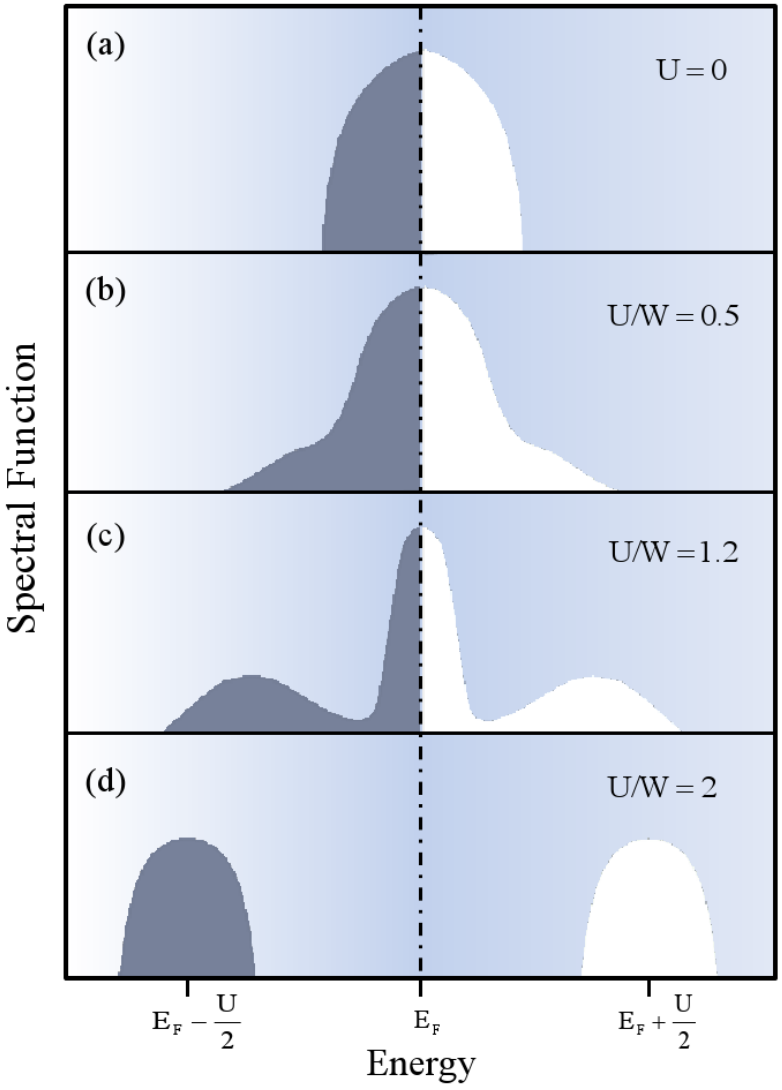

Figure 6.1: Schematic illustration of the spectral function in a material for different correlation energies U at zero temperature and half filling (same number of electrons as lattice sites). [7, 282, 283, 285] Depending on the ratio of the correlation energy U and the band width W for the non–correlated case one can classify the four scenarios into (a) non–correlated, (b) weakly correlated, (c) strongly correlated and (d) Mott insulator.

for NTCDA/Ag(111) and PTCDA/Ag(111) monolayer films as well, which have both a partially occupied LUMO derived density of substrate–adsorbate states. [287–289] In particular for the NTCDA monolayer film an order–disorder phase transition has been observed at low temperature, for which this DOS becomes nearly entirely occupied and the narrow peak at the Fermi level vanishes. This is exactly what is expected in the context of the Hubbard model. Accordingly the contribution from the lower Hubbard band decreases with increasing occupation as well as the hopping rate so that the narrow quasiparticle peak in between the upper and the lower Hubbard band disappears, and the upper Hubbard band is shifted below the Fermi level and increases in spectral weight. For the limit of a complete filled DOS (2 electrons per lattice site) only one band — an equivalent to the upper Hubbard band — is left, as it is expected for the the uncorrelated limit. This interrelation is discussed in more detail in [7, 15, 283]. Note that for C_{60}/Ag(111) monolayer films a similar fine structure is observed at the Fermi level upon doping with potassium and the signature varies with dopant concentration [5] as well as for TTF-TCNQ films. [25, 26, 290]

Summa summarum the results from the previous chapter in combination with recent work from others suggest that it may not be sufficient to consider organic thin films and metal–organic interfaces in a single particle picture under certain conditions but many–particle and correlation effects need to be taken into account additionally. Such effects are well known for transition metal compounds for which they have been studied intensely [6, 13, 116, 284] but for organic thin films they are still kind of exotic [5–7] Moreover, these correlation effects can lead to interesting, rich physics because of an sophisticated interplay between various material properties like the electric resistivity, heat conductivity, geometric structure, sample temperature and magnetic properties. For example lattice stress induced by pressure or doping can drive a Mott metal–insulator transition, which lowers the electric conductivity considerably. [6, 13, 284] On the molecular scale this can be related to shorter interatomic, intermolecular or adsorbate–substrate distances, respectively. When thinking of the Jan–Teller effect or the Peierls distortion it becomes obvious that this interrelation between the electronic structure and the geometric structure might also influence the electron–vibration coupling and consequently the thermal conductivity. Materials with strong, localized spins can have sophisticated magnetic properties as described by Kondo. [16] One could imagine that even molecular adsorbates which contain heavy elements with a partially occupied d/f shell might have similar material properties. Finally the data discussed in this work suggests that many–body and correlation effects which are primarily known for inorganic materials might also play a role for certain organic adsorbate thin films. It would be interesting to study these effects in more detail, in particular how much they contribute to the interface interaction.

A

Comparison between HF and DFT calculations

In principle, the Kohn–Sham functions and energies in the DFT calculations are purely mathematical operants. However, in practice they can approximate the electronic states and electron energies surprisingly well under certain conditions. Hence, DFT can provide reasonable orbitals and energies for organic molecules, and even the band structure in organic solids. [291] This is demonstrated here by a comparison of the results from Hartree–Fock and DFT calculations for benzene and anthracene in the following, as well as by calculations of quantum well states for alkanes in *appendix E*. The absolute Koopmans' and Kohn–Sham energies for the LUMO and the C_{mt} 1s orbital are different, but both approaches show the same trend with increasing polyacene size. Consequently, the calculations of the polyacene orbitals, which are shown in *section 3.3 and 3.3.4* can be carried out using DFT.

Of course, the quality of the HF and DFT calculations and consequently the orbital energies depend on the size of the basis set as well as on the functional in case of DFT. [292] For both, HF and DFT, the 6-311G basis set [292] was used, which models the inner shell orbitals with one contracted Gaussian function and the valence orbitals with three contracted Gaussian functions. Furthermore, the DFT calculations are carried out with the B3LYP functional, [60] which is optimized for light elements.

A.1 Core orbital and LUMO of benzene and pentacene

The iso–density surface of the benzene and pentacene LUMO and of the core orbitals are compared in Fig. A.1 between HF and DFT calculations, respectively. Both methods provide very similar valence and core orbitals. For benzene the orbitals are nearly identical. For pentacene only minor differences are observed, in particular with respect to the third antinode from top in the LUMO. The absolute

	HF			DFT		
	benzene	pentacene	ΔE	benzene	pentacene	ΔE
LUMO	3.70	0.57	3.13	-0.19	-2.61	2.42
core level	-305.77	-305.99	0.22	-276.96	-277.15	0.19

Table A.1: Comparison between the C_{mt} 1s and LUMO energies from HF and DFT calculations for benzene and pentacene. The respective orbitals are displayed in Fig. A.1.

orbital energies depend strongly on the calculation method, HF or DFT, respectively. However, the trend in the orbital energies from benzene to pentacene is similar. Tab. A.1 shows that the decrease in LUMO energy between benzene and pentacene is one order of magnitude larger than the decrease in C 1s energy, independent of the calculation method. Consequently, both, the HF and the DFT calculations, indicate the same trend in the LUMO and core level energies with increasing polyacene size.

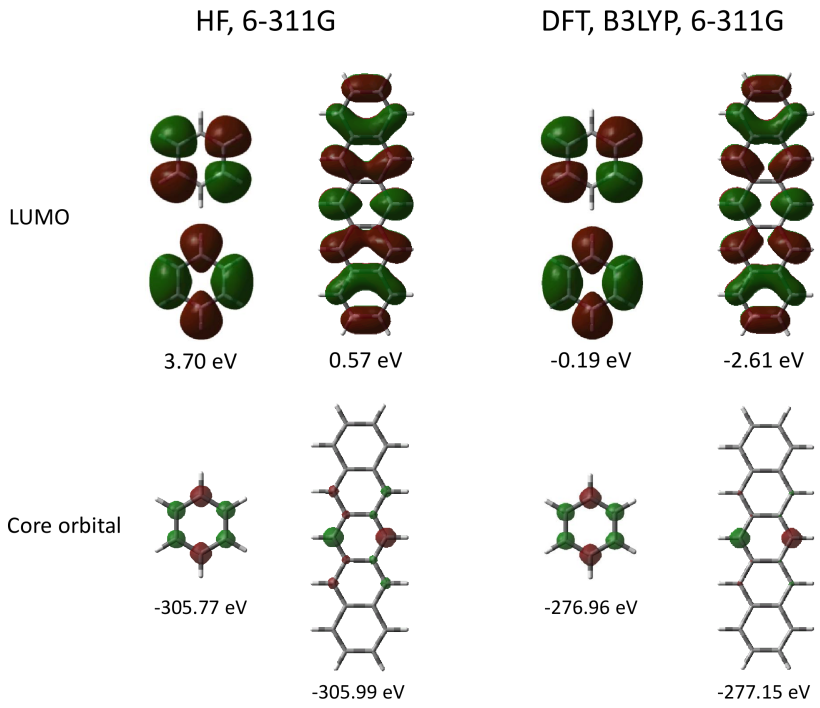

Figure A.1: (Color online) Comparison between Hartree–Fock and DFT calculations of LUMO and core orbitals of benzene and pentacene. In case of DFT all calculations were carried out with the 6-311G basis set and the B3LYP functional. The graph shows the iso–density surface (0.02 e/bohr^3) with the phase of the wave function being indicated by red and green color.

B

Comparison of different BTCDA and BTCDI sub–ML spectra

In Fig. B.1 and B.2 the C 1s and N 1s spectra of various BTCDI/Ag(111) films are shown, which were prepared under slightly different conditions and measured either at room temperature or at considerably lower temperature. The comparison of the spectrum in Fig. B.1 (a) with the data for the annealed films indicates that annealing affects the monolayer films significantly. In particular for the not annealed monolayer film the peak at $E_B = 287.5$ eV is significantly higher than the signal at 288.8 eV, the foot at 283 eV is emphasized and the spectral weight is shifted to lower binding energy with respect to the data for the tempered films.

A loss of BTCDI molecules from the first monolayer was observed if the annealing cycle was too long. Therefore the BTCDI/Ag(111) monolayer films were annealed in several short cycles and checked by PES until a good monolayer film was prepared. The spectra in Fig. B.1 (b, c, d) indicate that small variations in the annealing conditions can lead to significant changes in C 1s spectrum. In particular the relative intensity and the energy splitting of the double peak signature of the C_N 1s signal and the maximum of the C_C 1s peak is very sensitive to the annealing conditions. Furthermore, the spectrum in Fig. B.1 (d) is recorded for the same monolayer film as that in (e), but at 190 K sample temperature instead of 300 K. The similarity between both spectra indicates that cooling has only little effect on the C 1s spectrum from the BTCDI monolayer film.

Furthermore, all BTCDI C 1s monolayer spectra can be fitted consistently with at least six Voigt profiles as shown exemplarily in Fig. B.1 (e). It is discussed in *section 4.4* that the core level signal is related to many–body excitations. Consequently the peaks in this fit approach cannot be interpreted in the one–electron picture which is suitable for the multilayer data. For example the different C_C 1s and C_N 1s peaks cannot be directly related to chemically different carbon species. Moreover, the discussion in *section 4.4* rather suggests that the various peaks can be interpreted in the context of satellite and main peaks to first order.

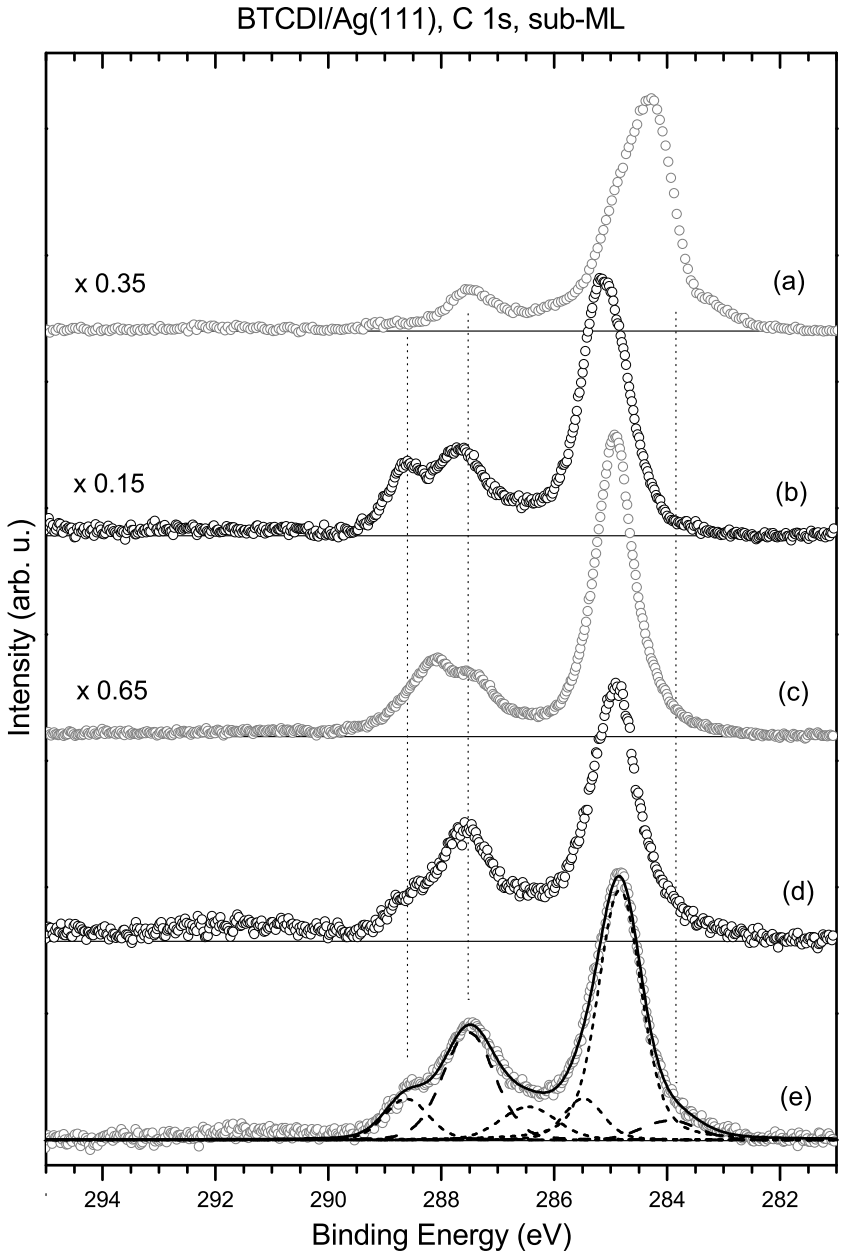

Figure B.1: C 1s core level spectra of various BTCDI/Ag(111) sub–ML films for slightly different annealing conditions and sample temperatures T during the measurements: (a) not annealed and $T = 300$ K, (b) annealed in two cycles ($t = 10 + 3$ min) at 120° C and $T = 300$ K, (c) $t = 5 + 10$ min at 120° C and $T = 300$ K, (d) annealed in several cycles ($t = 5 + 2 + 1 + 2 + 1$ min) at 120° C and measured at $T = 190$ K, (e) the sample from (d) measured at $T = 300$ K. Additionally, the result of a peak fit for spectrum (e) is shown from which the charge transfer parameters in Tab. 4.1 are determined.

In Fig. B.2 the N 1s signal for various BTCDI/Ag(111) monolayer films is depicted. The data in Fig. B.2 (a, b, c) corroborate the finding that the intensity ratio in the core level spectra is sensitive to the annealing conditions. In Fig. B.2 (a), where the film was annealed at 100° C, the relative intensity of the low energy peak is considerably lower than for the remaining spectra, where the film was annealed at 120° C. Furthermore, after recording the spectrum in Fig. B.2 (c) the same sample was cooled to 200 K and the spectrum in Fig. B.2 (d) was recorded. Accordingly, cooling effects the N 1s spectrum significantly in contrast to the C 1s spectrum. In particular the relative intensity of the low–energy peak increases. This is corroborated by the spectrum in Fig. B.2 (e) from a different BTCDI monolayer film.

For the BTCDA/Ag(111) monolayer films annealing has also a significant influence on the electronic structure, similar to the observations for BTCDI. In particular for the not annealed monolayer film in Fig. B.3 (a) a distinct shoulder is observed at $E_B = 284.3$ eV in the leading edge of the prominent C_C 1s peak at $E_B = 285.5$ eV. After annealing the peak maximum is shifted to $E_B = 285.1$ eV and the low energy shoulder is decreased. Additionally the prominent C_O 1s peak is shifted from $E_B = 289.3$ eV to 289.0 eV. Accordingly annealing increases the chemical shifts with respect to the multilayer film. Consequently it can be assumed that annealing increases the interface interaction and the covalent character, respectively. Furthermore, the differential shifts between the two C_C 1s peaks corroborate the statement in *section 4.4.2* that the covalent interface interaction can lead to differential chemical shifts between the satellite and the main peak.

From the fits in Fig. B.1, B.2, B.3 and 4.11 the charge transfer parameters in Tab. 4.1 can be determined under the simplifying assumption that the dashed peaks in the fits can be interpreted as main peak and the peaks plotted with short dashes as satellite contributions. The respective values for the BTCDI and BTCDA monolayer films are shown together in Fig. B.4 and B.5.

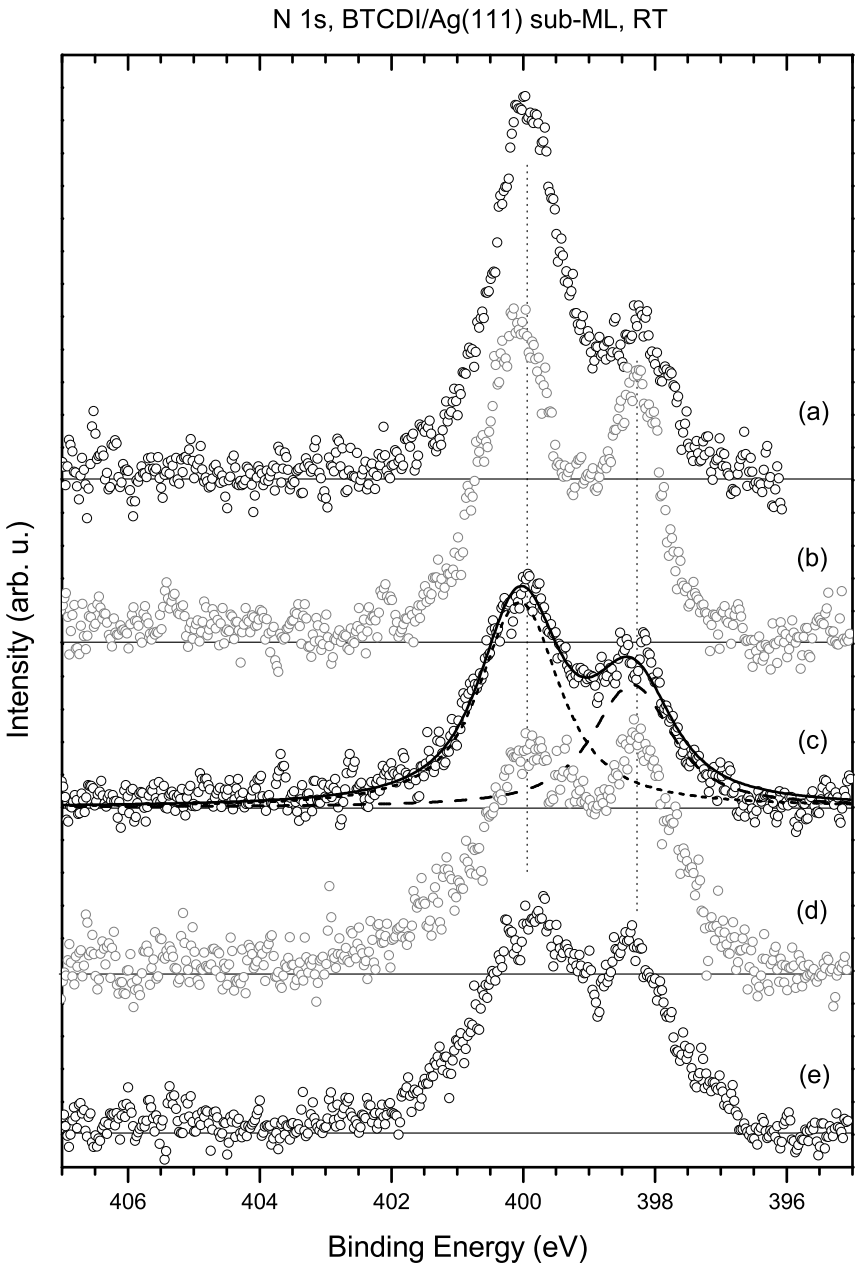

Figure B.2: N 1s core level spectra of various BTCDI/Ag(111) sub–ML films for slightly different conditions, e.g. annealing time t and sample temperature T during the measurements: (a) annealed for $t = 4$ min at 100° C and $T = 300$ K, (b) annealed in two cycles ($t = 10 + 5$ min) at 120° C and $T = 300$ K — same film as for Fig. B.1 (c), (c) annealed in several cycles ($t = 5 + 2 + 1 + 2 + 1$ min) at 120° C and $T = 300$ K — same film as for Fig. B.1 (d, e), (d) the film from (c) measured at T = 200 K, (e) annealed in two cycles ($t = 10 + 3$ min) at 120° C and measured at $T = 210$ K. Additionally, the result of a peak fit for spectrum (c) is shown from which the charge transfer parameters in Tab. 4.1 are determined.

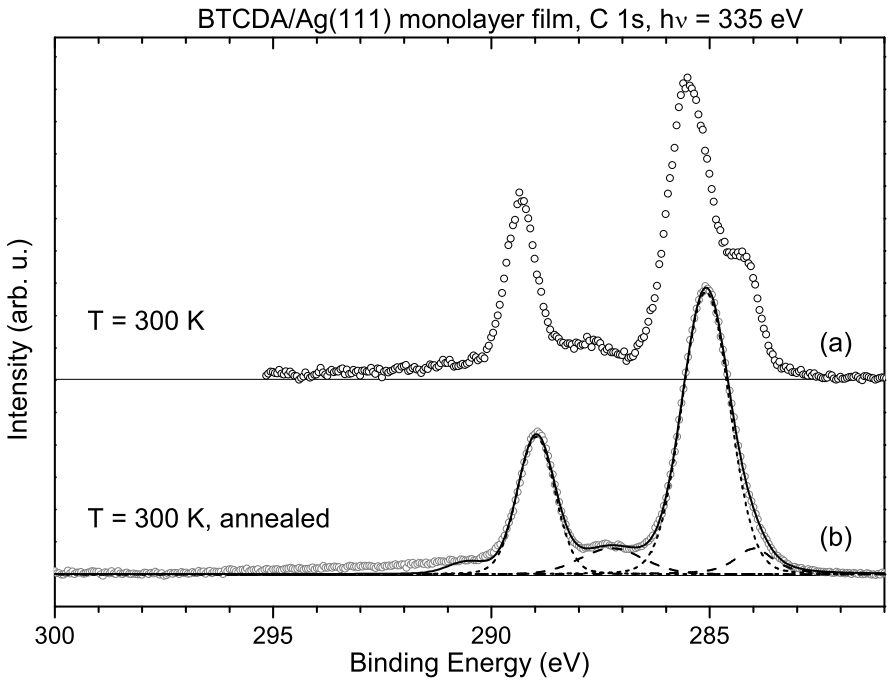

Figure B.3: C 1s core level spectra of two different BTCDA/Ag(111) monolayer films. (a) deposited and measured at 300 K sample temperature and not annealed (b) annealed from a multilayer film for 5 min at 60° C. Additionally the peak fit is indicated from which the charge transfer parameters in Tab. 4.1 are determined.

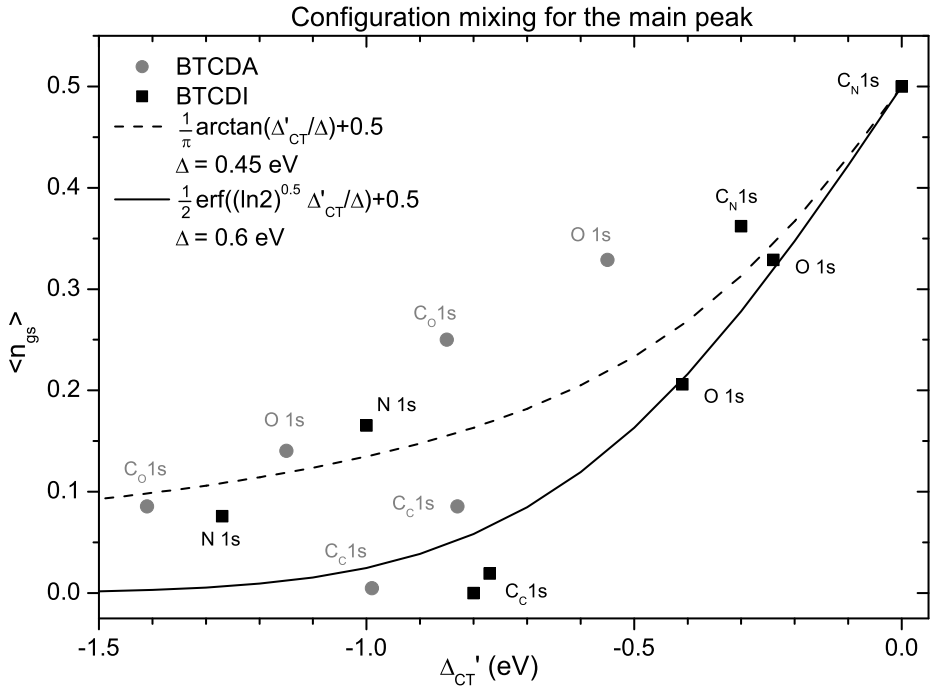

Figure B.4: Configuration mixing for the main peak of different core level signals from the BTCDI and BTCDA sub–ML films. The contribution of the ground state configuration $< n_{gs} > = \cos^2\theta'$ to eigenstate which is related to the main peak is plotted over the charge transfer energy Δ'_{CT} for the minimum and maximum values given in Tab. 4.1. Additionally the arctan function indicates the expected trend for the case that the coupling between the respective molecular level and the substrate states induces a density of adsorbate states distribution $\rho_a(\epsilon)$ which is of Lorentzian shape, and the error function indicates the respective trend for a Gaussian distribution. The example curves are plotted for the coupling parameter $\Delta = 0.45$ eV and 0.6 eV, respectively.

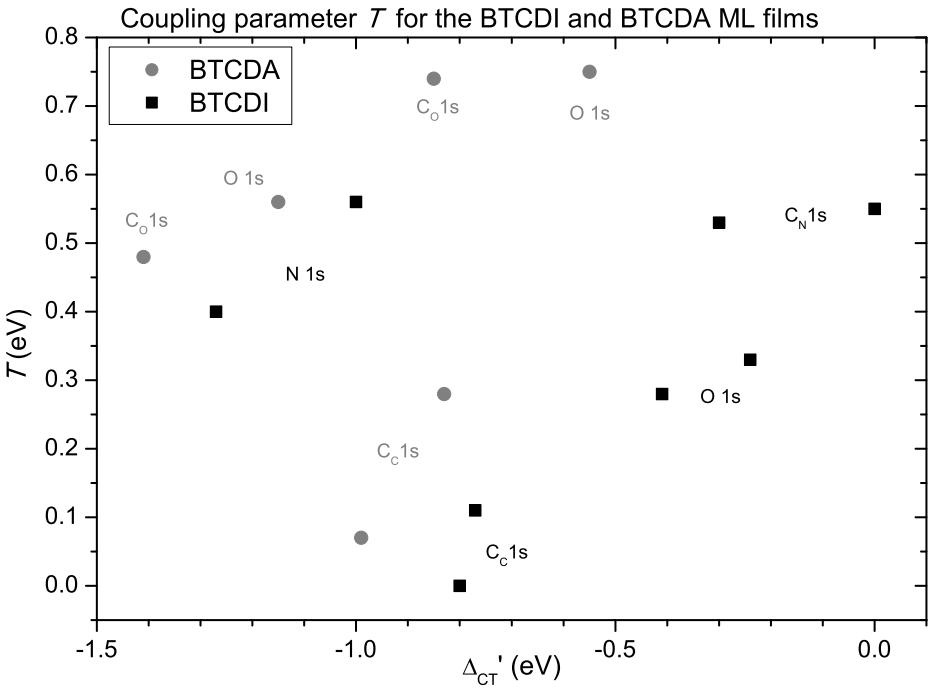

Figure B.5: The values of the coupling parameter T in Tab. 4.1 for the BTCDA and BTCDI sub–ML film, which corresponds to the off–diagonal element of the Hamiltonian H, are plotted over the charge transfer energy Δ'_{CT}. Note, that for each core level two data points are indicated, which correspond to the minimum and the maximum value of T, respectively.

C

Phthalocyanine thin films on Ag(111)

It has been shown in *chapter 5*, that there are significant chemical shifts in the core level and in the valence spectra of the SnPc/Ag(111) monolayer film with respect to the multilayer film. These chemical shift were investigated in detail in [A4]. It was found that they vary with sample temperature and SnPc coverage in the sub–ML regime. In particular two trends were found: Firstly, the chemical shifts in the N 1s and C 1s core level spectra decrease with increasing SnPc coverage from half a monolayer to 1 ML. Secondly, for a SnPc coverage lower than 0.8 ML the chemical shifts were at 130 K sample larger than at room temperature. The magnitude of the chemical shift, was considered as an indicator for the strength of the substrate–adsorbate coupling. This interpretation is in agreement with a previous LEED and XSW investigation of the film structure, in which a variation of the adsorbate–substrate distance was taken as an indicator for the strength of the adsorbate–substrate interaction. [214, 225]

In Fig. C.1 some N K–NEXAFS spectra are shown for different sub–ML coverages and temperatures. As the multilayer spectrum is very similar to that of H_2Pc it is referred to [216] for a detailed assignment of the peaks. The finding that transitions into the LEMO contribute significantly to peak A is important with respect to the current discussion. As the monolayer spectrum resembles the multilayer spectrum well, peak *A* has also contributions from transitions into the LEMO. Its signature and the kink at its leading edge can be interpreted as significant indications for a strong substrate–adsorbate interaction and many–body excitations as it has been discussed in *chapters 4 and 5*. This particular peak is significantly decrease in the monolayer spectrum. This can be related to the partial occupation of the LUMO derived DOS, which becomes evident from the valence spectra in Fig. C.2.

Moreover, peak *A* decreases further with decreasing SnPc coverage and increasing interaction strength, respectively. According to Fig. C.1 (b) and (c) the peak A decreases additionally with decreasing sample temperature, which is also attributed to an increase of the interaction strength. These interrelations imply that the occupation of the LUMO derived DOS can be varied within a certain range. In return the LUMO derived DOS can be studied for different degrees of occupation

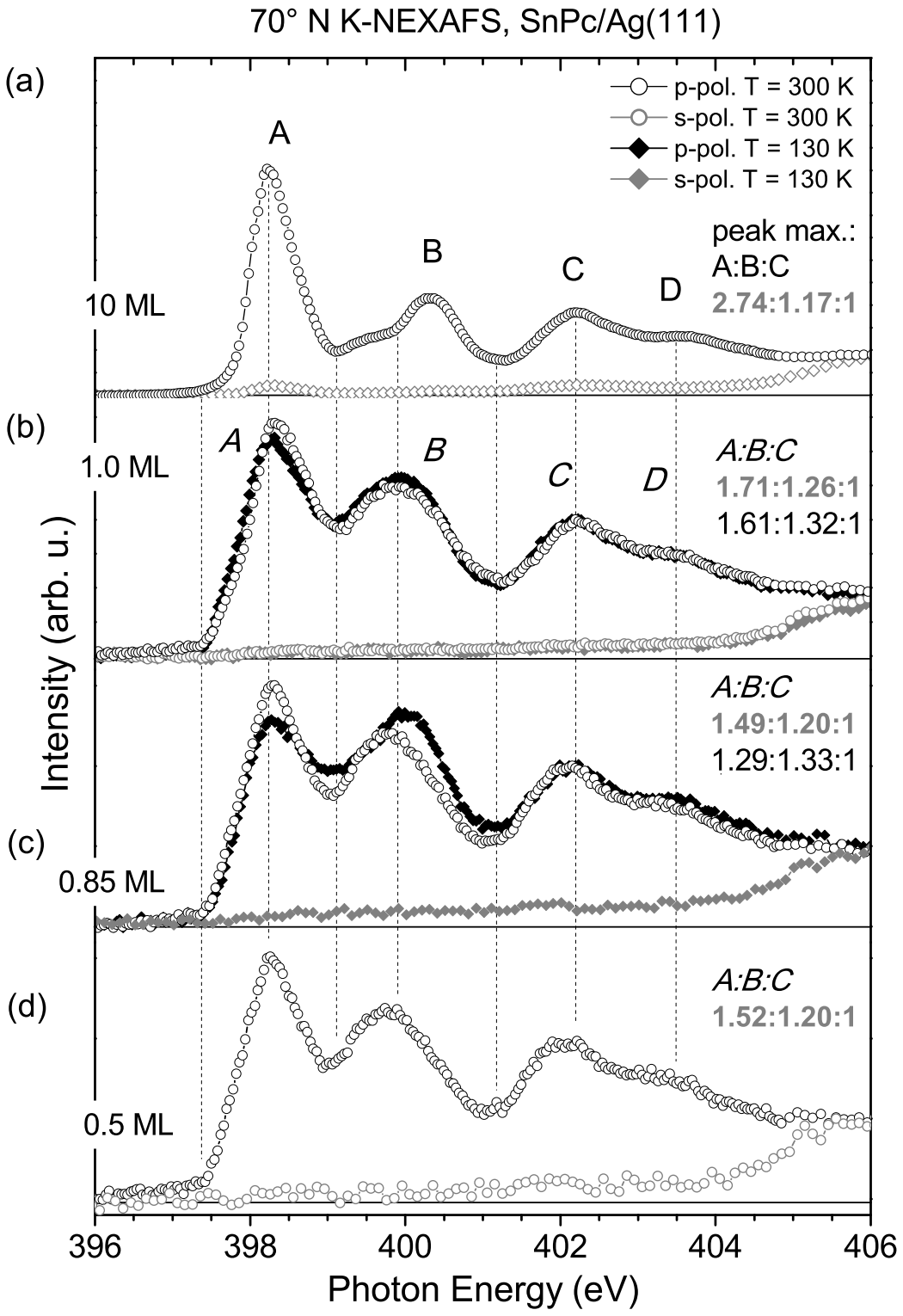

Figure C.1: N K–NEXAFS spectra of a 10 ML SnPc/Ag(111) film and various sub–ML films at room temperature and 130 K sample temperature. On the right hand side the ratio of the peak heights is indicated for (grey) room temperature and (black) 130 K. Note that the peak areas yield the same ttrend. The spectra were recorded with 70° angle of incidence of the x–ray beam. The partial yield detector was operated with 300 V retarding field.

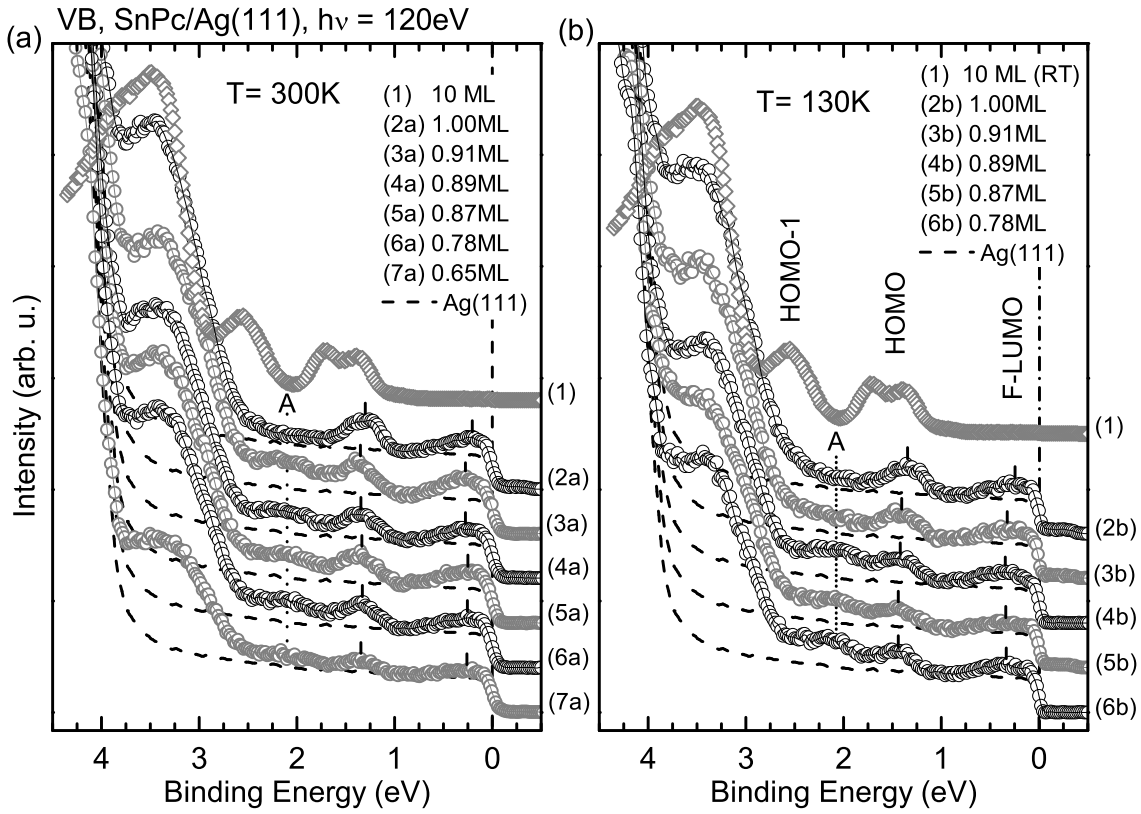

Figure C.2: Angle integrated valence spectra of a 10 ML SnPc/Ag(111) film (top) and different monolayer films at room temperature (a) and 130 K (b). The dashed line indicates the signal from a clean Ag(111) surface. All spectra were recorded at normal emission geometry.

as suggested in *chapter 6* in relation to the Hubbard model. Therefore a series of SnPc/Ag(111) films from 0.65 ML to 1 ML SnPc coverage was investigated at room temperature and 130 K. It seems as if the variations in the spectra are in agreement with the expected trend. For the low temperature films the signature of the LUMO DOS suggests, that it is more occupied than at room temperature, in particular when comparing spectrum (4b) to (4a). However, the variations in the spectra in Fig. C.2 are not very significant despite the film quality was good according to LEED and core level data. However, aspects like energy resolution, count rate, angular dependence and sample temperature allow further optimization of these measurements.

D

Additional resonant Auger spectra

It is mentioned in *chapter 5* that the SnPc thin films have been investigated with resonant Auger spectroscopy at the C K and N K adsorption edge. However, only the most important data of the C K-edge is discussed in this chapter in order to keep it tight. Some complementary data is shown in this appendix, which confirms the interpretation of the resonant Auger spectra in *chapter 5* and additionally hints to related aspects.

D.1 SnPc/Ag(111) multilayer film

A two–dimensional autoionization spectrum is depicted in Fig. D.1 for a SnPc multilayer film at the N K absorption edge for p–polarized light. Accordingly the upper valence signal is considerably enhanced for 398.2 eV photon energy. This enhancement can be attributed to participant decay of the core excited state, which increases the CIS signal from the HOMO and HOMO-1. Note that the intensity of the HOMO-1 signal is considerably higher than that of the HOMO signal, whereas it is vice versa at the C K–edge. This can be interpreted so that the HOMO-1 has a higher density at the nitrogen species than at the carbon species and that it is vice versa for the HOMO. Furthermore, the broadening of the HOMO peak at resonance ($h\nu = 285.3$ eV) was attributed to interference and electron–vibration coupling. A similar broadening of the HOMO and HOMO-1 peak can be observed for 398.2 eV photon energy. In particular the two peaks are separated off resonance, but at resonance both contributions are broadened so that they overlap in kinetic energy.

Moreover, various autoionization spectra are compared to each other in Fig. D.2. These multilayer spectra have a rich fine structure, which changes considerably with photon energy. These spectator shifts and variations in the relative intensity of the different features are in agreement to the finding for the C K–edge.

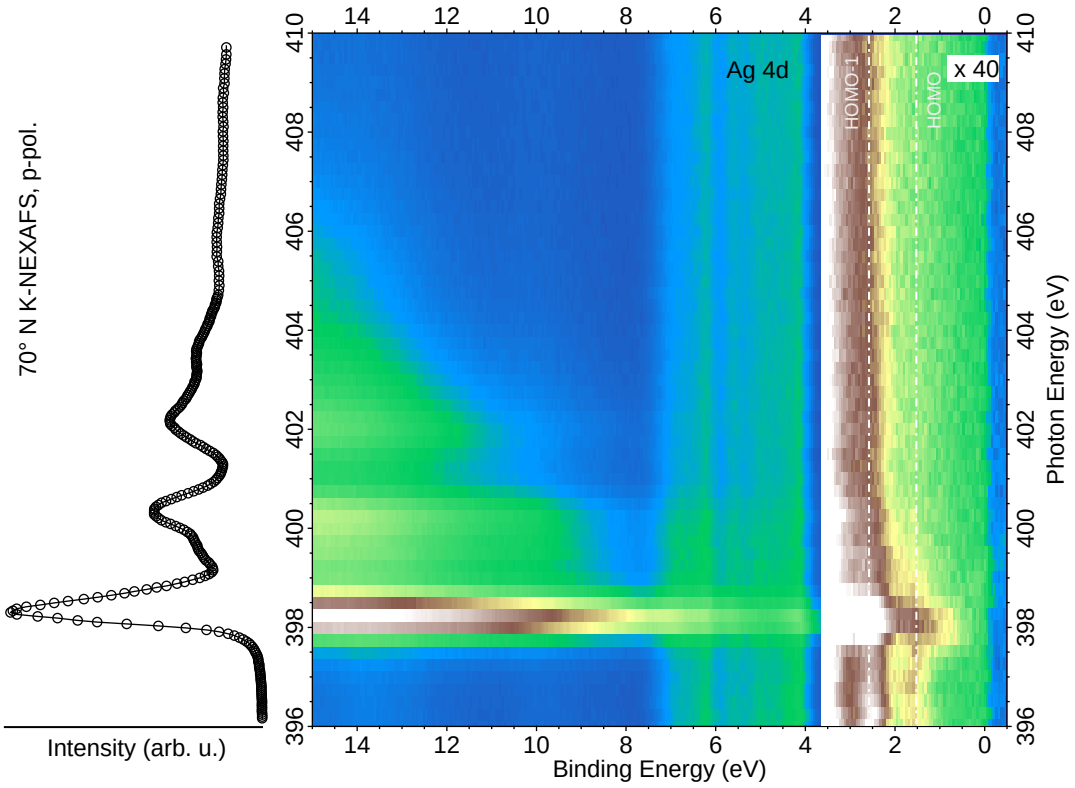

Figure D.1: (Color online) Photon energy dependence of the EDCs at the N K–absorption edge for a SnPc/Ag(111) multilayer film recorded at 70° angle of incidence with respect to the surface normal and p–polarized light. The signal between 0.5 eV and 3.5 eV binding energy is multiplied by 40 in order to visualize the resonant enhancements. The vertical lines mark the energy position of the CIS signal of the HOMO and the HOMO-1 off resonance. The corresponding N K–NEXAFS spectrum is plotted on the left hand side for better orientation.

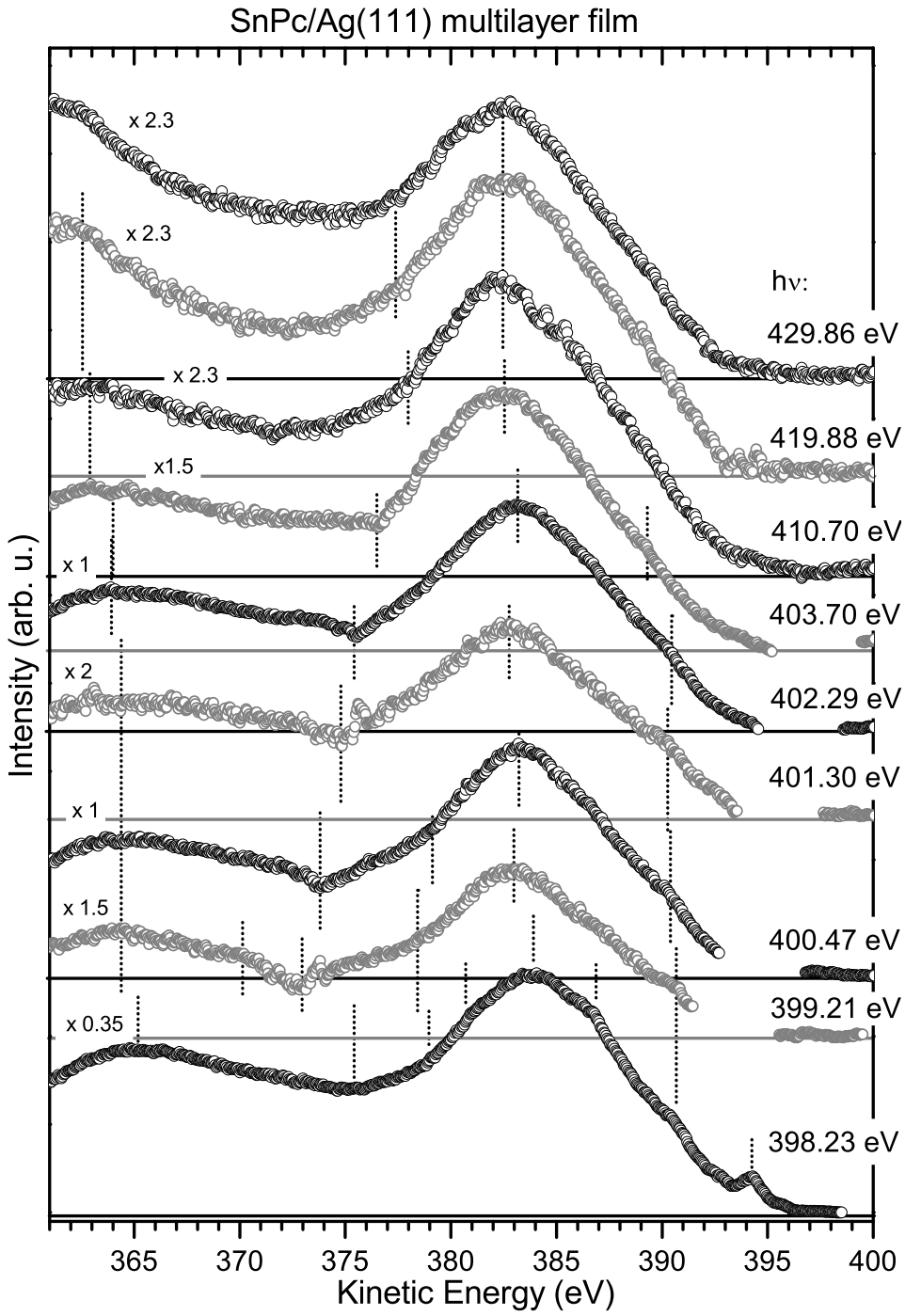

Figure D.2: N K–autoionization spectra of a SnPc/Ag(111) multilayer film for the photon energies indicated at the right hand side. The measurements were carried out for 70 ° angle of incidence and p–polarized x–ray light. The autoionization spectra are obtained from the EDCs by subtracting the PES contribution, which was recorded separately with hν = 395.60 eV. The energy position of some spectral features is indicated by vertical lines for better comparison.

D.2 SnPc/Ag(111) monolayer film

A two–dimensional autoionization spectrum for a SnPc/Ag(111) monolayer film is depicted in Fig. D.3 together with the respective N K–NEXAFS spectrum. The differences in the NEXAFS spectrum with respect to the multilayer spectrum are further discussed in *appendix C*. Note that the autoionization signal is very weak compared to the Ag 4d signal. Nevertheless one observes resonant enhancement of the valence signal between 0 eV and 4 eV binding energy for 398 eV and 399.8 eV photon energy. Moreover for $h\nu = 398$ eV the autoionization signal contributes continuously from the Fermi level to higher binding energy, analogous to the step–like autoionization signal in Fig. 5.16. As for the multilayer film the HOMO related CIS signal contributes only little to the N K–autoionization signal one can assume that this applies also for the monolayer film. Hence the autoionization signal between 0 eV and 2 eV binding energy in Fig. D.3 can be associated with signal from the LUMO. The inset in the upper left indicates that the signature of the autoionization changes when tuning the photon energy through the resonance which is related to interference effects as it is discussed in *section 5.2*. Moreover, this change in signature is similar to the interference effects in *section 5.2.2* and *5.2.4*, which were associated with electron–vibration coupling.

In Fig. D.4 some autoionization spectra are plotted for excitation energies corresponding to a maximum or a minimum in the N K–NEXAFS signal. The signature and the energy position of the spectral features is similar for the different curves. This is in agreement with the findings for the C K absorption edge in *section 5.2.3*.

Fig. D.5 shows a series of valence spectra over the binding energy scale when tuning the photon energy through the first two C K–NEXAFS peaks. Note that the depicted spectra are identical to those plotted in Fig. 5.17 over the kinetic energy scale. Therefore it is referred to section 5.2.2 for a detailed discussion of the data.

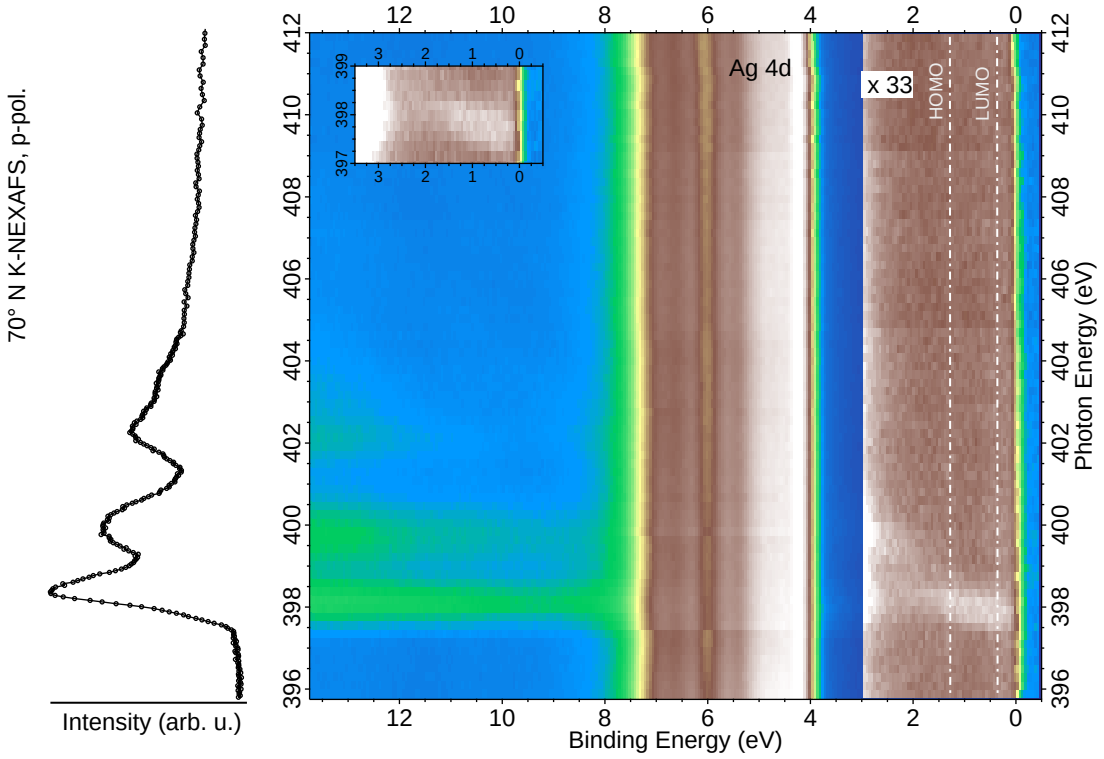

Figure D.3: (Color online) Photon energy dependence of the EDCs at the N K–absorption edge for a 1 ML SnPc/Ag(111) film recorded at 70° angle of incidence with respect to the surface normal and p–polarized light. The signal between 0.5 eV and 3.0 eV binding energy is multiplied by 33 in order to visualize the resonant enhancements. The vertical lines mark the energy position of the HOMO and the LUMO contribution off resonance. The corresponding N K–NEXAFS spectrum is plotted on the left hand side for better orientation.

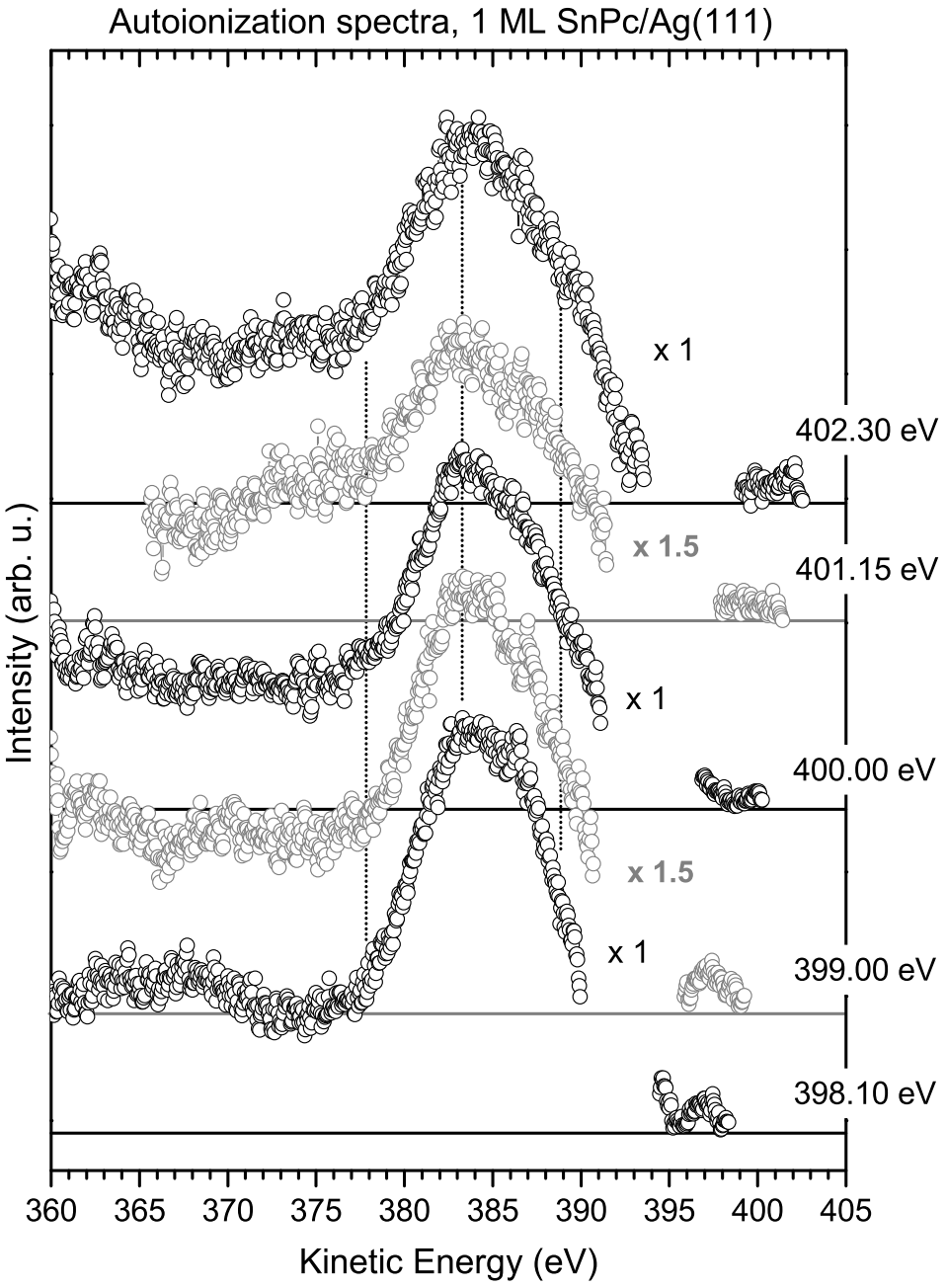

Figure D.4: N K–autoionization spectra of a SnPc/Ag(111) monolayer film for the photon energies indicated at the right hand side. The measurements were carried out at 70° angle of incidence for the p–polarized x–ray light. The autoionization spectra are obtained from the EDCs by subtracting the PES contribution, which was recorded separately with hν = 394.90 eV. The energy position of some spectral features is indicated by vertical lines for better comparison.

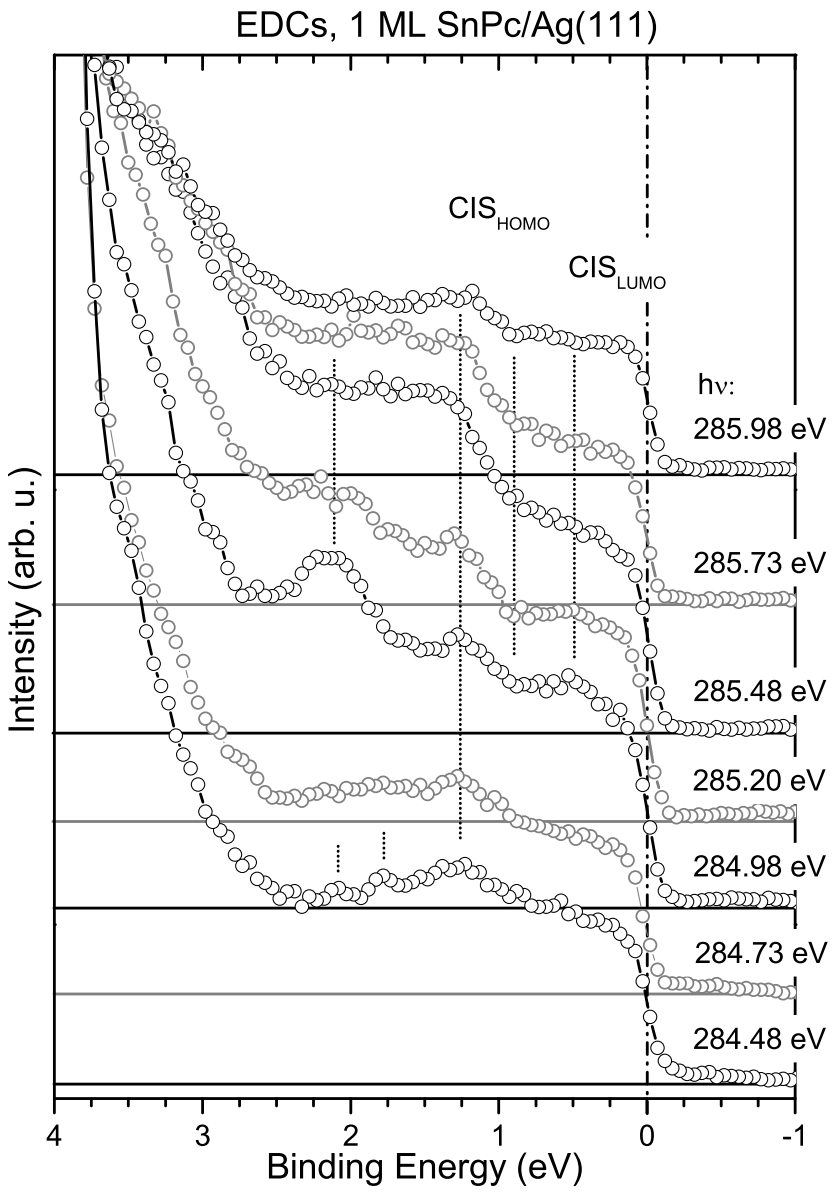

Figure D.5: Comparison of the valence EDCs of a 1 ML SnPc/Ag(111) film for the photon energies indicated in Fig. 5.14. The spectra were recorded at 70° angle of incidence for the p–polarized x–ray light. Note that the depicted spectra are identical to those plotted in Fig. 5.17 over the kinetic energy scale.

D.3 SnPc/PTCDA/Ag(111) film

Some valence EDCs for the heteromolecular SnPc/PTCDA/Ag(111) film are plotted in Fig. D.6. In principle these spectra reflect the trend in the SnPc/Ag(111) multilayer. Consequently they corroborate the finding from *section 5.2.4*, namely that the interaction between the SnPc and the PTCDA layer is weak and comparable to the intermolecular interaction in the multilayer film. In particular no significant resonant enhancement of the upper valence signal is observed except for 398.35 eV photon energy. In this EDC the signal of the HOMO-1 of SnPc is little enhanced due to participant decay as well as the signal from lower lying states. In contrast, the HOMO signal is not significantly enhanced.

Moreover, some valence spectra of a PTCDA/Ag(111) monolayer film are depicted in Fig. D.7 for selected photon energies,[1] which correspond to those indicated in Fig. 5.19 and 5.20. In principle the spectra have a broad signature, similar to what is observed for the SnPc/Ag(111) monolayer film. Moreover, the energy positions of the features α and γ depend on the excitation energy. The feature α shifts to higher kinetic energy with increasing photon energy and γ shifts to lower kinetic energy with increasing photon energy, in particular for excitations at the functional group for $h\nu = 298.1$. This is somewhat different to what was found for the SnPc/Ag(111) monolayer film, where only minor differences between the various autoionization spectra were observed. It might be related to the fact that the various carbon species in the phthalocyanine molecule are chemically similar but very different in case of PTCDA. The core level and NEXAFS spectra in Fig. 4.5 and 4.6 indicate that the carbon species in the functional group of the PTCDA molecule, differ strongly from the species in the perylene ring. In particular in the NEXAFS spectrum the difference in excitation energy between transitions into the LUMO+1 at the perylene ring and at the functional group is of the order of 4 eV. [46] But the energy separation between peak A and B in the C K–NEXAFS of the SnPc multilayer film in Fig. 5.6 is only ~ 1 eV. Note that these peaks A and B are attributed to transitions into the LEMO at the phenyl rings and at the C_N carbon species next to the nitrogen atoms, respectively.

[1] These particular spectra were recorded and normalized by J. Ziroff

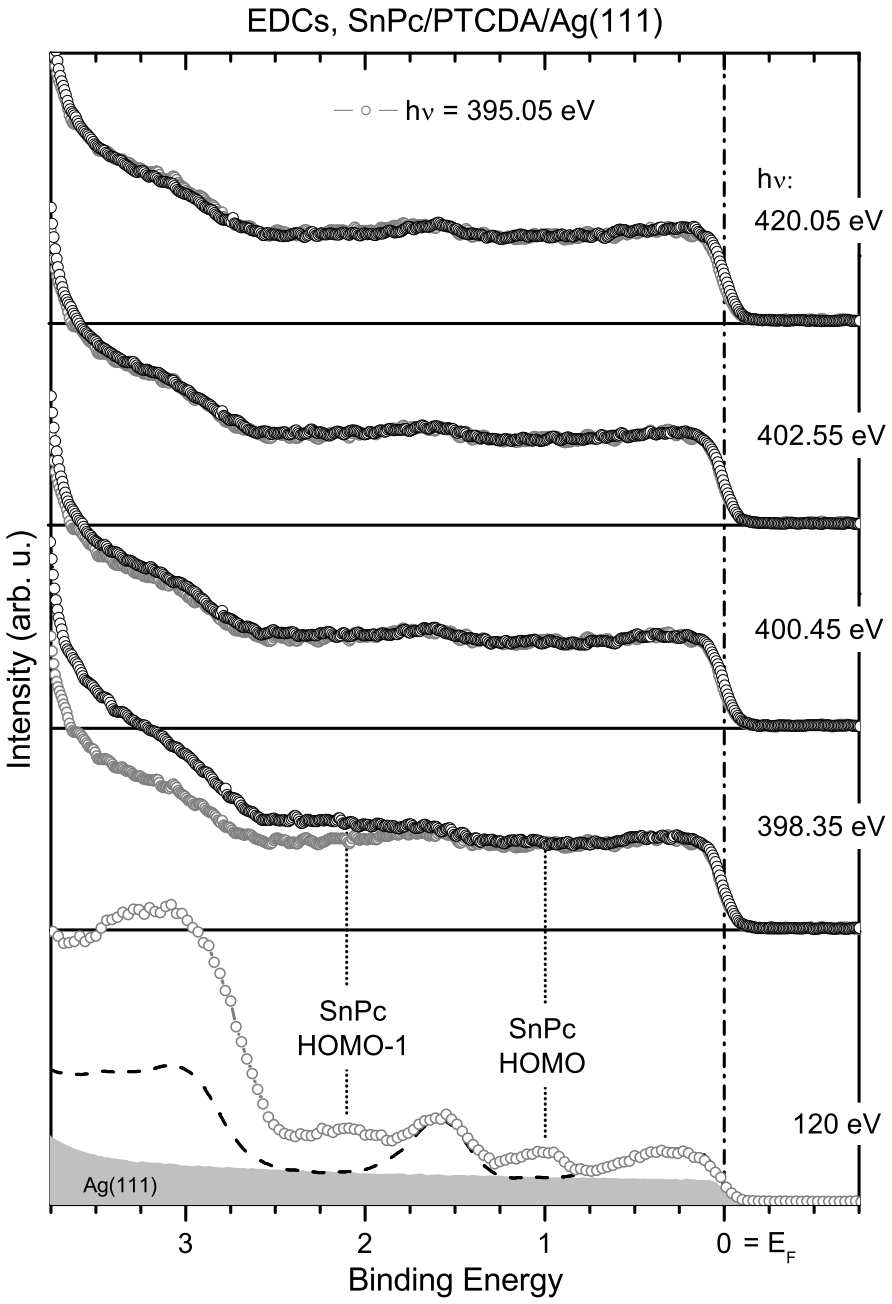

Figure D.6: Comparison of the valence EDCs of a SnPc/PTCDA/Ag(111) film for the photon energies indicated at the right hand side. The EDCs for photon energies higher than 395 eV (black) are plotted above the photoelectron spectra recorded at hν = 395.05 eV and 120 eV (grey) for better comparison. For hν = 120 eV the angle integrated valence spectrum of the clean Ag(111) surface is shown additionally as grey area.

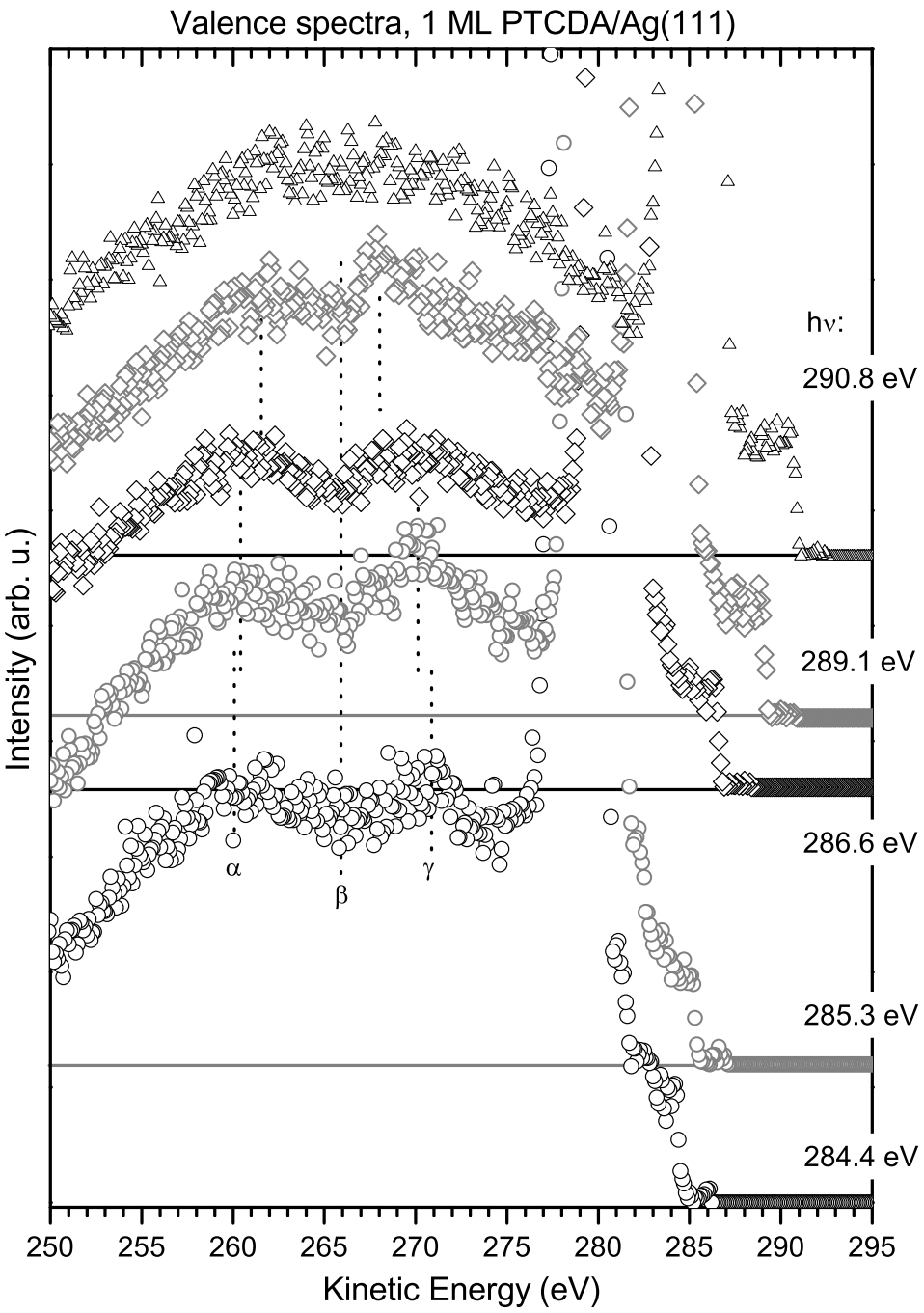

Figure D.7: Valence spectra for a PTCDA/Ag(111) monolayer film for the photon energies indicated in Fig. 5.19 and 5.20. Note that the raw spectra are shown including the contribution from the substrate.

E

Organic–inorganic semiconductor interface — alkyl/Si(111) SAMs

Self–assembled monolayers (SAMs) from alkyl chains which are directly bound to a silicon substrate have recently attracted attention due to several reasons. One aspect is that the alkyl–terminated silicon surface is comparatively inert and that these SAMs can be produced by hydrosilation, a wet chemical process, which in principle allows comparatively cheap mass production of such devices. [42, 293] Therefore those SAMs are useful for coating silicon based semiconductors. Additionally, they are interesting for organic electronics. The goal is to tailor the electronic and optical properties of such SAMs simply by choosing suitable molecules or by penetrating the molecular film in a controlled way which might even allow nano–patterning. [294] Therefore systematic studies of the interface interaction are necessary. In this context alkyl SAMs on silicon surfaces are promising as these systems allow to control and tune various interface properties. [295–297] Recent investigations of several collaborating groups were particularly focused on aspects that influence the charge transport through such SAMs. [39, 40, 68, 297–301, A2] Therefore a good knowledge of the electronic structure is crucial, in particular of the interface properties.

In this context these SAMs have been study by PES and NEXAFS with respect to three aspects: the electronic (band) structure in the alkyl chains, the alkyl/Si interface bond and how the electronic structure can be modified by irradiation with electrons and x–rays, which might be interesting for nano–patterning and lithography. The electronic band structure was investigated with photon–energy dependent UPS as discussed in detail in [A5]. The important aspects of these publications will be briefly summarized in *section E.1*, and additional material will be discussed, which facilitates the description of the electronic band structure. Furthermore, the influence of electron and x–ray irradiation on the alkyl SAMs was studied with PES and NEXAFS. Some of the results were already published in [A1, A2] and others will be discussed briefly in *section E.2*. Finally, some results are shown in section E.3 concerning the interface states due to the covalent alkyl–Si bond.

E.1 From single molecular orbitals to electronic bands

E.1.1 Brief review of the electronic band structure measurements

The electronic band structure of different alkyl/Si(111) SAMs with $C_{12}H_{25}$, $C_{14}H_{29}$, $C_{16}H_{33}$ and $C_{18}H_{37}$ chains was investigated using PES with variable photon energy between 20 eV and 200 eV. A typical data set is shown in Fig. E.1. Accordingly, significant dispersion is observed in particular for the C 2p band. Strong DOS effects contribute due to the finite chain length and an intermediate degree of order in the SAMs. It was discussed in [A5] for example that the wiggles in the C 2s band between $E_B = 15$ eV and 20 eV correspond to the different electronic states in the C 2s band. Moreover, instead of peak shifts as it is generally expected for dispersion, only a variation of the relative intensity is observed when tuning the photon energy from 30 eV to 95 eV.

The contribution of the finite alkyl chain length to this DOS effect was modeled by assuming one–dimensional quantum well states, which are confined at the single alkanes. As k is not a good quantum number for such short chains, the respective states are smeared out in momentum space. Consequently the alkyl band structure could be simulated by a number of equidistant quantum well states, which are broadened in k by a Gaussian distribution and follow the dispersion relation for polyethylene as it is illustrated in Fig. E.2. The disorder in the molecular layer was taken into account by considering an ensemble of molecules with slightly different orientation with respect to the surface normal. With this model the trends in the PES data could be well simulated. An remarkable aspect was that even the PES data for the comparatively short $C_{12}H_{25}$ SAM agrees well with this simulation which suggests that even for such short molecules the band structure is comparatively similar to that for polyethylene.

In the following it can be shown, that the discussed simple quantum well approach is compatible with the results from quantum chemical molecular orbital calculations. Moreover, this comparison even allows to model the $E(k)$ band structure of linear molecules from these calculations. Consequently, it is demonstrated that already pentane molecules resemble very well the $E(k)$ relation of polyethylene, which corroborates the experimental finding.

E.1.2 Quantum well states

The molecular orbitals of several alkanes of different length from C_5H_{12} to $C_{34}H_{70}$ were calculated with DFT using the B3LYP functional and a 6–31g basis set. For

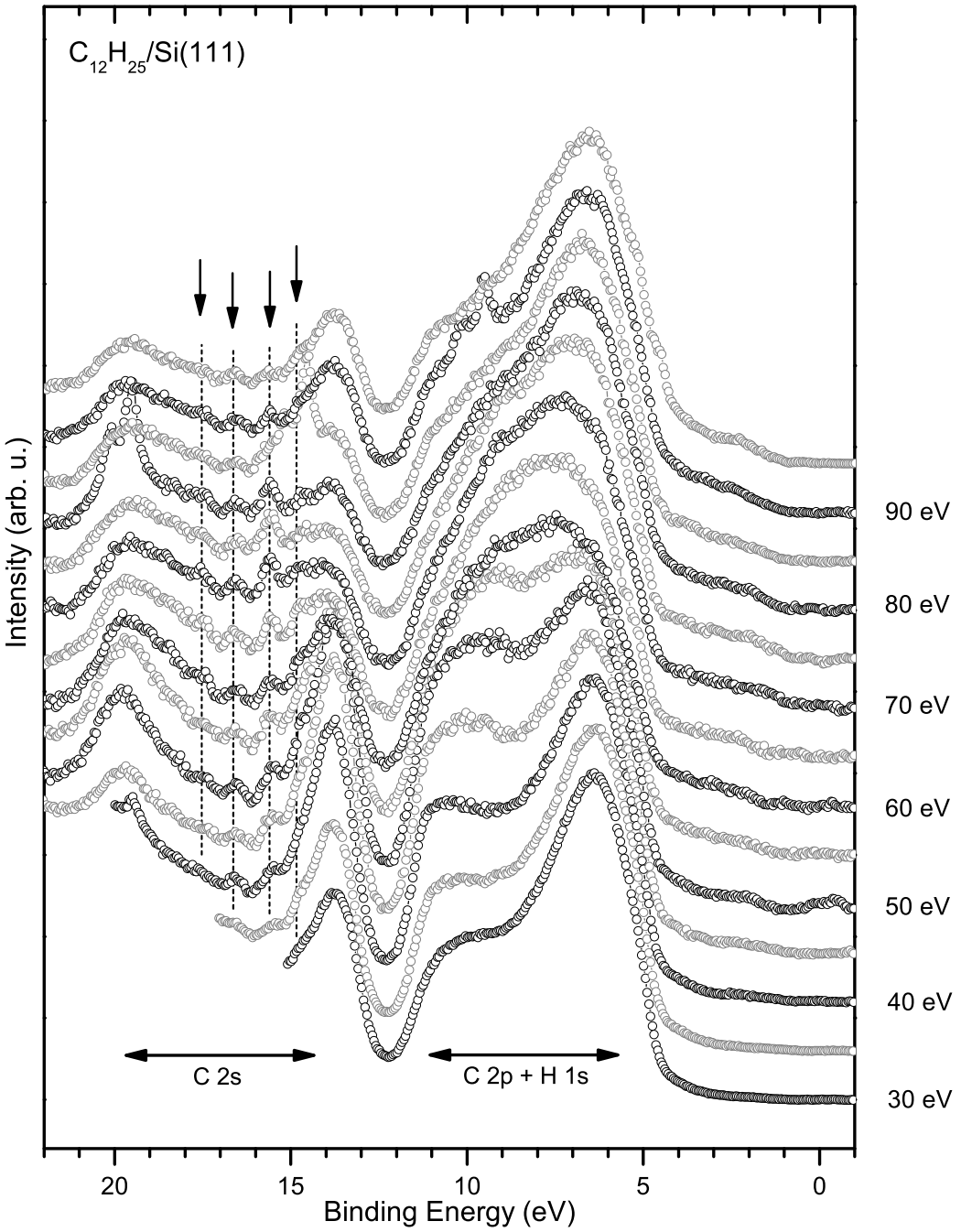

Figure E.1: Photon–energy dependent UPS spectra of the valence band structure of $C_{12}H_{25}$/Si(111). The data were recorded in normal emission geometry at the UE112–1PGM2 beamline at BESSY II with 2° analyzer acceptance angle. The arrows indicate the energy position of some C 2s states.

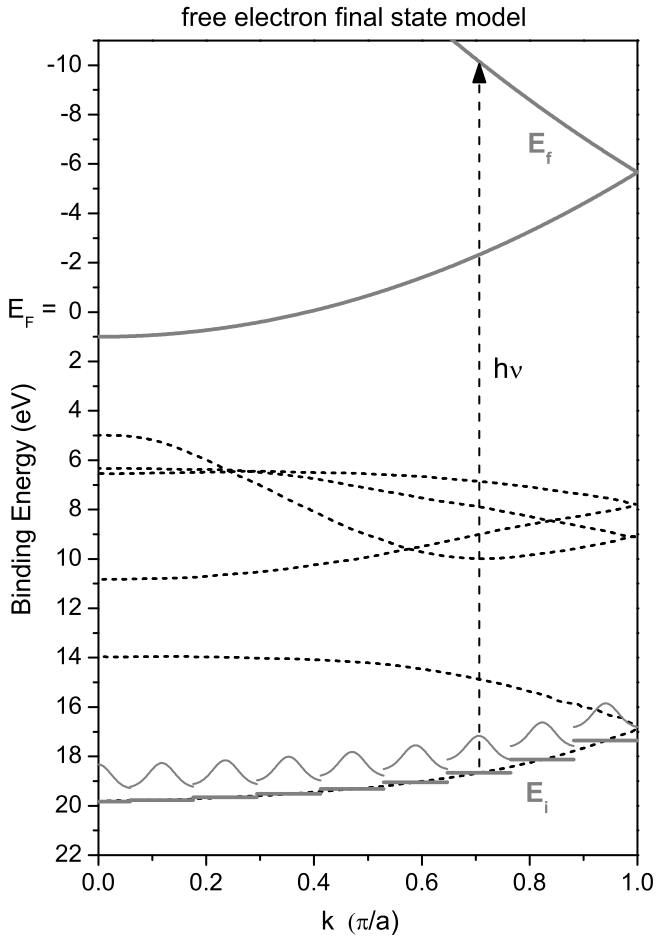

Figure E.2: Alkyl band structure modeled by quantum well states, which follow the dispersion relation $E(k)$ of polyethylene. The polyethylene band structure (dashed, black), the free electron final state E_f (solid, grey) and the quantum well states E_i (solid grey) are depicted. The finite length of the alkanes is taken into account by modeling the density of each quantum well state by a Gaussian in k direction.

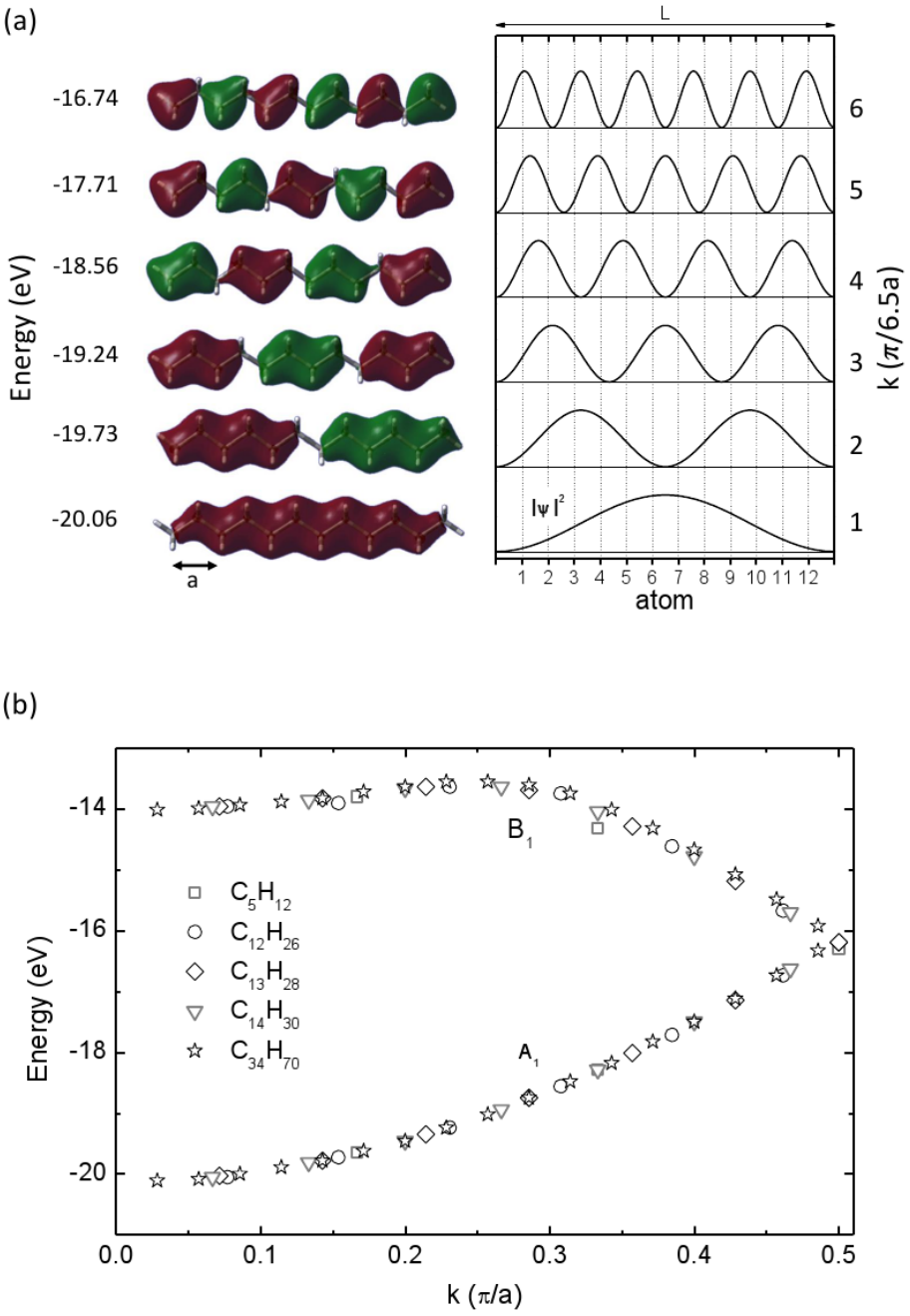

Figure E.3: (a) Analogy between the molecular orbitals of $C_{12}H_{26}$ (left) and states in a 1D quantum well (right). The molecular orbitals which are calculated with DFT and local density approximation correspond to the electronic states of the A_1 branch of the C 2s band. (b) $E(k)$ relation which is obtained by assigning the k value of the corresponding quantum well state to the molecular orbital.

all molecules an analogy could be found between the molecular orbitals from these calculations and the states for a one–dimensional quantum well. In Fig E.3 (a) it is shown exemplarily for $C_{12}H_{25}$ that the molecular orbitals and the quantum well states can be classified by the number of nodes and antinodes. It is obvious that for the quantum well the energy of the eigenstates increase with increasing number of nodes. The same trend is also found for the molecular orbitals of the C 2s band. Consequently the quantum number k of the respective quantum well can be assigned to each molecular orbital with energy E according to the DFT calculations. Therefore the comparison between molecular orbital and quantum well states yields a $E(k)$ relation.

A brief discussion for $C_{12}H_{25}$ demonstrates how the quantum number k is determined by this approach. For the ith state of the one–dimensional quantum well with length L it is

$$k_i = i\frac{\pi}{L}.$$

If one assumes that this quantum well is due to a linear chain of 12 atoms with interatomic distance d, then it is $L = 13d$. As the alkanes consist of a two atomic repeating unit of length $a = 2d$, which corresponds to the unit cell for the limit of an infinite chain, one can write $L = 6.5a$. In general this gives the relation for a linear chain consisting of n atoms with a two–atomic repeating unit:

$$k_i = i\frac{2\pi}{(n+1)a}$$

In Fig. E.3 (b) the $E(k)$ relation for the C 2s band is shown for various alkanes of different length. The energies of the different electronic states are calculated via DFT and the respective k values are assigned by comparing the molecular orbitals to 1D quantum well states as illustrated in Fig. E.3 (a). Fig. E.3 (a) shows that the so determined $E(k)$ relations agrees remarkably well with experimental data and true band structure calculations for ethylene. [302–308] Therefore this approach is straightforward for determining $E(k)$ relations from calculations or measurements which yield the binding energy and the orbital shape of electronic states, e.g. scanning tunneling microscopy or molecular orbital tomography with PES. [150, 309] Furthermore, Fig. E.3 (b) indicates the $E(k)$ relation of very short alkanes as pentane is already very similar to that for the infinite polyethylene chain.

This quantum well approach cannot only be of use in one–dimensional systems, but it can also be successfully applied to two and three–dimensional systems. The

electronic structure of thin metal films for example can be modeled by considering a quantum well in the direction of the surface normal. [310–315] Moreover, for coronene and hexa–benzopericoronene monolayer films a two–dimensional $E(\vec{k})$ relation is observed which resembles very well the band structure of graphene. [316]

E.2 Sensitivity to x–ray irradiation

It has been shown, that irradiation modifies the electronic structure which increases the electric conductivity through the SAM. [A1, A2] Therefore the sensitivity to x–rays, UV light and electron bombardment was studied in detail at the UE52–PGM beamline at BESSY II. Some of the key results are discussed here briefly.

In the first experiment several C K–NEXAFS spectra were recorded at the same spot on the sample. These measurements were done at fixed angle of incidence with respect to the surface normal (70°) and the polarization of the x–ray light was changed via the undulator. Various spectra were recorded quickly with alternating polarization (p, s, p, s...). The C K–NEXAFS spectra in Fig. E.4 contain three features at 284.5eV, 287 eV and 291 eV. In general only C 1s $\rightarrow \pi$ transitions contribute at photon energies below 286 eV. However, the signature of this signal is not as narrow as it is expected for transitions into π orbitals. Consequently the interpretation of this feature is not straightforward and therefore it will be discussed below. Moreover, the peaks at 287 eV and 291 eV can be associated with transitions into unoccupied σ symmetric C–H orbitals and C–C orbitals. Additionally, the average molecular orientation can be estimated from the linear dichroism for these σ peaks. [35] Accordingly the alkyl chains are predominantly standing upright with an average tilt angle of ca. 35° with respect to the surface normal, which is compatible with the findings from the band structure measurements in [A5].

Two major modifications are observed in the C K–NEXAFS spectra in Fig. E.4 with continuous irradiation. The peak at 284.7 eV increases for s– and p–polarization and the σ_{CC} contribution decreases in the spectra for p–polarization, whereas the intensity of the σ_{CH} peaks remains constant. This becomes even more evident in Fig. E.5, where the peak areas are plotted over the total emitted charge from the sample, which can be estimated by integrating the sample current over the irradiation time. Note that this is a measure for the irradiation dose, because

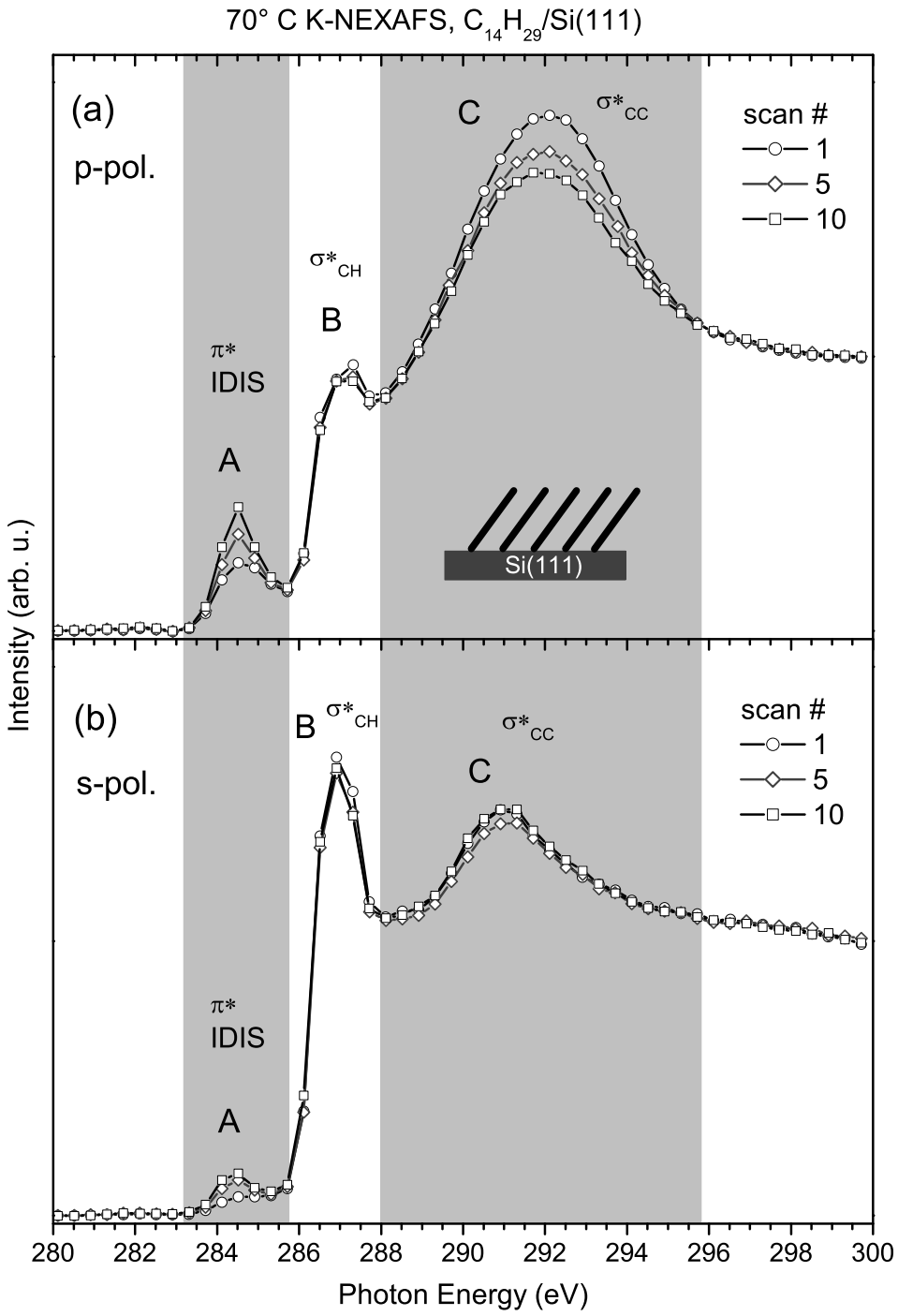

Figure E.4: 70° C K-NEXAFS of $C_{14}H_{29}$/Si(111) for increasing x-ray irradiation. The shaded areas indicate the energy range over which the spectra are integrated in order to determine the areas of the peaks A, B and C. The respective values are plotted in Fig. E.5 versus the radiation dose for the whole series of scans.

all spectra are recorded at the same spot at the sample which has a size of ca. $50 \times 500\,\mu m^2$.

Fig. E.5 illustrates the evolution of the area of (top) the 284.5 eV peak for the photon energy range indicated by the grey shading in Fig. E.4, (middle) the area of the σ_{CH} peak and (bottom) the area of the σ_{CC} peak. There is a monotonic increase of the 284.5 eV peak with increasing irradiation for both polarizations and a decrease of the σ_{CC} peak for p–polarization. Consequently the x–ray irradiation induces the formation of π orbitals, which is known for alkanes. [317–320] The fact that no significant modifications are observed for the σ_{CH} peaks indicates that the average molecular orientation of the alkyl chains does not change significantly with x–ray irradiation. Consequently the decrease of the σ_{CC} peak for p–polarization can be attributed to a change of the intramolecular electronic structure.

This is corroborated by the observation that the increase of the 284.5 eV peak from $0 - 3\,\mu C$ in Fig. E.5 is for p–polarization twice as large as for s–polarization. As for alkenes, e.g. for ethene or propene, the symmetry plane of the π orbitals is parallel to the molecular axis and the alkyl chains in the SAM are standing predominantly upright one expects exactly the opposite behavior. [35, 170] Another interesting aspect with respect to Fig. E.5 is the fact that the intensity of the 284.5 eV peak is relatively high in the first spectra compared to the increase with strong irradiation. Consequently, this signal cannot only be due to degradation from the irradiation but already the pristine sample contributes to the signal at 284.5 eV. Furthermore, in the first spectra in Fig. E.4 the signature of this signal is very broad, which is untypical for C 1s $\rightarrow \pi$ transitions. In particular the 284.5 eV peak for scan 1 in Fig. E.4 (a) rather resembles the signature of a σ resonance. As this peak is not observed for free alkanes it can be attributed to the interaction with the interface. [35, 170]

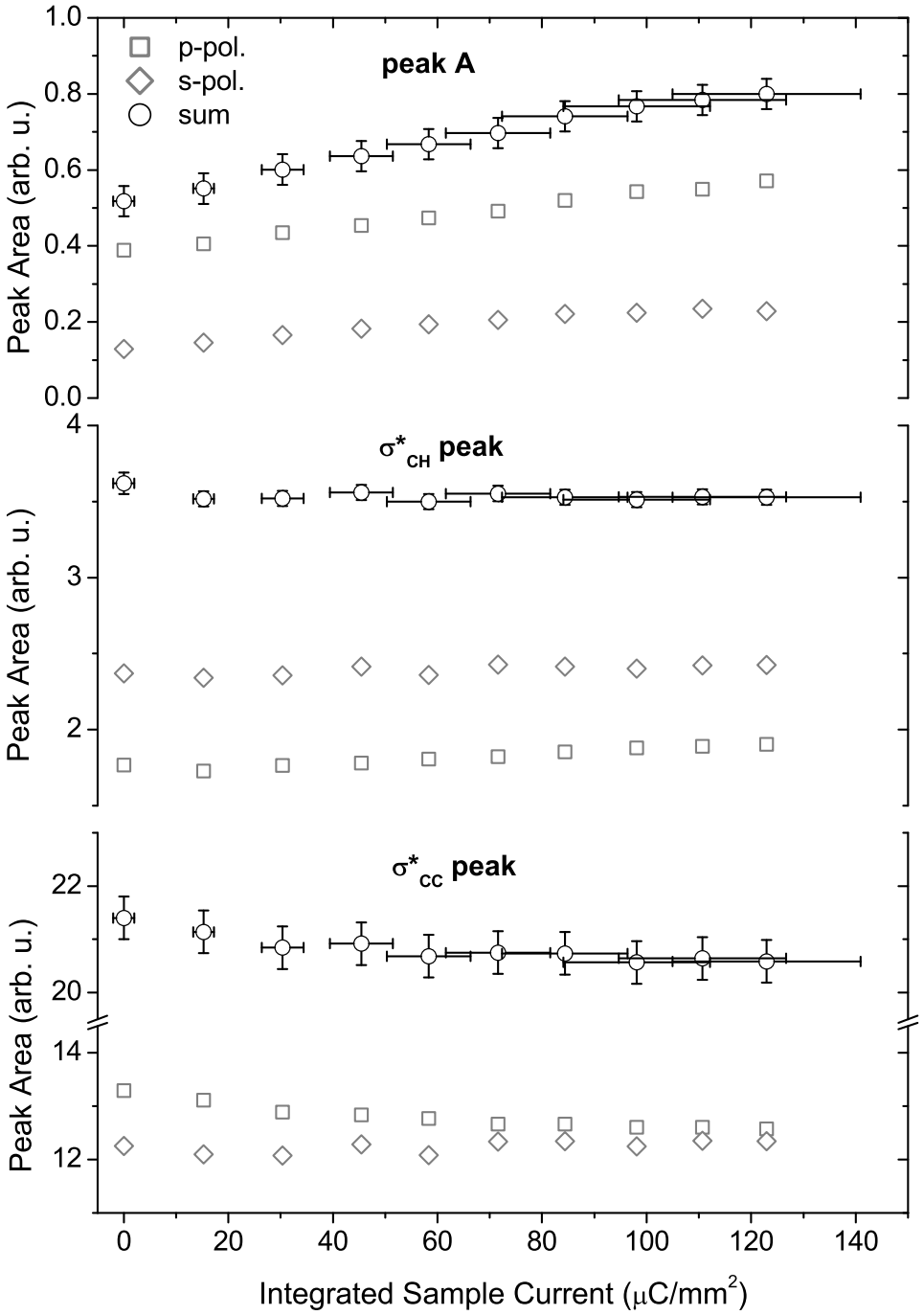

Figure E.5: Intensity of peak A, B and C in the C K-NEXAFS of $C_{14}H_{29}$/Si(111) for increasing x-ray irradiation. The x–axis gives a measure for the irradiation dose. It corresponds to the sample current integrated over time divided by the size of the illuminated spot at the sample. The values for 0 μC/mm^2, 58 μC/mm^2 and 123 μC/mm^2 are obtained from the spectra plotted in Fig. E.4.

E.3 Induced density of interface states

The formation of covalent Si–C bonds implies strong covalent adsorbate–substrate interaction and the formation of interface states, similar to what was discussed in the *chapters 4* and *5*. Furthermore silicon has a indirect band gab of only 1.1 eV while for the alkyl molecules the HOMO–LUMO gap is of the order of 5-7 eV. [39, 68, 300] Consequently, one expects that the formation of a density of substrate–adsorbate states leads to a continuous widening of the electronic gap at the interface when going from silicon (bulk) into the alkyl molecules, as it is schematically illustrated on the right hand side of Fig. E.6. Consequently, the interaction at the alkyl/Si interface leads to an induced density of interface states (IDIS) at the molecules. This scenario was verified by calculations of the electronic structure of these alkyl/Si(111) SAMs. [68]

From this picture it becomes evident that the C K–NEXAFS has contributions from excitations into the IDIS which contributes at lower photon energies than the C 1s $\rightarrow$ LEMO signal for the free alkane molecule. The dichroism for the 284.5 eV peak, namely the fact that its intensity is higher for p–polarization than for s–polarization is compatible with Si–C orbitals of σ symmetry. Furthermore, the new electronic states that are created by the x–ray irradiation have a similar symmetry. Consequently the increase of this peak with increasing x–ray radiation can at least partially be associated with a scenario where the IDIS gains more and more spectral weight. Furthermore, it is shown in [A1, A2] that for radiation doses higher than 240 $\mu C/mm^2$ peak A becomes for s–polarized light higher than for p–polarized light, as it is expected for excitations into regular unoccupied π orbitals.

The findings for the NEXAFS favors the following scenario the influence of x–ray irradiation on the alkyl/Si SAM. For low radiation doses the SAM is particularly modified at the alkyl/Si interface, so that the spectral weight of the IDIS is increased, which suggests that it extends further into the molecular layer. With increasing irradiation π orbitals are formed within the SAM, which are not related to the interface. Furthermore, it appears reasonable that the modifications of the SAM occur at first at the interface as they are primarily due to secondary electrons from the substrate.

The influence of the interface interaction can also be observed in the C 1s data in Fig. E.7. The spectra were recorded for a pristine $C_{18}H_{37}$ and $C_{12}H_{25}$ SAM with 335 eV and 700 eV photon energy in order to vary the surface sensitivity. In all spectra there is a main peak located at E_B = 285.2 eV (denominated C_C) which corresponds to the carbon species in the alkyl chains. [] Additionally a weak signal contributes at E_B = 284 eV. For the $C_{18}H_{37}$ SAM its relative intensity

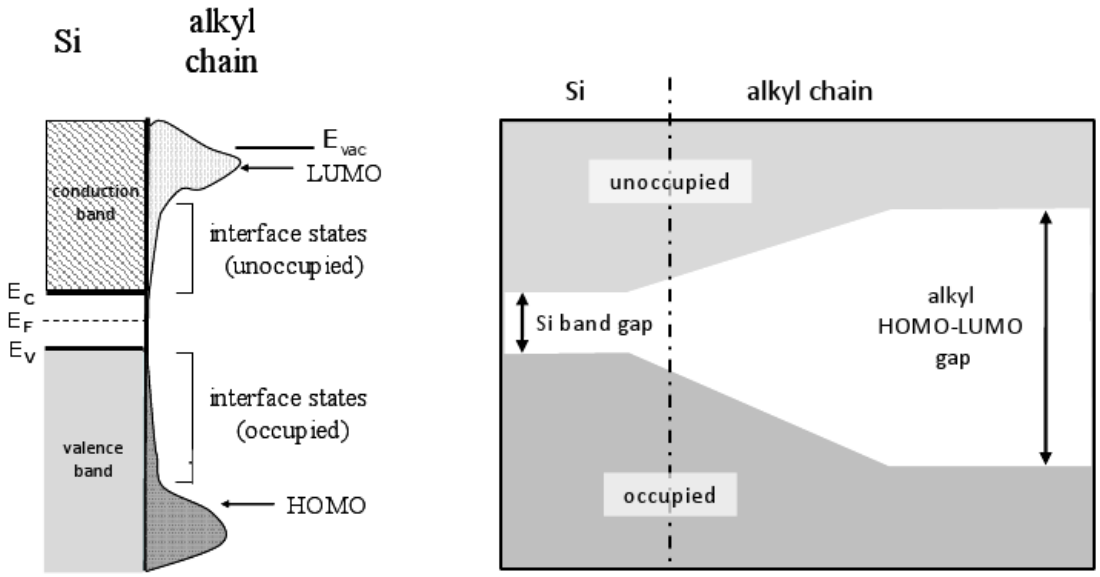

Figure E.6: Illustration of the DOS at the organic–inorganic interface in alkyl/Si SAMs.

with respect to the C_C peak increases with increasing bulk sensitivity, and it contributes even more for the $C_{12}H_{25}$ SAM. Therefore this signal can be attributed to the alkyl/Si interface, in particular to the Si–C bonds. [321, 322] Note that after investigating carefully the influence of irradiation on the C 1s spectra it can be excluded that the discussed effect is due to radiation–induced modifications of the SAM.

In Fig. E.8 the valence spectra of a $C_{12}H_{25}$/Si(111) and a $C_{18}H_{37}$/Si(111) SAM are plotted for 60 eV and 150 eV photon energy in order to vary the surface sensitivity. Additionally the corresponding spectra for a hydrogen terminated Si(111) crystal are depicted, which gives a good estimate for the silicon bulk contribution. Therefore the difference between the spectra for the alkyl/Si(111) SAM and those for the H/Si(111) surface can be attributed to the contribution from the SAM and the alkyl/Si interface. Accordingly, in spectrum (i) which was recorded with less surface sensitivity the SAM contributes significantly for binding energies larger than 1.9 eV. However, spectrum (iii), which was recorded for a comparatively thick SAM with higher surface sensitivity, has only significant SAM contributions for $E_B > 3.0$ eV. Consequently, the electronic states between 1.9 eV and 3.0 eV binding energy are located at the alkyl/Si interface. This is corroborated by the observation that these states contributed significantly to the spectrum (ii) which was recorded for a considerably thinner SAM. Consequently, this signal can be associated with the occupied IDIS.

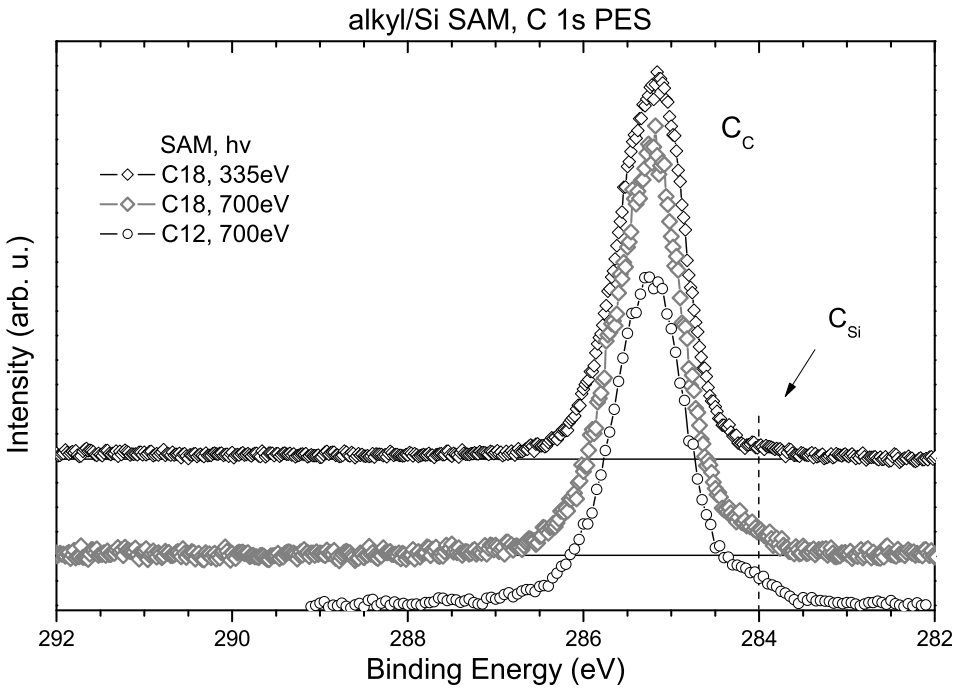

Figure E.7: C s1 core level spectra of a $C_{12}H_{25}$/Si(111) and a $C_{18}H_{37}$/Si(111) SAM with high surface sensitivity (hν=335 eV) and lower surface sensitivity (hν=700 eV).

Furthermore, in angle resolved valence spectra the signal from the IDIS can also be distinguished from the silicon bulk signal. In Fig. E.9 two spectra are depicted for a $C_{12}H_{25}$/Si(111) SAM, which were recorded with 130 eV and 150 eV photon energy, respectively. They are normalized to the intensity of the C 2p band between 5 eV and 9 eV binding energy. In the spectrum on the left hand side of Fig. E.9 three parabola shaped signals can be clearly identified between 1.5 eV and 5.5 eV binding energy. They can be assigned to the silicon band structure because of their strong dispersion. Moreover, for 2 eV $< E_B <$ 5 eV the intensity between these silicon signals is significantly higher than for $E_B <$ 2.0 eV.[1] This is exactly the energy range in which the IDIS contributes. The same effect is observed for the spectrum on the right hand side of Fig. E.9. This finding is in agreement with the scenario where the localized electronic states of a single impurity hybridize with a continuum of substrate states as it was discussed in *section 4.1*. Because the hybrid states are also quite localized at the impurity there is no dispersion relation $E(k)$ for these states. Therefore they contribute to a nondispersing photoemission signal.

[1] Note that for a detailed analisis of the angle–independent photoemission signal one needs to take scattering of photoelectrons into account.

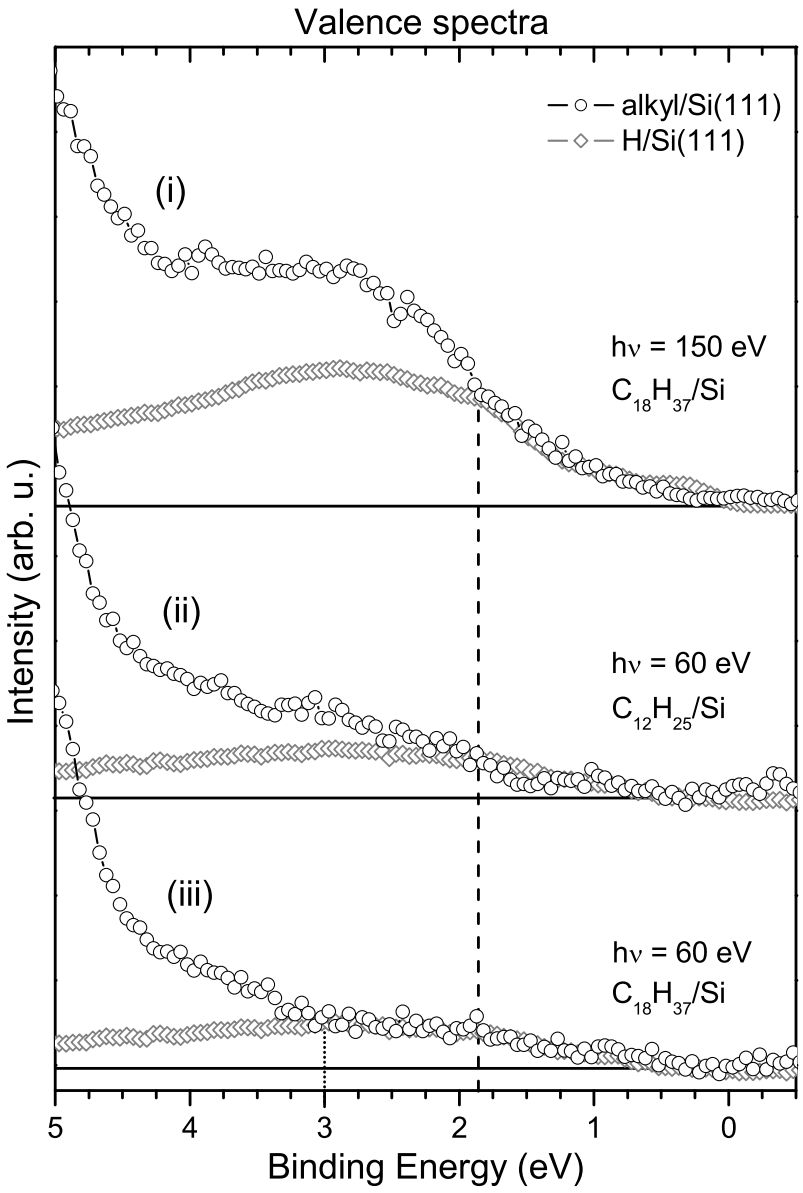

Figure E.8: Valence spectra of (○) a $C_{12}H_{25}$/Si(111) and a $C_{18}H_{37}$/Si(111) SAM for 60 eV and 150 eV photon energy. Valence spectra of (◇) a hydrogen terminated silicon surfaces H/Si(111) for 60 eV and 150 eV photon energy.

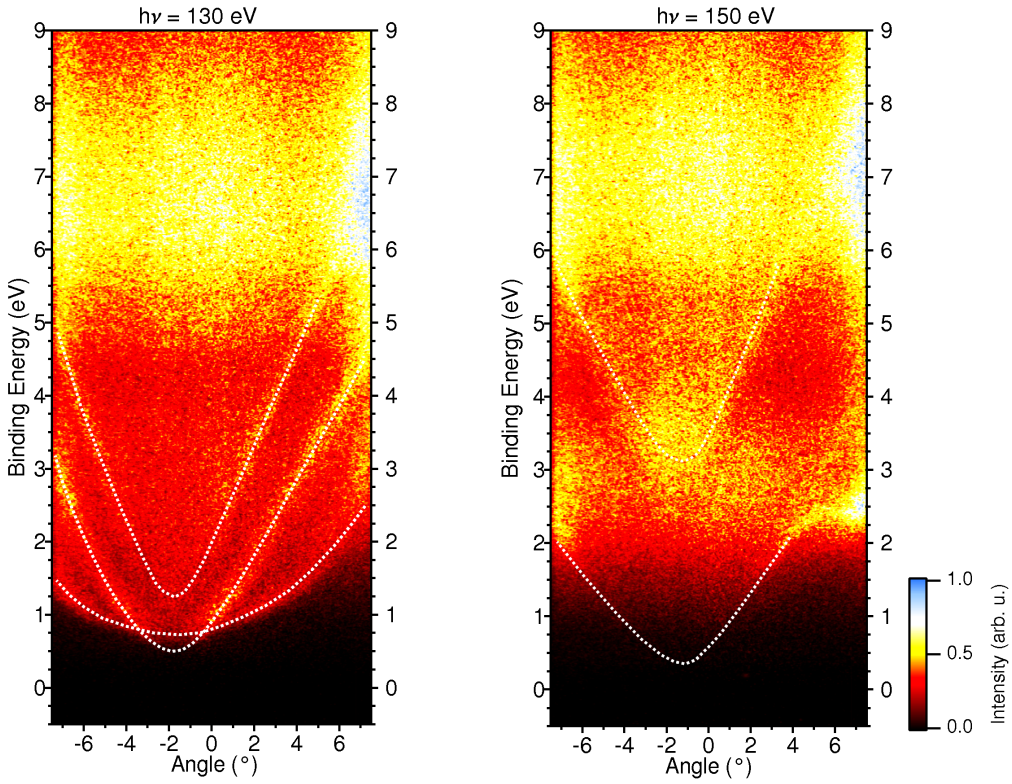

Figure E.9: Angle resolved valence spectra of a $C_{12}H_{25}$/Si(111) SAM on the left hand side for 130 eV photon energy and on the right hand side for 150 eV photon energy. The spectra are normalized to the region between 6 eV and 9 eV binding energy. The dispersion of the silicon valence band is indicated by white lines as guide for the eyes. Note that only raw data is shown.

E.4 Brief summary

The UPS study of the valence regime of the alkyl/Si(111) SAMs with variable photon energies indicates significant dispersion in the signal from the SAM. Additionally a strong density of states effect is observed, which is partially due to the finite alkyl chain length and partially due to a distribution of molecules with slightly different orientation. It was shown, that even for the comparatively short alkanes the electronic band structure is very similar to that of polyethylene. Moreover, it was demonstrated that in general the band structure can be well determined with the help of a quantum well approach in combination with a technique that provides the molecular orbitals and the energy of the relevant electronic states, e.g. calculations or PES for molecular orbital tomography. [150, 309] Furthermore, the signal from the alkyl/Si interface can be identified in the NEXAFS, core level and valence spec-

tra. The data indicate that an IDIS is formed at the alkyl/Si interface due to strong, covalent interaction. Additionally, it was shown that moderate x–ray irradiation increases the IDIS. This effect is in particular interesting for charge transport through the SAM, because it allows to modify the tunnel barrier. [39,294,300,301,A2] Moreover, one could imagine that in combination with suitable x–ray optics this effect can be of use for nano–patterning.

Bibliography

[1] F. Geiger, M. Stoldt, H. Schweizer, P. Bauerle, and E. Umbach. Electroluminescence from Oligothiophene–Based Light–Emitting Devices. *Adv. Mat.*, 5(12):922–925, DEC 1993.

[2] E. Umbach, M. Sokolowski, and R. Fink. Substrate-interaction, long-range order, and epitaxy of large organic adsorbates. *Applied Physics A: Materials Science & Processing*, 63:565–576, 1996. 10.1007/BF01567212.

[3] C. Väterlein, H. Neureiter, W. Gebauer, B. Ziegler, M. Sokolowski, P. Bäuerle, and E. Umbach. Organic light emitting devices based on vapor deposited films of end-capped sexithiophene: Evidence for Schottky barriers and transport limitations. *J. Appl. Phys.*, 82(6):3003–3013, 1997.

[4] F. Reinert and S. Hüfner. Photoemission spectroscopy - from early days to recent applications. *New Journal of Physics*, 7:34, APR 29 2005.

[5] W. L. Yang, V. Brouet, X. J. Zhou, Hyoung J. Choi, Steven G. Louie, Marvin L. Cohen, S. A. Kellar, P. V. Bogdanov, A. Lanzara, A. Goldoni, F. Parmigiani, Z. Hussain, and Z.-X. Shen. Band Structure and Fermi Surface of Electron-Doped C60 Monolayers. *Science*, 300:303–307, 2003.

[6] F. Kagawa, K. Miyagawa, and K. Kanoda. Unconventional critical behaviour in a quasi-two-dimensional organic conductor. *Nature*, 436(7050):534–537, July 2005.

[7] G. Kotliar, S. Y. Savrasov, K. Haule, V. S. Oudovenko, O. Parcollet, and C. A. Marianetti. Electronic structure calculations with dynamical mean-field theory. *Reviews of Modern Physics*, 78(3):865–951, JUL-SEP 2006.

[8] G. van der Laan, C. Westra, C. Haas, and G. A. Sawatzky. Satellite structure in photoelectron and Auger spectra of copper dihalides. *Phys. Rev. B*, 23(9): 4369–4380, May 1981.

[9] D. K. G. de Boer, C. Haas, and G. A. Sawatzky. Exciton satellites in photoelectron spectra. *Phys. Rev. B*, 29(8):4401–4419, Apr 1984.

[10] V. Kinsinger. *Untersuchung der elektronischen Struktur von Dihalogeniden der 3d–Übergangsmetalle*. PhD thesis, Universität des Saarlands, 1990.

[11] R Zimmermann. *XPS-Untersuchng der elektronischen Struktur von Halogeniden und Oxiden der 3–Übergangsmetallte Mangan und Kupfer und ihre Erklärung im Rahmen des Charge-Transfer Modells*. Diploma thesis, Universität des Saarlands, 1991.

[12] M. A. van Veenendaal and G. A. Sawatzky. Intersite interactions in Cu L-edge XPS, XAS, and XES of doped and undoped Cu compounds. *Phys. Rev. B*, 49(5):3473–3482, Feb 1994.

[13] Masatoshi Imada, Atsushi Fujimori, and Yoshinori Tokura. Metal-insulator transitions. *Rev. Mod. Phys.*, 70(4):1039–1263, Oct 1998.

[14] S. Biermann, A. Dallmeyer, C. Carbone, W. Eberhardt, C. Pampuch, O. Rader, M. Katsnelson, and A. Lichtenstein. Observation of Hubbard bands in γ–manganese. *JETP Letters*, 80(9):612–615, November 2004.

[15] C. Carbone, M. Veronese, P. Moras, S. Gardonio, C. Grazioli, P. H. Zhou, O. Rader, A. Varykhalov, C. Krull, T. Balashov, A. Mugarza, P. Gambardella, S. Lebegue, O. Eriksson, M. I. Katsnelson, and A. I. Lichtenstein. Correlated Electrons Step by Step: Itinerant-to-Localized Transition of Fe Impurities in Free-Electron Metal Hosts. *Phys. Rev. Lett.*, 104(11):116701, MAR 19 2010.

[16] J Kondo. Resitance minimum in dilute alloys. *Porgr. Theor. Phys.*, 32(1):37, 1964.

[17] J Kondo. Superconductivity of the two-dimensional Hubbard model with a small U. *J. Phys. Soc. Jap.*, 70(3):808–812, MAR 2001.

[18] R.W. Lof, M.A. Vanveenendaal, B. Koopmans, H.T. Jonkman, and G.A. Sawatzky. Band gap, excitons, and coulomb interactio in solid C_{60}. *Phys. Rev. Lett.*, 68(26):3924–3927, JUN 29 1992.

[19] P.J. Benning, F. Stepniak, D.M. Poirrier, J.L. Martins, J.H. Weaver, L.P.F. Chibante, and R.E. Smalley. Electronic properties of K–doped C_{60} — Photoemission and electron correlation. *Phys. Rev. B*, 47(20):13843–13847, MAY 15 1993.

[20] J.P. Lu. Metal–insulator transitions in degenerate Hubbard models and A_XC_{60}. *Phys. Rev. B*, 49(8):5687–5690, FEB 15 1994.

[21] M.R.C. Hunt, S. Modesti, P. Rudolf, and R.E. Palmer. Charge–transfer and structure in C_{60} adsorption on metal surfaces. *Phys. Rev. B*, 51(15):10039–10047, APR 15 1995.

[22] R. W. Lof, M. A. van Veenendaal, H. T. Jonkman, and G. A. Sawatzky. Band gap, excitons and Coulomb interactions of solid C60. *Journal of Electron Spectroscopy and Related Phenomena*, 72:83 – 87, 1995.

[23] O. Gunnarsson, E. Koch, and R.M. Martin. Mott transition in degenerate Hubbard models: Application to doped fullerenes. *Phys. Rev. B*, 54(16): 11026–11029, OCT 15 1996.

[24] O. Gunnarsson. Superconductivity in fullerides. *Rev. Mod. Phys.*, 69(2): 575–606, APR 1997.

[25] R. Claessen, M. Sing, U. Schwingenschlögl, P. Blaha, M. Dressel, and C. S. Jacobsen. Spectroscopic Signatures of Spin-Charge Separation in the Quasi-One-Dimensional Organic Conductor TTF–TCNQ. *Phys. Rev. Lett.*, 88(9): 096402, Feb 2002.

[26] M. Sing, U. Schwingenschlögl, R. Claessen, P. Blaha, J. M. P. Carmelo, L. M. Martelo, P. D. Sacramento, M. Dressel, and C. S. Jacobsen. Electronic structure of the quasi-one-dimensional organic conductor TTF-TCNQ. *Phys. Rev. B*, 68(12):125111, Sep 2003.

[27] J. M. P. Carmelo, K. Penc, L. M. Martelo, P. D. Sacramento, J. M. B. Lopes dos Santos, R. Claessen, M. Sing, and U. Schwingenschlägl. One-electron singular branch lines of the Hubbard chain. *EPL (Europhysics Letters)*, 67 (2):233, 2004.

[28] P. W. Anderson. Localized Magnetic States in Metals. *Phys. Rev.*, 124(1): 41–53, Oct 1961.

[29] H. Hertz. Über einen Einfluss des ultravioletten Lichtes auf die elektrische Entladung. *Ann. Physik*, 31:983, 1887.

[30] P. Lenard. *Ann. Physik*, 2:359, 1900.

[31] A. Einstein. *Ann. Physik*, 17:132, 1905.

[32] R. A. Millikan. A direct photoelectric determination of Planck's "h". *Phys. Rev.*, 7:355–388, 1916.

[33] S. Hüfner. *Photoelectron Spectroscopy.* Springer, 2003.

[34] L. Hedin, A.J. Freeman, R. Asahi, A. Continenza, R. Wu, W. Schattke, M. A. Van Hove, F. J. Garcia de Abajo, R. Diez Muino, N. Mannella, I. Bartos, K. Rossnagel, L. Kipp, M. Skibowski, F.J. Himpsel, and K.N. Altmann. *Solid–State Photoemission and Related Methods.* Wiley GmbH, 2003.

[35] J. Stöhr. *NEXAFS Spectroscopy.* Springer, 1992.

[36] T. A. Carlson, editor. *X–ray Photoelectron Spectroscopy.* Dowden, Hutchingon & Ross, Inc., 1978.

[37] D.R. Batchelor, Th. Schmidt, R. Follath, C. Jung, R. Fink, M. Knupfer, A. Schöll, T. Noll, F. Siewert, B. Büchner, and E. Umbach. An energy-dispersive VUV beamline for NEXAFS and other CFS/CIS studies. *Nuclear Instruments and Methods in Physics Research Section A: Accelerators, Spectrometers, Detectors and Associated Equipment*, 575(3):470 – 475, 2007.

[38] A. Schöll, Y. Zou, Th. Schmidt, R. Fink, and E. Umbach. Energy calibration and intensity normalization in high-resolution NEXAFS spectroscopy. *Journal of Electron Spectroscopy and Related Phenomena*, 129:1–8, 2003.

[39] A. Salomon, T. Böcking, C. K. Chan, F. Amy, O. Girshevitz, Cahen D., and A. Kahn. How Do Electronic Carriers Cross Si-Bound Alkyl Monolayers? *Phys. Rev. Lett.*, 95(26):266807, 2005.

[40] O. Seitz, T. Böcking, A. Salomon, J.J. Gooding, and D. Cahen. Importance of Monolayer Quality for Interpreting Current Transport through Organic Molecules: Alkyls on Oxide-Free Si. *Langmuir*, 22(16):6915–6922, 2006.

[41] T. Böcking, A. Salomon, D. Cahen, and J.J. Gooding. Thiol-Terminated Monolayers on Oxide-Free Si: Assembly of Semiconductor-Alkyl-S-Metal Junctions. *Langmuir*, 23:3236–3241, 2007.

[42] M.R. Linford, P. Fenter, P.M. Eisenberger, and C.E.D. Chidsey. Alkyl Monolayers on Silicon Prepared from 1-Alkenes and Hydrogen-Terminated Silicon. *J. Am. Chem. Soc.*, 117:3145–3155, 1995.

[43] J.F. Moulder, W.F. Stickle, Sobol P.E., and K.D. Bomben. *Handbook of X–ray Photoelectron Spectroscopy*. Perkin–Elmer, 1992.

[44] K.D. Childs, B.A. Carlson, J.F. LaVanier, L.A. Moulder, W.F. Pau, D.F. amd Stickle, and D.G. Watson. *Handbook of Auger Electron Spectroscopy*. Physical Electronics Industries, 1995.

[45] A. Schöll. *High–resolution investigation of the electronic structure of organic thin films*. PhD thesis, Universität Würzburg, 2003.

[46] F. Holch. *Investigation of Intermolecular Interaction in Organic Thin Films by means of NEXAFS Spectroscopy*. PhD thesis, Universität Würzburg, 2009.

[47] H. Oji, R. Mitsumoto, E. Ito, H. Ishii, Y. Ouchi, K. Seki, T. Yokoyama, T. Ohta, and N. Kosugi. Core hole effect in NEXAFS spectroscopy of polycyclic aromatic hydrocarbons: Benzene, chrysene, perylene, and coronene. *J. Chem. Phys.*, 109(23):10409–10418, 1998.

[48] R. Manne and T. Åberg. Koopmans' theorem for inner-shell ionization. *Chemical Physics Letters*, 7(2):282 – 284, 1970.

[49] R.L. Martin, D.D. Shirley, and C.S. Fadley. *Electron Spectroscopy: Theory, Techniques and Applications*, volume 1. Academic Press, 1978.

[50] H. Ågren, O. Vahtras, and V. Carravetta. Near-edge core photoabsorption in polyacenes: model molecules for graphite. *Chemical Physics*, 196(1-2):47 – 58, 1995.

[51] Y. Ma, F. Sette, G. Meigs, S. Modesti, and C. T. Chen. Breaking of ground-state symmetry in core-excited ethylene and benzene. *Phys. Rev. Lett.*, 63 (19):2044–2047, Nov 1989.

[52] D. Hübner, F. Holch, M. L. M. Rocco, K. C. Prince, S. Stranges, A. Schöll, E. Umbach, and R. Fink. Isotope effects in high–resolution NEXAFS spectra of naphthalene. *Chem. Phys. Lett.*, 415:188–192, 2005.

[53] R. Püttner, C. Kolczewski, M. Martins, A. S. Schlachter, G. Snell, M. Sant'Anna, J. Viefhaus, K. Hermann, and G. Kaindl. The C 1s NEXAFS spectrum of benzene below threshold: Rydberg or valence character of the unoccupied σ-type orbitals. *Chemical Physics Letters*, 393(4-6):361 – 366, 2004.

[54] A. P. Hitchcock, M. Pocock, C. E. Brion, M. S. Banna, D. C. Frost, C. A. McDowell, and B. Wallbank. Inner shell excitation and ionization of the monohalobenzenes. *Journal of Electron Spectroscopy and Related Phenomena*, 13(3):345 – 360, 1978.

[55] T. Yokoyama, K. Seki, I. Morisada, K. Edamatsu, and T. Ohta. X-ray absorption spectra of poly-p-phenylenes and polyacenes: localization of π orbitals. *Physica Scripta*, 41(1):189–192, 1990.

[56] A. P. Hitchcock, P. Fischer, Aharon. Gedanken, and M. B. Robin. Antibonding σ^* valence MOs in the inner-shell and outer-shell spectra of the fluorobenzenes. *J. Phys. Chem.*, 91(3):531–540, January 1987.

[57] M.B. Robin, I. Ishii, R. McLaren, and A.P. Hitchcock. Fluorination effects on the inner-shell spectra of unsaturated molecules. *Journal of Electron Spectroscopy and Related Phenomena*, 47:53 – 92, 1988.

[58] P. Väterlein, R. Fink, E. Umbach, and W. Wurth. Simulation of resonantly and off-resonantly excited x-ray emission spectra: An application for the $X\alpha$ scattered-wave method. *Phys. Rev. A*, 57(6):4275–4278, Jun 1998.

[59] K.H. Frank, P. Yannoulis, R. Dudde, and E.E. Koch. Unoccupied molecular orbitals of aromatic hydrocarbons adsorbed on Ag(111). *J. Chem. Phys.*, 89: 7569–7576, 1988.

[60] A. D. Becke. Density-functional thermochemistry. III. The role of exact exchange. *J. Chem. Phys.*, 98(7):5648–5652, 1993.

[61] J.P. Perdew and M. Levy. Physical Content of the Exact Kohn-Sham Orbital Energies: Band Gaps and Derivative Discontinuities. *Phys. Rev. Lett.*, 51 (20):1884–1887, Nov 1983.

[62] M.S. Hybertsen and S.G. Louie. Electron correlation in semiconductors and insulators: Band gaps and quasiparticle energies. *Phys. Rev. B*, 34(8):5390–5413, Oct 1986.

[63] L. Kronik, R. Fromherz, E. Ko, G. Gantefor, and J.R. Chelikowsky. Highest electron affinity as a predictor of cluster anion structures. *Nature Materials*, 1(1):49–53, September 2002.

[64] M.J. Allen and D.J. Tozer. Eigenvalues, integer discontinuities and NMR shielding constants in Kohn–Sham theory. *Mol. Phys.*, 100(4):433–439, 2002.

[65] D. P. Chong, O. V. Gritsenko, and E. J. Baerends. Interpretation of the Kohn–Sham orbital energies as approximate vertical ionization potentials. *J. Chem. Phys.*, 116(5):1760–1772, 2002.

[66] M. Moseler, B. Huber, H. Häkkinen, U. Landman, G. Wrigge, M. Astruc Hoffmann, and B. v. Issendorff. Thermal effects in the photoelectron spectra of Na_N^- clusters ($N = 4 - -19$). *Phys. Rev. B*, 68(16):165413, Oct 2003.

[67] O. Guliamov, L. Kronik, and K.A. Jackson. Photoelectron spectroscopy as a structural probe of intermediate size clusters. *J. Chem. Phys.*, 123(20): 204312, 2005.

[68] L. Segev, A. Salomon, A. Natan, D. Cahen, F. Amy, C. K. Chan, Kahn, and L. Kronik. Electronic structure of Si(111)-bound alkyl monolayers: Theory and experiment. *Phys. Rev. B*, 74(16):165323, 2006.

[69] S.L. Murov, I. Carmichael, and G.L. Hug. *Handbook of Photochemistry (2nd ed.)*. New York, 1993.

[70] A. F. Prikhotko, A. F. Skorobogatko, and L. I. Tsikora. *Optc. Spectrosc.*, 26: 524, 1969.

[71] R. Dudde, B. Reihl, and A. Otto. π^* and σ^* molecular orbitals of condensed films of chlorobenzenes and hexafluorobenzene observed by inverse photoemission. *J. Chem. Phys.*, 92(6):3930–3934, 1990.

[72] F. Amy, C. Chan, and A. Kahn. Polarization at the gold/pentacene interface. *Organic Electronics*, 6(2):85 – 91, 2005.

[73] E. E. Rennie, B. Kempgens, H. M. Koppe, U. Hergenhahn, J. Feldhaus, B. S. Itchkawitz, A. L. D. Kilcoyne, A. Kivimaki, K. Maier, M. N. Piancastelli, M. Polcik, A. Rudel, and A. M. Bradshaw. A comprehensive photoabsorption, photoionization, and shake-up excitation study of the C 1s cross section of benzene. *J. Chem. Phys.*, 113(17):7362–7375, 2000.

[74] H.W. Schnopper. Multiple Excitation and Ionization of Inner Atomic Shells by X Rays. *Phys. Rev.*, 131(6):2558–2560, Sep 1963.

[75] R. D. Deslattes, R. E. LaVilla, P. L. Cowan, and A. Henins. Threshold studies of a multivacancy process in the $K\beta$ region of argon. *Phys. Rev. A*, 27(2): 923–933, Feb 1983.

[76] J.W. Cooper. Near-threshold K-shell absorption cross section of argon: Relaxation and correlation effects. *Phys. Rev. A*, 38(7):3417–3424, Oct 1988.

[77] S. Svensson, B. Eriksson, N. Mårtensson, G. Wendin, and U. Gelius. Electron shake-up and correlation satellites and continuum shake-off distributions in X-Ray photoelectron spectra of the rare gas atoms. *Journal of Electron Spectroscopy and Related Phenomena*, 47:327 – 384, 1988.

[78] F.W. Lytle, R.B. Greegor, G.H. Via, J.M. Brwon, and G. Meitzner. Gas phase x–ray absorption spectroscopy with an electron yield detector. *J. de Phys.*, C8:149, 1986.

[79] J M Esteva, B Gauthe, P Dhez, and R C Karnatak. Double excitation in the K absorption spectrum of neon. *J. Phys. B*, 16(9):L263–L268, 1983.

[80] S. Hüfner and G. K. Wertheim. X-Ray Photoelectron Band Structure of Some Transition-Metal Compounds. *Phys. Rev. B*, 8(10):4857–4867, Nov 1973.

[81] S. Larsson. Theory of satellite excitations in inner shell x-ray photoelectron–spectra of nickel and copper compounds. *Chem. Phys. Lett.*, 32(3):401–406, 1975.

[82] S. Larsson. Satellites in ESCA inner–shell spectra of 3d° transition–metal complexes. *Journal of Electron Spectroscopy and Related Phenomena*, 8(3): 171–178, 1976.

[83] Y. Baer, J.-M. Imer, F. Patthey, and W.-D. Schneider. Core level spectroscopies of light rare-earth metals and insulators: single-impurity parameters, relative energy scales and charge screening. *Journal of Electron Spectroscopy and Related Phenomena*, 46(2):303 – 313, 1988.

[84] T. Uozumi, K. Okada, A. Kotani, R. Zimmermann, P. Steiner, S. Hüfner, Y. Tezuka, and S. Shin. Theoretical and experimental studies on the electronic structure of M2O3 (M = Ti, V, Cr, Mn, Fe) compounds by systematic

analysis of high-energy spectroscopy. *Journal of Electron Spectroscopy and Related Phenomena*, 83(1):9 – 20, 1997.

[85] R. Zimmermann, P. Steiner, R. Claessen, F. Reinert, S. Hüfner, P. Blaha, and P. Dufek. Electronic structure of 3d-transition-metal oxides: on-site Coulomb repulsion versus covalency. *J. Phys.*, 11(7):1657, 1999.

[86] R. Zimmermann, R. Claessen, F. Reinert, P. Steiner, and S. Hüfner. Strong hybridization in vanadium oxides: evidence from photoemission and absorption spectroscopy. *J. Phys.*, 10(25):5697, 1998.

[87] Paul S. Bagus and Eugene S. Ilton. Effects of covalency on the p -shell photoemission of transition metals: MnO. *Phys. Rev. B*, 73(15):155110, Apr 2006.

[88] J. C. Woicik, M. Yekutiel, E. J. Nelson, N. Jacobson, P. Pfalzer, M. Klemm, S. Horn, and L. Kronik. Chemical bonding and many-body effects in site-specific x-ray photoelectron spectra of corundum V2O3. *Phys. Rev. B*, 76 (16):077401, OCT 2007.

[89] E.S. Ilton and P.S. Bagus. Ligand field effects on the multiplet structure of the U4f XPS of UO2. *Surface Science*, 602(5):1114 – 1121, 2008.

[90] S. Hüfner and G.K. Wertheim. Multielectron effects in the XPS spectra of nickel. *Phys. Lett. A*, 51(5):299 – 300, 1975.

[91] J. Barth, G. Kalkoffen, and C. Kunz. Resonance enhancement of the nickel d-band photoemission. *Physics Letters A*, 74(5):360 – 362, 1979.

[92] P.A. Cox, J.K. Lang, and Y. Baer. Study of the 4f and valence band density of states in rare-earth metals. I. Theory of the 4f states. *J. Phys. F*, 11(1): 113, 1981.

[93] John C. Fuggle, F. Ulrich Hillebrecht, R. Zeller, Zygmunt Zołnierek, Peter A. Bennett, and Ch. Freiburg. Electronic structure of Ni and Pd alloys. I. X-ray photoelectron spectroscopy of the valence bands. *Phys. Rev. B*, 27(4): 2145–2178, Feb 1983.

[94] O. Gunnarsson and K. Schönhammer. *Handbook of the Physics and Chemistry of Rare Earths*, volume 10: High Energy Spectroscopy. Elsvier Science Publisher B. V., 1987.

[95] T. Miyahara, T. Hanyu, H. Ishii, H. Kataura, Y. Yanagihara, A. Fujimori, T. Koide, and H. Kato. Resonant Photoemission Study on Valence Band Satellites of Cu_xNi_{1-x} and Ag_xPd_{1-x} Alloy Systems. *J. Phys. Soc. Jap.*, 58 (6):2160–2166, 1989.

[96] E. Umbach. *Mechanismen und Anwendungen der Photoemission an Adsorbaten*. PhD thesis, Technische Universität München, 1980.

[97] O. Gunnarsson and K. Schönhammer. CO on Cu(100)—Explanation of the Three-Peak Structure in the X-Ray-Photoemission-Spectroscopy Core Spectrum. *Phys. Rev. Lett.*, 41(23):1608–1612, Dec 1978.

[98] J.C. Fuggle, E. Umbach, D. Menzel, K. Wandelt, and C.R. Brundle. Adsorbate line shapes and multiple lines in XPS; comparison of theory and experiment. *Solid State Communications*, 27(2):65 – 69, 1978.

[99] J.C. Fuggle and D. Menzel. Photoelectron Spectroscopy of Nitrogen adsorbed on Tungsten(110). *Vakuum–Technik*, 27(5):130–135, 1978.

[100] R.I. Masel, E. Umbach, J.C. Fuggle, and D. Menzel. XPS, UPS AND XAES studies of the adsorption of nitrogen, oxygen, and nitrogen oxides on W(110) at 300 and 100 K: II. Adsorption of NO. *Surface Science*, 79(1):26 – 38, 1979.

[101] C. R. Brundle, P. S. Bagus, D. Menzel, and K. Hermann. Adsorption of molecular nitrogen on nickel. II. Comparison of photoemission for $N2$/Ni(100) to CO/Ni(100) and to theory. *Phys. Rev. B*, 24(12):7041–7056, Dec 1981.

[102] P. S. Bagus and K. Hermann. Satellite structure of the core level spectrum of CO adsorbed on nickel surfaces: Model studies. *Surface Science*, 89(1-3): 588 – 595, 1979.

[103] P. S. Bagus, C. R. Brundle, K. Hermann, and D. Menzel. Photoemission and theoretical studies of the electronic structure of molecular nitrogen on nickel. *Journal of Electron Spectroscopy and Related Phenomena*, 20(2):253 – 258, 1980.

[104] K. Hermann, P. S. Bagus, C. R. Brundle, and D. Menzel. Adsorption of molecular nitrogen on nickel. I. Cluster-model theoretical studies. *Phys. Rev. B*, 24(12):7025–7040, Dec 1981.

[105] N. V. Dobrodey, L. S. Cederbaum, and F. Tarantelli. Dynamical core-hole screening in weak chemisorption systems. *Phys. Rev. B*, 57(12):7340–7351, Mar 1998.

[106] E. W. Plummer, W. R. Salaneck, and J. S. Miller. Photoelectron spectra of transition-metal carbonyl complexes: comparison with the spectra of adsorbed CO. *Phys. Rev. B*, 18(4):1673–1701, Aug 1978.

[107] U. Baston, M. Jung, and E. Umbach. Different bonding configurations of the aromatic anhydride NDCA on Ni(111) and O/Ni(111): a photoemission and TDS study. *Journal of Electron Spectroscopy and Related Phenomena*, 77(1): 75 – 89, 1996.

[108] A. Schöll, Y. Zou, Th. Schmidt, R. Fink, and E. Umbach. High-Resolution Photoemission Study of Different NTCDA Monolayers on Ag(111): Bonding and Screening Influences on the Line Shapes. *J. Phys. Chem. B*, 108(38): 14741–14748, 2004.

[109] H. Peisert, A. Petershans, and T. Chassé. Charge Transfer and Polarization Screening at Organic/Metal Interfaces: Distinguishing between the First Layer and Thin Films. *J. Phys. Chem. C*, 112(15):5703–5706, April 2008.

[110] D. Kolacyak, H. Peisert, and Th. Chassé. Charge transfer and polarization screening in organic thin films: phthalocyanines on Au(100). *Appl. Phys. A: Materials Science & Processing*, 95(1):173–178, April 2009.

[111] H. Peisert, D. Kolacyak, and T. Chassé. Site-Specific Charge-Transfer Screening at Organic/Metal Interfaces. *J. Phys. Chem. C*, 113(44):19244–19250, NOV 5 2009.

[112] K. Schönhammer and O. Gunnarsson. Shape of core level spectra in adsorbates. *Solid State Communications*, 23(10):691 – 693, 1977.

[113] E. Umbach. Satellite structures in photoemission spectra from different types of absorbates. *Surface Science*, 117(1-3):482 – 502, 1982.

[114] A. Kotani and Y. Toyozawa. *J. Phys. Soc. Jpn.*, 37:912, 1974.

[115] S. Asada and S. Sugano. Satellites in X-Ray photoelectron Spectra of Transition-Metal Compounds. *J. Phys. Soc. J.*, 41(4):1291–1299, 1976.

[116] S. Asada and S. Sugano. A model calculation for studying the effects of electron transfer on shake-up satellites in transition-metal compounds. *J. Phys. C*, 11(18):3911, 1978.

[117] F.S. Tautz. Structure and bonding of large aromatic molecules on noble metal surfaces: The example of PTCDA. *Progress in Surface Science*, 82(9-12):479 – 520, 2007.

[118] L. Kilian, A. Hauschild, R. Temirov, S. Soubatch, A. Schöll, A. Bendounan, F. Reinert, T.-L. Lee, F. S. Tautz, M. Sokolowski, and E. Umbach. Role of Intermolecular Interactions on the Electronic and Geometric Structure of a Large π-Conjugated Molecule Adsorbed on a Metal Surface. *Phys. Rev. Lett.*, 100(13):136103, 2008.

[119] N. D. Lang and A. R. Williams. Core holes in chemisorbed atoms. *Phys. Rev. B*, 16(6):2408–2419, Sep 1977.

[120] D. R. Hamann. Path Integral Theory of Magnetic Alloys. *Phys. Rev. B*, 2 (5):1373–1392, Sep 1970.

[121] B. Gumhalter. Atomic and extra-atomic relaxation and infrared catastrophe in the core spectra of chemisorbed atoms. *J. Phys. C*, 10(8):L219, 1977.

[122] F. Forster, S. Hüfner, and F. Reinert. Rare gases on noble-metal surfaces: An angle-resolved photoemission study with high energy resolution. *J. Phys. Chem. B*, 108(38):14692–14698, SEP 23 2004.

[123] A. Bendounan, F. Forster, J. Ziroff, F. Schmitt, and F. Reinert. Quantitative analysis of the surface reconstruction induced band-gap in the Shockley state on monolayer systems on noble metals. *Surface Science*, 600(18):3865 – 3869, 2006. Berlin, Germany: 4-9 September 2005, Proceedings of the 23th European Conference on Surface Science.

[124] J. Ziroff, P. Gold, A. Bendounan, F. Forster, and F. Reinert. Adsorption energy and geometry of physisorbed organic molecules on Au(111) probed by surface-state photoemission. *Surface Science*, 603(2):354 – 358, 2009.

[125] E. Umbach. Characterization Of Organic Overlayers On Well-Defined Substrates. *Progress In Surface Science*, 35(1-4):113–127, 1990.

[126] Y. Zou, L. Kilian, A. Schöll, Th. Schmidt, R. Fink, and E. Umbach. Chemical bonding of PTCDA on Ag surfaces and the formation of interface states. *Surface Science*, 600(6):1240 – 1251, 2006.

[127] K. Flechtner, A. Kretschmann, H.-P. Steinrück, and J.M. Gottfried. NO-Induced Reversible Switching of the Electronic Interaction between a Porphyrin-Coordinated Cobalt Ion and a Silver Surface. *J. Am. Chem. Soc.*, 129(40):12110–12111, October 2007.

[128] N.D. Lang and J.K. Norskov. Interaction of helium with a metal–surface. *Phys. Rev. B*, 27(8):4612–4616, 1983.

[129] W. Weiss and E. Umbach. Intensity anomalies in adsorbate photoemission spectra for varying surface composition: Xe/Ni(111) and Xe/Na/Ni(111). *Surface Science Letters*, 249(1-3):L333 – L337, 1991.

[130] P.S. Bagus, C.J. Nelin, E.S. Ilton, M. Baron, H. Abbott, E. Primorac, H. Kuhlenbeck, S. Shaikhutdinov, and H.-J. Freund. The complex core level spectra of CeO2: An analysis in terms of atomic and charge transfer effects. *Chem. Phys. Lett.*, 487(4-6):237 – 240, 2010.

[131] C. J. Nelin, P. S. Bagus, E. S. Ilton, S. A. Chambers, H. Kuhlenbeck, and H.-J. Freund. Relationships between complex core level spectra and materials properties. *Int. J. Quantum Chem.*, 110(15):2752–2764, 2010.

[132] C.R. Brundle and K. Wandelt. Combined SIMS/XPS studies of adsorption at single–crystal copper, nickel and copper nickel surfaces. *Vacuum*, 31(10-1): 491, 1981.

[133] A. Schöll, Y. Zou, L. Kilian, D. Hübner, D. Gador, C. Jung, S.G. Urquhart, Th. Schmidt, R. Fink, and E. Umbach. Electron-Vibron Coupling in High-Resolution X-Ray Absorption Spectra of Organic Materials: NTCDA on Ag(111). *Phys. Rev. Lett.*, 93(14):146406, 2004.

[134] A. Schöll, Y. Zou, D. Hübner, S.G. Urquhart, Th. Schmidt, R. Fink, and E. Umbach. A comparison of fine structures in high-resolution x-ray-absorption spectra of various condensed organic molecules. *J. Chem. Phys.*, 123(4):044509, 2005.

[135] F. S. Tautz, M. Eremtchenko, J. A. Schaefer, M. Sokolowski, V. Shklover, K. Glöckler, and E. Umbach. A comparison of the chemisorption behaviour of PTCDA on different Ag surfaces. *Surface Science*, 502-503:176 – 184, 2002.

[136] F.S. Tautz, M. Eremtchenko, J.A. Schaefer, M. Sokolowski, V. Shklover, and E. Umbach. Strong electron-phonon coupling at a metal/organic interface: PTCDA/Ag(111). *Phys. Rev. B*, 65(12), MAR 15 2002.

[137] M. Jung, U. Baston, G. Schnitzler, M. Kaiser, J. Papst, T. Porwol, H.-J. Freund, and E. Umbach. The electronic structure of adsorbed aromatic molecules: Perylene and PTCDA on Si(111) and Ag(111). *J. Molec. Struc.*, 293:239 – 244, 1993.

[138] J. Taborski, P. Väterlein, H. Dietz, U. Zimmermann, and E. Umbach. NEXAFS investigations on ordered adsorbate layers of large aromatic molecules. *Journal of Electron Spectroscopy and Related Phenomena*, 75:129 – 147, 1995. Future Perspectives for Electron Spectroscopy with Synchrotron Radiation.

[139] K. Glöckler, C. Seidel, A. Soukopp, M. Sokolowski, E. Umbach, M. Böhringer, R. Berndt, and W. D. Schneider. Highly ordered structures and submolecular scanning tunnelling microscopy contrast of PTCDA and DM-PBDCI monolayers on Ag(111) and Ag(110). *Surface Science*, 405(1):1 – 20, 1998.

[140] I. Chizhov, A. Kahn, and G. Scoles. Initial growth of 3,4,9,10-perylenetetracarboxylic-dianhydride (PTCDA) on Au(111): a scanning tunneling microscopy study. *Journal of Crystal Growth*, 208(1-4):449–458, January 2000.

[141] Dietrich R. T. Zahn, Thorsten U. Kampen, and Henry Méndez. Transport gap of organic semiconductors in organic modified Schottky contacts. *Applied Surface Science*, 212-213:423 – 427, 2003. 11th International Conference on Solid Films and Surfaces.

[142] T. U. Kampen, A. Das, S. Park, W. Hoyer, and D. R. T. Zahn. Relation between morphology and work function of metals deposited on organic substrates. *Applied Surface Science*, 234(1-4):333 – 340, 2004. The Ninth International Conference on the Formation of Semiconductor Interfaces,.

[143] A. Hauschild, K. Karki, B.C.C. Cowie, M. Rohlfing, F.S. Tautz, and M. Sokolowski. Molecular Distortions and Chemical Bonding of a Large π-Conjugated Molecule on a Metal Surface. *Phys. Rev. Lett.*, 94(3):036106, Jan 2005.

[144] J.C. Swarbrick, J. Ma, J.A. Theobald, N.S. Oxtoby, J.N. O'Shea, N.R. Champness, and P.H. Beton. Square, Hexagonal, and Row Phases of PTCDA and PTCDI on Ag—Si(111)$\sqrt{3}$ x $\sqrt{3}$R30°. *J. Phys. Chem. B*, 109(24):12167–12174, June 2005.

[145] A. Gerlach, S. Sellner, F. Schreiber, N. Koch, and J. Zegenhagen. Substrate-dependent bonding distances of PTCDA: A comparative x-ray standing-wave study on Cu(111) and Ag(111). *Phys. Rev. B*, 75(4):045401, 2007.

[146] S. Duhm, A. Gerlach, I. Salzmann, B. Bröker, R.L. Johnson, F. Schreiber, and N. Koch. PTCDA on Au(111), Ag(111) and Cu(111): Correlation of interface charge transfer to bonding distance. *Organic Electronics*, 9(1):111 – 118, 2008.

[147] H. Huang, S. Chen, X. Gao, W. Chen, and A.T.S. Wee. Structural and Electronic Properties of PTCDA Thin Films on Epitaxial Graphene. *ACS Nano*, 3(11):3431–3436, November 2009.

[148] L. Romaner, D. Nabok, P. Puschnig, E. Zojer, and C. Ambrosch-Draxl. Theoretical study of PTCDA adsorbed on the coinage metal surfaces, Ag(111), Au(111) and Cu(111). *New J. Phys.*, 11(5):053010 (21pp), 2009.

[149] A. Hauschild, R. Temirov, S. Soubatch, O. Bauer, A. Schöll, B.C.C. Cowie, T.-L. Lee, F.S. Tautz, and M. Sokolowski. Normal-incidence x-ray standing-wave determination of the adsorption geometry of PTCDA on Ag(111): Comparison of the ordered room-temperature and disordered low-temperature phases. *Phys. Rev. B*, 81(12):125432, Mar 2010.

[150] J. Ziroff, F. Forster, A. Schöll, P. Puschnig, and F. Reinert. Hybridization of Organic Molecular Orbitals with Substrate States at Interfaces: PTCDA on Silver. *Phys. Rev. Lett.*, 104:233004, 2010.

[151] Y. Zou. *Electronic properties of organic molecular thin films in condensed and interfacial states with metal substrates.* PhD thesis, Universtität Würzburg, 2003.

[152] A. Schöll, Y. Zou, M. Jung, Th. Schmidt, R. Fink, and E. Umbach. Line shapes and satellites in high-resolution x-ray photoelectron spectra of large π-conjugated organic molecules. *J. Chem. Phys.*, 121(20):10260–10267, 2004.

[153] G. Gavrila. *Electronic Properties and Chemistry of Metal / Organic Semiconductor/ S-GaAs(100) Heterostructures*. PhD thesis, Technischen Universität Chemnitz, 2005.

[154] S. Krause, M.B. Casu, A. Schöll, and E. Umbach. Determination of transport levels of organic semiconductors by UPS and IPS. *New J. Phys.*, 10(8):085001, 2008.

[155] A. Kraft, R. Temirov, S. K. M. Henze, S. Soubatch, M. Rohlfing, and F. S. Tautz. Lateral adsorption geometry and site-specific electronic structure of a large organic chemisorbate on a metal surface. *Phys. Rev. B*, 74(4), JUL 2006.

[156] M. Eremtchenko, J. A. Schaefer, and F. S. Tautz. Understanding and tuning the epitaxy of large aromatic adsorbates by molecular design. *Nature*, 425 (6958):602–605, OCT 9 2003.

[157] C. H. Schwalb, S. Sachs, M. Marks, A. Schöll, F. Reinert, E. Umbach, and U. Höfer. Electron Lifetime in a Shockley-Type Metal-Organic Interface State. *Phys. Rev. Lett.*, 101(14):146801, Sep 2008.

[158] S. Sachs, C.H. Schwalb, M. Marks, A. Schöll, F. Reinert, E. Umbach, and U. Höfer. Electronic structure at the perylene-tetracarboxylic acid dianhydride/Ag(111) interface studied with two-photon photoelectron spectroscopy. *J. Chem. Phys.*, 131(14):144701, 2009.

[159] C. H. Schwalb, M. Marks, S. Sachs, A. Schöll, F. Reinert, E. Umbach, and U. Höfer. Time-resolved measurements of electron transfer processes at the PTCDA/Ag(111) interface. *European Physical Journal B*, 75:23–30, 2010. 10.1140/epjb/e2010-00106-6.

[160] M. Leonhardt, O. Mager, and H. Port. Two-component optical spectra in thin PTCDA films due to the coexistence of alpha- and beta-phase. *Chem. Phys. Lett.*, 313(1-2):24–30, NOV 5 1999.

[161] N. Nicoara, O. Custance, D. Granados, J.M. Garcia, J.M. Gomez-Rodriguez, A.M. Baro, and J. Mendez. Scanning tunnelling microscopy and spectroscopy on organic PTCDA films deposited on sulfur passivated GaAs(001). *J. Phys.*, 15(38):S2619–S2629, OCT 1 2003.

[162] J.J. Weimer, E. Umbach, and D. Menzel. The properties of K and coadsorbed CO + K on Ru (001): II. Electronic structure. *Surface Science*, 159(1):83 – 107, 1985.

[163] E. Umbach, S. Kulkarni, P. Feulner, and D. Menzel. A multimethod study of the adsorption of NO on Ru(001) : I. XPS, UPS and XAES measurements. *Surface Science*, 88(1):65 – 94, 1979.

[164] A. Hornung, D. Zemlyanov, M. Muhler, and G. Ertl. The catalytic reduction of NO by H2 on Ru(0 0 0 1): Observation of NHads species. *Surface Science*, 600(2):370 – 379, 2006.

[165] C. Wäckerlin, D. Chylarecka, A. Kleibert, K. Müller, C. Iacovita, F. Nolting, T.A. Jung, and N. Ballav. Controlling spins in adsorbed molecules by a chemical switch. *Nature Communications*, 1(5):61–67, August 2010.

[166] J.C. Fuggle, T.E. Madey, M. Steinkilberg, and D. Menzel. X-ray photoelectron satellites from adsorbed species. *Chem. Phys. Lett.*, 33(2):233 – 236, 1975.

[167] J.C. Fuggle, T.E. Madey, M. Steinkilberg, and D. Menzel. Photoelectron spectroscopic studies of adsorption of CO and oxygen on Ru(001). *Surface Science*, 52(3):521 – 541, 1975.

[168] X. Bao, M. Muhler, B. Pettinger, R. Schlögl, and G. Ertl. On the nature of the active state of silver during catalytic oxidation of methanol. *Catalysis Letters*, 22:215–225, 1993. 10.1007/BF00810368.

[169] X. Bao, M. Muhler, Th. Schedel-Niedrig, and R. Schlögl. Interaction of oxygen with silver at high temperature and atmospheric pressure: A spectroscopic and structural analysis of a strongly bound surface species. *Phys. Rev. B*, 54 (3):2249–2262, Jul 1996.

[170] P. Väterlein. *Modellrechnungen zur elektronischen Struktur großer organischer Moleküle*. PhD thesis, Universität Würzburg, 1996.

[171] I. Nakai, H. Kondoh, T. Shimada, M. Nagasaka, R. Yokota, K. Amemiya, H. Orita, and T. Ohta. N+NO Reaction on Rh(111) Surfaces Studied with Fast Near-Edge X-ray Absorption Fine Structure Spectroscopy: Role of NO Dimer as an Extrinsic Precursor. *J. Phys. Chem. B*, 110(51):25578–25581, 2006. PMID: 17181188.

[172] M. Nagasaka, H. Kondoh, K. Amemiya, I. Nakai, T. Shimada, R. Yokota, and T. Ohta. Mechanism of Ammonia Formation on Rh(111) Studied by Dispersive Near-Edge X-ray Absorption Fine Structure Spectroscopy. *J. Phys. Chem. C*, 114(5):2164–2170, 2010.

[173] N. Ueno, K. Suzuki, S. Hasegawa, K. Kamiya, K. Seki, and H. lnokuchi. Angle-resolved photoemission spectroscopy of ultrathin films of H2-phthalocyanine on MoSo2 surfaces. *J. Chem. Phys.*, 99:7169–7174, 1993.

[174] S. Kera, H. Yamane, H. Fukagawa, T. Hanatani, K.K. Okudaira, K. Seki, and N. Ueno. Angle resolved UV photoelectron spectra of titanyl-phthalocyanine monolayer films on graphite. *Journal of Electron Spectroscopy and Related Phenomena*, 156-158:135 – 138, 2007. Electronic Spectroscopy and Structure: ICESS-10.

[175] S. Doniach and M. Sunjic. Many-electron singularity in X-ray photoemission and X-ray line spectra from metals. *J. Phys. C*, 3(2):285–291, 1970.

[176] G. D. Mahan. Theory of photoemission in simple metals. *Phys. Rev. B*, 2 (11):4334–4350, DEC 1 1970.

[177] J.D. Dow and D.R. Franceschetti. Determination of X-Ray Photoemission Line-Shape Asymmetrie from Threshold Exponents. *Phys. Rev. Lett.*, 34 (21):1320–1323, May 1975.

[178] G.D. Mahan. Collective excitations in X-ray spectra of metals. *Phys. Rev. B*, 11(12):4814–4824, 1975.

[179] C. C. Chang. Auger electron spectroscopy. *Surface Science*, 25(1):53 – 79, 1971.

[180] M.P. Seah. Quantitative Auger electron spectroscopy and electron ranges. *Surface Science*, 32(3):703 – 728, 1972.

[181] E. Umbach and Z. Hussain. Angle-Dependent Changes of Auger Line Shapes from Adsorbed Molecules. *Phys. Rev. Lett.*, 52(6):457–460, Feb 1984.

[182] H. Ueba. Theory of resonant photoemission of adsorbates on metal surfaces. *Surface Science*, 242(1-3):266 – 276, 1991.

[183] A. Föhlisch. Ultrafast charge transfer and nuclear dynamics studied with resonant X-ray spectroscopy. *Appl. Phys. A*, 85(4):351–359, December 2006.

[184] P. A. Brühwiler, O. Karis, and N. Martensson. Charge-transfer dynamics studied using resonant core spectroscopies. *Reviews of Modern Physics*, 74: 703, 2002.

[185] H. Ikeura-Sekiguchi and T. Sekiguchi. Attosecond Electron Delocalization in the Conduction Band through the Phosphate Backbone of Genomic DNA. *Phys. Rev. Lett.*, 99:228102, 2007.

[186] M.P. de Jong, R. Friedlein, S.L. Sorensen, G. Öhrwall, W. Osikowicz, C. Tengsted, S.K.M. Jönsson, M. Fahlman, and W.R. Salaneck. Orbital-specific dynamic charge transfer from Fe(II)-tetraphenylporphyrin molecules to molybdenum disulfide substrates. *Phys. Rev. B*, 72(3):035448, Jul 2005.

[187] U. Höfer, I.L. Shumay, C. Reuss, U. Thomann, W. Wallauer, and T. Fauster. Time–resolved coherent photoelectron spectroscopy of quantized electronic states on metal surfaces. *Science*, 277(5331):1480–1482, SEP 5 1997.

[188] P. M. Echenique, R. Berndt, E. V. Chulkov, Th. Fauster, A. Goldmann, and U. Höfer. Decay of electronic excitations at metal surfaces. *Surface Science Reports*, 52(7-8):219 – 317, 2004.

[189] J. Luning, J.E. Rubensson, C. Ellmers, S. Eisebitt, and W. Eberhardt. Site- and symmetry-projected band structure measured by resonant inelastic soft x-ray scattering. *Phys. Rev. B*, 56(20):13147–13150, NOV 15 1997.

[190] O. Fuchs. *Resonante inelastische Röntgenstreuung an Berylliumsulfid.* Diploma thesis, Universität Würzburg, 2001.

[191] C. Dallera, M. Grioni, A. Shukla, G. Vanko, and J.L. Sarrao. Truly bulk-sensitive spectroscopic measurements of valence in heavy fermion materials. *J. Synchr. Rad.*, 9(Part 4):242–245, JUL 2002.

[192] L. Weinhardt, O. Fuchs, E. Umbach, C. Heske, A. Fleszar, and W. Hanke. Resonant inelastic soft x-ray scattering, x-ray absorption spectroscopy, and density functional theory calculations of the electronic bulk band structure of CdS. *Phys. Rev. B*, 75(16):165207, APR 2007.

[193] J. Gråsjö, E. Andersson, J. Forsberg, L. Duda, E. Henke, W. Pokapanich, O. Björneholm, J. Andersson, A. Pietzsch, F. Hennies, and J.-E. Rubensson. Local Electronic Structure of Functional Groups in Glycine As Anion, Zwitterion, and Cation in Aqueous Solution. *J. Phys. Chem. B*, 113(49): 16002–16006, 2009. PMID: 19916538.

[194] N. Mårtensson, M. Weinelt, O. Karis, M. Magnuson, N. Wassdahl, A. Nilsson, J. Stöhr, and M. Samant. Coherent and incoherent processes in resonant photoemission. *Appl. Phys. A*, 65:159–167, 1997.

[195] A. Nilsson, N. Wassdahl, M. Weinelt, O. Karisa, T. Wiell, P. Bennich, J. Hasselström, A. Föhlisch, J. Stöhr, and M. Samant. Local probing of the surface chemical bond usingX-ray emission spectroscopy. *Appl. Phys. A*, 65:147–154, 1997.

[196] H. Gel'mukhanov and, F. Ågren. Resonant X-ray Raman scattering. *Physics Reports*, 312(3-6):87 – 330, 1999.

[197] J. Schnadt, P.A. Brühwiler, L. Patthey, J.N. O'Shea, S. Sodergren, M. Odelius, R. Ahuja, O. Karis, M. Bassler, P. Persson, H. Siegbahn, S. Lunell, and N. Martensson. Experimental evidence for sub-3-fs charge transfer from an aromatic adsorbate to a semiconductor. *Nature*, 418(6898): 620–623, August 2002.

[198] F. Hennies, S. Polyutov, I. Minkov, A. Pietzsch, M. Nagasono, H. Ågren, L. Triguero, M.-N. Piancastelli, W. Wurth, F. Gel'mukhanov, and A. Föhlisch. Dynamic interpretation of resonant x-ray Raman scattering: Ethylene and benzene. *Phys. Rev. A*, 76(3):032505, SEP 2007.

[199] C.J. Schramm, R.P. Scaringe, D.R. Stojakovic, B.M. Hoffman, J.A. Ibers, and T.J. Marks. Chemical, spectral, structural, and charge transport properties of the "molecular metals" produced by iodination of nickel phthalocyanine. *J. Am. Chem. Soc.*, 102(22):6702–6713, 1980.

[200] Y. Shirota. Organic materials for electronic and optoelectronic devices. *J. Mat. Chem.*, 10(1):1–25, 2000.

[201] P. Peumans and S.R. Forrest. Very-high-efficiency double-heterostructure copper phthalocyanine/C-60 photovoltaic cells. *Appl. Phys. Lett.*, 79(1):126–128, JUL 2 2001.

[202] A. Kahn, N. Koch, and W.Y. Gao. Electronic structure and electrical properties of interfaces between metals and pi-conjugated molecular films. *J. Pol. Science B*, 41(21):2529–2548, NOV 1 2003.

[203] M Knupfer and H Peisert. Electronic properties of interfaces between model organic semiconductors and metals. *Physica Status Solid A*, 201(6):1055–1074, MAY 2004.

[204] N. Ueno and S. Kera. Electron spectroscopy of functional organic thin films: Deep insights into valence electronic structure in relation to charge transport property. *Progress in Surface Science*, 83:490–557, 2008.

[205] S. Kera, A. Abduaini, M. Aoki, K.K. Okudaira, N. Ueno, Y. Harada, Y. Shirota, and T. Tsuzuki. Characterization of ultrathin films of titanyl phthalocyanine on graphite: PIES and UPS study. *Thin Solid Films*, 327-329:278 – 282, 1998.

[206] M.-S. Liao and S. Scheiner. Electronic structure and bonding in metal phthalocyanines, Metal=Fe, Co, Ni, Cu, Zn, Mg. *J. Chem. Phys.*, 114(22): 9780–9791, 2001.

[207] T. Schwieger, H. Peisert, M. S. Golden, M. Knupfer, and J. Fink. Electronic structure of the organic semiconductor copper phthalocyanine and K-CuPc studied using photoemission spectroscopy. *Phys. Rev. B*, 66(15):155207, Oct 2002.

[208] S. Kera, H. Yamane, I. Sakuragi, K.K. Okudaira, and N. Ueno. Very narrow photoemission bandwidth of the highest occupied state in a copper-phthalocyanine monolayer. *Chem. Phys. Lett.*, 364(1-2):93 – 98, 2002.

[209] C. Bobisch, Th. Wagner, A. Bannani, and R. Möller. Ordered binary monolayer composed of two organic molecules: Copper-phthalocyanine and 3,4,9,10-perylene-tetra-carboxylicdianhydride on Cu(111). *J. Chem. Phys*, 119:9804–9808, 2003.

[210] S. Kera, Y. Yabuuchi, H. Yamane, H. Setoyama, K. K. Okudaira, A. Kahn, and N. Ueno. Impact of an interface dipole layer on molecular level alignment at an organic-conductor interface studied by ultraviolet photoemission spectroscopy. *Phys. Rev. B*, 70:6, 2004.

[211] K. Walzer, T. Toccoli, A. Pallaoro, R. Verucchi, T. Fritz, K. Leo, A. Boschetti, and S. Iannotta. Morphological and optical properties of titanyl phthalocyanine films deposited by supersonic molecular beam epitaxy (SuMBE). *Surface Science*, 573(3):346–358, DEC 20 2004.

[212] L. Lozzi, S. Santucci, S. La Rosa, B. Delley, and S. Picozzi. Electronic structure of crystalline copper phthalocyanine. *J. Chem. Phys.*, 121(4):1883–1889, 2004.

[213] S. Kera, M.B. Casu, K.R. Bauchspieß, D. Batchelor, Th. Schmidt, and E. Umbach. Growth mode and molecular orientation of phthalocyanine molecules on metal single crystal substrates: A NEXAFS and XPS study. *Surface Science*, 600(5):1077 – 1084, 2006.

[214] C. Stadler, T.-L. Lee, S. Hansen, J. Zegenhagen, F. Pollinger, C. Kumpf, and E. Umbach. Structural investigation of the adsorption of SnPc on Ag(111) using normal-incidence x-ray standing waves. *Phys. Rev. B*, 74:35404–35411, 2006.

[215] T. Nishi, K. Kanai, Y. Ouchi, M.R. Willis, and K. Seki. Oxygen effects on the interfacial electronic structure of titanyl phthalocyanine film: p-Type doping, band bending and Fermi level alignment. *Chem. Phys.*, 325(1):121 – 128, 2006. Electronic Processes in Organic Solids.

[216] S. Kera, M. B. Casu, A. Schöll, Th. Schmidt, D. Batchelor, E. Rühl, and E. Umbach. High-resolution inner-shell excitation spectroscopy of H_2-phthalocyanine. *J. Chem. Phys.*, 125:8, 2006.

[217] S. Kera, H. Fukagawa, T. Kataoka, S. Hosoumi, H. Yamane, and N. Ueno. Spectroscopic evidence of strong π–π interorbital interaction in a lead-phthalocyanine bilayer film attributed to the dimer nanostructure. *Phys. Rev. B*, 75:121305, 2007.

[218] E. Salomon, N. Papageorgiou, T. Angot, A. Verdini, A. Cossaro, L. Floreano, A. Morgante, L. Giovanelli, and G. Le Lay. Lead Phthalocyanine Films by

Near Edge X-ray Absorption Fine Structure Spectroscopy. *J. Phys. Chem. C*, 111(33):12467–12471, 2007.

[219] N. Ueno, S. Kera, K. Sakamoto, and K. Okudaira. Energy band and electron-vibration coupling in organic thin films: photoelectron spectroscopy as a powerful tool for studying the charge transport. *Appl. Phys. A*, 92(3):495–504, August 2008.

[220] I. Kröger, B. Stadtmüller, C. Stadler, J. Ziroff, M. Kochler, A. Stahl, F. Pollinger, T.-L. Lee, J. Zegenhagen, F. Reinert, and C. Kumpf. Sub-monolayer growth of copper-phthalocyanine on Ag(111). *New J. Phys.*, 12 (8):083038, 2010.

[221] W. Chen, L. Wang, D.C. Qi, S. Chen, X.Y. Gao, and A.T.S. Wee. Probing the ultrafast electron transfer at the CuPc/Au(111) interface. *Appl. Phys. Lett.*, 88(18):184102, 2006.

[222] N. Peltekis, B.N. Holland, L.F.J. Piper, A. DeMasi, K.E. Smith, J.E. Downes, I.T. McGovern, and C. McGuinness. The local electronic structure of tin phthalocyanine studied by resonant soft X-ray emission spectroscopies. *Applied Surface Science*, 255(3):764 – 766, 2008. 11th International Conference on the Formation of Semiconductor Interfaces (ICFSI-11).

[223] H. Peisert, I. Biswas, L. Zhang, B. E. Schuster, M. B. Casu, A. Haug, D. Batchelor, M. Knupfer, and T. Chasse. Unusual energy shifts in resonant photoemission spectra of organic model molecules. *J. Chem. Phys.*, 130 (19), MAY 21 2009.

[224] H. Peisert, I. Biswas, U. Ayguel, A. Vollmer, and T. Chasse. Electronic structure of cobalt phthalocyanine studied by resonant photoemission: Localization of Co-related valence band states. *Chem. Phys. Lett.*, 493(1-3): 126–129, JUN 17 2010.

[225] C. Stadler, S. Hansen, I. Kröger, C. Kumpf, and E. Umbach. Tuning intermolecular interaction in long-range ordered sub-monolayer organic films. *Nature Physics*, 5:153–185, 2009.

[226] M.E. Greif. *Geometrische und elektronische Struktur ultradünner organischer Heteroschichten: SnPc/PTCDA/Ag(111).* Diploma thesis, Universität Würzburg, 2010.

[227] O.K. Rice. *J. Chem. Phys.*, 1:375, 1933.

[228] U. Fano. *Nuovo Cimento*, 12:156, 1935.

[229] U. Fano. Effects of Configuration Interaction on Intensities and Phase Shifts. *Physical Review*, 124:1866 – 1878, 1961.

[230] L.C. Davis and L.L.A. Feldkamp. Resonant Photoemission involving Super-Coster-Kronig Transitions. *Phys. Rev. B*, 23(12):6239–6253, 1981.

[231] M. F. López, A. Höhr, C. Laubschat, M. Domke, and G. Kaindl. Resonant Photoemission vs. Coster-Kronig Auger Decay At the L III Thresholds of Ni Metal and CuO. *EPL*, 20(4):357, 1992.

[232] A. Kivimäki, H. Aksela, S. Aksela, and O.P. Sairanen. M(2,3)M(4,5)M(4,5) Super-Coster-Kronig spectra of solid Ga and resonance effects around the 3p threshold. *Phys. Rev. B*, 47(8):4181–4186, FEB 15 1993.

[233] T. Kinoshita, T. Ikoma, A. Kakizaki, T. Ishii, J. Fujii, H. Fukutani, K. Shimada, A. Fujimori, T. Okane, and S. Sato. Evidence for Fano interference in spun polarization of the 6eV satellite in Ni valence band photoemission. *Phys. Rev. B*, 47(11):6787–6790, MAR 15 1993.

[234] M.Y. Adam, S. Stranges, M. Desimone, S. Svensson, and F.C. Farnoux. Coster–Kronik decay of 3p core–excited states of atomic zinc. *Phys. Rev. A*, 49(3):1797–1805, MAR 1994.

[235] A. Föhlisch, P. Feulner, F. Hennies, A. Fink, D. Menzel, D. Sanchez-Portal, P. M. Echenique, and W. Wurth. Direct observation of electron dynamics in the attosecond domain. *Nature*, 436(7049):373–376, July 2005.

[236] R. Bruhn, E. Schmidt, H. Schröder, and B. Sonntag. Resonant Satellite Photoemission of atomic Cu. *J. Phys. B*, 15(13):L441–L444, 1982.

[237] J.M. Bizau, P. Gerard, F.J. Wuilleumier, and G. Wendin. Resonant Photoemission in atomic Calcium — a test case for atomic theory. *Phys. Rev. Lett.*, 53(22):2083–2086, 1984.

[238] D.-Q. Jiang, J.-C. Liu, X.-D. Yang, and P.-F. Lu. Resonant structure due to the 3p–>3d transition in the photoionization of Ca+. *Phys. Lett. A*, 288(2): 95 – 100, 2001.

[239] R. Bruhn, E. Schmidt, H. Schröder, and B. Sonntag. Resonant photoemission of atomic Mn. *Phys. Lett. A*, 90(1-2):41 – 44, 1982.

[240] L.H. Tjeng, C.T. Chen, J. Ghijsen, P. Rudolf, and F. Sette. Giant Cu 2p resonance in CuO valence band photoemission. *Phys. Rev. Lett.*, 67(4):501–504, JUL 22 1991.

[241] A. Tanaka and T. Jo. Resonant 3d, 3p and 3s photoemission in transition metal exides predicted at 2p threshold. *J. Phys. Soc. Jap.*, 63(7):2788–2807, JUL 1994.

[242] A. Gorschulter and H. Merz. Localized d–d excitations in NiO(100) and CoO(100). *Phys. Rev. B*, 49(24):17293–17302, JUN 15 1994.

[243] H.A. Kramers and W. Heisenberg. *Z. Phys.*, 31:681–708, 1925.

[244] D.J. Tannor and E.J. Heller. Polyatomic Raman scattering for general harmonic potentials. *J. Chem. Phys.*, 77(1):202–218, 1982.

[245] F. Gelḿukhanov and H. Ågren. Resonant inelastic x-ray scattering with symmetry-selective excitation. *Phys. Rev. A*, 49(6):4378–4389, Jun 1994.

[246] A. Cesar, F. Gelḿukhanov, Y. Luo, H. Ågren, P. Skytt, P. Glans, J.H. Guo, K. Gunnelin, and J. Nordgren. Resonant x-ray scattering beyond the Born-Oppenheimer approximation: Symmetry breaking in the oxygen resonant x-ray emission spectrum of carbon dioxide (vol 106, pg 3439, 1997). *J. Chem. Phys.*, 106(7):3439, AUG 15 1997.

[247] S. Svensson and A. Ausmees. Recent results on Auger resonant Raman spectroscopy of free atoms and molecules. *Applied Physics A: Materials Science & Processing*, 65:107–114, 1997.

[248] O. Björneholm, S. Sundin, S. Svensson, R. R. T. Marinho, A. Naves de Brito, F. Gel'mukhanov, and H. Ågren. Femtosecond Dissociation of Core-Excited HCl Monitored by Frequency Detuning. *Phys. Rev. Lett.*, 79(17):3150–3153, Oct 1997.

[249] M. Odelius, H. Ogasawara, D. Nordlund, O. Fuchs, L. Weinhardt, F. Maier, E. Umbach, C. Heske, Y. Zubavichus, M. Grunze, J.D. Denlinger, L.G.M. Pettersson, and A. Nilsson. Ultrafast Core-Hole-Induced Dynamics in Water Probed by X-Ray Emission Spectroscopy. *Phys. Rev. Lett.*, 94(22):227401, Jun 2005.

[250] O. Fuchs, M. Zharnikov, L. Weinhardt, M. Blum, M. Weigand, Y. Zubavichus, M. Bär, F. Maier, J. D. Denlinger, C. Heske, M. Grunze, and E. Umbach. Isotope and Temperature Effects in Liquid Water Probed by X-Ray Absorption and Resonant X-Ray Emission Spectroscopy. *Phys. Rev. Lett.*, 100(2): 027801, Jan 2008.

[251] L.G.M. Pettersson, T. Tokushima, Y. Harada, O. Takahashi, S. Shin, and A. Nilsson. Comment on "Isotope and Temperature Effects in Liquid Water Probed by X-Ray Absorption and Resonant X-Ray Emission Spectroscopy". *Phys. Rev. Lett.*, 100(24):249801, Jun 2008.

[252] O. Fuchs, M. Zharnikov, L. Weinhardt, M. Blum, M. Weigand, Y. Zubavichus, M. Bär, F. Maier, J. D. Denlinger, C. Heske, M. Grunze, and E. Umbach. Fuchs et al. Reply:. *Phys. Rev. Lett.*, 100(24):249802, Jun 2008.

[253] P. Skytt, P. Glans, J.-H. Guo, K. Gunnelin, C. Såthe, J. Nordgren, F. Kh. Gel'mukhanov, A. Cesar, and H. Ågren. Quenching of Symmetry Breaking in Resonant Inelastic X-Ray Scattering by Detuned Excitation. *Phys. Rev. Lett.*, 77(25):5035–5038, Dec 1996.

[254] S. Sundin, F. Gel'mukhanov, H. Ågren, S.J. Osborne, A. Kikas, O. Björneholm, A. Ausmees, and S. Svensson. Collapse of Vibrational Structure in the Auger Resonant Raman Spectrum of CO by Frequency Detuning. *Phys. Rev. Lett.*, 79(8):1451–1454, Aug 1997.

[255] A. Cesar, H. Ågren, A. Naves de Brito, S. Svensson, L. Karlsson, M. P. Keane, B. Wannberg, P. Baltzer, P. G. Fournier, and J. Fournier. Vibronic and electronic states of doubly charged H_2S studied by Auger and charge transfer spectroscopy and by ab initio calculations. *J. Chem. Phys.*, 93(2): 918–931, 1990.

[256] F. Hennies, S. Polyutov, I. Minkov, A. Pietzsch, M. Nagasono, F. Gel'mukhanov, L. Triguero, M.N. Piancastelli, W. Wurth, H. Ågren, and A. Föhlisch. Nonadiabatic effects in resonant inelastic X-ray scattering. *Phys. Rev. Lett.*, 95(16):163002, OCT 14 2005.

[257] F. Hennies, A. Pietzsch, M. Berglund, A. Föhlisch, T. Schmitt, V. Strocov, H.O. Karlsson, J. Andersson, and J.-E. Rubensson. Resonant Inelastic Scattering Spectra of Free Molecules with Vibrational Resolution. *Phys. Rev. Lett.*, 104(19):193002, MAY 14 2010.

[258] C. Guillot, Y. Ballu, J. Paigna, J. Lecante, P. Jain, K.P.and Thiry, R. Pincheaux, Y. Petroff, and L.M. Falicov. Resonant Photoemission in Nickel Metal. *Phys. Rev. Lett.*, 39:1632, 1977.

[259] O. Björnholm, J.N. Andersen, C. Wigren, A. Nilsson, R. Nyholm, and N. Martensson. Resonant Photoemission at core level shake–up thresholds — valence band statellites in nickel. *Phys. Rev. B*, 41(15):10408–10412, MAY 15 1990.

[260] A. Föhlisch, O. Karis, M. Weinelt, J. Hasselström, A. Nilsson, and N. Mårtensson. Auger Resonant Raman Scattering in Itinerant Electron Systems: Continuum Excitation in Cu. *Phys. Rev. Lett.*, 88(2):027601, Dec 2001.

[261] C. Scheuermann. *Hochauflösende Photoemissionsspektroskopie an SnPc/Ag(111) Grenzflächen.* Diploma thesis, Universität Würzburg, 2007.

[262] I. Reid, Y. Zhang, A. Demasi, A. Blueser, L. Piper, J.E. Downes, A. Matsuura, G. Hughes, and K.E. Smith. Electronic structure of the organic semiconductor copper tetraphenylporphyrin (CuTPP). *Applied Surface Science*, 256(3):720 – 725, 2009.

[263] V.Yu. Aristov, O.V. Molodtsova, V.V. Maslyuk, D.V. Vyalikh, T. Bredow, I. Mertig, A.B. Preobrajenski, and M. Knupfer. Electronic properties of potassium-doped FePc. *Organic Electronics*, 11(8):1461 – 1468, 2010.

[264] L. Weinhardt, M. Bär, M. Blum, J.D. Denlinger, W. Yang, F. Reinert, E. Umbach, and C. Heske. Resonant inelastic x–ray scattering at N_2 molecules in the gas phase. *in preparation*, 2010.

[265] L. Weinhardt, O. Fuchs, D. Batchelor, M. Bär, M. Blum, J.D. Denlinger, W. Yang, A. Schöll, F. Reinert, E. Umbach, and C. Heske. Resonant inelastic x–ray scattering at C_{60} thin films. *submitted*, 2010.

[266] S. Hüfner. Mott insulation in transition metal compounds. *Zeitschrift für Physik B*, 61(2):135–138, June 1985.

[267] S. Hüfner, T. Riesterer, and F. Hulliger. The electronic structure and the correlation energy in NiS. *Solid State Communications*, 54(8):689 – 693, 1985.

[268] I. Pollini. Coulomb correlation energy versus covalence in transition-metal compounds. *Journal of Electron Spectroscopy and Related Phenomena*, 152 (3):107 – 114, 2006.

[269] P. Weightman, T. D. Thomas, and D. R. Jennison. KVV Auger spectrum of F_2: The importance of hole–hole correlation. *J. Chem. Phys.*, 78(4):1652–1662, 1983.

[270] V.K. Thorsmølle, B. Wenger, J. Teuscher, C. Bauer, and J.-E. Moser. Dynamics of Photoinduced Interfacial Electron Transfer and Charge Transport in Dye-Sensitized Mesoscopic Semiconductors. *Chimia*, 61:631–634, 2007.

[271] C.R. McNeill and N.C. Greenham. Charge transport dynamics of polymer solar cells under operating conditions: Influence of trap filling. *Appl. Phys. Lett.*, 93(20):203310, 2008.

[272] A. Troisi, D.L. Cheung, and D. Andrienko. Charge Transport in Semiconductors with Multiscale Conformational Dynamics. *Phys. Rev. Lett.*, 102(11), MAR 20 2009.

[273] T. Vehoff, Y.S. Chung, K. Johnston, A. Troisi, D.Y. Yoon, and D. Andrienko. Charge Transport in Self-Assembled Semiconducting Organic Layers: Role of Dynamic and Static Disorder. *J. Phys. Chem. C*, 114(23):10592–10597, JUN 17 2010.

[274] H. Guo, P. Saalfrank, and T. Seideman. Theory of photoinduced surface reactions of admolecules. *Progress in Surface Science*, 62(7-8):239 – 303, 1999.

[275] A.H. Zewail. Femtochemistry: Atomic-Scale Dynamics of the Chemical Bond. *J. Phys. Chem. A*, 104(24):5660–5694, 2000.

[276] R. Kosloff, G. Katz, and Y. Zeiri. Dynamics of charge transfer states on metal surfaces: The competition between reactivity and quenching. *Faraday Discuss.*, 117:291–301, 2000.

[277] J. Hubbard. Electron correlation in narrow energy bands. *Proceedings of the Royal Society of London A*, 276(1364):238–257, 1963.

[278] J. Hubbard. Electronic correlations in narrow energy bands 2. degenerate band case. *Proceedings of the Royal Society of London A*, 277(1368):237–259, 1964.

[279] J. Hubbard. Electron correlation in narrow energy bands 3. improved solution. *Proceedings of the Royal Society of London A*, 281(1384):401+, 1964.

[280] J. Hubbard. Electron correlation in narrow energy bands 4. the atomic representation. *Proceedings of the Royal Society of London A*, 285(1403):542–560, 1965.

[281] J. Hubbard. Electron correlation in narrow energy bands 5. a perturbation expansion about the atomic limit. *Proceedings of the Royal Society of London A*, 296(1403):82–99, 1967.

[282] G. Kotliar and D. Vollhardt. Strongly Correlated Materials: Insights From Dynamical Mean-Field Theory. *Physics Today*, 57(3):53–59, 2004.

[283] A Georges and G. Kotliar. Hubbard model in infinite dimensions. *Phys. Rev. B*, 45(12):6479–6483, MAR 15 1992.

[284] J. Kunes, A.V. Lukoyanov, V.I. Anisimov, R.T. Scalettar, and W.E. Pickett. Collapse of magnetic moment drives the Mott transition in MnO. *Nature Materials*, 7(3):198–202, March 2008.

[285] M. Sing. Professorial Dissertation, Universität Würzburg, 2010.

[286] M. Kochler. *High–resolution photoelectron spectroscopy at thin CuPc films on nobel metal (111) surfaces.* Diploma thesis, Universität Würzburg, 2009.

[287] S. Hame. *Hochauflösende Photoelektronenspektroskopie an dünnen Filmen von NTCDA auf Ag(111)*. Diploma thesis, Universität Würzburg, 2007.

[288] T. Laugks. *Tieftemperaturphasen von PTCDA und NTCDA auf Ag(111)*. Diploma thesis, Universität Würzburg, 2008.

[289] A. Schöll, L. Kilian, Y. Zou, J. Ziroff, S. Hame, F. Reinert, E. Umbach, and R. H. Fink. Disordering of an Organic Overlayer on a Metal Surface Upon Cooling. *Science*, 329(5989):303–305, 2010.

[290] M. Sing, J. Meyer, M. Hoinkis, S. Glawion, P. Blaha, G. Gavrila, C. S. Jacobsen, and R. Claessen. Structural vs electronic origin of renormalized band widths in TTF-TCNQ: An angular dependent NEXAFS study. *Phys. Rev. B*, 76(24):245119, Dec 2007.

[291] P. Fulde. *Electronic Correlations in Molecules and Solids*. Springer, 1995.

[292] J. B. Foresman and A. Frisch. *Exploring Chemistry with Electronic Structure Methods*. Gaussian, 1996.

[293] A.B. Sieval, A.L. Demirel, J.W.M. Nissink, M.R. Linford, J.H. van der Maas, W.H. Jeu, H. Zuilhof, and E.J.R. Sudhölter. Highly Stable Si-C Linked Functionalized Monolayers on the Silicon (100) Surface. *Langmuir*, 14:1759–1768, 1998.

[294] D.K. Aswal, S. Lenfant, D. Guerin, J.V. Yakhmi, and D. Vuillaume. Self assembled monolayers on silicon for molecular electronics. *Analytica Chimica Acta*, 568(1-2):84–108, may 2006.

[295] R. Cohen, N. Zenou, D. Cahen, and S. Yitzchaik. Molecular electronic tuning of Si surfaces. *Chem. Phys. Lett.*, 279(5-6):270 – 274, 1997.

[296] R. Cohen, L. Kronik, A. Shanzer, D. Cahen, A. Liu, Y. Rosenwaks, J.K. Lorenz, and A.B. Ellis. Molecular Control over Semiconductor Surface Electronic Properties:â€‰ Dicarboxylic Acids on CdTe, CdSe, GaAs, and InP. *J. Am. Chem. Soc.*, 121(45):10545–10553, 1999.

[297] A. Vilan, O. Yaffe, A. Biller, A. Salomon, A. Kahn, and D. Cahen. Molecules on Si: Electronics with Chemistry. *Advanced Materials*, 22(2):140–159, 2010.

[298] Adi Salomon, Till Böcking, J. Justin Gooding, and David Cahen. How Important Is the Interfacial Chemical Bond for Electron Transport through Alkyl Chain Monolayers? *Nano Letters*, 6(12):2873–2876, 2006. PMID: 17163722.

[299] O. Seitz, A. Vilan, H. Cohen, C. Chan, J. Hwang, A. Kahn, and D. Cahen. Effect of doping on electronic transport through molecular monolayer junctions. *J. Am. Chem. Soc.*, 129(24):7494+, JUN 20 2007.

[300] A. Salomon, T. Böcking, O. Seitz, T. Markus, F. Amy, C. Chan, W. Zhao, D. Cahen, and A. Kahn. What is the Barrier for Tunneling Through Alkyl Monolayers? Results from n- and p-Si–Alkyl/Hg Junctions. *Advanced Materials*, 19:445–450, 2007.

[301] A. Salomon, H. Shpaisman, O. Seitz, T. Böcking, and D. Cahen. Temperature-dependent electronic transport through alkyl chain monolayers: Evidence for a molecular signature. *J. Phys. Chem. C*, 112(10):3969–3974, MAR 13 2008.

[302] J.E. Falk and R.J. Fleming. Calculation of the electronic energy band structure of polyethylene. *J. Phys. C*, 6:2954–2966, 1973.

[303] A. Karpfen. Ab initio studies on polymers. V. All-trans-polyethylene. *J. Chem. Phys.*, 75(1):238–245, 1981.

[304] K. Seki, N. Ueno, U.O. Karlsson, R. Engelhardt, and E.-E. Koch. Valence bands of oriented finite linear chain molecular solids as model compounds of polyethylene studied by angle-resolved photoemission. *Chem. Phys.*, 105 (1-2):247–265, June 1986.

[305] C. Zubrägel, F. Schneider, M. Neumann, G. Hähner, C. Wöll, and M. Grunze. Electronic structure of alkane chains. Complete one-dimensional band structures of the valence states. *Chem. Phys. Lett.*, 219:127–131, 1994.

[306] H. Ishii, E. Morikawa, S. J. Tang, D. Yoshimura, E. Ito, K. Okudaira, T. Miyamae, S. Hasegawa, P. T. Sprunger, N. Ueno, K. Seki, and V. Saile. Electronic structure and molecular orientation of well-ordered polyethylene oligomer (n-C44H90) on Cu(100) and Au(111) surfaces studied by UV photoemission and low energy electron diffraction. *Journal of Electron Spectroscopy and Related Phenomena*, 101-103:559–564, June 1999.

[307] D. Yoshimura, H. Ishii, Y. Ouchi, T. Miyamae, S. Hasegawa, K.K. Okudaira, N. Ueno, and K. Seki. Simulation study of angle-resolved photoemission spectra and intramolecular energy-band dispersion of a poly(tetrafluoroethylene) oligomer film. *J. Chem. Phys.*, 120(22):10753–10762, 2004.

[308] D. Yoshimura, H. Ishii, Y. Ouchi, E. Ito, T. Miyamae, S. Hasegawa, K.K. Okudaira, N. Ueno, and K. Seki. Angle-resolved ultraviolet photoelectron spectroscopy and theoretical simulation of a well-ordered ultrathin film of tetratetracontane ($n-C44H90$) on Cu(100): Molecular orientation and intramolecular energy-band dispersion. *Phys. Rev. B*, 60(12):9046–9060, Sep 1999.

[309] P. Puschnig, S. Berkebile, A.J. Fleming, G. Koller, K. Emtsev, T. Seyller, J.D. Riley, C. Ambrosch-Draxl, F.P. Netzer, and M.G. Ramsey. Reconstruction of Molecular Orbital Densities from Photoemission Data. *Science*, 326:702–706, 2009.

[310] T. Miller, A. Samsavar, G. E. Franklin, and T.C. Chiang. Quantum-Well States in a Metallic System: Ag on Au(111). *Phys. Rev. Lett.*, 61(12):1404–1407, Sep 1988.

[311] J.J. Paggel, T. Miller, and T.-C. Chiang. Quantum-Well States as Fabry–Pérot Modes in a Thin–Film Electron Interferometer. *Science*, 283(5408): 1709–1711, 1999.

[312] T.-C. Chiang. Photoemission studies of quantum well states in thin films. *Surface Science Reports*, 39(7-8):181 – 235, 2000.

[313] M. Milun, P. Pervan, and D. P. Woodruff. Quantum well structures in thin metal films: simple model physics in reality? *Reports on Progress in Physics*, 65(2):99, 2002.

[314] A. Ernst, J. Henk, M. Lüders, Z. Szotek, and W. M. Temmerman. Quantum-size effects in ultrathin Ag films on V(001): Electronic structure and photoelectron spectroscopy. *Phys. Rev. B*, 66(16):165435, Oct 2002.

[315] L. Huang, X. G. Gong, E. Gergert, F. Forster, A. Bendounan, F. Reinert, and Z. Zhang. Evolution of a symmetry gap and synergetic quantum well states in ultrathin Ag films on Au(111) substrates. *Europhysics Letters*, 78 (5):57003, 2007.

[316] M. Wiessner, J. Ziroff, A. Schöll, L. Dössel, P. Puschnig, K. Müllen, F. Forster, and F. Reinert. *in preparation*, 2010.

[317] M. Zharnikov, W. Geyer, A. Golzhauser, S. Frey, and M. Grunze. Modification of alkanethiolate monolayers on Au-substrate by low energy electron irradiation: Alkyl chains and the S/Au interface. *Phys. Chem. Chem. Phys.*, 1(13):3163–3171, Jul 1999.

[318] M. Zharnikov, S. Frey, K. Heister, and M. Grunze. Modification of Alkanethiolate Monolayers by Low Energy Electron Irradiation: Dependence on the Substrate Material and on the Length and Isotopic Composition of the Alkyl Chains. *Langmuir*, 16(6):2697–2705, 2000.

[319] M. Zharnikov and M. Grunze. Modification of thiol-derived self-assembling monolayers by electron and x-ray irradiation: Scientific and lithographic aspects. *J. Vac. Scie. Tech. B*, 20(5):1793–1807, 2002.

[320] A.S. Duwez. Exploiting electron spectroscopies to probe the structure and organization of self-assembled monolayers: a review. *Journal of Electron Spectroscopy and Related Phenomena*, 134(2-3):97–138, February 2004.

[321] A.T.S. Wee, K. Li, and C.C. Tin. Surface chemical states on LPCVD-grown 4H-SiC epilayers. *Applied Surface Science*, 126:34–42, 1998.

[322] M.L. Shek. Observations regarding a c(4x4) C-Si(100) surface. *Surface Science*, 414:353–362, 1998.

Own Publications

[A1] F. Amy, C.K. Chan, W. Zhao, J. Hyung, M. Ono, T. Sueyoshi, S. Kera, G. Nesher, A. Salomon, L. Segev, O. Seitz, H. Shpaisman, A. Schöll, M. Häming, T. Böcking, D. Cahen, L. Kronik, N. Ueno, E. Umbach, and A. Kahn. Radiation Damage to Alkyl Chain Monolayers on Semiconductor Substrates Investigated by Electron Spectroscopy. *J. Phys. Chem. B*, 110: 21826–21832, 2006.

[A2] O. Seitz, A. Vilan, H. Cohen, J. Hwang, M. Häming, A. Schöll, E. Umbach, A. Kahn, and D. Cahen. Doping Molecular Monolayers: Effect on Electrical Transport Through Alkyl Chains on Si. *Adv. Funct. Mater.*, 18:1 – 3, 2008.

[A3] M.L.M. Rocco, M. Häming, D.R. Batchelor, R. Fink, A. Schöll, and E. Umbach. Electronic relaxation effects in condensed polyacenes: A high-resolution photoemission study. *J. Chem. Phys.*, 129(7):074702, 2008.

[A4] M. Häming, C. Scheuermann, A. Schöll, F. Reinert, and E. Umbach. Coverage dependent organic-metal interaction studied by high-resolution core level spectroscopy: SnPc (sub)monolayers on Ag(111). *Journal of Electron Spectroscopy and Related Phenomena*, 174(1-3):59 – 64, 2009. Advanced Spectroscopies of Molecular Materials for Electronics.

[A5] M. Häming, J. Ziroff, E. Salomon, O. Seitz, D. Cahen, A. Kahn, A. Schöll, F. Reinert, and E. Umbach. Electronic band structure and ensemble effect in monolayers of linear molecules investigated by photoelectron spectroscopy. *Phys. Rev. B*, 79(15):155418, 2009.

[A6] M. Häming, M. Greif, M. Wiener, A. Schöll, and F. Reinert. Characterization of ultra-thin organic hetero-interfaces – SnPc/PTCDA/Ag(111). *Surface Science*, 604(19-20):1619 – 1622, 2010.

[A7] M. Häming, M. Greif, C. Sauer, A. Schöll, and F. Reinert. Electronic structure of ultrathin heteromolecular organic-metal interfaces: SnPc/PTCDA/Ag(111) and SnPc/Ag(111). *Phys. Rev. B*, 82(23):235432, 2010.

List of Figures

List of Tables

Danksagung

Bei der Entstehung dieser Arbeit haben viele Personen auf ganz unterschiedliche Art und Weise mitgewirkt. Dadurch durfte ich sehr lehrreiche, abwechslungsreiche und interessante Jahre durchleben mit zum Teil unvergesslichen Erlebnissen, die ich nicht missen möchte. Bei all diesen Mitstreitern möchte ich mich an dieser Stelle ganz herzlich bedanken, besonders bei den im Folgenden aufgeführten Personen.

Vielen Dank an meine beiden Doktorväter, *Prof. Dr. E. Umbach* und *Prof. Dr. F. Reinert*, die beide viel Interesse an meiner Arbeit zeigten und mir immer viel Freiraum ließen, um meiner Neugierde nachzugeben und eigene Ideen umzusetzen. Da nach dem Wechsel von Prof. Umbach nach Karlsruhe Prof. Reinert mehr und mehr Betreuungsaufgaben übernommen hat, konnte ich letztlich von beiden profitieren. Die Diskussionen mit ihnen waren immer sehr fruchtbar und haben neue Denkanstöße gegeben.

Besonderen Dank gilt *Dr. Achim Schöll*, der mich in vielerlei Hinsicht sehr gut betreut, unterstützt und gefördert hat, besonders bei Messzeiten. Er hat einen Grundstein für diese Arbeit gelegt, indem er mir recht früh beigebracht hat, wie man möglichst effizient viel aus den Maschinen herauskitzelt — und wie man sich zur Not auch eine Woche lang ausschließlich aus dem Süßigkeitenautomat ernährt... Seine lockere Art ist sehr angenehm.

Prof. Dr. R. Claessen danke ich für die Erstellung des Zweitgutachtens und *P.D. Dr. R. F. Fink* für seine Teilnahmen am Promotionskolloquium als dritter Prüfer.

Für das Gelingen dieser Arbeit waren auch die vielen Helfer bei BESSY wichtig. Besonderen Dank gilt hier *Dr. David R. Batchelor*, der die UE52-PGM Beamline gewartet, optimiert und weiterentwickelt hat, so dass wir immer sehr gute Messbedingungen hatten. Durch sein Interesse an unseren Messungen und den daraus folgenden intensiven Diskussionen hat er mir einiges beigebracht. Sein besonderer Humor hat die Messzeiten aufgelockert und zum Erlebnis gemacht. Außerdem war die Truppe vom SMART immer recht hilfsbereit, besonders *Dr. Thomas Schmidt* und *Dr. Florian Maier*. Desweiteren hat sich *Dr. Gianina Gavrilla* bei den Messzeiten am UE112 Strahlrohr sehr engagiert. Dem Synchrotron Team aus Würzburg, das viele Mitglieder hat, danke ich für die gute Zusammenarbeit und eine ordentliche Portion Galgenhumor, wie z.B. *Tina Graber*, *Christoph Scheuermann*, *Markus Scholz*, *Simon Hame*, *Michael Greif* usw.

Obrigada, *Prof. Dr. M. L. Rocco*! Durch sie bekam ich es mit Polyacen Molekülen zu tun und wurde in eine fruchtbare deutsch–brasilianische Zusammenarbeit involviert. Sie und ihre Familie waren sehr gastfreundlich, was uns besonders schöne Aufenthalte in Rio bescherte.

Meine ehemaligen Diplomanden *Christoph Scheuermann* und *Michael Wießner* haben maßgeblich bei der Planung, dem Aufbau und der Inbetriebnahme einer Spektroskopiekammer zu Beginn meiner Doktorandenzeit mitgewirkt. Hierbei muss auch die Mechanikwerkstatt gelobt werden, die letztlich all meine Wünsche sehr gut umgesetzt.

Die alkyl/Si SAMs wurden im Weizmann Institut in Israel von *Dr. O. Seitz* unter der Leitung von *Prof. Dr. D. Cahen* hergestellt, sowie von *Dr. Till Böcking* an der University of New South Wales in Australien.

Aufgrund meiner Mitgliedschaft im Graduiertenkolleg *GRK 1221*, durfte ich an einigen interessanten Vorlesungen und Seminaren teilnehmen und bekam somit einen besseren Zugang zu chemischen Aspekten.

Bei der gesamten Arbeitsgruppe möchte ich mich für die gute Atmosphäre und den lockeren Umgang bedanken. Die folgenden Personen haben besonders dazu beigetragen: *Dr. Florian Holch* war lange mein sehr geschätzter Büromitbewohner und Gesprächspartner bezüglich Physik und Alltagsfragen. Die Butterbemme werde ich nie mehr vergessen... *Ingo Kröger* hatte immer hilfreiche Tips bezüglich Präparation und Wachstum von Dünnschichten parat. Der Büronachbar *Dr. Lothar Weinhardt* diskutierte mit mir bereitwillig über RIXS und resonante Augerspektroskopie. Die Gespräche mit *Johannes Ziroff* waren aufgrund seiner Expertise und seiner klar strukturierenden Art immer sehr fruchtbar. Auf Messzeiten entpuptte er sich als Rincewind des Labors... *Dr. Frank Forster* teilte mit mir bereitwillig sein Fachwissen und auch gerne manch anderes...

Zum Schluss bedanke ich mich ganz herzlich bei meiner Familie, die mich immer voll unterstützt und mir mit Rat und Tat zur Seite steht.